Untangling cosmic collisions: a study of particle acceleration and magnetic fields in merging galaxy clusters

Osinga, E.

Untangling Cosmic Collisions

A study of particle acceleration and magnetic fields in merging galaxy clusters

Untangling Cosmic Collisions

A study of particle acceleration and magnetic fields in merging galaxy clusters

Proefschrift

ter verkrijging van
de graad van doctor aan de Universiteit Leiden,
op gezag van de rector magnificus prof.dr.ir. H. Bijl,
volgens besluit van het college voor promoties
te verdedigen op woensdag 1 november 2023
klokke 12.30 uur

door

Erik Osinga

geboren te Amsterdam, Nederland
in 1995

Promotor:
Prof.dr. H.J.A. Röttgering

Co-promotor:
Dr. R.J. van Weeren

Promotiecommissie:

Prof.dr. H. Hoekstra	
Prof.dr. I.A.G. Snellen	
Dr. A. Bonafede	(University of Bologna, Italy)
Prof.dr. M. Brüggen	(University of Hamburg, Germany)
Prof.dr. K. Dolag	(Ludwig Maximilian University Munich, Germany)
Dr. J. Hlavacek-Larrondo	(University of Montréal, Canada)

Cover:	*Cosmic yarn ball collision. A collision of galaxy clusters as yarn balls, digital art style.* Generated with the assistance of DALL·E 2 and edited in GIMP by the author.
Style:	TU Delft template, with modifications by Moritz Beller and the author. `https://github.com/Inventitech/phd-thesis-template`
ISBN:	978-94-6419-933-8
Printed by:	Gildeprint

An electronic version of this dissertation is available at
`http://scholarlypublications.universiteitleiden.nl/`.

Wetenschap is voortgezette twijfel

Opa Piet

To Tjissa, my Universe

Contents

1

Introduction

Just after the Universe came into being, it was an unimaginably small and hot soup of elementary particles, technically called a quark-gluon plasma (Adams et al., 2005). This soup was almost perfectly uniform, smoothed out by the postulated initial rapid expansion called inflation (Guth, 1981; Steinhardt, 1983; Linde, 1990) which likely ended before the universe was 10^{-32} seconds old. The fact that it was not perfectly uniform is predicted by quantum physics causing minute temperature fluctuations in the plasma.

As the Universe expanded more slowly after inflation, the extremely high density and temperatures started to decline, and when the Universe was a millionth of a second old, quarks combined into protons, neutrons and their antiparticle counterparts. After a full second, the Universe was cool enough that particles and antiparticles could annihilate each other and most of the energy in normal matter was converted to radiation. This marked the start of the radiation-dominated epoch of the Universe, which would last until the Universe is ~50,000 years old. During this period, the physics of everything is still rather simple, as the Universe consisted of an ionised plasma of predominantly protons, electrons, and photons forming an opaque plasma from which no light escapes. The interaction between photons and matter prevented the clumping of normal matter until after 380,000 years. Then, the Universe was cool enough for protons and electrons to finally combine into atoms for the first time (the event wrongfully termed "recombination") and the Universe became transparent. Dark matter, on the other hand, was not prevented from clumping by radiation, and could already freely grow from the initial energy density perturbations for the past 330,000 years. This has given the head-start on structure formation that is required to match the observed structure in the late-time Universe (e.g. Fig 1.1).

1.1 Large scale structure

The first radiation emitted after recombination can now be observed as the cosmic microwave background (CMB; e.g. Penzias & Wilson, 1965; Kogut et al., 1993; Hinshaw et al., 2009; Planck Collaboration et al., 2020a). The most recent observations of the CMB, made by the Planck satellite, provide strong support for the hot big bang model of an expanding Universe, with the tiny fluctuations generated by the inflationary period observed as slight temperature variations in the otherwise uniform background radiation (Planck

1

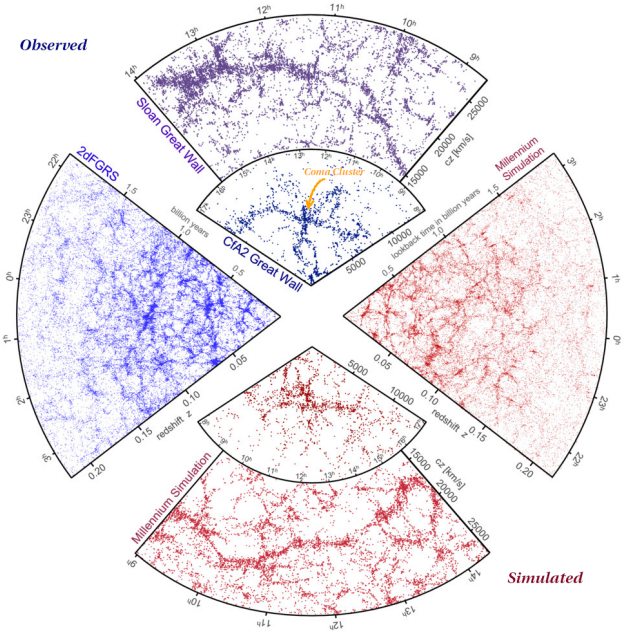

Figure 1.1: Distribution of the local large-scale structure of the Universe. The top half (in blue) shows the observed matter distribution, from three redshift surveys: CfA2 (Geller & Huchra, 1989), 2dFGRS (Colless et al., 2001) and SDSS (Gott et al., 2005). The Coma Cluster, one of the nearest and most massive clusters is indicated by the orange arrow. The lower half (in red) shows the simulated distribution from the Millenium simulations (Springel et al., 2005). Adapted from Springel et al. (2006).

Collaboration et al., 2020c). The concordance cosmological model, the ΛCDM model, fits these observations exquisitely, posing a Universe that consists, in terms of energy density, of 68% dark energy (Λ), 27% cold dark matter (CDM) and 5% ordinary baryonic matter (Planck Collaboration et al., 2020b). In the ΛCDM model, the clumped regions of dark matter, also called "haloes", grow hierarchically through accretion of matter and mergers with other haloes, described well by the Press-Schechter formalism (Press & Schechter, 1974; Lacey & Cole, 1993). As baryonic matter was accreted onto these halos, the first stars and galaxies formed by cooling and condensing gas (White & Rees, 1978). In turn, these galaxies aggregated into groups and clusters of galaxies, forming the large-scale structure as we observe it today. The gravitational collapse of the haloes can happen in all three spatial dimensions, usually first forming 2D "sheets" which collapse into 1D "filaments" which merge to form 0D "nodes" at the intersection between filaments. Most of the mass of the Universe is contained within these structures, while most of the volume of the Universe is occupied by the evolved versions of the initially underdense regions, now called voids.

Aligning structure

The described path of structure formation finally results in a filamentary matter distribution that looks like a *cosmic web* as shown in Figure 1.1. One of the largest cosmic structures is the Sloan Great Wall (Gott et al., 2005), a ~ 420 Mpc complex of superclusters. Although

not gravitationally bound, the Sloan Great Wall is a structure in the sense that it presents a network of connected matter aligning over cosmological scales. Because of their rarity, these largest scale structures present useful tests for the ΛCDM paradigm as they can constrain the initial fluctuation field or possibly challenge the uniformity of it (e.g. Sheth & Diaferio, 2011). Similarly, patterns in the orientation of galaxies within the large-scale structure can be used to test the cosmological model, since galaxies will be affected by the tidal forces imparted on them during structure formation (Codis et al., 2018; Kraljic et al., 2020). Extending this idea, the radio jets coming from active supermassive black holes (See Sect. 1.3) in the centres of galaxies could also be useful tools to trace the uniformity of the Universe on very large scales. A possible connection between radio jets and the large-scale structure of the Universe was implied by studies finding non-uniform jet orientations over large regions of the sky (Taylor & Jagannathan, 2016; Contigiani et al., 2017). However, small systematic effects in how the data was taken or analysed might result in significant non-uniformity and bias these results. Studies that incorporate redshifts to be less affected by such systematics, such as the study we perform in Chapter 2, have yet to conclusively find significant alignment of radio jets over large regions in the Universe (Panwar et al., 2020; Osinga et al., 2020; Simonte et al., 2023).

On slightly smaller scales, at the nodes of the cosmic web, where the filamentary structures meet each other, the largest gravitationally bound structures in the Universe are formed: galaxy clusters. These objects are the main focus of this thesis.

1.2 Galaxy clusters

Galaxy clusters are the most massive virialised objects to have formed from the merging of smaller haloes. They typically have masses[1] in the range $M_{500} = 10^{14} - 10^{15} M_{\odot}$, with dark matter making up 80% of the total mass (e.g. Vikhlinin et al., 2006). These large masses imply that clusters must have originated from large collapsing regions at high redshift, (radii of ~ 15 comoving Mpc at $z \sim 2$; Muldrew et al., 2015), which implies that clusters can be considered a representative sample of the Universe, in which the mean matter content is universal. This makes clusters an important laboratory for cosmology, as the number counts and gas mass fraction can be used to constrain cosmological parameters (e.g. Ettori et al., 2009; Planck Collaboration et al., 2016b). Clusters also provide important evidence for dark matter, with the most notable example being the Bullet Cluster (Clowe et al., 2004, 2006; Bradač et al., 2006; Paraficz et al., 2016, see also Fig. 1.2).

The intracluster medium

The galaxies inside a cluster make up only a few per cent of the total mass budget or roughly 10% of all the baryonic mass in a cluster. Most of the baryonic mass is contained in the hot ($\sim 10^7 - 10^8$ K or $\sim 1 - 10$ keV) and dilute ($10^{-2} - 10^{-4}$ particles cm^{-3}) plasma in the intracluster medium (ICM). Because of the extreme temperatures, the main cooling mechanism is thermal emission in the X-ray through optically thin bremsstrahlung (e.g. Forman & Jones, 1982). The characteristic spatial scales for density and temperature gradients are ~ 100 kpc, with clusters often showing a strongly rising density profile and steeply dropping temperature profile near their cores ($< 0.3 R_{500}$; Hudson et al., 2010). Given that the sound

[1] The mass is often expressed in terms of M_{500}, which is the mass enclosed in the radius R_{500}, where the density is 500 times the critical density of the Universe, but in principle, any number could be set here.

1

Figure 1.2: Composite image of the Bullet Cluster (NASA). Red shows the hot X-ray emitting baryonic gas, as observed by the Chandra X-ray observatory (Markevitch et al., 2002). Blue shows the distribution of matter as reconstructed from gravitational lensing (Clowe et al., 2004, 2006; Bradač et al., 2006; Paraficz et al., 2016), and the galaxies are shown in the background optical image from the Hubble Space Telescope (NASA,ESA) and the Magellan Telescope (University of Arizona). The baryonic gas clearly collided and is behind both the main mass component (i.e. dark matter) and the galaxies, which both did not collide.

speed in galaxy clusters is on the order of 10^3 km s^{-1}, typical disturbances take 10^8 years to cross these scales. In comparison, the mean free path of particles in the ICM is on the order of 10 kpc, so thermal particles collide only every 10^7 years. This means that the ICM must be treated as a weakly collisional fluid, complicating the magnetohydrodynamic (MHD) description (e.g. Kunz et al., 2012).

Gravity dominates the physics in galaxy clusters, and as a result, clusters are found to be relatively *self-similar*. This means that they have properties that simply scale with mass and redshift of the dark matter halo (e.g. Kaiser, 1986; Kravtsov & Borgani, 2012; Böhringer et al., 2012). This self-similarity holds for integrated properties such as temperature, X-ray luminosity and total mass (i.e. including baryons), as well as radial profiles of electron density, pressure and gas temperature (e.g. Croston et al., 2008; Arnaud et al., 2010a; Baldi et al., 2012). These relations do however show significant scatter in regions where baryonic physics becomes important, such as the cooling core region ($r < 0.3R_{500}$) and regions of infalling or accreting substructures (Ghirardini et al., 2019). Baryonic physics can thus contribute significantly to the virialisation process of clusters while presenting only less than 20% of the total mass budget. In particular, non-thermal pressure support from turbulence, bulk gas motions, magnetic fields and cosmic rays is found to be at the level of 10% of the total pressure support in local galaxy clusters (e.g. Eckert et al., 2019). Therefore, it is important to constrain non-thermal physics in galaxy clusters to get a full picture of structure formation, which is particularly relevant in the current era of precision cosmology (Turner, 2022).

Additionally, the ICM can be heavily perturbed by the interaction between clusters and their surrounding medium. Clusters are currently still forming and growing, through accretion of matter from their surroundings and mergers with other clusters. In fact,

mergers of massive clusters are the most energetic events since the Big Bang, able to release up to 10^{64} ergs (10^{57} joules) into the ICM on Gyr timescales. This energy is dissipated through weak shocks and turbulence, mainly heating the ICM (Markevitch & Vikhlinin, 2007). The turbulence is expected to be Kolmogorov-like (Kolmogorov, 1941), meaning that energy is transported from large scales to small scales with an energy spectrum of $E(k) \propto k^{-5/3}$ where k is the wavenumber (i.e. k=$2\pi/\ell$ with ℓ the physical scale). The scales on which turbulence is injected depend on the mechanism, with feedback from radio galaxies (Sect. 1.3) disturbing the ICM on scales of tens of kpc, to Mpc-scale injection during cluster mergers. In the relaxed (i.e. non-merging) Perseus cluster, the first direct measurements of turbulent motions were made by the Hitomi satellite (Hitomi Collaboration et al., 2016). These observations showed that the ICM of the Perseus cluster is fairly quiescent, with turbulent driving scales less than 100 kpc, consistent with AGN injected turbulence (Hitomi Collaboration et al., 2018).

Turbulence and shocks can also amplify magnetic fields and accelerate particles to relativistic energies on Mpc scales (Brunetti & Jones, 2014; van Weeren et al., 2019). Clusters thus provide a unique laboratory to study magnetic fields, particle acceleration and plasma physics on large scales and at high energies. Some fundamental physical questions include how particles are accelerated and heated in the ICM, what role large-scale magnetic fields play and how plasma physics affects the formation of the large-scale Universe. Radio observations of galaxy clusters are particularly well suited to answer these questions, as will be explained in the following sections.

1.3 Radio observations of galaxy clusters

Due to the highly dynamic nature of the ICM, galaxy clusters host a diverse range of interesting radio sources. In this thesis, when 'radio emission' is mentioned, it mainly means radio emission from frequencies of approximately 10 MHz to 10 GHz, which corresponds to wavelengths between 30 meters and 3 centimetres. Almost all of the radio emission received at these frequencies is synchrotron emission. Synchrotron emission occurs when charged particles[2] are accelerated in magnetic fields and emit radiation as they spiral along the field lines.

Radio galaxies

Although the galaxies only make up a few per cent of the total mass, the supermassive black holes in the centre of the galaxies can significantly impact the ICM (Fabian, 2012). If enough material is present surrounding a supermassive black hole, a hot accretion disk of infalling matter can form. Magnetic fields surrounding the accretion disk get strongly twisted, winding into a cone above the poles of the black hole. There, two opposite jets of relativistic plasma are launched, a process that can extract rotational energy from the black hole (e.g. Blandford & Znajek, 1977). These jets can stay collimated for tens or hundreds of kpc depending on the interaction between the jets and the ambient medium (Turner & Shabala, 2023). As the jet pushes into the ambient medium, it can form diffuse plumes or lobes. The relativistic electrons in the plasma emit synchrotron radiation, creating a radio galaxy (Fig 1.3) from an active galactic nucleus (AGN).

[2]We typically only see synchrotron emission from electrons as the power radiated is inversely proportional to the rest-mass to the power four and protons are ~ 2000 times heavier than electrons.

1

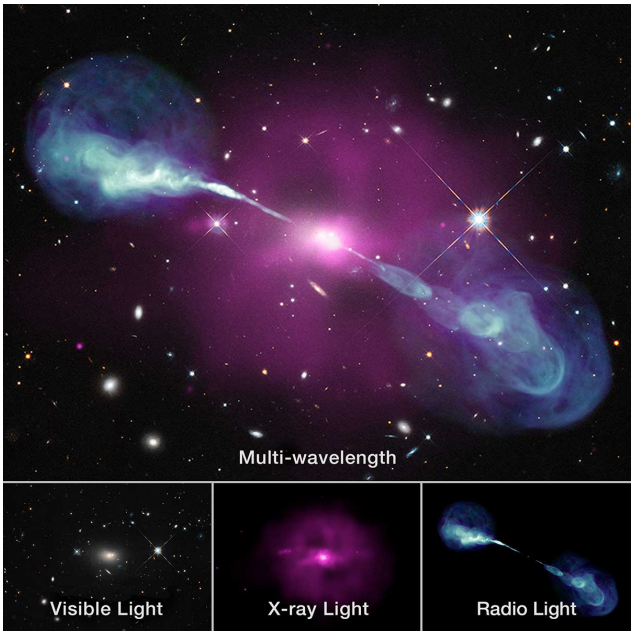

Figure 1.3: Multi-wavelength view of the radio galaxy Hercules A. In optical light, the galaxy hosting the supermassive black hole in the centre is visible. The hot gas surrounding the galaxy can be seen in X-rays, while the radio light reveals the large extended radio galaxy with collimated jets resulting in two lobes. Credit: X-ray: NASA/CXC/SAO; optical: NASA/STScI; radio: NSF/NRAO/VLA.

In galaxy clusters, the radio jets originating from AGN are often found to bend away from the direction of motion of the host galaxy as they are subject to ram pressure when moving through the ICM, causing *tailed* radio galaxies (e.g. Miley, 1980; Garon et al., 2019). When the tails are bent with a angles less than 90 degrees, they are typically called wide-angle tailed radio galaxies, while more extremely bent sources are called narrow-angle tailed radio galaxies (e.g. Fig. 1.4). The sizes of these sources can extend well beyond the host galaxy, with linear sizes from a few kpc up to a Mpc (e.g. Wilber et al., 2018). Additionally, with the advent of low-frequency telescopes such as the Low-Frequency Array (LOFAR, see Sect. 1.3.1), more examples are being found of old radio plasma that has lost a considerable amount of energy due to synchrotron and inverse Compton radiation, but is being re-energised through processes in the dynamic ICM (de Gasperin et al., 2017; van Weeren et al., 2017; Mandal et al., 2020).

Diffuse radio emission

On larger scales, radio observations of merging galaxy clusters have revealed that a large fraction of the volume of a cluster is filled with magnetic fields and ultra-relativistic electrons which can not be directly related to AGN activity (Feretti et al., 2012; van Weeren et al., 2019). This emission is generally labelled as *diffuse radio emission*, and it implies relativistic electrons with GeV energies (Lorentz factors of $\gamma > 10^3$) that spiral around μG magnetic fields in the clusters (Brunetti & Jones, 2014). Diffuse radio emission can be

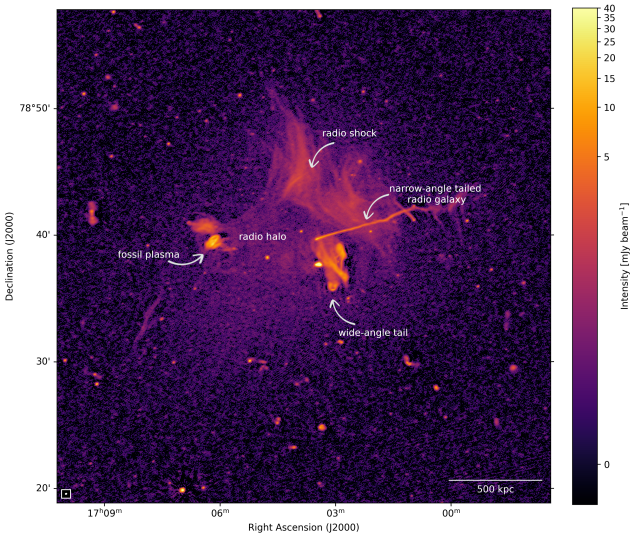

Figure 1.4: LOFAR 144 MHz image of the galaxy cluster Abell 2256 (Osinga et al., 2023a), with various types of radio emission annotated. The spherical region of enhanced radio emission near the centre is the radio halo, while the filamentary structure in the top right shows a radio shock. Various regular AGN are shown as point sources, as well as resolved bent-tailed radio AGN and re-energised plasma sources.

classified into two main categories. First, it includes radio halos, which are Mpc-sized regions of radio emission that are centrally located (e.g. Bonafede et al., 2022; Cuciti et al., 2022). Second, it comprises radio shocks (also called radio relics), which are elongated arc-shaped structures generally found on the outskirts of clusters. This thesis does not study radio shocks in detail, and therefore only a brief overview of radio shocks is presented. A more detailed introduction to radio halos and the relevant physics is given below.

Radio shocks

Radio shocks are observed about three times less frequently than radio halos in massive merging clusters (Botteon et al., 2022a), probably because they require a favourable orientation of the merger axis to be detected. The radio shocks are believed to trace merger-induced shock waves (Ensslin et al., 1998; Hoeft & Brüggen, 2007), and thus shock waves should be observable in the X-ray from temperature and density discontinuities in the ICM. These discontinuities are most easily observed if the merger is in the plane of the sky. In many cases, shock waves, co-located with radio shocks, are indeed observed in the X-ray (e.g. Tab. 2 in van Weeren et al., 2019). Due to high compression at the shock front, the turbulent magnetic field in the ICM is expected to be amplified and aligned with the propagating plane of the shock (Ensslin et al., 1998). This should result in linearly polarised emission, confirmed by observations at GHz frequencies often finding polarisation fractions of $10-50\%$ (e.g. Di Gennaro et al., 2021c; Rajpurohit et al., 2022a).

In an idealised case of a merger between two massive unperturbed clusters, it is expected that at the first encounter, two equatorial shocks are launched perpendicular to the merging axis as the ICM is compressed along the merger axis. Subsequently, two axial shocks, often

simply called merger shocks, are launched in opposite directions along the merger axis (e.g. Ha et al., 2018; Lee et al., 2020). Equatorial shocks are difficult to observe as they are less energetic than merger shocks, and in fact, only one has been observed (Gu et al., 2019). Merger shocks are typically observed on the outskirts of galaxy clusters (e.g. van Weeren et al., 2016a; Hoang et al., 2017), which agrees with simulations finding that the kinetic energy through the shocks peaks roughly 1 Gyr after shock launching, because the Mach number and shock surface area grow faster than the ICM density decreases (Vazza et al., 2012; Ha et al., 2018). This results in shocks that are typically brightest $\gtrsim 1$ Mpc from the centre of galaxy clusters.

In reality, the turbulent nature of the ICM causes a complex shock front that is composed of many shocks with different Mach numbers. Radio observations are more sensitive to the high Mach number shocks with efficient electron acceleration, while X-ray observations probe the average Mach number of the shock front (Wittor et al., 2021). Both wavelengths are thus needed to understand the complex dynamics and particle acceleration within shocks in the ICM.

Radio halos

Radio halos are characterised by low surface brightness radio emission ($\sim \mu$Jy arcsec^{-2} at 1 GHz frequencies) that generally follows the baryonic distribution of the ICM, thus being brightest at the centre of the cluster (e.g. Giovannini et al., 1993; Feretti et al., 1997a,b; Giacintucci et al., 2005; Clarke & Ensslin, 2006; Rajpurohit et al., 2018; Hlavacek-Larrondo et al., 2018; Botteon et al., 2020b; Bonafede et al., 2022). The radiation typically has a steep spectrum ($\alpha < -1$; van Weeren et al., 2019, with $S \propto \nu^{\alpha}$, where ν denotes the frequency and S the flux density) and is thus significantly brighter at low frequencies. In contrast to the high degree of polarisation of radio shocks, radio halos are almost always completely unpolarised. Three studies have claimed polarised emission from radio halos (Govoni et al., 2005; Bonafede et al., 2009; Girardi et al., 2016), but a clear detection remains elusive as the polarised signal might be related to shocks seen in projection (Pizzo et al., 2011; Rajpurohit et al., 2021a). Although radio halos should be intrinsically polarised, the turbulent nature of the ICM causes strong Faraday rotation and depolarisation (See also Sect. 1.4.2) near the centre of clusters preventing a clear detection (Govoni et al., 2013; Loi et al., 2018, 2019; Sur et al., 2021). The large size of radio halos implies that the relativistic electrons cannot all be generated at a single location in the cluster (e.g. the centre) and diffuse outwards. The typical lifetime of a GeV electron in a μG magnetic field is less than 10^8 yr given synchrotron and inverse Compton losses (van Weeren et al., 2019), while the time required for these electrons to cover Mpc distances is orders of magnitude larger ($10^9 - 10^{10}$ yr) given typical ICM bulk or plasma diffusion velocities of 10^2 km s^{-1} (Bagchi et al., 2002). This is known as the diffusion problem and requires some type of in-situ acceleration of electrons to solve (Jaffe, 1977). The two main models proposed to solve the diffusion problem for radio halos are the hadronic model and the turbulent re-acceleration model.

Hadronic model

The hadronic model states that the relativistic electrons are secondary products of collisions between cosmic ray protons (CRp) and thermal protons (e.g. Dennison, 1980; Blasi et al., 2007; Blasi & Colafrancesco, 1999), which circumvents the diffusion problem because relativistic protons have lifetimes larger than the age of the Universe and can thus easily

accumulate and distribute throughout the ICM. CRp should be present to some degree in the ICM, injected by AGN (e.g. Shi et al., 2022) and accelerated by shock waves and turbulence (e.g. Wittor, 2021). Once generated, CRp are basically confined to the cluster forever (~ 10 Gyr; Brunetti & Jones, 2014), though these cannot be directly detected. However, the presence of CRp should result in γ-ray emission from decay products of the hadronic interactions. The decay chain should go as follows (e.g. Blasi & Colafrancesco, 1999)

$$p + p \rightarrow \pi^0 + \pi^+ + \pi^- + \text{other} \tag{1.1}$$

$$\pi^0 \rightarrow \gamma\gamma \tag{1.2}$$

$$\pi^\pm \rightarrow \mu^\pm + \nu_\mu/\bar{\nu}_\mu \rightarrow e^\pm + \nu_e/\bar{\nu}_e + \bar{\nu}_\mu/\nu_\mu, \tag{1.3}$$

where the proton-proton collisions produce neutral and charged pions. The neutral pions quickly decay into gamma rays, while the charged pions decay into muons and muon neutrinos, which are also unstable and decay into cosmic ray electrons (or positrons).

This model thus poses a possible solution for generating relativistic electrons throughout the cluster volume, with a relatively straightforward prediction for the amount of gamma-ray emission from neutral pion decay. However, despite more than two decades of searches, such a γ-ray signal has not yet conclusively been detected (Reimer et al., 2003; Ackermann et al., 2014, 2015). So far, upper limits on the gamma-ray emission have ruled out the purely hadronic model for the nearest most massive cluster (Coma cluster; Brunetti et al., 2012). Although recently a gamma-ray signal was detected from the Coma Cluster by the Fermi Large Area Telescope (Xi et al., 2018; Adam et al., 2021; Baghmanyan et al., 2022), it is not clear whether the signal is associated with the ICM. Tentative evidence pointed towards the emission being extended, in line with a signal from the ICM, but due to the limited resolution of Fermi-LAT possible contamination of AGN could not be ruled out. However, even assuming that the signal can be fully attributed to the ICM, the purely hadronic model was still ruled out for the Coma Cluster and the CRp were constrained to encompass less than 2% of the thermal energy within R_{500} (Adam et al., 2021).

Another argument against proton-proton collisions being the main fueling mechanism of radio halos is the existence of radio halos with ultra-steep spectra ($\alpha < -1.5$) (Brunetti et al., 2008). Producing such a steep spectrum through hadronic collisions requires a steep spectrum for the CRp energy distribution as well, which integrated over the cluster volume would imply energy densities of CRp that are of the same order as the thermal energy density. Other than this scenario being unrealistic given the knowledge of the thermal properties of the ICM and pressure balance, ultra-steep spectrum radio halos would then also produce a large amount of γ-rays, strongly violating γ-ray upper limits (Ackermann et al., 2014, 2015).

Turbulent re-acceleration

The turbulent re-acceleration model poses to solve the diffusion problem by in-situ stochastic acceleration of electrons. Stochastic acceleration, also called Fermi-II-type acceleration (Fermi, 1949), occurs in any magnetised medium with random motions (i.e. turbulence). As a charged particle randomly collides with magnetised clouds in the ICM, it can either gain or lose energy depending on if the collision was head-on or tail-on. For any particle moving in a particular direction surrounded by randomly moving magnetised clouds, a

1

head-on collision is more likely than a tail-on collision and thus particles are, on average, accelerated in a turbulent medium.

This process is likely important in the ICM, as a fraction of the energy injected by cluster mergers is channelled into turbulence, fueling the pursuit of various models of turbulent acceleration (Brunetti & Blasi, 2005; Brunetti & Lazarian, 2016, 2011; Pinzke et al., 2017). However, because of the stochastic nature, Fermi-II acceleration is rather inefficient and the acceleration of thermal electrons is not sufficient to produce radio halos (Petrosian & East, 2008). The proposed solution is therefore *re-acceleration* of supra-thermal, or mildly relativistic, electrons. This requires a large rather uniform population of supra-thermal electrons throughout the cluster volume, and their origin is still uncertain (e.g. Nishiwaki & Asano, 2022). It is possible that these seed electrons are injected into the ICM by AGN (Vazza et al., 2021), or that they are leftovers from previous merger events. Alternatively, they could be produced by the hadronic model, which might more naturally explain the distribution throughout the cluster volume.

The turbulent re-acceleration model is currently the favoured model to explain radio halos, owing to various successful predictions. The model naturally predicts a connection between radio halos and mergers, which has been firmly established observationally (Cassano et al., 2010b; Wen & Han, 2013; Cuciti et al., 2015; Cassano et al., 2023). In this model, radio halos are expected to show a radio spectrum that steepens after some frequency ν_s set by the balance between acceleration and energy losses (Cassano et al., 2010a). Ultra-steep spectra can thus be observed at $\nu \geq \nu_s$, explaining ultra-steep spectrum radio halos which cannot exist in the purely hadronic scenario. The turbulent energy available, ultimately set by the mass and mass ratio of the merger should correlate with ν_s, making radio halos in low-mass clusters more easily observable at lower frequencies. Indeed, observations with low-frequency telescopes in mass-selected samples are now clearly finding a connection between radio halo occurrence and cluster mass (Cuciti et al., 2021a,b). Finally, the spatial distribution of the spectral index across radio halos is often patchy and disordered and shows a sub-linear point-to-point correlation with X-ray emission, consistent with a turbulent acceleration scenario with inhomogeneous conditions across the cluster volume (e.g. Botteon et al., 2020b; Bonafede et al., 2022; Rajpurohit et al., 2023).

1.3.1 Instrument: The Low Frequency Array

The study of particle acceleration and diffuse radio emission is best performed at low frequencies, as can be appreciated from the predictions of the turbulent re-acceleration model, and the generally steep radio spectra of the diffuse radio emission. The low-frequency instrument of choice for this thesis is the Low-Frequency Array (LOFAR; van Haarlem et al., 2013). LOFAR is the largest low-frequency radio interferometer to date, with baseline lengths of over 1000 km. It consists of 52 stations, spread out over eight countries in Europe, although more stations are planned. At the time of writing, the collaborative countries and distribution of stations are as follows: the Netherlands (38 stations), Germany (six stations), Poland (three stations), France (one station), Ireland (one station), Latvia (one station), Sweden (one station) and the United Kingdom (one station). Stations are planned also in Italy and Bulgaria. All stations comprise two types of antennas, the Low-Band Antennas (LBA) and the High-Band Antennas (HBA). The HBA antennas work in the frequency range of 110-240 MHz while the LBA antennas work down to the

lowest ground-based observable frequency (10-90 MHz). Below approximately 10 MHz, the ionosphere reflects radio waves back into space, preventing observations from Earth. Above 10 MHz, the ionosphere still significantly refracts radio waves, altering them by causing time delays, amplitude variations and rotation of the polarisation angle. Because the ionosphere is highly variable in space and time, different stations see differently distorted waves, requiring advanced direction-dependent calibration at high time and frequency resolution to make science-quality images (van Weeren et al., 2016b; de Gasperin et al., 2019, 2020; Tasse et al., 2021). Ionospheric distortions scale inversely with frequency, which is why LOFAR observations have been mainly focused on the HBA band, with sky surveys such as the LOFAR Two-metre Sky survey (LoTSS; Shimwell et al., 2017, 2019, 2022) leading the way. LoTSS is mapping the whole northern sky between $120-168$ MHz at $6''$ resolution to a noise level below $100\,\mu$Jy beam^{-1}. It has currently detected over 4 million radio sources, and is expected to detect ~ 15 million once complete.

Recent advances in calibration and imaging techniques are also significantly opening up the sub-100 MHz sky. The LBA counterpart to LoTSS is the LOFAR LBA Sky Survey (LoLSS; de Gasperin et al., 2021, 2023), being performed at the most sensitive part of the LBA band, $44-66$ MHz. A new, more experimental, survey has very recently started to explore the lowest frequency window from $10-30$ MHz, i.e. where wavelengths reach 10 meters or larger. This survey aims to cover the entire northern sky above 20° declination (where sources can be observed at favourable elevations), and is called the LOFAR Decametre Sky Survey (LoDeSS). Remarkably, in just over two years, the observations have already covered the proposed sky area due to the incredibly large field-of-view of LOFAR stations (> 200 deg^2) at these long wavelengths, and the multi-beam functionality of a digital telescope such as LOFAR. Whether this data can be reduced and imaged with the same success as LoLSS and LoTSS still remains to be seen, but science-quality images have recently been made at decametre wavelengths (Osinga et al., 2023a; Groeneveld et al., 2023), providing an optimistic outset.

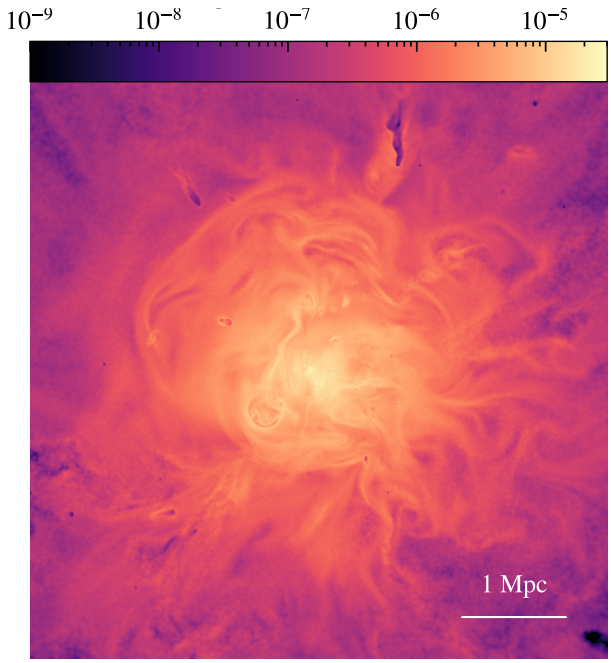

Figure 1.5: The magnetic field strength (in G) and structure as observed in an extremely high resolution cosmological zoom-in simulation centred on a massive galaxy cluster. The image shows a slice of 100 kpc thickness. The field is clearly ordered on many different scales, from kpc up to Mpc scales. Image credit: U. Steinwandel (2023).

1.4 Cluster magnetic fields

Magnetic fields permeate the Universe on a wide range of scales, spanning from the $\sim$ 100 Gauss magnet on the fridge and the $\sim$ 1G magnetic field surrounding the Earth to the $\sim 5\times10^{-6}$ G magnetic field in our galaxy (e.g. Haverkorn, 2015). These fields extend to Mpc scales in galaxy clusters (e.g. Osinga et al., 2022) and are thought to exist at nano-Gauss levels on even larger scales in the intergalactic medium (e.g. Amaral et al., 2021). Although the origin and evolution of these Mpc scale magnetic fields, or cosmic magnetic fields, are one of the major mysteries in astrophysics, theoretical work and simulations show that if a very weak seed field ($< 10^{-10}$ G) is present, small-scale dynamo processes can amplify the fields to μG values in galaxy clusters (Ryu et al., 2008; Vazza et al., 2014, 2018; Donnert et al., 2018; Steinwandel et al., 2022). For the origin of the seed field, two main hypotheses have been proposed (Cho, 2014). The magnetic fields could be primordial in origin, arising in the early Universe before recombination or during structure formation (Widrow et al., 2012). Alternatively, cosmic magnetic fields could also be seeded from astrophysical processes. Supernovae, galactic outflows and AGN can inject magnetised material into the intergalactic medium which can then be transported to larger scales (Rees, 2006). Both mechanisms could be important, and the degree of influence they have on the final magnetic field is an important ingredient for simulations of magnetic field amplification (e.g. Donnert et al., 2018).

Magnetic fields in galaxy clusters can have a significant impact on energy transport in the ICM, possibly suppressing Kelvin-Helmholtz instabilities that would otherwise form at the boundaries between hot and cold gas during a merger or disruption event (ZuHone et al., 2011, 2015). Virtually all models of cosmic ray acceleration also depend crucially on the magnetic field properties of clusters (Brunetti & Jones, 2014). However, not much is known about the properties of present-day magnetic fields in galaxy clusters.

Magnetic field strength

The strength is the best-constrained property of cluster magnetic fields, estimated to be in the range of $1-10\mu$G, from equipartition estimates from diffuse radio emission (e.g. Stroe et al., 2014; Giovannini et al., 1993, i.e assuming that the total energy density of the relativistic plasma is equally divided between cosmic rays and magnetic fields, which is similar to the minimum energy condition) and Faraday rotation experiments (e.g. Murgia et al., 2004; Govoni et al., 2006; Guidetti et al., 2008; Bonafede et al., 2010; Vacca et al., 2010, 2012; Govoni et al., 2017; Stuardi et al., 2021), which will be explained in more detail in the next section. In principle, cluster magnetic field strengths can also be constrained from X-ray observations. Inverse Compton scattering of low-energy CMB photons off of the relativistic electrons in the ICM should create a non-thermal power-law of X-ray emission on top of the thermal bremsstrahlung (e.g. Sarazin & Kempner, 2000). However, such a measurement has never been confirmed unambiguously, resulting in sub-μG lower limits on the volume averaged magnetic field strength in clusters (Wik et al., 2014; Gastaldello et al., 2015; Cova et al., 2019; Rojas Bolivar et al., 2021; Tümer et al., 2023). A tentative detection was made recently (Mirakhor et al., 2022), but more data is needed to confirm this.

Magnetic field structure

The structure of the cluster magnetic field remains elusive, with studies finding power spectra of magnetic field fluctuations with exponent n in the range of $n = 2$ to $n = 4$ (assuming they follow a power-law, e.g. Murgia et al., 2004; Govoni et al., 2006; Guidetti et al., 2008; Bonafede et al., 2010; Vacca et al., 2010, 2012; Govoni et al., 2017). This is roughly consistent with the Kolmogorov expectation of incompressible turbulence, which yields a power-law with $n = 3.67$ (Kolmogorov, 1941). The minimum and maximum scales on which this power-law holds is also not well-constrained but should follow the turbulence length scales. Turbulence can be injected on many different scales, from kpc scales due to AGN feedback and galactic outflows, up to Mpc scales during major cluster mergers (e.g. Fig 1.5). The smallest scales can be probed with high-resolution polarisation studies of nearby objects, such as the nearby brightest cluster galaxy Cygnus A, where it was found that the magnetic field shows fluctuations on sub-kpc scales (Sebokolodi et al., 2021). The largest scales are more difficult to probe and require a statistical analysis of many independent sight-lines (e.g. Osinga et al., 2022), or polarised structures that span the scale of the cluster (e.g. Govoni et al., 2005).

Dependence on cluster properties

Finally, it is unclear how the magnetic field properties depend on cluster properties such as mass, dynamical state, temperature or redshift. While clusters are remarkably self-similar in their thermal properties (see Sect. 1.2), the self-similarity of their non-thermal properties

is not well established. There are simulations that show that there is a fixed ratio of energy components in clusters throughout a cluster's history, with gravitational energy mostly being dissipated into thermal energy, then turbulent energy and finally magnetic energy (Miniati & Beresnyak, 2015). Observationally this is less clear, as in some cases extreme mergers are found with significantly increased non-thermal pressure (e.g. Ghirardini et al., 2018).

The magnetic field strength B is often assumed to scale with the electron density n_e as $B = B_0 \left(\frac{n_e(r)}{n0}\right)^{\eta}$ (e.g. Bonafede et al., 2010), where B_0 denotes the central magnetic field strength. This strength is frequently set independently of the central electron density n_0. However, a possible scaling between B_0 and n_0 was observed in a small compiled sample of clusters studied in the literature (Govoni et al., 2017), indicating also some self-similarity in the magnetic field properties. However, larger samples of homogeneously selected and analysed clusters are needed to confidently assert such a scaling.

The evolution of cluster magnetic fields as a function of cosmic time is also not well-constrained, due to the difficulty of observing clusters at high redshifts. However, LOFAR observations of a small sample of radio halos in high-redshift ($z = 0.6 - 1.0$) galaxy clusters (Di Gennaro et al., 2021a,b, 2023) have shown that clusters already have similar μG magnetic field strengths when the Universe was half its age. This implies that magnetic field amplification happens early during cluster formation, indicating that the magnetic field amplification process must be efficient and fast.

1.4.1 Instrument: The Karl G. Jansky Very Large Array

Radio polarisation observations of Faraday rotation and depolarisation, induced by the magnetised ICM, present the most promising tool for studying magnetic fields. Polarised studies are best performed at GHz frequencies because sources depolarise very quickly towards lower frequencies. At GHz frequencies, there is a good balance between sources still being polarised and the fractional bandwidth of the observations being large enough that their polarised properties can be determined accurately. The instrument of choice to study magnetic fields in this thesis is the Karl G. Jansky Very Large Array (VLA; Thompson et al., 1980).

The VLA is a radio interferometer located in New Mexico (United States), that was built between 1973 and 1980. In contrast to LOFAR which only consists of antennas, the VLA consists of 27 dishes 25 meters in diameter that can in principle observe between 73 MHz and 50 GHz. The dishes are on rail tracks shaped in a "Y" which allows different telescope configurations. The largest configuration gives a longest baseline of 36 km, resulting in a maximum resolution of $1.3''$ in the L-band ($1 - 2$ GHz).

1.4.2 Technique: Faraday rotation and depolarisation

Faraday rotation is the rotation of the polarisation angle of light caused by birefringent properties of a magnetised plasma. The observed rotation of the polarisation angle is strongly wavelength dependent,

$$\chi(\lambda) = \chi_0 + \mathrm{RM}\,\lambda^2, \tag{1.4}$$

with χ denoting the polarisation angle, λ the wavelength and RM the *rotation measure*. In the case of a simple emitting source located behind a screen of magnetised plasma

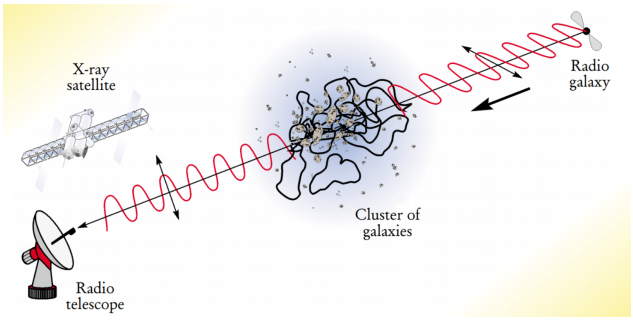

Figure 1.6: Illustration of a Faraday rotation experiment. A radio galaxy is emitting polarised synchrotron radiation with a certain intrinsic polarisation angle. As the wave hits the magnetised plasma inside the cluster, the angle is rotated depending on the wavelength according to Eq. 1.4. By measuring the rotation with a radio telescope, and the plasma density with an X-ray satellite, the magnetic field of the plasma can be obtained. Credit: Philipp P. Kronberg, Physics Today, December 2002

(e.g. a radio source behind a cluster, see Fig 1.6), the RM is equal to the more generalised Faraday depth (ϕ). The Faraday depth of a source is directly proportional to the line-of-sight component of the magnetic field weighted by the electron density as (Burn, 1966; Brentjens & de Bruyn, 2005)

$$\phi(\mathbf{r}) = 812 \int n_e \mathbf{B} \cdot d\mathbf{r} \, \mathrm{rad\,m^{-2}}, \tag{1.5}$$

where $\mathbf{B}$ is the magnetic field vector in units of μGauss, n_e is the electron density in particles per cm^{-3} and d$\mathbf{r}$ the infinitesimal path length increment in kpc, oriented along the line of sight. Generally, a magnetic field pointing towards the observed is defined with $\phi(\mathbf{r}) > 0$.

If the magnetised screen itself also emits polarised radio emission along the line of sight, Equation 1.5 still holds but the interpretation becomes a bit more complex. Now, a single line of sight can have multiple Faraday depth values, or even an extended Faraday depth structure if the screen has an appreciable thickness along the line of sight. In general, we observe (Burn, 1966)

$$P(\lambda^2) = \int_{-\infty}^{+\infty} F(\phi) e^{2i\phi\lambda^2} d\phi, \tag{1.6}$$

where P and F denote the polarised intensity as a function of wavelength or Faraday depth, respectively. This equation is similar to a Fourier transform, except that only ϕ can take unbounded values while λ^2 is positive by definition, and not measured at all values of $\lambda^2 > 0$. Still, it is possible to invert this equation given some assumptions, in a process called RM synthesis (Brentjens & de Bruyn, 2005). This allows an estimate of the Faraday dispersion function $F(\phi)$. If the wavelength coverage is good enough (analogous to uv-coverage in interferometry), polarised emission at different Faraday depths along the line of sight can be separated.

By combining radio observations of polarised sources with X-ray data, which provides insights into the thermal electron densities, it is thus possible to study the magnetic fields in galaxy clusters using Eq 1.5. Unfortunately, most radio sources are observed to be unpolarised. A typical VLA observation in the L-band of 1 hour only detects about 6 polarised sources over the entire field-of-view (e.g. Osinga et al., 2022). The number count of

polarised sources is also weakly dependent on polarised flux density F_p, as $N(> F_p) \propto F_p^{-0.6}$ (Rudnick & Owen, 2014), i.e. observing for 4 times longer only results in 1.5 times more sources.

There are several mechanisms that can cause depolarisation of radio sources. First, random fluctuations in the magnetic field across the emitting source will cause different intrinsic polarisation angles, thus causing intrinsic depolarisation that is wavelength independent. Second, internal depolarisation can occur when a radio source is emitting at different Faraday depths along the line of sight (i.e. the medium producing the synchrotron emission is also doing the Faraday rotation). Third and most important in the context of this thesis, there is external depolarisation if the magnetised plasma that constitutes the foreground screen is highly turbulent, as in the case of galaxy clusters. Because interferometers have a finite resolution (restoring beam size), we measure the sum of many waves along slightly offset sightlines which have picked up different Faraday depths and thus interfere destructively.

To illustrate the magnitude of the external depolarisation in the case of galaxy clusters, imagine a simple scenario of a constant magnetic field in the ICM with a random orientation in cells of size Λ_c kpc. The observed RM (Eq. 1.5) then results from a random walk process. Because of the central limit theorem, the distribution of RMs is expected to tend towards a Gaussian with zero mean, and variance given by (e.g. Murgia et al., 2004)

$$\sigma^2_{\rm RM} = 812^2 \Lambda_c \int (n_e B_{\parallel})^2 dl, \tag{1.7}$$

where $B_{\parallel}$ is the magnetic field strength parallel to the line of sight in μG. Observing this variance within a single resolution element causes a dramatic reduction of the polarisation fraction p (e.g. Burn, 1966) that goes as

$$p = p_0 \exp(-2\sigma^2_{\rm RM}\lambda^4), \tag{1.8}$$

where p_0 denotes the intrinsic polarisation fraction of the source. As both the magnetic field strength and electron densities generally increase towards the centre of clusters, we are expected to observe more and more depolarised sources, which has indeed been observed and can be used to constrain cluster magnetic field parameters (Bonafede et al., 2011; Osinga et al., 2022).

1.5 This thesis

This thesis starts by investigating the anisotropy of the large-scale structure using the LOFAR Two-metre Sky Survey, because previous studies have found that radio jets tend to align across large portions of the sky (Sect. 1.1). If confirmed, this would have significant implications for large-scale structure formation in the Universe. Subsequently, the thesis focuses on understanding the physics of particle acceleration and magnetic fields in galaxy clusters. While considerable advances have been made in understanding the non-thermal properties of galaxy clusters, there are still significant gaps in our knowledge.

Diffuse radio emission is almost exclusively found in high mass clusters, owing to more energetic mergers simply producing more luminous radio emission. However, the most massive clusters are the rarest density peaks in the Universe, while less massive clusters

($M_{500} < 5 \times 10^{14} M_{\odot}$ often used as a boundary) are much more common (e.g. Böhringer et al., 2017). Knowledge of particle acceleration is currently thus limited to the tip of the iceberg of the cluster population. In less massive clusters, with smaller turbulent energy budgets, turbulent re-acceleration may become less important, and hadronic interactions might power low-luminosity radio halos (Cassano et al., 2012; Brunetti & Jones, 2014). Due to the expected steep spectrum and faint nature of radio emission in lower mass clusters, deep radio observations at low frequencies are required.

Studies on magnetic field properties in galaxy clusters are still in their infancy, with only a handful of individual clusters studied so far (Murgia et al., 2004; Govoni et al., 2006; Guidetti et al., 2008; Bonafede et al., 2010; Vacca et al., 2010, 2012; Govoni et al., 2017; Stuardi et al., 2021; Anderson et al., 2021). These studies form an inhomogeneously selected sample of clusters, analysed with varied approaches, prohibiting general conclusions on magnetic field properties. Typically, each study observes fewer than five polarized radio sources, and these radio galaxies are often embedded within the intracluster medium (ICM). As a result, a question arises regarding whether these studies truly investigate the magnetized ICM or if they attribute polarization variations, which may be local to the radio sources, to the properties of the ICM.

In this thesis, we aim to answer the following questions:

- Are the angles of radio jets aligned over large scales in the Universe, possibly tracing anisotropy in the large-scale structure? (**Chapter 2**)
- Do lower mass clusters also host radio halos, and are their properties in line with radio halos observed in higher mass clusters? (**Chapter 3**)
- Is it possible to calibrate and image LOFAR observations down to the lowest frequency window of 10-30 MHz, and if so, is there a new population of diffuse cluster radio sources that can be uncovered? (**Chapter 4**)
- What are the properties of the magnetic fields in nearby and massive galaxy clusters? (**Chapter 5,6**)

In **Chapter 2**, the alignment of the jets of radio galaxies over cosmological scales is investigated. We compiled a sample of 7,555 double-lobed radio galaxies from the first data release of the LOFAR Two-metre Sky Survey to test the null hypothesis that their jet angles are randomly distributed across angular (2D) and physical (3D) scales. The results showed a significant departure from a random distribution of angles on scales of about four degrees on the sky, implying the observed jet angles align across large regions. However, no such alignment signal was found in a 3D analysis using the sub-sample of 4,212 sources to which a redshift could be attributed. Additionally, the alignment effect correlated strongly with an apparent source property, radio flux density, instead of a physical property such as radio power. The results thus pointed towards the interpretation that the alignment effect is caused by an unknown systematic bias in the data, rather than a physical alignment.

In **Chapter 3**, a systematic search for diffuse radio emission in low-mass galaxy clusters is carried out. We analysed the deepest images ever made at 150 MHz as part of the LOFAR Two-metre Sky Survey Deep fields, which reached noise levels below 30 μJy beam^{-1} at

$6''$ resolution. These observations revealed a new high-redshift radio halo at $z = 0.77$ in a relatively low mass cluster ($M_{500} = 3.3^{+1.1}_{-1.7} \times 10^{14} M_{\odot}$) and a tentative radio halo detection in another low mass cluster, Abell 2201 ($M_{500} = 2.67^{+0.27}_{-0.26} \times 10^{14} M_{\odot}$). Deep upper limits on other low-mass clusters that showed no diffuse radio emission were set. Although the sample size was relatively small, results were consistent with the known relation between radio halo power and cluster mass, extrapolated down to lower masses.

In **Chapter 4**, LOFAR is pushed to the limit as we observe the nearby galaxy cluster Abell 2256 down to the extremely low frequency of 16 MHz. LOFAR images between 16 and 168 MHz were presented, filling in the last unexplored window of Abell 2256. We detected and resolved the filamentary radio shock, radio halo and various ultra-steep spectrum sources. By adding in literature data at higher frequencies, we measured the integrated radio spectrum of the radio halo between 24 and 1500 MHz, and the radio shock between 24 and 3000 MHz. Both classes of diffuse emission showed single power-law spectra, with the radio halo being significantly steeper ($\alpha = -1.56 \pm 0.02$) than the radio shock ($\alpha = -1.00 \pm 0.02$). A new fossil plasma source was also detected with an extremely steep spectrum of $\alpha = -1.9 \pm 0.1$. Finally, the purely hadronic model was ruled out for Abell 2256 by combining the radio data with 13.5 years of γ-ray observations from the Fermi Large Area Telescope.

In **Chapters 5 and 6**, VLA observations of 124 Planck clusters from the *Chandra-Planck Legacy Program for Massive Clusters of Galaxies* are presented. The aim of these observations was to statistically infer the magnetic field properties of galaxy clusters through a stacking experiment. By stacking all clusters, 819 polarised radio sources were found, providing a relatively dense sampling of sight lines through clusters. **Chapter 5** presents the analysis of the depolarisation of radio sources in this sample. For the first time, a clear trend was detected of background sources increasingly depolarising as their projected radius to the cluster centre decreases. Using X-ray data from Chandra to constrain the electron densities, theoretical models with magnetic fields treated as Gaussian random fields were compared to the data. The data were best described by models with a central magnetic field strength of $5 - 10\,\mu$G and power-law indices between $n = 1$ and $n = 4$. **Chapter 6** improves this analysis by adding the information from the Faraday rotation of the sources. We observed a clear increase in the scatter of rotation measures towards the centre of galaxy clusters, consistent with an average magnetic field strength on the order of 3μG. Combining the depolarisation and rotation measure and comparing to a full forward model, the best agreement was found for an average magnetic field with a central strength of 5μG and a thermal gas density scaling of $B \propto n_e^{0.5}$. The power spectrum of the magnetic field was found to be consistent with the expectation from Kolmogorov turbulence, with maximum fluctuation scales of over 300 kpc, implying turbulence injected on large scales.

1.6 Future outlook

The detection of gravitational waves (Abbott et al., 2016) and the first image of a black hole (Event Horizon Telescope Collaboration et al., 2019) are compelling examples of the fact that scientific breakthroughs often come from technological advances. At the time of writing this thesis, major technological advances in radio astronomy are on the horizon, with the Square Kilometre Array (SKA) as the culmination. Even before the SKA becomes

operational, many projects will improve our understanding of the non-thermal content of galaxy clusters.

LOFAR will undergo a big upgrade to LOFAR2.0 (e.g. Edler et al., 2021), which involves upgrading the electronics of all the stations and a synchronized clock system for the Dutch stations. Currently, LOFAR can only observe in either the LBA or the HBA, and LBA observations can only utilise 48 out of the 96 LBA dipole antennas that are present per station. The electronics upgrade will allow the use of 144 dipoles simultaneously, thus allowing all LBA antennas and HBA antennas to observe at the same time. Combined with the synchronised clock system that will reduce phase errors, the upgrade is expected to improve the LBA imaging sensitivity by roughly a factor of five. Even as the SKA comes online, LOFAR will be the only telescope able to make high-resolution images below 100 MHz, which will offer a unique view of lower energy acceleration processes, particularly in low-mass clusters. LOFAR2.0 will be an important step in uncovering the origin of the seed pool of relativistic electrons that is thought to be present throughout the ICM. In addition, the new WEAVE spectrograph on the William Herschel Telescope on La Palma, currently doing commissioning observations, will take over a million spectra of bright LOFAR-selected radio sources (Smith et al., 2016). This will allow the study of (proto-)cluster radio galaxies at high redshift but also provide a large dataset to test radio galaxy alignment in three dimensions with majorly improved number statistics.

At GHz frequencies, precursors of the SKA such as MeerKAT (Jonas & MeerKAT Team, 2016) and The Australian Square Kilometre Array Pathfinder (ASKAP; Schinckel et al., 2012) will revolutionise our view of the magnetised universe. MeerKAT observations have a significantly larger field-of-view and higher sensitivity than VLA observations at the same frequency, due to the larger number of smaller-sized dishes operating at a lower system temperature (MeerKAT has 64 dishes of 13.5-meter diameter, while the VLA has 27 dishes of 25 meters in diameter). MeerKAT will thus be a great tool for deep polarisation studies of individual galaxy clusters with tens of polarised background sources detected per cluster. This will enable the study of detailed radial magnetic field profiles, potentially without assuming spherical symmetry. It will provide valuable information about the degree of self-similarity of magnetic fields in clusters.

ASKAP consists of 36, 12 meter dishes able to observe between $700 - 1800$ MHz. One of the surveys ASKAP is currently undertaking is the Polarization Sky Survey of the Universe's Magnetism (POSSUM; Gaensler et al., 2010), where early results are already showing interesting cluster science for both magnetic fields and particle acceleration (Anderson et al., 2021; Loi et al., 2023). However, the real power of POSSUM will come from the fact that it will observe the entire sky south of $+30^{\circ}$, resulting in a grid of polarised sources with an expected density of 25 deg^{-1}, which is 25 times higher than the currently best grid available from the NRAO VLA Sky Survey (NVSS; Condon et al., 1998). With at least 1397 massive clusters detected by Planck (Planck Collaboration et al., 2016a) in the survey area, this will yield unprecedented statistics for studying magnetic fields as a function of cluster properties and stacking towards the outskirts of clusters and filaments, where the magnetic field is poorly constrained. Together with the ongoing Very Large Array Sky Survey (VLASS; Lacy et al., 2020) covering the northern sky, unparalleled constraints will be set on the strength and structure of magnetic fields in the intergalactic medium, providing crucial input for cosmic magnetogenesis models.

Further in the future, in the first phase of the SKA project, the higher frequency antennas (SKA1-mid, > 350 MHz) might already be sensitive enough to detect polarisation in radio halos (Loi et al., 2019). This would allow highly detailed studies of magnetic fields and turbulence in the ICM. The lower frequency antennas (SKA1-low, < 350 MHz) will allow much greater samples of diffuse emission up to high redshifts. SKA1-low might even be able to finally constrain the contribution of the hadronic model by directly detecting radio halos in relaxed galaxy clusters with low levels of turbulence (Cassano et al., 2015). As the SKA becomes fully operational, the study of the non-thermal properties of clusters will undergo a transformation, and only time will tell what we will discover about the Universe.

2

Alignment in the orientation of LOFAR radio sources

Various studies have laid claim to finding an alignment of the polarization vectors or radio jets of active galactic nuclei over large distances, but these results have proven controversial and so far, there is no clear explanation for this observed alignment. To investigate this case further, we tested the hypothesis that the position angles of radio galaxies are randomly oriented in the sky by using data from the Low-Frequency Array (LOFAR) Two-metre Sky Survey (LoTSS). A sample of 7,555 double-lobed radio galaxies was extracted from the list of 318,520 radio sources in the first data release of LoTSS at 150 MHz. We performed statistical tests for uniformity of the two-dimensional (2D) orientations for the complete 7,555 source sample. We also tested the orientation uniformity in three dimensions (3D) for the 4,212 source sub-sample with photometric or spectroscopic redshifts. Our sample shows a significant deviation from uniformity (p-value $< 10^{-5}$) in the 2D analysis at angular scales of about four degrees, mainly caused by sources with the largest flux densities. No significant alignment was found in the 3D analysis. Although the 3D analysis has access to fewer sources and suffers from uncertainties in the photometric redshift, the lack of alignment in 3D points towards the cause of the observed effect being unknown systematics or biases that predominantly affect the brightest sources, although this has yet to be demonstrated irrefutably and should be the subject of subsequent studies.

Based on Osinga et al. (2020): *E. Osinga, G. K. Miley, R. J. van Weeren, T. W. Shimwell, K. J. Duncan, M. J. Hardcastle, A. P. Mechev, H. J. A. Röttgering, C. Tasse, W. L. Williams, A&A, 642, A70 (2020).*

2.1 Introduction

The large sizes (up to few megaparsecs) of extended extragalactic radio sources allow us to use them in tracing the history of galactic nuclear activity over hundreds of millions of years. Since their discovery, it has been revealed that most powerful radio jets have highly linear morphologies (e.g., Miley, 1980). In classical models of radio jets, the orientation is associated with the spin axis of a supermassive black hole (SMBH) in the nucleus of the host galaxy. The alignment of kpc and Mpc-scale radio emission with pc-scale jets (e.g., Fomalount & Miley, 1975) has demonstrated that the collimated jets hold a "memory" of their directions for more than 10^8 years. Our understanding of the accretion processes by which the SMBHs are "fed" or the mechanisms that determine the orientation of their spin axes is still incomplete.

An intriguing question concerns whether there could be some connection between the orientations of the SMBH spin axes and properties of the cosmic filaments in which the radio sources and their host galaxies are found. The possibility of such a connection has been suggested in recent evidence for non-uniformity in radio-source position angles over large regions of the sky found by Taylor & Jagannathan (2016) and Contigiani et al. (2017).

If the radio sources are indeed aligned with respect to the large-scale structure in which they are found, a possible cause could be attributed to angular momentum transfer during the early stages of galaxy formation. The tidal torques imparted on the collapsing halos are found to influence the spin and shape of galaxies in N-body simulations (e.g., White, 1984; Codis et al., 2012; Laigle et al., 2015; Codis et al., 2018; Kraljic et al., 2020). However, the angular momentum vectors of the active galactic nucleus (AGN) and the host galaxy are found to be misaligned and generally uncorrelated (Hopkins et al., 2012), indicating that this explanation is incorrect or incomplete.

Furthermore, there is substantial evidence that AGNs are associated with mergers, based on both observations and simulations (e.g., Chiaberge et al., 2015; Croton et al., 2006). If these mergers occur preferentially along the filaments of the large-scale structure, these could orient the central SMBHs in a particular way, resulting in a preferential alignment of the extended radio sources. Hence, if the alignment of radio sources on large scales is confirmed, this would have significant implications for models of the formation of galaxies and active galactic nuclei.

Additional evidence that there may be a connection between the orientation of the spin axes of SMBHs that power active galactic nuclei and the cosmic filaments in which they lie comes from observations of large-scale statistical alignments in the optical polarization position angles of quasars (e.g., Hutsemékers, 1998; Hutsemékers & Lamy, 2001; Jain et al., 2004). Evidence has also been found for the polarization angle of quasars to be either parallel or perpendicular to the large-scale structures they inhabit (e.g., Hutsemékers et al., 2014; Pelgrims & Hutsemékers, 2016).

A more extensive investigation of the large-scale distribution of radio source orientations is warranted. Surveys with the Low-Frequency Array (LOFAR) High Band Array (HBA; van Haarlem et al., 2013) are especially suited for carrying out such studies, because they (i) are conducted at sufficiently low frequencies to detect steep-spectrum extended synchrotron radio structures, (ii) have the sufficient angular resolution, with a ~6″ half-power beam width (HPBW), to resolve 50 (100) kpc-sized radio sources out to redshift ~ 1 (>6), and (iii) have the sensitivity and dynamic range needed to detect and measure

orientations for an unprecedented number of sources.

Here, we describe such an investigation using position angles of radio sources from the LOFAR Two-metre Sky Survey Data Release I (LoTSS-DR1; Shimwell et al., 2019). We first describe the data in Section 2.2. The criteria we used to select sources with well-defined position angles from the 318,520 radio sources from the survey are discussed in Section 2.3. The statistical methods we used to explore non-uniformity in the source alignments are explained in Section 2.4. Our results are given in Section 2.5, where we report evidence for non-uniformity in the source alignments. Finally, in Sections 2.6 and 2.7, we discuss the robustness and implications of the results.

Throughout this study, we adopt the Planck 15 cosmology (Planck Collaboration et al., 2016c). This cosmology is defined by the following relevant parameters: $H_0 = 67.8$ $\mathrm{kms}^{-1}\mathrm{Mpc}^{-1}$, $\Omega_m = 0.308$, $\Omega_\Lambda = 0.692$.

2.2 The data

Our sample is taken from the LoTSS, a sensitive low-frequency (120-168 MHz) survey that will ultimately cover the entire northern sky. The first data release comprises 2% of the whole survey (424 square degrees) in the HETDEX Spring Field region (right ascension 10h45m to 15h30m and declination 45° to 57°; Shimwell et al., 2019). It contains more than 300,000 radio sources that have a signal-to-noise ratio (S/N) of > 5. The images have a HPBW resolution of $\sim 6''$, a median sensitivity of 71 μJy/beam, and a positional accuracy better than $\sim 0.2''$

The data used were taken from the "value-added" radio + optical catalogueue of Williams et al. (2019) of 318,520 LoTSS sources. This includes, where possible, identifications and redshifts of the optical counterparts. The optical identifications were made using either a likelihood ratio method or by human visual classification through the LOFAR Galaxy Zoo[1]. Spectroscopic redshifts in the added-value catalogue were taken, where available, from the Sloan Digital Sky Survey Data Release 14 (Abolfathi et al., 2018). Otherwise, photometric redshifts were estimated using a hybrid methodology based on traditional template fitting and machine learning (see Duncan et al., 2019).

2.3 Source selection

For the alignment uniformity analysis, our goal was to select double-lobed radio sources with clearly defined position angles from the LoTSS value-added catalogue. To identify such sources, we used the following method:

First, we filter the catalogue to contain only high S/N extended sources. We define sources as extended if they have a major axis that is larger than five times the restoring beam size. The adopted selection criteria are:

$$S_{\mathrm{peak}}/N > 10 \text{ and } a > 30'',$$

where S_{peak} is the peak flux density of the LOFAR source at 144 MHz and a is the size of the major axis of the source. The major and minor axes of some sources are not directly provided for sources that have been processed by the LOFAR Galaxy Zoo (LGZ). Instead,

[1] https://www.zooniverse.org

an equivalent "LGZ_Size" and "LGZ_Width" parameter is provided. The construction of the source dimensions from the LGZ data is described in Williams et al. (2019). Throughout this study, we set the major and minor axes of the sources processed by LGZ as the "LGZ_Size" and "LGZ_Width," respectively. Additionally, uncertainties for the LGZ shape parameters (source size, width, and position angle) are not provided by the value-added catalogue. We discuss any effects due to uncertainties in the position angles in Section 2.6.

Next, we keep only the sources with a double-lobed structure. We enforce this criterion by imposing the condition that sources must be fitted by multiple Gaussian components by the initial source finder PyBDSF (Mohan & Rafferty, 2015). This is indicated by the "S_Code" of the source in the catalogue. It is also possible that the source is a bright resolved nearby galaxy and these are identified with the "ID_flag" code where the first digit is 2. We remove these sources as well, using:

$$S\_Code = M \text{ and } ID\_flag \neq 2.$$

Imposing these criteria results in a reduction of the sample of 318,520 sources to a sample of 7,688 bright extended linear sources. We check the catalogue for sources that might have been identified multiple times by examining the distance from every source to its nearest neighbour. We investigate all sources that have a nearest neighbour within ten synthesized beams (1 arcminute). If the source has a different optical identification from its nearest neighbour, we can be reasonably sure that it is not a duplicate entry. When the source has an optical identification while the nearest neighbour does not, or both the source and the nearest neighbour lack an optical identification, we cannot be certain that these entries are not duplicates. To err on the side of caution, we remove all sources from our sample that have a nearest neighbour within ten synthesized beams, unless they have a different optical identification from their nearest neighbour. We find that 165 sources have a nearest neighbour within ten synthesized beams, and 32 of these have a different optical identification from their nearest neighbour. We expect that removing the other 133 entries would not impact the strength of a possible alignment effect since radio source alignments have been claimed on scales of at least a degree (Taylor & Jagannathan, 2016; Contigiani et al., 2017) and these source separations are on a smaller angular scale than this. Thus, the final sample contains 7,555 selected sources.

2.4 Statistical methods

To determine the departure from uniformity in the alignment of radio sources on the sky, an appropriate statistical method must be used that accounts for effects due to the geometry of the celestial sphere. We shall do this by introducing the concepts of "parallel transport" and "dispersion measure."

2.4.1 Parallel transport

The position angle in the LoTSS catalogue is defined as the angle of the major axis of a source measured east of the local m (north) direction. To have a consistent definition of the position angle across all pointings, we translated the position angles to be measured east of the direction of the north celestial pole.

Because the position angle is defined with respect to the local meridian, the vectors corresponding to the position angles on different points of the celestial sphere cannot be

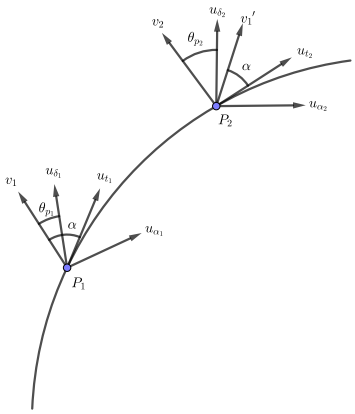

Figure 2.1: Illustration of parallel transport. Vector v_1 corresponding to a position angle θ_{p_1} and vector v_2 corresponding to position angle θ_{p_2} are shown. In order to compare v_1 to v_2, v_1 must be parallel-transported along the great circle indicated by the curve from location P_1 to location P_2. The transported vector is indicated by v_1' and the local basis vectors are denoted by (u_δ,u_α). In parallel transport, the angle α between the vector tangent to the sphere u_t and the vector v remains fixed. Figure adapted from Jain et al. (2004).

compared directly. These vectors must be transported along the great circle joining these points. Following Jain et al. (2004) and Contigiani et al. (2017), we use the parallel transport method, by which the radio source "vectors" can be transported to a different position on the celestial sphere. This method is described below for completeness.

We parametrize the celestial sphere with local unit vectors $(\vec{u}_r, \vec{u}_\delta, \vec{u}_\alpha)$ which point, respectively, to the centre of the sphere, north along the local meridian and eastwards on the sphere. We wish to compare the position angles, θ_{p_1} and θ_{p_2} , of sources 1 and 2 with positions, P_1 and P_2, on the celestial sphere (Figure 2.1). The vector resulting from the position angle, θ_{p_1} , of source 1 at location, P_1, is given, in terms of the local basis, by

$$\vec{v}_1 = \cos\theta_{p_1}\vec{u}_{\delta_1} + \sin\theta_{p_1}\vec{u}_{\alpha_1}. \tag{2.1}$$

To define a coordinate-invariant inner product we parallel transport the vector, $\vec{v}_1$, to the position, P_2, to obtain vector, $\vec{v_1}'$. Vector $\vec{v_1}'$ then makes an angle, θ_p' , with respect to the local north-pointing vector, $\vec{u}_{\delta_2}$. To find the transported angle ,θ_p', let $\vec{u}_s$ be the unit vector perpendicular to the plane containing the two radial vectors $\vec{u}_{r_1}$ and $\vec{u}_{r_2}$. Thus, $\vec{u}_s$ is found by

$$\vec{u}_s = \frac{\vec{u}_{r_1} \times \vec{u}_{r_2}}{|\vec{u}_{r_1} \times \vec{u}_{r_2}|}. \tag{2.2}$$

Consider now the unit vectors, $\vec{u}_{t_1}$ and $\vec{u}_{t_2}$, at points, P_1 and P_2, and tangent to the great circle connecting P_1 and P_2. These vectors are given by:

$$\vec{u}_{t_{1,2}} = \vec{u}_s \times \vec{u}_{r_{1,2}}. \tag{2.3}$$

In terms of the local basis, these vectors can be written as:

$$\vec{u}_{t_1} = \vec{u}_{\delta_1} \cdot \vec{u}_{t_1} \vec{u}_{\delta_1} + \vec{u}_{\alpha_1} \cdot \vec{u}_{t_1} \vec{u}_{\alpha_1}, \tag{2.4}$$

where

$$\vec{u}_{\delta_1} \cdot \vec{u}_{t_1} = \frac{-\sin\delta_1 \cos\delta_2 + \cos\delta_1 \sin\delta_2 \cos(\theta_{p_1} - \theta_{p_2})}{\sqrt{1 - \left(\vec{u}_{r_1} \cdot \vec{u}_{r_2}\right)^2}}, \tag{2.5}$$

$$\vec{u}_{\alpha_1} \cdot \vec{u}_{t_1} = \frac{\sin\delta_2 \sin(\alpha_2 - \alpha_1)}{\sqrt{1 - \left(\vec{u}_{r_1} \cdot \vec{u}_{r_2}\right)^2}}, \tag{2.6}$$

$$\vec{u}_{\delta_2} \cdot \vec{u}_{t_2} = \frac{-\sin\delta_2 \cos\delta_1 + \cos\delta_2 \sin\delta_1 \cos(\theta_{p_1} - \theta_{p_2})}{\sqrt{1 - \left(\vec{u}_{r_1} \cdot \vec{u}_{r_2}\right)^2}}, \tag{2.7}$$

$$\vec{u}_{\alpha,2} \cdot \vec{u}_{t_2} = \frac{-\sin\delta_1 \sin(\alpha_1 - \alpha_2)}{\sqrt{1 - \left(\vec{u}_{r_1} \cdot \vec{u}_{r_2}\right)^2}}. \tag{2.8}$$

As $\vec{v}_1$ is parallel-transported along the great circle to position, P_2 , with its angle with respect to the tangent of the great circle remaining fixed. Thus, to determine the angle by which the vector has turned due to this transport, we consider the orientation of $\vec{u}_{t_1}$ and $\vec{u}_{t_2}$ with respect to the local basis at the two points where the sources lie. We call ξ_1 the angle between $\vec{u}_{t_1}$ and $\vec{u}_{\alpha_1}$, and ξ_2 the angle between $\vec{u}_{t_2}$ and $\vec{u}_{\alpha_2}$. These angles are given, per definition of the inner product, by

$$\xi_{1,2} = \arccos(\vec{u}_{\alpha_{1,2}} \cdot \vec{u}_{t_{1,2}}). \tag{2.9}$$

Thus, the transported $\vec{v_1}'$ makes an angle $\theta'_{p,1} = \theta_{p,1} + (\xi_2 - \xi_1)$ defined with respect to the local coordinates in P_2. Hence we can now define the generalized dot product between $\vec{v}_1$ and $\vec{v}_2$ as the dot product between the transported vector $\vec{v_1}'$ and $\vec{v}_2$:

$$\vec{v}_1 \odot \vec{v}_2 = \vec{v_1}' \cdot \vec{v}_2 = \cos(\theta_{p_1} - \theta_{p_2} + \xi_2 - \xi_1). \tag{2.10}$$

Equation 2.10 can generally be used in any problem that considers angles on a sphere. In particular, when comparing the difference between position angles, it makes sense to redefine the generalized inner product between two position angles as

$$(\theta_{p_1}, \theta_{p_2}) = \cos[2(\theta_{p_1} - \theta_{p_2} + \xi_2 - \xi_1)], \tag{2.11}$$

where, since the position angles range from 0 to π, it assumes values of $\in (-1, 1)$ and where $+1$ expresses the perfect alignment between θ_{p_1} and θ_{p_2} and -1 indicates perpendicular orientations.

2.4.2 Statistical test

To test the significance of a possible alignment in source position angles, we use the dispersion measure (Jain et al., 2004; Contigiani et al., 2017). We briefly repeat the definition of the dispersion measure here for completeness.

The dispersion depends only on the differences between neighbouring position angles and it is, therefore, a suitable choice when testing for alignment on different scales. The dispersion measure of source, i, as a function of a position angle, θ, is defined as

$$d_{i,n}(\theta) = \frac{1}{n}\sum_{k=1}^{n}(\theta,\theta_k), \tag{2.12}$$

where n is the number of nearest neighbours that are considered around source i, including the source itself, and θ_k is the position angle of the respective neighbours. The generalized inner product (θ,θ_k) is defined by Equation 2.11.

The position angle θ that maximizes the dispersion around source i is analogous to the definition of the mean position angle of source i and its n nearest neighbour s. The magnitude of $d_{i,n}|_{max}$ is, then, a measure of the dispersion around this mean. The dispersion can take a maximum value of 1, which corresponds to perfect alignment of all n nearest neighbours. To find the value of θ that maximizes the dispersion, we take the derivative of Equation 2.12 with respect to θ and, after some intermediate steps, we arrive at the following expression for $d_{i,n}|_{max}$:

$$d_{i,n}|_{max} = \frac{1}{n}\left[\left(\sum_{k=1}^{n}\cos\theta_k\right)^2 + \left(\sum_{k=1}^{n}\sin\theta_k\right)^2\right]^{1/2}. \tag{2.13}$$

The statistic, so that we may test for the non-uniformity of alignment in a sample of N sources, is then defined as:

$$S_n = \frac{1}{N}\sum_{i=1}^{N} d_{i,n}|_{max}, \tag{2.14}$$

which is simply the average of the maximum dispersion for a number of nearest neighbours, n, calculated over all N sources in the sample. This statistic thus measures the strength of a local alignment signal in the full sample of N sources while considering the n nearest neighbours of every source.

The significance level for rejecting the null hypothesis that a sample of sources is randomly oriented is then given by comparing the statistic of the dataset, S_n , to the distribution of the statistic for simulated samples that are randomly oriented. It is found through a one-tailed significance test, expressed as:

$$SL = 1 - \Phi\left(\frac{S_n - \langle S_n|_{MC}\rangle}{\sigma_n}\right), \tag{2.15}$$

where Φ is the cumulative standard normal distribution function. Here, $< S_n|_{MC} >$ and σ_n are, respectively, the expectation value and standard deviation of S_n in the absence of alignment. These values can be found through Monte Carlo simulations of randomly oriented sources.

Jain et al. (2004) verified that for randomly oriented samples of sources, S_n is normally distributed if $N \gg n \gg 1$ is satisfied. With the dispersion measure and the resulting statistic, the significance level at which the hypothesis of uniformity in the position angles should be rejected can be calculated on a local scale by probing different numbers of nearest

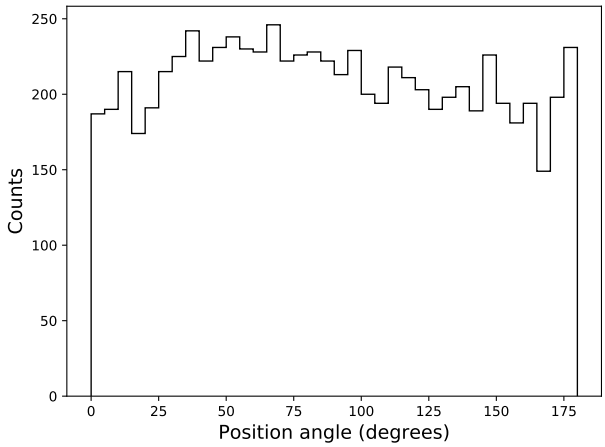

Figure 2.2: Position angle distribution of the complete sample of selected sources.

neighbours. Since the number of nearest neighbours can be translated to fixing apertures with angular radii extending to the n-th nearest neighbour around all sources, S_n can be used to probe the significance of alignment on different angular scales. We note that different S_n are not independent since the dispersion is an average of n neighbours. This statistic thus probes alignment up to scales corresponding to n and once a signal is detected for some n, a preferentially positive signal is expected for larger n.

If the redshifts of the sources are known, this method can be extended to probing nearest neighbours in 3D space. In this way, the dependence of a possible alignment effect and S_n as a function of physical scale can be probed.

2.5 Results

We first tested the uniformity of the LoTSS radio source position angles over the complete 424 square degrees of the available survey to give an indication of possible systematic effects. The distribution of position angles is given in Figure 2.2. We expect the position angles to be uniformly distributed over this relatively large patch of the sky if no systematic effects are present. From Figure 2.2, we can see that no major systematic effects are present, although the distribution is not quite uniform. To check if the distribution is consistent with a uniform distribution of sources, we applied the Kolmogorov-Smirnov (K-S) test (e.g., Frommert et al., 2012). The K-S test resulted in a p-value of 0.030 per cent. This is strong evidence for rejecting the null hypothesis that the distribution of position angles over the complete sample is uniform, which indicates some systematic (survey-wide) bias in our sample. Still, the local alignment signal might be stronger or weaker depending on the nature of the effect that is causing the alignment.

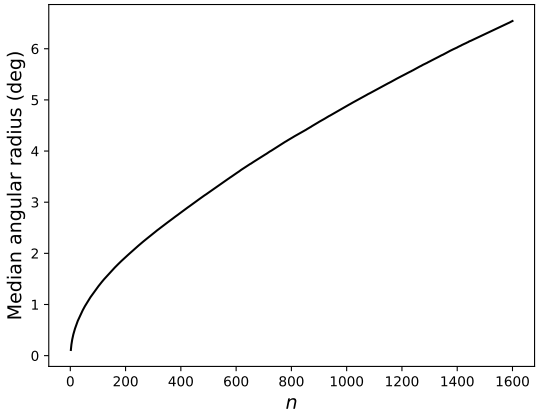

Figure 2.3: Median angular radius corresponding to drawing a circular aperture around every source with an angular radius bound by the n-th neighbour around that source.

2.5.1 Two-dimensional analysis

To determine whether the hypothesis of uniformity in position angles on different angular scales should be rejected and if so, at what significance level, we compared results for the observed LoTSS sample with those for 1,000 simulated randomly distributed position angle samples. These samples were generated by randomly shuffling the position angles among the sources to maintain the same global position angle distribution and source positions.

The sample was checked for local alignment by probing the statistic, S_n , for different numbers of nearest neighbours. To express the statistic in terms of angular scale, a circular aperture with a radius extending to the n-th neighbour of every source is drawn. We translated the number of nearest neighbours to an approximate corresponding angular scale by taking the median angular radius of all these apertures. This dependency is shown in Figure 2.3.

The significance level at which the null hypothesis should be rejected (of the position angles being uniformly distributed) is given as a function of the number of nearest neighbours (or corresponding angular scale) in Figure 2.4. There is strong evidence that the hypothesis of uniformity in radio source position angles should be rejected on angular scales of about four degrees, with a significance level of $< 10^{-5}$.

To investigate the effect further, we split our sample into four equal frequency flux density bins to have the maximum number of sources in every bin, as given in Table 2.1. For each bin, this table includes the median flux density, the median redshift, the median source angular size, and the maximum significance level at which the null-hypothesis of position angle uniformity should be rejected, taken from Figure 2.5.

Figure 2.5 shows the significance level of position angle alignment for the four flux density bins as a function of angular distance. Interestingly, the highest flux density bin shows very strong evidence for alignment, up to scales of roughly ten degrees, but most significantly around four degrees, while all other bins are consistent with uniform

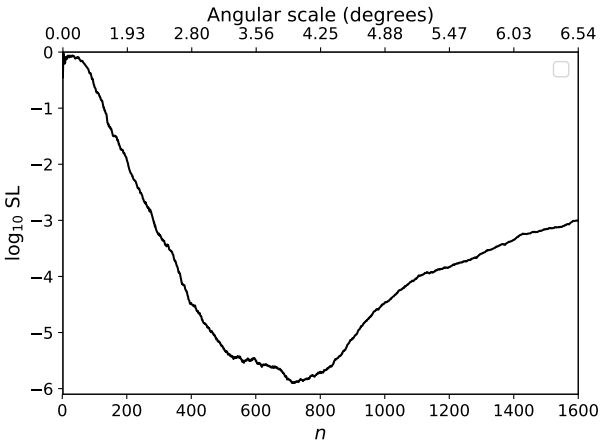

Figure 2.4: Logarithm of the significance level for which uniformity in position angles as a function of the number of nearest neighbours n should be rejected for the sample of 7,555 selected sources. The conversion to angular scale is shown in Fig. 2.3.

distributions. This shows that the effect seen in the total sample is caused by the highest flux density sources only.

Table 2.1: Parameters that cut the initial sample of selected sources into four equal frequency total flux density f bins. The maximum significance level to reject uniformity is also shown.

Bin number	Flux range (mJy)	Median flux (mJy)	Median redshift	Median size ($''$)	Significance level
0	f <12	7	0.55	42	$1.1{\cdot}10^{-2}$
1	12 < f <33	20	0.54	51	$1.5{\cdot}10^{-1}$
2	33 < f <96	54	0.57	59	$2.9{\cdot}10^{-1}$
3	96 < f	227	0.63	68	$7.7{\cdot}10^{-11}$

2.5.2 Three-dimensional analysis

We carried out an analysis of alignment uniformity using 3D source positions, after removing all sources from our sample that do not have a spectroscopic or photometric redshift tabulated in the value-added catalogue (Williams et al., 2019; Duncan et al., 2019). This reduced the size of our sample to 4,212 sources. The number of photometric and spectroscopic redshifts is 2,311 and 1,901, respectively. We emphasize that the statistical method is exactly the same for this analysis. The only difference between the 2D and 3D analysis is that 3D source positions are now used to find the n nearest neighbours for every source. The distribution of position angles of these 4,212 sources is shown in Figure 2.6. The K-S test indicates a p-value of 1.0 per cent, indicating that for this sample of 4,212 sources, there is weak evidence for rejecting the null hypothesis for the uniformity of position angles.

In the analysis for local alignment, the samples were compared again with 1,000 simulated uniformly distributed position angle samples, generated by randomly shuffling the position angles among the sources. To repeat the analysis in three dimensions, each source

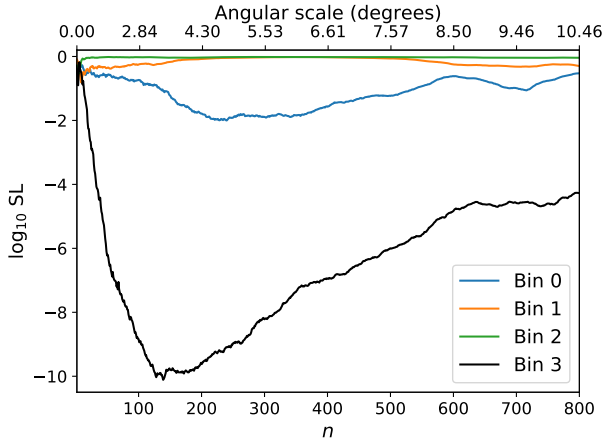

Figure 2.5: Logarithm of the significance level for the sample of sources split into four equal frequency bins of increasing total flux density. The flux cuts are defined in Table 2.1.

was assigned a position in 3D space according to their right ascension, α, declination, δ, and comoving distance, r, as follows:

$$\begin{aligned} x &= r\cos\alpha\cos\delta, \\ y &= r\sin\alpha\cos\delta, \\ z &= r\sin\delta. \end{aligned} \tag{2.16}$$

The nearest neighbours were then computed in 3D space according to these positions to probe for alignment on local scales.

Figure 2.7 shows the significance level at which the hypothesis of uniformity in position angles can be rejected for the 4,212 sources that have a redshift, both in a 3D and a 2D analysis. The 3D analysis does not show strong evidence for an alignment effect.

Since the sources with the largest flux densities are the main contributor to the alignment effect in the 2D analysis, we also calculated the significance for the highest flux density sources in the 3D analysis. We split the 4,212 sources into four equal frequency total flux density bins, which defines the highest flux density bin as all sources with a total flux density > 108 mJy. This makes the flux cut for the highest flux density bin slightly higher than the equivalent in the 2D analysis, but we decide to use this flux cut to have a fairer comparison between the different flux density bins within the 3D analysis.

The significance level at which position angle uniformity can be rejected for the highest flux density bin in 3D is shown in Figure 2.8. This figure shows, interestingly, that the 2D analysis of these 1,051 sources still shows strong evidence for alignment up to scales of four degrees. However, this signal is not present in the 3D analysis. No signal was found in the other flux density bins, either in 2D or in 3D.

The difference between the 2D and 3D analysis indicates that the 2D alignment effect is due to some unknown systematic effect, since a physical effect would invariably cause stronger alignment in the 3D analysis than in the 2D analysis. Additionally, we inspected

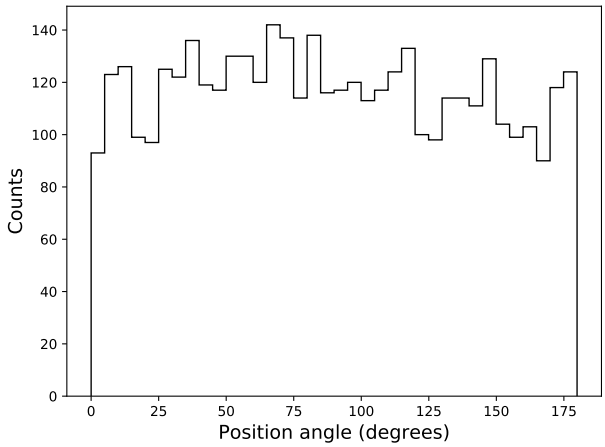

Figure 2.6: Distribution of position angles for the sample of 4,212 sources that have a redshift measurement.

whether the most radio luminous sources are also the most aligned sources, which would be expected from the similar median redshift per flux density bin. However, no alignment signal was found in either the 2D or 3D analysis of the 1,051 highest radio power sources.

Although it reduces the sub-sample sizes even further, we also tested if the results depend on whether the redshifts were photometric or spectroscopic. Figure 2.9 shows the results for the 523 sources that have a spectroscopic redshift. The figure shows that in both the 2D analysis and 3D analysis of these subsets no significant signal is present. This is not surprising given the small number of sources in the spectroscopic subsample.

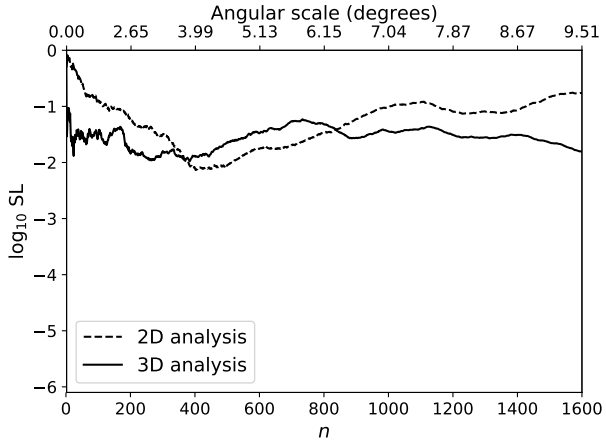

Figure 2.7: Logarithm of the significance level at which position angle uniformity should be rejected, as a function of the number of nearest neighbours n for the 4,212 sources in that have redshifts available. The dashed line indicates the results of the 2D analysis and the solid line the results of the 3D analysis.

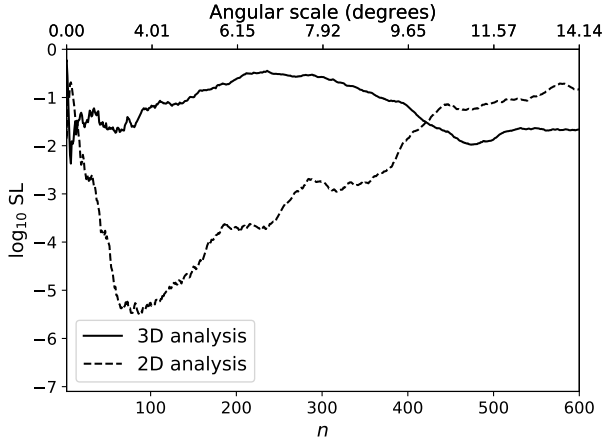

Figure 2.8: Logarithm of the significance level at which position angle uniformity should be rejected as a function of the number of nearest neighbours n for the 1,051 sources with total flux density > 108 mJy and a redshift measurement. The dashed line indicates the results of the 2D analysis and the solid line the results of the 3D analysis.

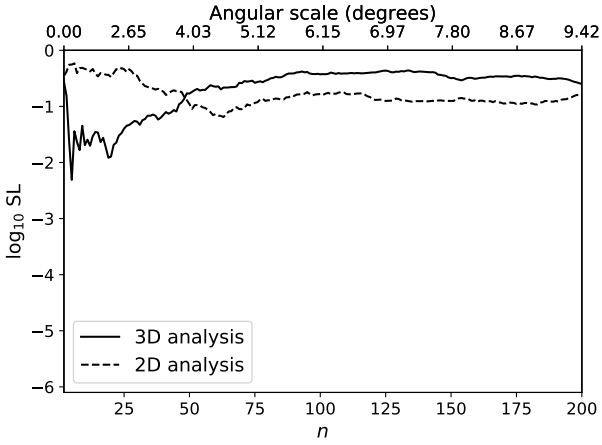

Figure 2.9: Logarithm of the significance level at which position angle uniformity should be rejected as a function of the number of nearest neighbours n for the 523 sources with total flux density > 108 mJy and a spectroscopic redshift measurement. The dashed line indicates the results of the 2D analysis and the solid line the results of the 3D analysis.

2.6 Discussion

2.6.1 Robustness of the results

The robustness of the results depends on the uncertainties of the position angles that were fit to the sources. The position angles of sources in the LOFAR value-added source catalogue do not all include uncertainties. The subset of sources that was classified in the LGZ project do not come with position angle uncertainties. To examine the position angle uncertainties, we are thus restricted to using the sources that are classified by the source finder PyBDSF only. To examine the position angle uncertainties, we plot the 1σ uncertainties as given by the catalogue for these sources. These are shown in Figure 2.10. The figure shows that 81% of the sources have position angle uncertainties smaller than ten degrees. Thus, we can approximate the uncertainty in the final significance level by assuming every source in our sample has a 1σ uncertainty of 10. Since most sources have smaller uncertainties, this assumption is likely to overestimate the uncertainty in the fitted position angles and, thus, in the final significance level.

To approximate the error in the final significance level as a function of a 1σ error of ten degrees in the position angle, we must propagate this error through the statistical analysis of Section 2.4. However, there is no straightforward procedure to define the general error on the extracted significance level as a function of the error on the measured position angles. Simple error propagation can be applied to the calculation of S_n, but it becomes complicated when a one-tailed significance level is extracted. This is due to the dependence of the significance level on the position of S_n in the distribution of $S_n|_{MC}$ (Equation 2.15). If S_n lies far from the mean of the normal distribution, a given change in S_n will lead to a smaller change in significance level than when S_n lies near the mean of the distribution of $S_n|_{MC}$. This is a direct effect of the cumulative normal distribution function being steepest near the mean and flattest near the edges. Moreover, considering that for every sample, $S_n|_{MC}$ is found by simulating 1,000 random datasets by randomly shuffling the position angles of the sources, the distribution of $S_n|_{MC}$ will be unique for every sample that we have considered. Therefore, we can only approximate the error on concrete results and cannot give a general 1σ confidence level that will apply for a range of samples.

The initial sample of sources rejected uniformity at a significance level of $< 10^{-5}$ (Figure 2.4). The signal was found with a number of nearest neighbours between 467 and 916, corresponding to an angular scale between 3.1 and 4.6 degrees. Figure 2.11 shows the distribution of the simulated data and the highly significant value of S_n for these two bounds. We calculate the error on S_{467} and S_{916} and translate these errors to bounds on the significance values.

Assigning for each position angle in our sample a 1σ error of 10 degrees and applying standard error propagation, we find for the resulting values of S_{467} and S_{916}, 0.070 ± 0.0025 and 0.065 ± 0.0026, respectively. Taking the 1σ lower and upper bound of S_{467} and calculating the significance level of these two bounds results in the lower and upper bound logarithmic significance levels of -3.37 and -7.03. For S_{916} , the same method leads to lower and upper bound logarithmic significance levels of -3.24 and -7.16. Thus, strong evidence to reject uniformity in this sample at scales between 3.1 and 4.5 degrees is still found after applying possible uncertainties in the position angles. We can conclude that assuming a 1σ error of ten degrees on the position angle of all sources, the effect of an uncertainty in the position angles is quite powerful, but the significance level does remain

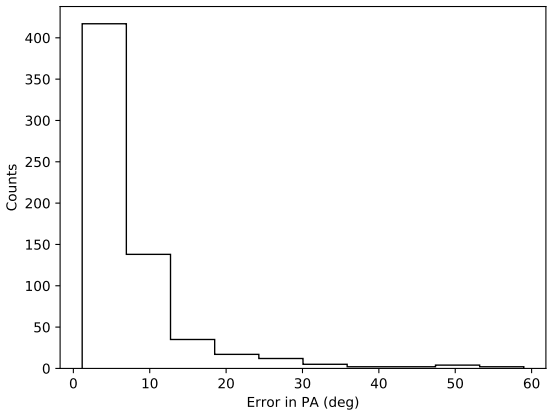

Figure 2.10: 1σ uncertainties on the position angles of sources in our sample that are not classified by the LOFAR galaxy zoo, but by the source finder only.

strong enough to reject uniformity. Thus, the resulting significance level of $\log SL = -5.0$ to reject uniformity found in Figure 2.4 for angular scales between 3.1 and 4.6 degrees should be stated with the approximate bound of $\log SL = -5.0 \pm 2.0$.

As stated previously in this chapter, the difference in significance level for the same variation in S_n is dependent on the position of S_n, thus, it is also dependent on the significance level itself. Therefore, we reiterate that the change of two orders of magnitude in significance, found for the subset considered in this section, should not be applied to different subsets. We can apply the same calculation to the 3D analysis of the initial sample (Figure 2.7), where no result was found. We chose to investigate $n = 500$, which corresponds to a significance level of $10^{-1.6}$. This results in $\log SL = -1.7^{+0.71}_{-0.97}$; still without changing the signal to strong ($< 10^{-3}$) evidence for alignment. Repeating the same calculations for the 2D analysis of the highest flux density sources that have an available redshift (Fig. 2.8) results in the approximate bounds $\log SL = -5.3^{+1.4}_{-1.6}$ for n = 100.

2.6.2 Interpretation of the results

Our complete sample of 7,555 double sources with a well-defined orientation was found to be inconsistent with a uniform distribution with a K-S test significance of 0.030 percent, which already indicates a global systematic effect in the data. However, the analysis of local alignment depends on the contrast between the statistic, S_n , found for our dataset and the statistic, $S_n|_{MC}$, found in absence of alignment. The statistic in absence of alignment was generated by randomly shuffling the position angles amongst the sources to maintain the same geometry and global position angle distribution. The advantage of this method over generating position angles from the uniform distribution $\mathcal{U}[0, 180)$ is that it diminishes the effect of a possible global systematic present in our data sample. This is due to a global systematic then also being included in the distribution of the statistic $S_n|_{MC}$. Therefore, as long as $n \ll N$, where N is the number of sources in the sample that is examined, the effect

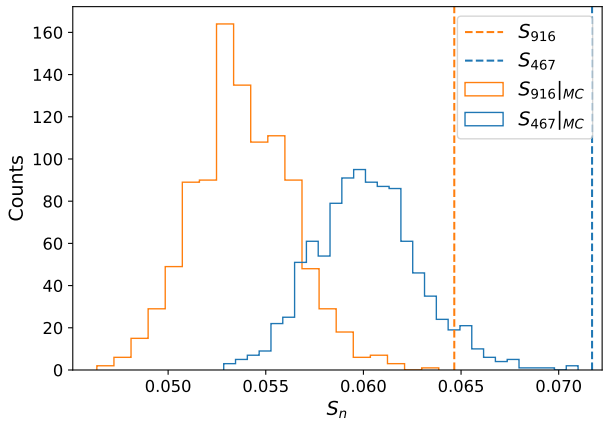

Figure 2.11: Distribution of the 1,000 simulated values $S_n|_{MC}$ and the highly significant values S_n for $n = 467$ and $n = 916$. Plotted for the initial sample of sources.

of the deviation from uniformity of the whole sample will not have considerably impacted the result of the significance of local alignment.

To identify which particular sources are causing the observed signal, we examine which sources show the strongest alignment effect in 2D space. For this, we use the calculated maximum dispersion measure $d_{i,n}|_{max}$ (Equation 2.13), which measures the significance of the alignment of a source, i, and its nearest neighbours, n . We plot the maximum dispersion for every source in the initial sample of 7,555 sources as a function of right ascension and declination for $n = 700$ in Figure 2.13. From this figure, it becomes apparent that there is not a single region where the alignment is most pronounced, but rather, that there is an alternation between strongly aligned and less strongly aligned regions. This contradicts the observed effect being attributed to a survey-wide systematic effect, as then all sources would have similar maximum dispersion, regardless of their position. Additionally, the scale of the alternation between aligned and non-aligned regions is larger than the typical separation between LOFAR pointings (2.58 degrees; Shimwell et al., 2019), which makes the origin of the systematic effect even more elusive.

We also found that the alignment signal was most significant for sources with the largest flux densities, as indicated by Figures 2.5 and 2.8. However, an analysis of the sources with the highest radio power did not show an alignment effect, either in 2D or in 3D. Thus, it seems that only apparent source properties, rather than physical source properties, are correlated with the alignment effect, which could point towards an intrinsic effect of the survey, although radio power and source brightness are not strongly correlated for radio sources. Most importantly, the fact that the alignment effect is not present when using the 3D positions of the high flux density sources to find the nearest neighbours but is present when using 2D source positions (Fig. 2.8) may indicate a systematic error in the survey images or overall catalogue, which is most noticeable or perhaps only present for the highest flux density sources. However, interpreting this result is not straightforward

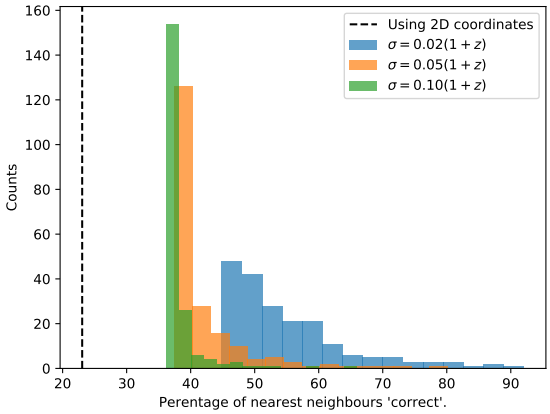

Figure 2.12: Percentage of the $n = 101$ nearest neighbours of every source in the photo-z perturbed sample of 1,051 brightest sources that agrees with the nearest neighbours found in the unperturbed sample. See text for more details.

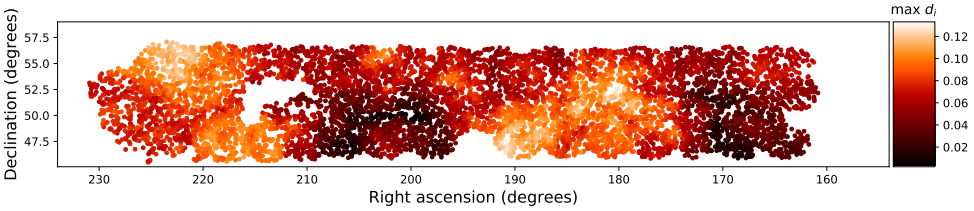

Figure 2.13: Scatter plot of the maximum dispersion measure (Equation 2.13) for every source, which indicates the strength of an alignment signal, of the selected sample of 7,555 radio sources plotted for $n = 700$ as a function of right ascension and declination.

due to the relatively large uncertainties in the third (redshift) dimension.

To further examine the impact of redshift uncertainties, we investigated whether 2D source positions are a better indicator of physical proximity than 3D source positions given different uncertainties in the photo-z estimates. This was done for the sample in Fig. 2.8 with the 1,051 highest flux density sources that showed a signal in 2D around $n = 101$ and no signal in 3D. We assumed, for this simulation, that the "true" source positions are given by the spectroscopic redshifts and best available photo-z estimates (i.e., that the photo-z scatters around the true redshift). The goal is to investigate what fraction of nearest neighbours that are found by using 3D positions agrees with the nearest neighbours found using the "true" source positions.

The redshift of sources with a photo-z estimate was perturbed by a Gaussian with standard deviations of the usual form $\sigma(1+z)$ and spectroscopic redshifts were left intact. The $n = 101$ nearest neighbours in 3D were then found for every source given the perturbed redshifts and the fraction of "correct" nearest neighbours was calculated. What we mean by "correct" here is that a nearest neighbour that was found is also one of the $n = 100$

nearest neighbours using the "true" source positions, thus, we do not take the ordering into account (as the statistical method for a single value of n does not do either). Figure 2.12 shows the result of re-sampling the photometric redshifts 200 times and computing the fraction of "correct" nearest neighbours. The figure shows that using 2D coordinates leads to finding 23% of the true physically close sources, while using 3D coordinates leads to finding more than 35% of the physically close sources, even with standard deviations as as large as $0.1 \times (1+z)$. Our assumed scatter of $0.1 \times (1+z)$ represents a conservative upper limit on the expected precision of the LoTSS photometric redshift estimates, with the typical scatter for the radio population found to range from $0.03 \times (1+z)$ for radio sources dominated by stellar emission and 0.08 to $0.1 \times (1+z)$ for the more difficult quasar and AGN population (see Duncan et al., 2019).

Thus, for this sample of sources and $n = 101$, it would be likely to find a stronger alignment using 3D coordinates if the alignment effect is correlated with physical source positions. However, we are finding stronger alignment using 2D coordinates, which qualitatively implies that the alignment effect is more correlated with observed 2D source positions than it is with 3D source positions.

2.6.3 Scale of the alignment

The angular scale of the observed alignment effect is substantially larger than that of the two previous radio structure studies. Taylor & Jagannathan (2016) investigated an area of 1.2 square degrees, and were thus limited to finding alignment within this area. Therefore, the angular scale of one degree found in that study might be underestimated and may still be in agreement with the results of this study. Contigiani et al. (2017), however, did not suffer this limitation, as they studied an area of 7000 square degrees and found an effect up to scales smaller than 2.5 degrees, with the maximum alignment signal at 1.5 degrees, while the distribution of source redshifts is not significantly different from that in this study. While the scale of the maximum effect does not agree with the angular scale of larger than three degrees found in this study, Contigiani et al. (2017) limited their search to angular scales below 2.5 degrees, so the signal may perhaps be present on larger scales in the FIRST survey as well. Further research into radio jet alignment at larger angular scales is thus needed.

Should the effect turn out to be physical, it is useful to compute the approximate physical scale corresponding to the effect that is observed. We computed the physical scale corresponding to the angular scale at which the alignment was found in this study by assuming the median redshift of the sample of sources for which a redshift is available (z = 0.56). Converting the angular scale of four degrees to comoving distances yields a corresponding physical scale of 103 h^{-1}Mpc. Although, as expected due to the limits in angular scales of the previous studies, the physical scale of 100 h^{-1}Mpc found in this study does not agree with the physical scale of the two previous studies of radio lobe alignment discussed earlier, it is in agreement with physical scales where other studies have found AGN alignment effects. As stated in Section 1, several studies have found that the radio polarization of quasars is preferentially aligned either perpendicular or parallel to the major axis of the surrounding large-scale large quasar groups (LQGs). These effects range from distances of the order of 150 Mpc (Tiwari & Jain, 2013) to distances larger than 300 h^{-1}Mpc (Pelgrims & Hutsemékers, 2016). The physical scales found in this study agree with the

physical scale for alignment with large-scale structures and coincides with the observed first peak of the Baryon Acoustic Oscillations (BAO; Eisenstein et al., 2005), while still abiding by the upper limits of homogeneity of the Universe, found to be on the order of 260 h^{-1}Mpc (e.g., Yadav et al., 2010).

2.7 Conclusion

In this study, we analyze the uniformity in the position angles of extended radio sources with well-defined linear double structures from the initial instalment of the LOFAR Two-metre Sky Survey (LoTSS). The combination of low frequencies (with sensitivity to extended structures) and the relatively high angular resolution of LOFAR makes it an excellent survey in the search for systematic alignments in the position angles of radio sources.

We extracted 7,555 LoTSS-extended sources with well-defined position angles from the 318,520 sources in the radio/optical value-added catalogue of LOFAR sources in the HETDEX Spring Field region. To test for the alignment of position angles in this sample, the spherical nature of position angles and the effect of transporting these angles over the celestial sphere were taken into account using statistical methods originally developed to test for the alignment of polarization vectors. We find evidence for alignment in our initial sample of sources. The null hypothesis that the position angles are distributed uniformly can be rejected with a significance level of $< 10^{-5}$ for an angular scale of four degrees, with the most non-uniformity present for radio sources with the largest flux densities.

Approximately half of the sources in our final sample have estimated redshifts available, either photometric or spectroscopic. This allows us to analyze the uniformity of radio source position angles in 3D space, but no strongly significant deviation from uniformity was found. We think it is more likely that the effect is caused by systematic effects, given the fact that the 2D analysis of the same reduced sample of sources still show an effect. However, the results are not straightforward to interpret due to the added uncertainties on the photometric redshifts, leaving no indisputable conclusion.

Understanding the systematic effect or physical effect that causes the observed alignment in different radio surveys is beyond the scope of this study, but should be investigated further. In particular, these subtle effects will be important for cosmological analyses with radio data, such as weak lensing studies with the Square Kilometer Array (e.g., Harrison et al., 2016; Bonaldi et al., 2016).

The number of sources considered here comprises less than 2% of the complete LoTSS survey. Hence, future studies by LOFAR should result in information about radio source alignments caused by substantially more subtle effects than we are presently able to determine. Additionally, the WEAVE-LOFAR project (Smith et al., 2016) will obtain over a million spectra of radio sources in LoTSS, which will allow for a much more detailed study of alignment in 3D space. This will provide the statistics needed to prove or disprove whether the alignment effect observed in this study is physical.

Acknowledgements

We kindly thank the anonymous referee for the comments and instructive insights. EO and RJvW acknowledge support from the VIDI research programme with project number 639.042.729, which is financed by the Netherlands Organisation for Scientific Research (NWO). MJH acknowledges support from STFC [ST/R000905/1].

WLW acknowledges support from the ERC Advanced Investigator programme NewClusters 321271. WLW also acknowledges support from the CAS-NWO programme for radio astronomy with project number 629.001.024, which is financed by the Netherlands Organisation for Scientific Research (NWO). KJD acknowledges support from the ERC Advanced Investigator programme NewClusters 321271. APM would like to acknowledge the support from the NWO/DOME/IBM programme "Big Bang Big Data: Innovating ICT as a Driver For Astronomy", project #628.002.001. HR acknowledges support from the ERC Advanced Investigator programme NewClusters 321271. LOFAR is the Low Frequency Array designed and constructed by ASTRON. It has observing, data processing, and data storage facilities in several countries, which are owned by various parties (each with their own funding sources), and which are collectively operated by the ILT foundation under a joint scientific policy. The ILT resources have benefitted from the following recent major funding sources: CNRS-INSU, Observatoire de Paris and Université d'Orléans, France; BMBF, MIWF-NRW, MPG, Germany; Science Foundation Ireland (SFI), Department of Business, Enterprise and Innovation (DBEI), Ireland; NWO, The Netherlands; The Science and Technology Facilities Council, UK; Ministry of Science and Higher Education, Poland. This research made use of the Dutch national e-infrastructure with support of the SURF Cooperative (e-infra 180169) and the LOFAR e-infra group. The Jülich LOFAR Long Term Archive and the German LOFAR network are both coordinated and operated by the Jülich Supercomputing Centre (JSC), and computing resources on the Supercomputer JUWELS at JSC were provided by the Gauss Centre for Supercomputing e.V. (grant CHTB00) through the John von Neumann Institute for Computing (NIC). This research made use of the University of Hertfordshire high-performance computing facility and the LOFAR-UK computing facility located at the University of Hertfordshire and supported by STFC [ST/P000096/1].

3

Diffuse radio emission from galaxy clusters in the LoTSS Deep Fields

Low-frequency radio observations are revealing an increasing number of diffuse synchrotron sources from galaxy clusters, primarily in the form of radio halos or radio relics. The existence of this diffuse synchrotron emission indicates the presence of relativistic particles and magnetic fields. It is still an open question as to exactly what mechanisms are responsible for the population of relativistic electrons driving this synchrotron emission. The LOFAR Two-metre Sky Survey Deep Fields offer a unique view of this problem. Reaching noise levels below 30 μJy/beam, these are the deepest images made at the low frequency of 144 MHz. This chapter presents a search for diffuse emission in galaxy clusters in the first data release of the LOFAR Deep Fields. We detect a new high-redshift radio halo with a flux density of 8.9 ± 1.0 *mJy and corresponding luminosity of* $P_{144\mathrm{MHz}} = (3.6 \pm 0.6) \times 10^{25}$ *W Hz*$^{-1}$ *in an X-ray detected cluster at* $z = 0.77$ *with a mass estimate of* $M_{500} = 3.3^{+1.1}_{-1.7} \times 10^{14} M_{\odot}$*. Deep upper limits are placed on clusters with non-detections. We compare the results to the correlation between halo luminosity and cluster mass derived for radio halos found in the literature. This study is one of a few to find diffuse emission in low mass (*$M_{500} < 5 \times 10^{14} M_{\odot}$*) systems and shows that deep low-frequency observations of galaxy clusters are fundamental for opening up a new part of parameter space in the study of non-thermal phenomena in galaxy clusters.*

Based on Osinga et al. (2021): *E. Osinga, R. J. van Weeren, J. M. Boxelaar, G. Brunetti, A. Botteon, M. Brüggen, T. W. Shimwell, A. Bonafede, P.N. Best, M. Bonato, R. Cassano, F. Gastaldello, G. di Gennaro, M. J. Hardcastle, S. Mandal, M. Rossetti, H. J. A. Röttgering, J. Sabater, C. Tasse, A&A, 648, A11 (2021).*

3.1 Introduction

Galaxy clusters are the largest virialised conglomerations of baryons and dark matter in the Universe as well as the densest parts of the large-scale matter structure of the Universe. An increasing number of galaxy clusters are revealing diffuse synchrotron radio emission (van Weeren et al., 2019), which indicates the presence of magnetic fields and a pool of relativistic electrons in the intra-cluster medium (ICM). The properties and origin of the pool of relativistic electrons are still not fully clear (Brunetti & Jones, 2014), and neither are the exact properties of the magnetic fields of galaxy clusters (Donnert et al., 2018).

The diffuse radio emission in merging galaxy clusters has been broadly classified into two main classes: radio halos and radio relics (Feretti et al., 2012; van Weeren et al., 2019). Radio halos are diffuse radio structures that roughly follow the thermal ICM distribution as observed by X-ray observations. Radio relics, also called radio shocks, are elongated and polarised structures found in the outskirts of galaxy clusters that are tracing merger-induced shock waves (Brunetti & Jones, 2014; Brüggen et al., 2012).

The currently favoured model for radio halos is the turbulent re-acceleration model, which poses that merger-induced turbulence (re-)accelerates cosmic-ray electrons which produce the radio halo (e.g. Brunetti & Lazarian, 2007; Paul et al., 2011; Miniati & Beresnyak, 2015). The turbulent re-acceleration model is supported by observations that show that radio halos are generally found in merging systems (e.g. Cassano, 2010; Cassano et al., 2013; Wen & Han, 2013; Kale et al., 2015; Cuciti et al., 2015; Eckert et al., 2017). A possible contribution may come from the hadronic model, which states that relativistic electrons are products of hadronic collisions between relativistic protons and thermal ions (e.g. Blasi & Colafrancesco, 1999; Dolag & Enßlin, 2000). However, upper limits to gamma-ray emission expected from the decay products, in particular upper limits on the Coma cluster (e.g. Jeltema & Profumo, 2011; Zandanel & Ando, 2014; Brunetti et al., 2012, 2017), and the very steep spectra observed in a fraction of radio halos (e.g. Brunetti et al., 2008; Wilber et al., 2018) rule out a dominant contribution from this channel, although a scenario where secondaries are re-accelerated by turbulence is not excluded (e.g. Brunetti & Lazarian, 2011; Pinzke et al., 2017; Brunetti et al., 2017).

Radio halos are more commonly found in higher-mass clusters, owing to the known scaling relation between the radio power and host cluster X-ray luminosity or mass (Liang et al., 2000; Cassano et al., 2013; Bîrzan et al., 2019). This scaling relation was found to exhibit a bi-modal behaviour, with merging systems lying on the correlation and with more relaxed systems generally being less luminous or undetected in the radio band at a level significantly below the correlation (e.g. Cassano et al., 2013; Cuciti et al., 2015). This behaviour corroborates the idea that the kinetic energy dissipated during merger events powers radio halos.

Some exceptions to the scaling relation and merger connection have been found. There are a few cases of over-luminous radio halos (i.e. halos found in low X-ray luminosity clusters). Although with only a few detections (e.g. Giovannini et al., 2009, 2011), the classification of these sources remains uncertain. Radio halos have also been found to be present in (semi-) relaxed clusters (Bonafede et al., 2014; Sommer et al., 2017; Savini et al., 2019), suggesting that minor mergers in massive clusters might also have the potential to dissipate enough energy to power cluster-scale emission, although again, these are only a few examples.

Most radio halos observed at gigahertz frequencies have spectral indices slightly lower than $\alpha = -1$ (Giovannini et al., 2009; Feretti et al., 2012, where $S_\nu \propto \nu^\alpha$). In a number of cases, ultra-steep ($\alpha \lesssim -1.6$) spectrum radio halos (USSRH) have been observed (e.g. Dallacasa et al., 2009; Macario et al., 2013; Wilber et al., 2018). The turbulent re-acceleration model predicts that less energetic mergers, often associated with lower mass systems, could generate halos with lower synchrotron break frequencies (< 1GHz; Cassano, 2010). Observing radio halos close to the break frequency leads to finding steeper spectrum halos. Because USSRHs are expected to be discovered at low frequencies and to be associated mainly with low-mass clusters, the correlation between the radio halo luminosity at 120 MHz and the X-ray luminosity of the cluster is predicted to be steeper and more scattered than at higher radio frequencies (Cassano, 2010).

There are still many open questions relating to the origin and formation of radio halos. Due to the higher occurrence rate and radio luminosity of halos with increasing cluster mass (Cassano et al., 2013; Cuciti et al., 2015), most of the understanding has been built on studies of relatively massive ($> 5\times10^{14} M_\odot$) galaxy clusters. However, it is important to study radio halos in low-mass systems to understand their origin. Only a few radio halos have been detected below cluster masses of $5\times10^{14} M_\odot$, with the lowest mass cluster being A3562 (Venturi et al., 2003) at $2.44^{+0.21}_{-0.24}\times10^{14} M_\odot$ (see Bîrzan et al., 2019, for a recent compilation of halos from the literature).

The fact that the turbulent re-acceleration model predicts that an increasing fraction of halos in lower mass clusters should have a steep spectrum implies that lower mass systems should be more easily detected at lower frequencies (e.g. Cassano, 2010; Brunetti & Jones, 2014). Furthermore, less massive clusters have a smaller turbulent energy budget, which implies that the effect of turbulent re-acceleration may become less dominant at lower cluster masses. Consequently, a possible transition from turbulent halos to halos powered by hadronic interactions is predicted (e.g. Cassano et al., 2012; Brunetti & Jones, 2014). The transition depends on the number of cosmic ray protons available in galaxy clusters, which is still not understood.

The LOFAR Deep Fields (Tasse et al., 2020; Sabater et al., 2020; Kondapally et al., 2020; Duncan et al., 2020) are a set of deep LOFAR observations on three fields which have high-quality multi-wavelength ancillary data available. These fields provide a unique opportunity to study radio halos in the low-mass and low-luminosity regimes due to the low frequency and large depth of the observations. This relatively unexplored regime can elucidate mechanisms of halo formation in low-mass clusters that exhibit lower levels of turbulent motions. In this work, we present a search for diffuse emission associated with galaxy clusters in the LOFAR Deep Fields. Throughout, we assume a flat ΛCDM cosmology with $H_0 = 70 \mathrm{kms}^{-1}\mathrm{Mpc}^{-1}$, Ω_m=0.3 and $\Omega_\Lambda = 0.7$. We define the spectral nature of the radio emission as $S_\nu \propto \nu^\alpha$ where S_ν is the measured flux density at the frequency ν and α is the spectral index.

3.2 Data

The LOFAR surveys key science project aims to survey the Northern sky at 120-168 MHz at several depth tiers with the LOFAR High Band Antenna. The wide survey aims to reach a sensitivity of 100 μJy beam^{-1}over the entire northern sky (Shimwell et al., 2017, 2019), while the Deep Fields are a set of deeper images of a few selected fields. This work makes

use of the first data release of the LOFAR Two Metre Sky Survey (LoTSS) Deep Fields (Tasse et al., 2020; Sabater et al., 2020; Kondapally et al., 2020; Duncan et al., 2020), which currently consists of three fields with a wealth of multi-wavelength data available: the European Large-Area ISO Survey-North 1 (ELAIS-N1; Oliver et al. 2000), Boötes (Jannuzi & Dey, 1999) and the Lockman Hole (Lockman et al., 1986), which cover a combined area of > 50 deg^2. The final aim of the LoTSS Deep Fields is to reach noise levels of $10-15\mu$Jy beam^{-1} (Tasse et al., 2020) near the pointing centre.

In the first data release, the Lockman Hole and Boötes field were observed for 80 and 112 hours, reaching noise levels in the centre of the fields of ~ 22 and 32 μJy beam^{-1} respectively. The observations and data reduction process of these two fields are described in detail by Tasse et al. (2020). The ELAIS-N1 field was observed for 170 hours, reaching noise levels of ~ 20 μJy beam^{-1}. This field required a custom data reduction strategy due to a different observing setup and bandwidth coverage, which is detailed by Sabater et al. (2020).

Table 3.1: Sample of sources extracted from the LOFAR Deep Fields. The mass, redshift and R_{500} are obtained from the PSZ2 catalogue (Planck Collaboration et al., 2016a) or from the MCXC catalogue (Piffaretti et al., 2011) if the source was not present in the former catalogue, unless otherwise noted. For the WHL clusters M_{500} was estimated from the richness, as detailed in Section 3.5.7. Mass uncertainties are not available for MCXC clusters.

Source Name	Field	Redshift	M_{500} ($10^{14}M_\odot$)	R_{500} (Mpc)	Radio classification
MCXC J1033.8+5703	Lockman	0.0463	0.128	0.35	No detection
MCXC J1036.1+5713	Lockman	0.7699	3.25	0.78	Halo
MCXC J1053.3+5720	Lockman	0.34	0.487	0.49	No detection
PSZ2 G147.88+53.24	Lockman	0.60	6.47 ± 0.60	1.06	Halo
PSZ2 G149.22+54.18	Lockman	0.1369	$5.87^{+0.23}_{-0.22}$	1.22	Halo
SpARCS1049+56	Lockman	1.71[1]	2.52 ± 0.86[2]	0.51	AGN
SDSSC4-3094	Lockman	0.04632[3]			AGN
PSZRX G084.01+46.28	ELAIS-N1	0.0675	$1.37^{+0.33}_{-0.36}$	0.77	No detection
PSZ2 G084.69+42.28	ELAIS-N1	0.13	$2.70^{+0.27}_{-0.26}$	0.94	Uncertain
WHL J160439.5+543139	ELAIS-N1	0.2655	2.95 ± 0.50	0.93	Detection uncertain
WHL J161135.9+541635	ELAIS-N1	0.3407	3.40 ± 0.58	0.94	No detection
WHL J161420.1+544254	ELAIS-N1	0.3273	2.85 ± 0.48	0.89	Detection uncertain

[1] (Webb et al., 2015)
[2] Derived from M_{200} given in Finner et al. (2020), see Section 3.5.5.
[3] (Miller et al., 2005)

3.3 Methods

We identified all clusters within 2.5 degrees of the pointing centre in the ELAIS-N1 and Lockman Hole fields that were present in the second *Planck* catalogue of Sunyaev-Zel'dovich detected sources (PSZ2; Planck Collaboration et al., 2016a), the Meta-Catalogue of X-ray detected Clusters of galaxies (MCXC; Piffaretti et al., 2011) or the Combined Planck-RASS catalogue of X-ray-SZ clusters (ComPRASS; Tarrío et al., 2019). Seven clusters in the aforementioned catalogues are present in the deep fields, of which the details are given in Table 3.1. We also checked the optically selected (SDSS data) cluster catalogue WHL (Wen

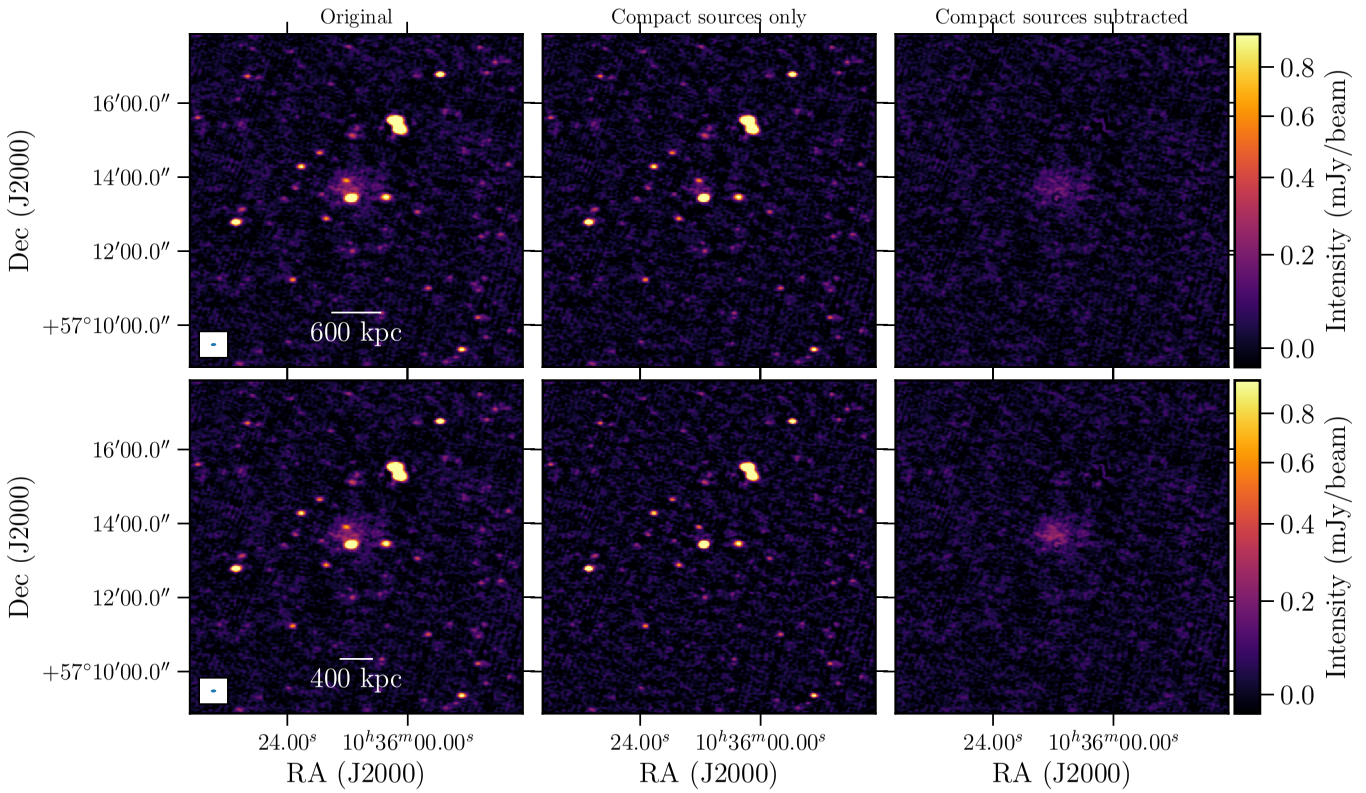

Figure 3.1: Compact source subtraction process for the cluster MCXCJ1036.1+5713. The left column shows the original image, the middle column the image containing only the compact emission, and the right column shows the final compact source subtracted image. All images are made with the same parameters, except the *uv*-cut for the central image. The top compact source only image was made with a *uv*-cut of 2547λ (i.e. 600 kpc at the cluster redshift) while the bottom image was made with a *uv*-cut of 3820λ (i.e. 400 kpc). The restoring beam size is 9”×5”.

et al., 2012) for clusters showing signs of diffuse emission and visually identified three more clusters that show hints of diffuse emission, although these are more likely to be AGN-related extended emission. Finally, we also add the SpARCS1049+56 cluster to our sample, which was identified by Webb et al. (2015) to be a very high redshift ($z = 1.71$) cluster in the Lockman Hole field. As a fortuitous bonus, the cluster SDSSC4-3094 identified in the Sloan Digital Sky Survey (Miller et al., 2005) at $z = 0.04632 \pm 0.00083$ lies in the same region of the sky as SpARCS1049+56 and is therefore added to the sample. Details on the total of 12 clusters are given in Table 3.1, seven and five of which are in Lockman and ELAIS-N1 respectively. The Boötes deep field observations do not overlap with any clusters from the PSZ2, MCXC or ComPRASS catalogues. No clear diffuse emission from cluster objects was picked up from visual identification of the field, including the 12 spectroscopically confirmed clusters at $z > 1$ found by Eisenhardt et al. (2008).

3.3.1 Target extraction and imaging

Once clusters are identified, we followed an 'extract and subtract' procedure to optimise the sensitivity of the deep images to diffuse emission in the direction of the cluster by allowing for easy re-imaging. First, we made small ($\sim 0.3^\circ \times 0.3^\circ$) boxes around the identified targets. The *uv*-data corresponding to this box were extracted from the full dataset with the following method. A direction-dependent calibrated model, from the pipeline described in Tasse et al. (2020); Sabater et al. (2020), of all components outside the boxed region was subtracted from the model data. This leaves visibilities that contain only sources in the boxed region. We then phase-shifted to the centre of the extracted region, averaged the data in time and frequency to reduce the size and performed 7 rounds of direction-dependent self-calibration with the DDF pipeline[1] (Tasse, 2014; Smirnov & Tasse, 2015; Tasse et al., 2018) to improve the quality of the extracted image compared to that in the original deep field maps. In the original deep field maps, the facets used for direction-dependent calibration are larger as the distance to the pointing centre increases, causing more calibration errors related to the assumed constant beam model and ionosphere over a single facet. This extraction procedure mitigates these errors by manually defining a smaller sub-region than the original facet around the target of interest. The primary beam correction on these extracted and self-calibrated visibilities was done by multiplication with a constant factor of the primary beam response at the centre of the extracted region, which is a good assumption since the extraction region is much smaller than the size of the LOFAR primary beam (full width at half maximum $\sim 2.5^\circ$). The details of the extraction process are described in van Weeren et al. (2021) and the method has been used with various other LOFAR observations (e.g. Hardcastle et al., 2019; Mandal et al., 2020; Botteon et al., 2020b,c).

To properly disentangle the extended diffuse emission from compact sources, compact sources were subtracted. This was done as follows: first, an image of only the compact sources was made by ignoring short baselines that are sensitive to extended emission. The inner *uv*-cut was initially calculated such that it corresponds to emission of a certain largest linear physical size at the cluster redshift, based on the mass of the cluster. As an example, for the low mass system MCXCJ1036.1+5713 we found that the *uv*-cut of 2547λ (i.e. 600 kpc at $z = 0.77$) was too small to properly exclude all diffuse emission. A *uv*-cut of 3820λ

[1] https://github.com/mhardcastle/ddf-pipeline

(i.e. 400 kpc) shows better separation of diffuse emission and compact sources, as shown in Figure 3.1. As higher mass clusters often have larger radio halos, it makes sense to have lower *uv*-cuts (in kpc) with lower cluster mass.

The clean component model of the compact image was subtracted from the visibilities of the extracted dataset, leaving only the visibilities corresponding to the diffuse extended emission. This emission was imaged with a Gaussian taper corresponding to 50 kpc at the cluster redshift, using multi-scale clean, with `WSClean` (version 2.7.3) (Offringa et al., 2014; Offringa & Smirnov, 2017) to properly deconvolve the diffuse emission. The complete compact source subtraction process is illustrated in Figure 3.1 for the cluster MCXCJ1036.1+5713 as an example.

3.3.2 Measuring radio halo properties

To measure the properties of the diffuse emission, we fitted the radio halos with an exponential profile. This has a few advantages over manually defining the halo region. Commonly, the radio halo flux density is measured by integrating the surface brightness over an area bounded by isophotes (e.g. 3σ contours). However, this causes the resulting flux density to be dependent on the sensitivity of the observations. It is more rigorous to fit the halos with a profile and analytically integrate that profile up to a certain radius. It has been shown that exponential profiles can provide characteristic scales relatively independent of the sensitivity of the radio observations (Murgia et al., 2009). In this work we consider the simplest, spherically symmetric, exponential profile for most of the halos, which has been found to be representative of radio halos (Murgia et al., 2009), although in some cases observations of radio halos have shown strong deviations from spherical symmetry (e.g. van Weeren et al., 2016a; Wang et al., 2018). The surface brightness model is given by

$$I(\vec{r}) = I_0 e^{-\vec{r}/r_e}, \tag{3.1}$$

where I_0 and r_e are the central surface brightness and the e-folding radius, respectively. To compare the e-folding radii of the halos to the radii of the halos that are normally quoted in the literature (r_H), we assume $r_H/r_e = 2.6$, as was found by Bonafede et al. (2017) for 8 clusters with measured r_H within 3σ isophotes and fitted r_e.

The presented fitting of Equation (3.1) and halo radio flux density estimations were done with a newly developed algorithm[2]. The algorithm is described in detail by Boxelaar et al. (2021), and we briefly explain it here. The fitting algorithm is based on fitting methods first presented by Murgia et al. (2009). The difference here is that profiles are fitted to a two-dimensional image directly rather than to a radially averaged one-dimensional data array. This allows fitting of a non-circular model as well, although for simplicity we assume a circular model in this work. Theoretically, one could fit both a circular and a non-circular model and compare a goodness of fit statistic (e.g. reduced χ^2) of both models to determine which model is a better fit. However, the determination of the morphology of the diffuse emission is beyond the goal of this study and requires high signal-to-noise data to determine statistically significant differences in the goodness of fit statistic.

The total flux density S of the fitted radio emission is obtained by integrating Eq. (3.1). The analytical expression for the total flux density is $S = 2\pi I_0 r_e^2 \left(1 - e^{-d}(d+1)\right)$, where d

[2] `https://github.com/JortBox/Halo-FDCA`

denotes the radius (in e-folding radii) up to which is being integrated. Here we choose to integrate up to $2.6r_e$, following Bonafede et al. (2017). For comparison, integrating up to $2.6r_e$ results in a total flux density that is 73% of the flux density found when integrating the model to infinity.

The best-fit estimates for the peak surface brightness and e-folding radius are found through Bayesian inference and maximum likelihood estimation. To sample the likelihood function, we use a Monte Carlo Markov Chain, implemented within the *emcee* module (Foreman-Mackey et al., 2013). This method allows us to find the full posterior distribution for the model parameters. Given observed data $V(\vec{r}_i)$ (which represents the radio surface brightness at position $\vec{r}_i$) and fit parameter vector $\vec{\theta} = (I_0, r_e)$, we assume that all the compact source subtracted images can be expressed as $V(\vec{r}_i) = I(\vec{r}_i) + \epsilon_i$ where $I(\vec{r})$ is defined in Eq. (3.1) and the underlying noise ϵ_i is independent and identically distributed as $\mathcal{N}(0, \sigma^2_{\rm rms})$. The independence of individual pixels is assured by re-gridding the images such that the pixel area approximately equals the beam area while preserving the total flux. The probability density function $f(\vec{r}_i; \vec{\theta})$ for an observation then reads

$$f(\vec{r}_i; \theta) = \frac{1}{\sqrt{2\pi}\sigma_{\rm rms}} \exp\left(-\frac{(V(\vec{r}_i) - I(\vec{r}_i; \theta))^2}{2\sigma^2_{\rm rms}} \right). \tag{3.2}$$

This results in a log-likelihood function which is given by

$$\ln \mathcal{L}(\theta) = -n \ln\ \sqrt{2\pi}\sigma_{\rm rms} - \frac{1}{2\sigma^2_{\rm rms}} \sum_{i=1}^{n} (V(\vec{r}_i) - I(\vec{r}_i; \theta))^2, \tag{3.3}$$

where the sum is taken over the n re-gridded pixels. Maximising the log-likelihood function for θ allows us to find the best-fit model parameter vector $\hat{\theta}$.

The uncertainty of the total flux density of the halos f_H is calculated by adding the uncertainty due to map noise (i.e. the uncertainty on best-fit parameters $\sigma_{\rm fit}$), the absolute flux density scale $\delta_{\rm cal}$ and compact source subtraction $\sigma_{\rm sub}$ in quadrature (cf. Cassano et al., 2013).

$$\sigma_{f_H} = \sqrt{(\delta_{\rm cal} f_H)^2 + \sigma^2_{\rm fit} + \sigma^2_{\rm sub}}. \tag{3.4}$$

The uncertainty on the best-fit parameters $\sigma_{\rm fit}$ is given by the 16th and 84th percentile of the converged MCMC chain (i.e. 1σ) and we assume a 10% error on the absolute flux scale of the LOFAR images $\delta_{\rm cal}$ (Sabater et al., 2020) and a 1% error on the compact source subtraction process $\sigma_{\rm sub}$. The latter error is calculated as 1% of the flux contained in the compact sources only image within $2.6r_e$ of the centre of the fitted halo. This 1% error is consistent with measuring the residual flux in the compact source subtracted images at the location of bright compact sources.

For determining the upper limits in the case of non-detections, we used a similar method to that of Bonafede et al. (2017), which injects mock halos into the visibility data (see also Brunetti et al., 2007; Venturi et al., 2008). We injected mock halos following the exponential profile in Eq. (3.1). Following Bonafede et al. (2017), we added power spectrum fluctuations of the form $P(\Lambda) \propto \Lambda^n$, where Λ is the spatial scale, to account for surface brightness fluctuations observed in real radio halos. We set Λ between 10-250 kpc and $n = 11/3$ (Govoni et al., 2005, 2006; Bonafede et al., 2017).

The initial value of I_0 and r_e were chosen such that the expected radio power of the halo follows the $P_{1.4\mathrm{GHz}} - M_{500}$ correlation by Cassano et al. (2013). Specifically, we first calculated $P_{1.4\mathrm{GHz}}$ from the cluster mass, then set r_e according to the correlation between $P_{1.4\mathrm{GHz}} - r_e$ given by Murgia et al. (2009) and finally scaled I_0 such that the exponential model integrates up to the expected radio power of the halo. The resulting model was injected (i.e. Fourier transformed and added) into the visibility data at a location close to the cluster but absent of contaminating radio sources. The data were then cleaned and imaged in the same way as the original image. We define the halo as detected if the $3\sigma_{\mathrm{rms}}$ contours cover at least 3 beams. Provided the halo is detected, the I_0 was gradually lowered by steps of σ_{rms} to find a more stringent upper limit on the radio power. Conversely, if the halo is not detected, the I_0 was gradually increased until it is detected. We inject halos close to the clusters instead of on the centre of the clusters to avoid being biased low on the upper limits. Residual emission from point sources or an undetected halo near the cluster centre might otherwise contribute to flux measurement of the injected halos. Off cluster injection does assume, however, that there are no calibration artefacts due to bright sources in the cluster.

3.4 Verification on simulated halos

When determining the properties of diffuse radio emission, it is important to not only keep track of the statistical uncertainties, but to also consider additional sources of error. We test in this section two main effects. The first is the effect of the limited *uv* coverage of radio telescopes, particularly at shorter baselines, which may cause resolving out some diffuse emission. The second is the point source subtraction process, which may also erroneously subtract some diffuse emission, depending on the *uv*-cut used.

To test the fitting procedure, the sensitivity of the LOFAR observations to different scales of emission and the point source subtraction process, we injected mock halos with different I_0 and r_e into a single LOFAR observation (~ 8 hours of data) of the Lockman Hole field. The full observations are not used for this test due to the computational intensity of the imaging and point-source subtraction process on the full dataset. The local rms at the region of injection is around 100 μJy beam^{-1}. We assume a redshift of $z = 0.30$ for the conversion of the e-folding radius to angular size. We then compare the injected properties with the properties derived from fitting. Six different halos have been injected into the data, which are shown in Fig. 3.2.

Table 3.2: Results of fitting exponential profiles to mock halos of different properties. The injected flux density and resulting flux density are defined as the flux fitted within $2.6r_e$. The uncertainty in the flux density here does not include an absolute flux scale uncertainty, as the injected halo flux densities would change accordingly.

I_0 inject [μJy arcsec^{-2}]	r_e inject [kpc]	S_ν inject [mJy]	I_0 observed [μJy arcsec^{-2}]	r_e observed [kpc]	S_ν observed [mJy]
12.0	65	20.9	$8.6^{+1.0}_{-0.9}$	82^{+8}_{-8}	23.7 ± 3.5
24.0	65	41.9	$17.3^{+0.9}_{-0.9}$	79^{+3}_{-3}	44.5 ± 5.0
36.0	65	62.8	$26.3^{+0.9}_{-0.8}$	77^{+2}_{-2}	63.8 ± 6.8
12.0	80	31.7	$10.2^{+0.8}_{-0.8}$	94^{+7}_{-6}	36.7 ± 4.7
12.0	100	49.6	$10.0^{+0.6}_{-0.7}$	118^{+7}_{-6}	57.9 ± 6.9
12.0	120	71.4	$10.2^{+0.5}_{-0.6}$	140^{+7}_{-5}	83.2 ± 9.4

We subtracted point sources by employing a *uv*-cut of 200 kpc, corresponding to 3443λ.

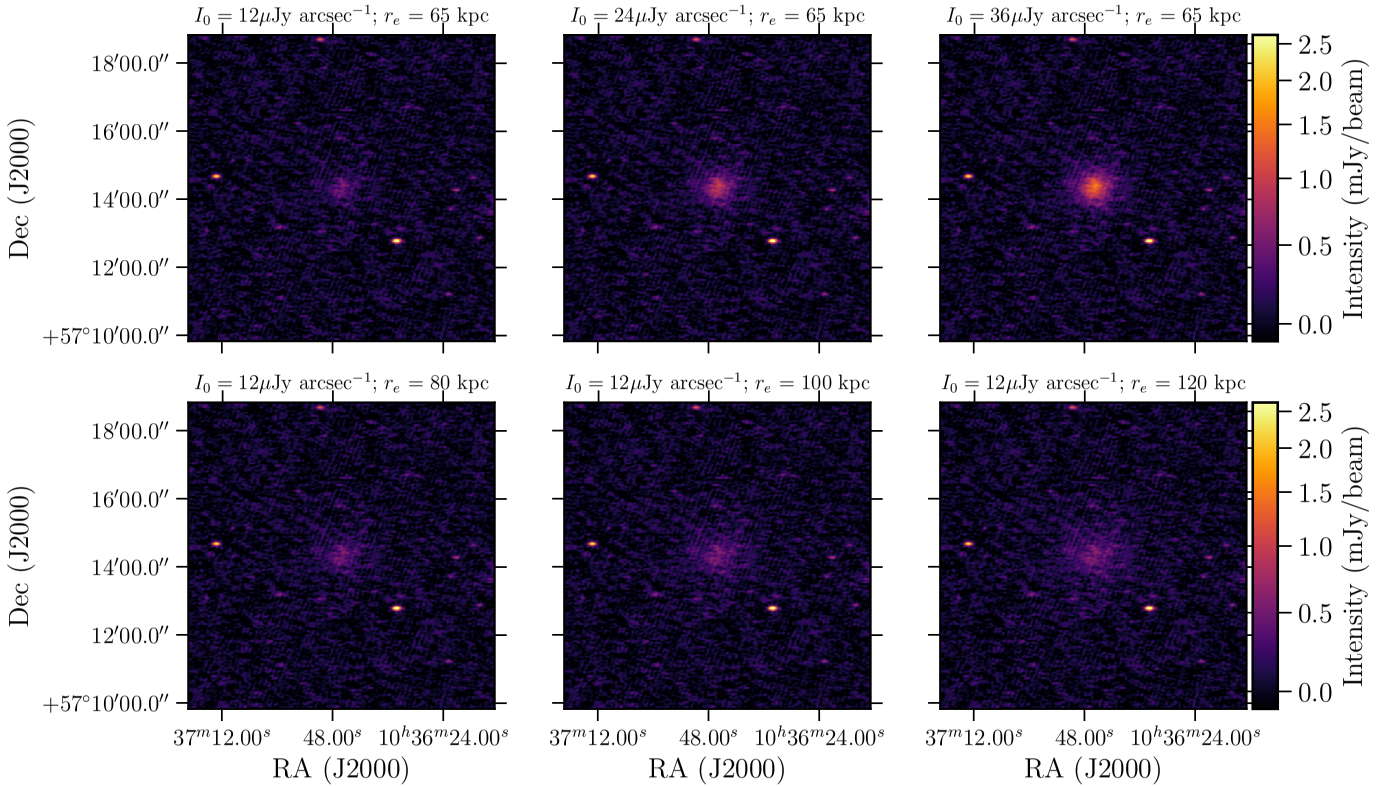

Figure 3.2: Six mock halos injected into a single 8-hour LOFAR observation of the Lockman Hole field. The different properties of the halos are given in the title figures.

The compact source subtracted images are then fitted following the procedure outlined in Section 3.3.2. The resulting best-fit parameters and injected parameters are given in Table 3.2. We find that we generally recover the correct flux density within the 68% uncertainty, although we are biased slightly higher than the injected flux density. This is because some of the central brightness structure of the mock halos is subtracted out by the compact source subtraction process. This causes generally underestimated I_0 and overestimated r_e, which also causes generally slightly overestimated S_ν of about 10%, because the integrated flux density scales with r_e^2. This bias is important to keep in mind throughout the rest of this work. The test does show that LOFAR is sensitive to the extended emission of halos following an exponential profile, since we are not resolving out a significant amount of flux. This is in line with what for example Hoang et al. (2018) and Botteon et al. (2020b) have found for the injection of larger halos into LOFAR observations. The full observations are about a factor of ~ 3 deeper than the single pointing used here, so we do not expect significant difference from these results for halos with a central surface brightness down as low as $I_0 \sim 4\mu$Jy arcsec^{-2}.

3.5 Results

Here we report the results of the fitting procedure for each cluster. Unless otherwise stated, we have performed the fitting on the compact source subtracted images tapered to a resolution corresponding to 50 kpc at the cluster redshift. To calculate the radio luminosity, we assume a spectral index of $\alpha = -1.5 \pm 0.2$ for clusters where spectral index estimates are not available. We choose this range to cover the typical spectra of halos, including steep-spectrum halos (van Weeren et al., 2019). The azimuthally averaged surface brightness profiles and corner plots of the MCMC chain can be found in Appendix I.

3.5.1 PSZ2G147.88+53.24

PSZ2 G147.88+53.24 is a massive, high-redshift ($z = 0.6$; Planck Collaboration et al., 2016a) galaxy cluster. Diffuse emission was recently reported by Di Gennaro et al. (2021a), where the emission is classified as a giant radio halo. Di Gennaro et al. (2021a) measure a total flux density of 14.4 ± 2.3 mJy at 144 MHz by arithmetically subtracting the radio galaxies flux densities from the total flux density at low-resolution. The diffuse emission has a largest linear size of around 700 kpc. We employ a *uv*-cut corresponding to 400 kpc at the cluster redshift (3447λ) for the compact source subtraction process. We confirm the detection of Di Gennaro et al. (2021a) in our deeper image, which is shown in Figure 3.3 where we show the low-resolution compact source subtracted radio contours overlaid on the g, r, z optical image from the Legacy survey (Dey et al., 2019). The high-resolution radio emission is shown the right panel of Figure 3.3. The source to the north-west of the central radio galaxy in Figure 3.3 might be contributing to the low-resolution (compact source subtracted) radio contours, given the peculiar feature that is present in the low-resolution contours. Therefore, we decide to fit the halo with and without a mask covering the north-western source. The masked region is shown as the green region in Figure 3.3.

As this cluster is at a high redshift, 50 kpc corresponds almost to the high-resolution beam size (at $z = 0.6$, 50 kpc corresponds to 7.5"). Therefore, we taper to lower resolution, using a 10" Gaussian taper, to make the fitting procedure converge better. The full

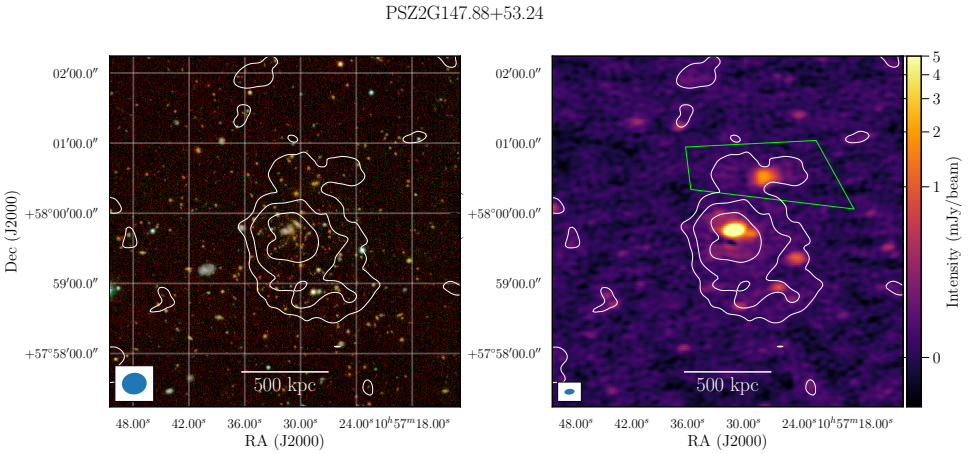

Figure 3.3: Low-resolution LOFAR diffuse emission from the cluster PSZ2G147.88+53.24 overlaid on *grz* filters from the Legacy survey (Dey et al., 2019) (left) and overlaid on the high resolution radio intensity image (right). The contours are plotted at $[3,6,12]\sigma$, where $\sigma = 83\mu$Jy beam^{-1}. The restoring beam sizes are $21'' \times 19''$ and $9'' \times 5''$ for the low-resolution and high-resolution radio images respectively. The green region marks the region masked from the fitting procedure.

width at half maximum of the restoring beam of the low-resolution image is $21.3'' \times 18.5''$. Without any masking, the best-fit parameters are $I_0 = 4.4 \pm 0.3$ μJy arcsec^{-2}, r_e=194 $\pm$ 10 kpc. Integrating the model in Equation (3.1) up to $2.6r_e$ with the best-fit parameters leads to a flux density at 144 MHz of 16.9 ± 2.0 mJy. This corresponds to a 1.4 GHz power of $P_{1.4\text{GHz}} = (1.1 \pm 0.4) \times 10^{24}$W Hz^{-1} assuming $\alpha = -1.5 \pm 0.2$. When employing the mask shown in the right panel of Figure 3.3, we find best-fit parameters $I_0 = 4.5 \pm 0.3$ μJy arcsec^{-2} and $r_e = 186 \pm 11$ kpc, which correspond to a consistent integrated flux density of 16.0 ± 2.0 mJy at 144 MHz.

The resulting flux densities are a bit higher, but consistent within the error bounds with the value of 14.4 ± 2.3 mJy reported by Di Gennaro et al. (2021a). This is to be expected, because our observations are deeper and Section 3.4 showed that we are likely biased a bit high on the flux density values due to the compact source subtraction process. Manually measuring the flux within 3σ contours results in slightly better agreement with a flux density of 14.7 ± 1.6 mJy.

3.5.2 PSZ2G149.22+54.18

PSZ2G149.22+54.18, or Abell 1132 is a quite massive cluster, with a mass of $5.87^{+0.23}_{-0.22} \times 10^{14} M_\odot$ (Planck Collaboration et al., 2016a) that is undergoing a merging event (Cuciti et al., 2015). It is located at a redshift of $z = 0.1369$ (Struble & Rood, 1991). Diffuse emission was not picked up by previous VLA observations at 1.4 GHz (Giovannini & Feretti, 2000), but was clearly detected by previous observations with LOFAR (Wilber et al., 2018). The central diffuse emission was classified as an ultra steep spectrum radio halo with $\alpha = -1.75 \pm 0.19$ between 144 and 325 MHz. The connection between the diffuse emission in the halo and the diffuse emission at the edge of the giant tailed radio galaxy was tentatively raised by

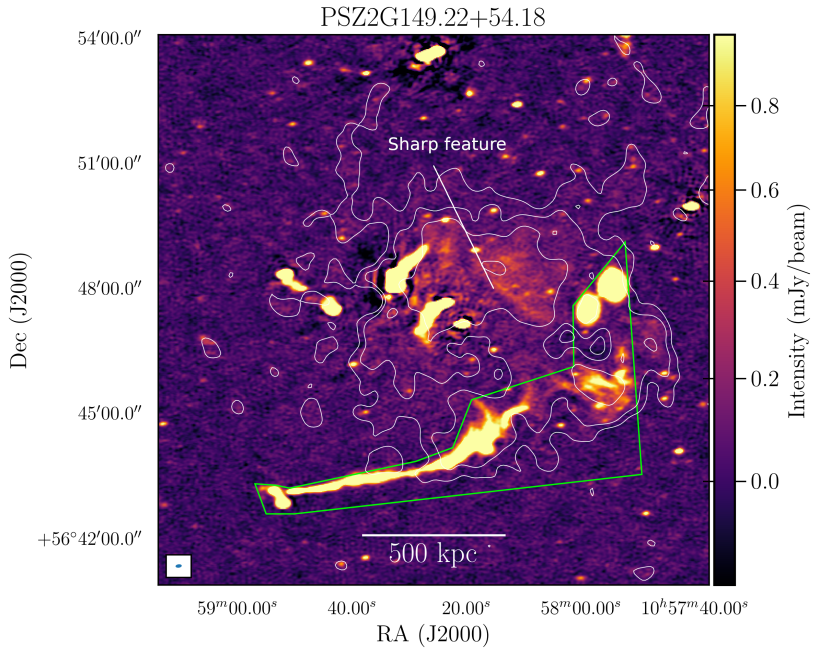

Figure 3.4: High-resolution ($9'' \times 5''$) LOFAR radio intensity image of Abell 1132 with low-resolution compact source subtracted contours at $[3, 6, 12, ..]\sigma$, where $\sigma = 149 \mu$Jy beam^{-1}. The beam size of the low-resolution contours is $28'' \times 24''$. The green box indicates the region that is masked from the fitting procedure.

Wilber et al. (2018), and is now clearly observed in the low-resolution contours shown in Figure 3.4. We note that the halo size seems larger than previously determined, with the size inside the 3σ contours being $\sim$ 1.0 Mpc $\times$0.9 Mpc in the east-west and north-south direction, respectively.

To allow for a better comparison to the previous LOFAR observations, the compact source subtraction was done by using a *uv*-cut corresponding to 500 kpc at the cluster redshift (i.e. 1000λ in the *uv* plane). Since the giant head-tail radio galaxy blends in with the emission of the halo, we manually mask the tail from the fitting procedure. The mask is shown in the green box in Figure 3.4.

The best-fit parameters are 5.7 ± 0.1 μJy arcsec^{-2} and $r_e = 235 \pm 4$ kpc. These correspond to a total flux density of the halo of 244.9 ± 29.7 mJy at 144 MHz, translating to $P_{1.4\text{GHz}} = (2.5 \pm 0.3) \times 10^{23}$W Hz^{-1}, assuming $\alpha = -1.75$, which is in agreement with the value reported by Wilber et al. (2018). The extent of the halo within the 3σ contour level is larger in our deep image than in the image of Wilber et al. (2018), which again points out that fitting the halo provides more robust flux density measurements than measuring the flux density within certain isophotes. Manually measuring the flux in the 3σ contours (without a mask) results in a flux density of 261 ± 31 mJy, which is consistent with the flux from integrating the best-fit radial profile up to $2.6r_e$. Although the halo is a bit more elongated in the east-west direction than in the north-south direction, the comparison with the manually measured flux density within 3σ contours indicates that the circular model is

still a reasonable assumption.

3.5.3 PSZ2G084.69+42.28

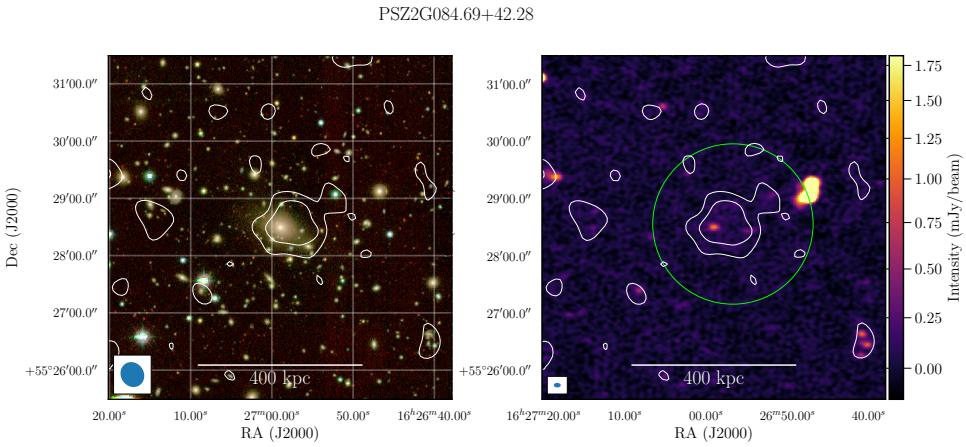

Figure 3.5: Low-resolution LOFAR diffuse emission from the cluster PSZ2G084.69+42.28 overlaid on *grz* filters from the Legacy Survey (left) and overlaid on the high-resolution radio intensity image (right). The contours are at $[2,4]\sigma$, where $\sigma = 152\mu$Jy beam^{-1}. The high- and low-resolution beam sizes are $7'' \times 5''$ and $27'' \times 24''$ respectively. The fitting procedure was performed only within the region of the image contained by the green circle.

PSZ2G084.69+42.28 or Abell 2201, is a relatively low mass ($2.67^{+0.27}_{-0.26} \times 10^{14} M_{\odot}$; Planck Collaboration et al. 2016a) galaxy cluster at a redshift of 0.13 (La Franca et al., 2002), which has not been studied extensively. This cluster has the lowest mass estimate in our sample of PSZ clusters with a detection. We pick up weak diffuse emission from the cluster centre. This emission is visible in the low-resolution compact source subtracted contours overlaid on the high-resolution image in the left panel of Figure 3.5. The optical image overlay is shown in the right panel, which shows that the diffuse emission surrounds the brightest cluster galaxy (BCG).

Since the diffuse emission is very small in size, we employ a *uv* cut of 2390λ, corresponding to 200 kpc at the cluster redshift. Given the size, it is possible that the emission is AGN-related. We enforce that the spherical profile is only fit in a region of approximately 400 kpc by masking out the outer regions, because the emission is only barely picked up above the noise. This mask is shown in the right panel of Fig. 3.5. The best-fit values are found to be $I_0 = 2.0^{+0.7}_{-0.6}$ μJy arcsec^{-2} and $r_e = 57^{+18}_{-13}$ kpc. Integrating the analytical model up to $2.6r_e$ results in a total flux density of 5.5 ± 1.6 mJy at 144 MHz or a radio luminosity at 144 MHz of $(2.6 \pm 0.8) \times 10^{23}$ W Hz^{-1}. Assuming a spectral index of $\alpha = -1.5 \pm 0.2$, we obtain a radio power of $P_{1.4\mathrm{GHz}} = (8.6 \pm 4.5) \times 10^{21}$ W Hz^{-1},

Assuming $r_H/r_e = 2.6$ (Bonafede et al., 2017), the radius of the diffuse emission is about 150 kpc, which is much smaller than typical radio halos and would imply a ratio $R_H/R_{500} = 0.16$ that falls in the typical range of mini-halos (Giacintucci et al., 2017). Thus based on the size we would identify this as AGN-related emission or a mini-halo. However, according to Cassano et al. (2007) radio halos do not follow a self-similar scaling, with their

size decreasing more rapidly than that of the hosting cluster with decreasing mass (see also Murgia et al., 2009). Thus, it is not unexpected that a radio halo would be smaller than halos found in high mass systems.

3.5.4 MCXCJ1036.1+5713

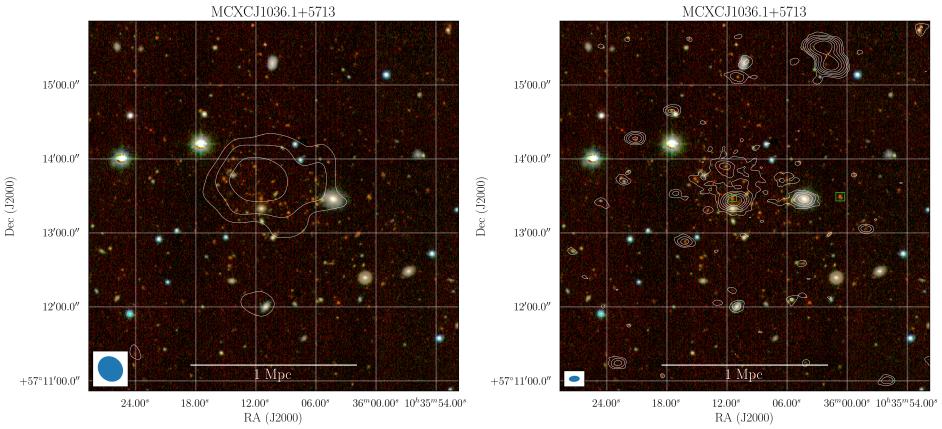

Figure 3.6: Optical image (*grz* filters) of the cluster MCXCJ1036.1+5713 from the Legacy Survey with compact source subtracted low-resolution ($22'' \times 19''$) LOFAR contours overlaid (left) and high-resolution compact source contours overlaid (right). Contours at $[3, 6, 12]\sigma$, where σ=86 μJy beam^{-1} and 38 μJy beam^{-1} respectively. The green boxes denote the galaxies with SDSS spectra available.

This cluster was detected by the 400 deg^2 *ROSAT* PSPC Galaxy Cluster Survey (Burenin et al., 2007) and lies at a redshift of $z = 0.203$ according to Piffaretti et al. (2011). However, the optical image shown in Figure 3.6 does not show a clear overdensity of low-redshift galaxies, but rather shows an overdensity of small, red galaxies, which suggests that the detected cluster lies at higher redshift. Figure 3.7 shows the SDSS photometric redshift estimates (Ahumada et al., 2020) of galaxies within a radius of roughly $1.5'$ from the central radio source, and indeed an overdensity is apparent at $z = 0.6-0.7$ rather than at $z = 0.2-0.3$. The optical counterpart to the central bright radio source shown in the high-resolution contours (denoted by the green box) has a spectroscopic redshift of $z = 0.76991$ (Ahumada et al., 2020). Another nearby source, which appears to be in the same cluster, also has a spectroscopic redshift of $z = 0.76391$. For these reasons, we adopt a redshift of $z = 0.77$ for this cluster.

Correcting the X-ray luminosity given by the MCXC for this change in redshift, we find a mass estimate of $M_{500} = 3.3^{+1.1}_{-1.7} \times 10^{14} M_{\odot}$. using the relation between L_{500} and M_{500} found by Arnaud et al. (2010b). The one sigma error reported is underestimated, as this only takes into account the intrinsic scatter in the $L_X - M$ relation.

While masses derived from X-ray luminosity are generally less well constrained than masses derived from the Sunyaev-Zel'dovich effect, the fact that the cluster is not present in the *Planck* Sunyaev Zel'dovich catalogue (Planck Collaboration et al., 2016a) can also be used to constrain the mass. From visual inspection of the Compton parameter maps released by Planck Collaboration et al. (2016d), we note that there are various detections in

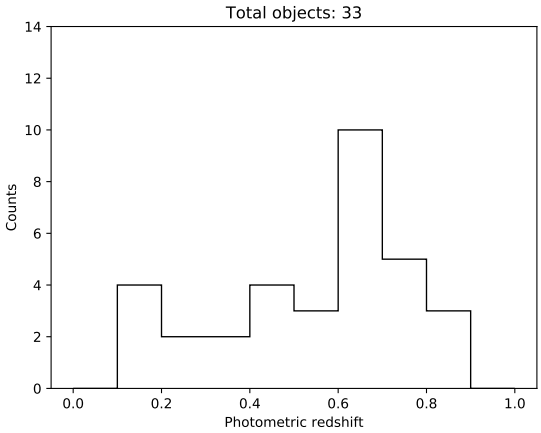

Figure 3.7: SDSS photometric redshifts of galaxies within a radius of roughly 1.5′ from the central radio source of the cluster MCXCJ1036.1+5713.

a region of four degrees around this cluster, which makes it likely that the non-detection of this cluster is simply due to a low signal-to-noise ratio and thus low mass of the cluster. The completeness of the PSZ2 catalogue as a function of mass and redshift (Fig. 26 in Planck Collaboration et al., 2016a) indicates that for the cluster redshift of $z = 0.77$, the catalogue is 50% and 80% complete for masses of ~ 6.0 and $\sim 7.5 \times 10^{14} M_{\odot}$ respectively. This provides us a fiducial upper limit to the mass of the cluster of $\sim 7.5 \times 10^{14} M_{\odot}$).

The compact source subtraction process for this cluster is shown in Figure 3.1. The final panel shows a clear detection of extended diffuse radio emission, which can be best observed from the radio-optical overlay given in Figure 3.6. Because of the large size of this emission (> 800 kpc), we classify this source as a radio halo.

We find best-fit parameters $I_0 = 7.7 \pm 0.5 \mu$Jy arcsec^{-2} and $r_e = 124 \pm 7$ kpc. Integrating the analytical profile given in Eq. 3.1 results in a flux density of 9.8 ± 1.1 mJy. Assuming a spectral index of -1.5 ± 0.2, this translates to a radio luminosity of $P_{1.4\mathrm{GHz}} = (1.2 \pm 0.4) \times 10^{24}$ W Hz^{-1} at 1.4 GHz[3].

3.5.5 SpARCS1049+56

SpARCS1049+56 is a very high redshift ($z = 1.71$) cluster where star formation is actively taking place in the core, at a rate of 860 ± 130 M$_{\odot}$ yr^{-1} (Webb et al., 2015). The mass of the cluster was determined via infrared weak lensing to be $M_{200} = (3.5 \pm 1.2) \times 10^{14}$ M$_{\odot}$ (Finner et al., 2020).

We pick up some diffuse emission from this cluster. The compact source subtracted radio contours overlaid on the high-resolution radio map are shown in Fig. 3.8. The radio-optical overlay is shown in Appendix II, Figure 3.23. As the cluster is located at such a high redshift, it is difficult to properly subtract the compact sources from the diffuse

[3]For completeness we note that assuming a redshift of z=0.203 would give a mass of $M_{500} = 0.88 \times 10^{14} M_{\odot}$ and a radio luminosity of $P_{1.4\mathrm{GHz}} = (3.8 \pm 1.7) \times 10^{24}$ W Hz^{-1}

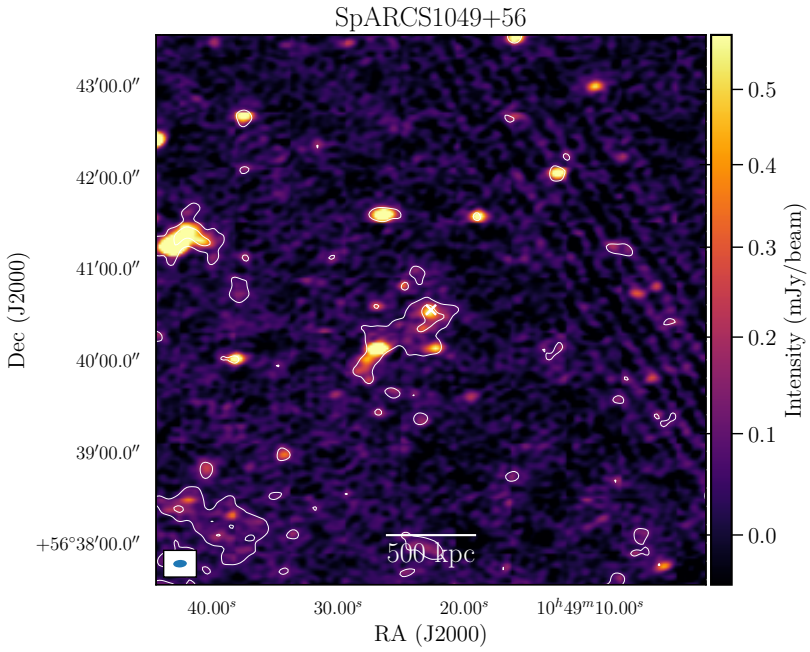

Figure 3.8: High-resolution ($9'' \times 5''$) LOFAR radio intensity image of SpARCS1049+56 with low-resolution ($14'' \times 9''$) compact source subtracted contours showing diffuse emission at $[3, 6]\sigma$, where $\sigma = 48\mu$Jy beam^{-1}. The white cross marks the location of the brightest cluster galaxy.

component. It is clear that there is still some AGN-related emission contributing to the low-resolution contours, given the correlation between compact source locations and the location of the diffuse emission.

We believe that the emission that is being picked up in the core is most likely AGN related, also because radio halos are expected to be intrinsically less luminous (by a factor of $B^2/B^2_{\rm CMB}$) with higher redshift due to inverse Compton losses (e.g. Enßlin & Röttgering, 2002; Cassano et al., 2006b, 2019). Even assuming a magnetic field of a few μG for the cluster at $z = 1.71$ (e.g. Domínguez-Fernández et al., 2019), the synchrotron radiation would be reduced by about two orders of magnitude, making the detection of such a halo extremely unlikely by simple energetic arguments.

3.5.6 SDSSC4-3094

A nearby galaxy cluster, SDSSC4-3094, identified in the Sloan Digital Sky Survey (Miller et al., 2005) at $z = 0.04632 \pm 0.00083$ happens to be located in the same extracted region as SpARCS1049+56. The radio-optical overlay is shown in Appendix II (Figure 3.24). From this cluster we detect diffuse emission shown in Fig. 3.9 to the south-west of the BCG. This emission is not following the radio galaxy distribution and seems like genuine diffuse emission. However, it is likely not a radio halo, given the one-sided morphology. to the south-east. We classify this emission as remnant AGN emission based on the morphology

and low surface brightness.

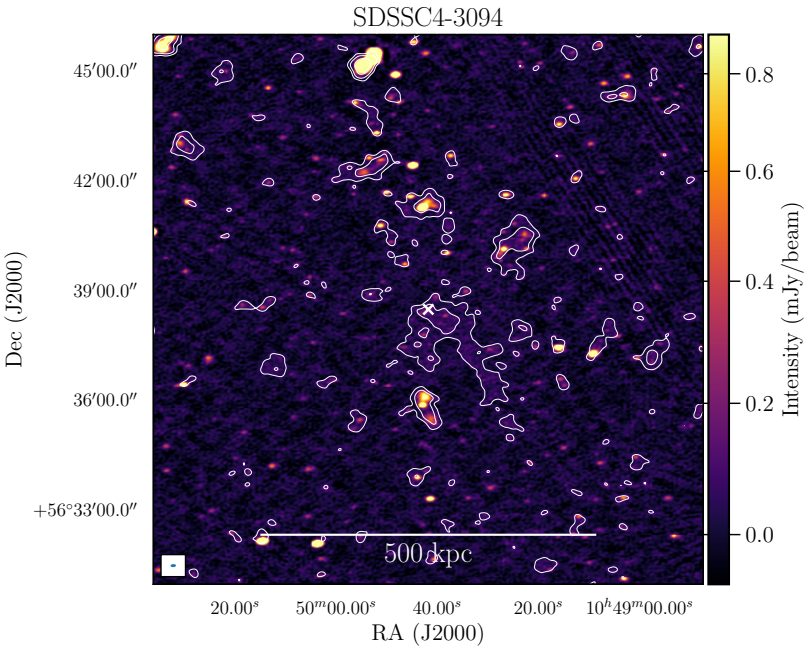

Figure 3.9: SDSSC4-3094 LOFAR radio intensity map with a restoring beam of $9'' \times 5''$, with low-resolution ($21'' \times 19''$) compact source subtracted contours showing diffuse emission at $[3, 6, 12..]\sigma$, where $\sigma = 74\mu$Jy beam^{-1}. The white cross marks the location of the brightest cluster galaxy.

3.5.7 Upper limits on non-detections

The three WHL clusters that we identified showing possible diffuse emission are fairly unknown clusters. All radio-optical overlays for the WHL clusters are shown in Appendix II. Because these are optically detected clusters, we can estimate their mass from the richness. We use the relation given by Wen et al. (2012)

$$\log M_{200} = (-1.49 \pm 0.05) + (1.17 \pm 0.03) \log R_{L^*} \tag{3.5}$$

where R_{L^*} is the cluster richness as reported in Wen et al. (2012) and M_{200} is the mass in units of $10^{14} M_\odot$. To convert the masses to M_{500} we use $M_{500} = 0.72\ M_{200}$, which assumes a Navarro–Frenk–White profile with a concentration parameter $c = 5$ for the cluster scale dark matter halo (Navarro et al., 1996; Pierpaoli et al., 2003). The results of the subtract and extract procedure are briefly stated per cluster.

WHLJ160439.5+543139 This cluster is located at a redshift of $z = 0.2655$ and shows a head-tail radio galaxy to the south-east of the likely BCG (Fig. 3.10). From the richness we estimate a mass $M_{500} = (2.95 \pm 0.50) \times 10^{14} M_\odot$. We tentatively detect diffuse emission surrounding the BCG, but due to the complexity of the emission from a head-tail radio galaxy, the AGN emission cannot be fully subtracted. To provide an upper limit on a halo

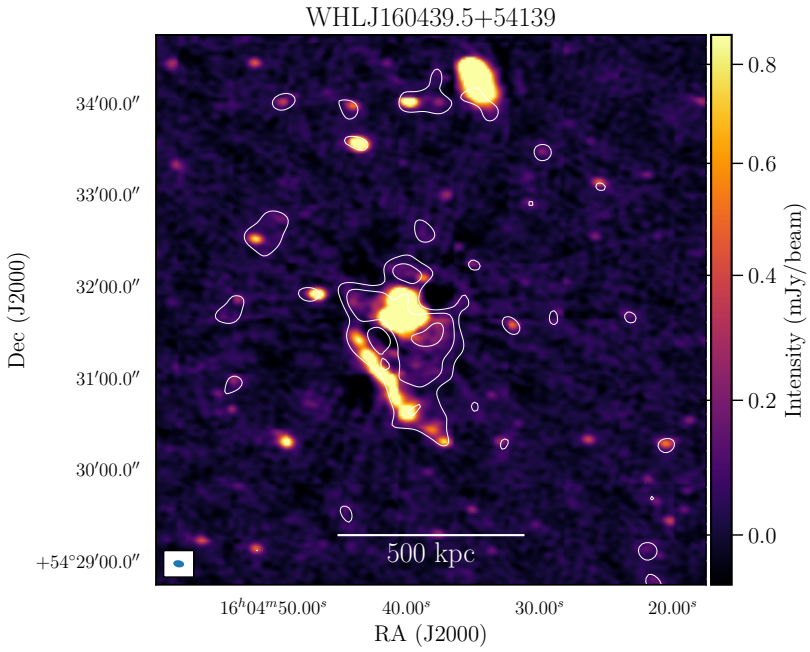

Figure 3.10: WHLJ160439.5+543139 high-resolution ($7'' \times 5''$) LOFAR radio intensity image with low-resolution ($17'' \times 15''$) compact source subtracted contours at $[3, 6, 12, ..]\sigma$, where $\sigma = 72\mu$Jy beam^{-1}.

detection, we inject halos slightly east of the cluster, in a region without contaminating radio sources. Following the correlations mentioned in Section 3.3.2, we initially set $I_0 = 7.7\mu$Jy arcsec^{-2}and $r_e = 65$ kpc. We find that the halo is easily detected for these values, as shown in the first panel of Figure 3.11. The resulting upper limit is found for $I_0 = 2.4\mu$Jy arcsec^{-2}, as is shown in the bottom left panel of Figure 3.11. This results in an integrated flux density of 3.0 mJy, which translates to an upper limit on the radio power at 144 MHz of $P_{144\text{MHz}} = 7.4 \times 10^{23}$ W Hz^{-1}.

WHLJ161135.9+541635 This cluster lies at a redshift of $z = 0.3407$, with an estimated mass of $M_{500} = (3.4 \pm 0.6) \times 10^{14} M_\odot$ and was selected visually because there seemed to be diffuse emission around the likely BCG in the wide-field image. However, after extraction and subtraction, no diffuse emission was detected, as shown in Figure 3.12. For this cluster we find an upper limit for the values $I_0 = 3.5\mu$Jy arcsec^{-2}and $r_e = 80$ kpc, corresponding to a total flux density of 4.4 mJy. This translates to an upper limit of $P_{144\text{MHz}} = 2.0 \times 10^{24}$ W Hz^{-1}.

WHLJ161420.1+544254 This WHL cluster also has a rather complex radio morphology, which combined with the leftover calibration artefacts prohibited the clear separation of AGN and diffuse emission (Fig. 3.13). The cluster lies at a redshift of $z = 0.3273$ with a mass of $M_{500} = (2.85 \pm 0.50) \times 10^{14} M_\odot$. For this cluster we find an upper limit for the values $I_0 = 3.1\mu$Jy arcsec^{-2}and $r_e = 64$ kpc, corresponding to an integrated flux density of 2.6 mJy and a radio power of $P_{144\text{MHz}} = 1.1 \times 10^{24}$ W Hz^{-1}.

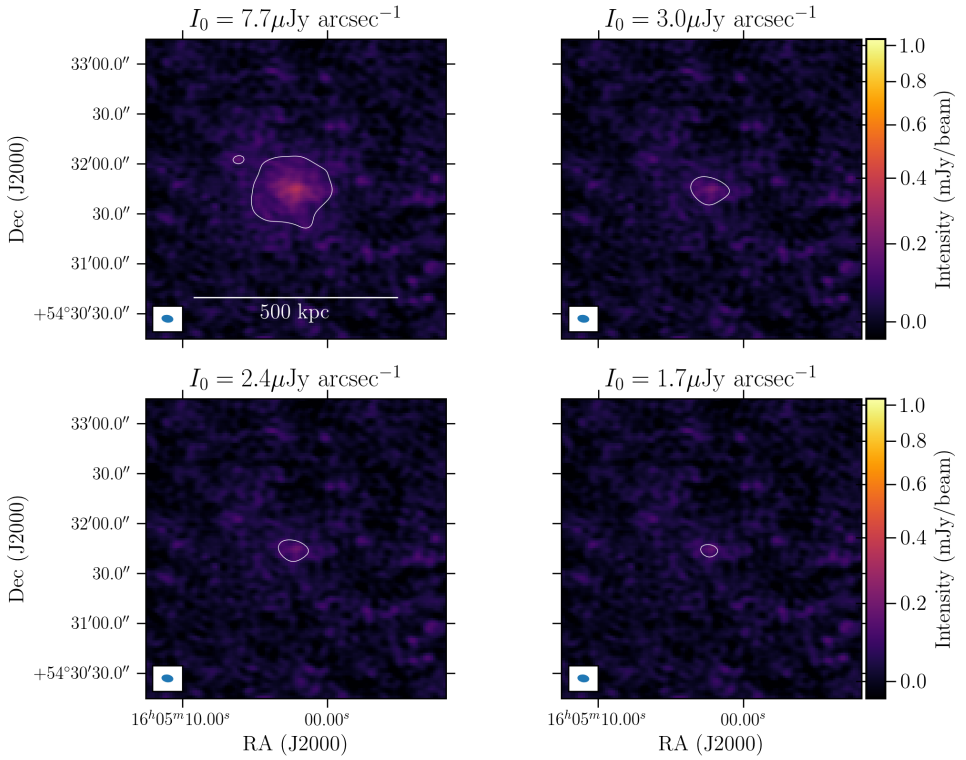

Figure 3.11: Injected mock halos with decreasing surface brightness near the cluster WHLJ160439.5+543139. Contours are plotted at 3σ, where $\sigma = 25\mu$Jy beam^{-1}. The halo is still defined as detected in the bottom left panel, but not defined as detected in the bottom right panel.

PSZRX G084.01+46.28 or Abell 2149 is quoted to have a redshift of 0.1068 in the PSZ2 and MCXC catalogues, however it has been identified as a duplicate cluster with a redshift measurement discrepancy of more than 10 per cent in the MCXC catalogue (see table B.1. of Piffaretti et al., 2011). Rines & Diaferio (2006) also noted the discrepancy between the redshift of 0.1068 quoted by the NORAS catalogue (Böhringer et al., 2000) and $z = 0.0675$ in the eBCS catalogue (Ebeling et al., 2000). They noticed that the X-ray peak of the RASS image lies near an apparent BCG at the lower redshift. We adopt for this source the lower redshift of 0.0675 as well, since, as is shown in Figure 3.14 the radio emission is also concentrated around the brightest cluster galaxy (BCG; at coordinates 16h01m28.10s +53°56m:50.8s) which is located at a redshift of $z = 0.06544$ (Ahn et al., 2013).

Since the redshift was overestimated, the mass of this cluster is overestimated as well. We calculate the corrected mass by assuming $z = 0.0675$ and interpolating the mass-redshift degeneracy curve given by the ComPRASS catalogue (Tarrío et al., 2019). This results in a corrected cluster mass of $M_{500} = 1.37^{+0.25}_{-0.27} \times 10^{14} M_\odot$.

This cluster is a difficult case since there is extended AGN emission surrounding the BCG, with a peculiar, bull head-like shape. Therefore, the central part of a radio halo would

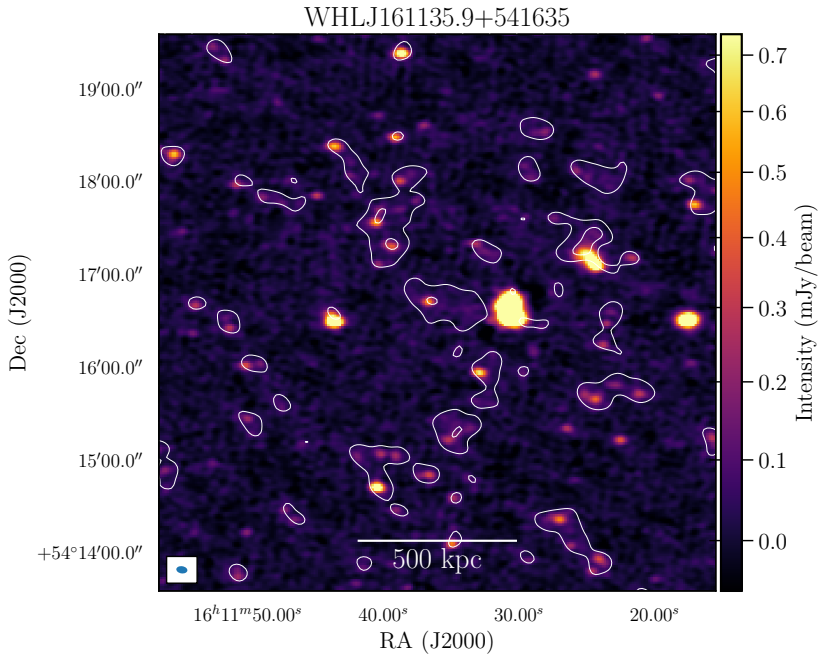

Figure 3.12: WHLJ161135.9+541635 high-resolution ($7'' \times 5''$) LOFAR radio intensity image with low-resolution ($20'' \times 18''$) compact source subtracted contours at $[3, 6, 12, ..]\sigma$, where $\sigma = 62\mu$Jy beam^{-1}

be obscured. However, the bull-head feature is quite narrow and we see no clear extended emission outside of it. We derive an upper limit by injection of a mock halo close to the cluster. The value of r_e found by following the correlations mentioned in Section 3.3.2 is only 25 kpc because of the low mass of this cluster. We choose to set $r_e = 65$ kpc, as diffuse sources with an r_e of 25 kpc would generally not be classified as a radio halo. Setting a larger e-folding radius results a more conservative upper limit. The upper limit for the peak surface brightness I_0 is found to be 2.5μJy arcsec^{-2}, which results in a total flux density of 29 mJy or a radio power of $P_{144\text{MHz}} = 3.3 \times 10^{23}$ W Hz^{-1}.

MCXC J1033.8+5703 No diffuse emission is picked up from this cluster (Fig. 3.15 shows the optical emission with overlaid radio contours), which is not unexpected given the low mass of $M_{500} = 0.128 \times 10^{14} M_\odot$ (Piffaretti et al., 2011). If the mass is correct, this particular source is closer to a galaxy group than a galaxy cluster. Some galaxy groups have detected extended synchrotron emission, but their origin is not fully clear (e.g. Giacintucci et al., 2011; Nikiel-Wroczyński et al., 2017, 2019). Because is it unknown whether such low mass configurations of galaxies can host radio halos, we do not provide an upper limit for this cluster.

MCXC J1053.3+5720 This cluster is quite a low mass cluster according to the MCXC derived mass of $M_{500} = 0.487 \times 10^{14} M_\odot$ (Piffaretti et al., 2011). It shows no diffuse emission in Figure 3.16, as is expected from such a low mass cluster. Although the mass is at least above a few times $10^{13} M_\odot$, the MCXC derived mass is still about a factor of five lower than

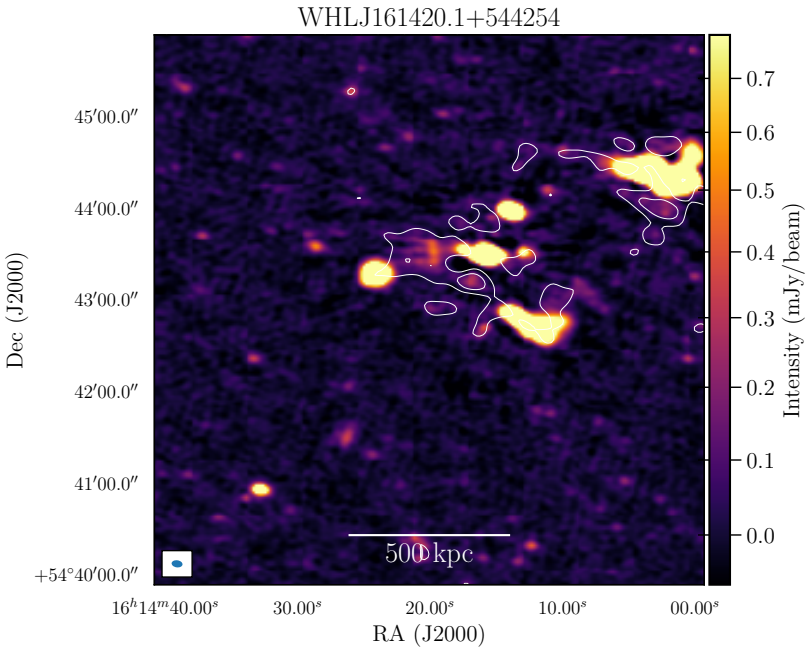

Figure 3.13: WHLJ161420.1+544254 high-resolution ($7'' \times 5''$) LOFAR radio intensity image with low-resolution ($16'' \times 13''$) compact source subtracted contours at $[3, 6, 12, ..]\sigma$, where $\sigma = 66\mu$Jy beam^{-1}

the lowest mass cluster with a halo detection. Therefore, we do not consider it informative to provide an upper limit on such a cluster.

Table 3.3: Resulting best-fit values for I_0 and r_e, as well as the total flux density $S_\nu^{\rm fit}$ from integrating the spherical model with the best-fit values. Parameter d denotes half of the largest linear size of the 3σ contours in e-folding radii, and $S_\nu^{\rm dfit}$ is the flux density obtained by integrating up to that value of d. $S_\nu^{3\sigma}$ is the flux density measured within 3σ (2σ for PSZ2G084.69+42.28) contours and $S_\nu^{2.6r_e}$ is the flux density measured in a spherical region with a radius of $2.6r_e$.

Source Name	I_0[μJy arcsec^{-2}]	r_e[kpc]	$S_\nu^{\rm fit}$	d	$S_\nu^{\rm dfit}$	$S_\nu^{3\sigma}$	$S_\nu^{2.6r_e}$	$\chi^2_{\rm red}$
PSZ2G147.88+53.24	$4.4^{+0.3}_{-0.3}$	194^{+11}_{-10}	16.9 ± 2.0	2.5	16.4 ± 2.0	14.7 ± 1.6	16.0 ± 1.8	0.79
PSZ2G147.88+53.24 (mask)	$4.5^{+0.3}_{-0.3}$	186^{+11}_{-11}	16.0 ± 2.0	2.2	14.0 ± 1.7	13.0 ± 1.4	15.5 ± 1.7	0.79
PSZ2G149.22+54.18	$5.7^{+0.1}_{-0.1}$	235^{+4}_{-3}	244.9 ± 29.7	2.5	236.8 ± 29.0	261.0 ± 30.6	271.3 ± 31.7	1.24
PSZ2G084.69+42.28	$2.0^{+0.7}_{-0.6}$	57^{+18}_{-13}	5.5 ± 1.6	1.9	4.3 ± 1.2	3.4 ± 0.5	4.7 ± 0.8	0.05
MCXCJ1036.1+5713	$7.7^{+0.5}_{-0.5}$	124^{+7}_{-6}	9.8 ± 1.1	3.6	11.7 ± 1.3	9.9 ± 1.1	8.6 ± 0.9	0.57

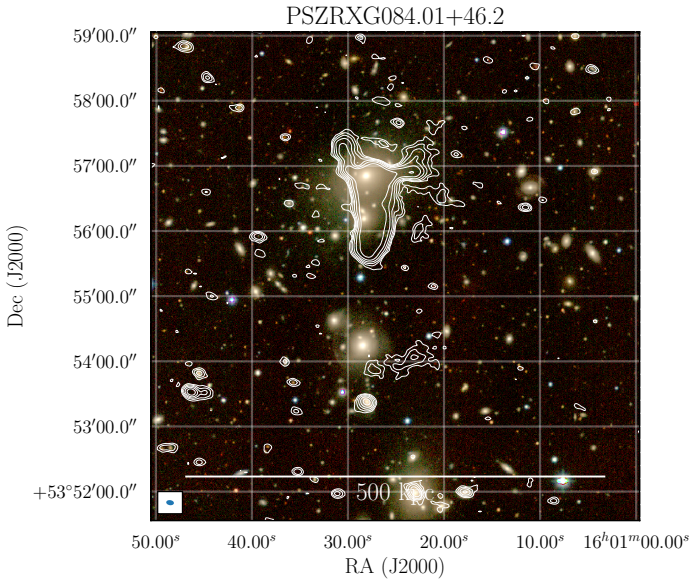

Figure 3.14: Optical (*grz* filters) image from the Legacy survey with high-resolution ($7'' \times 5''$) LOFAR radio contours overlaid for the cluster PSZRXG084.01+46.28. Contours are spaced at $[3, 6, 12, ..]\sigma$ where $\sigma = 39\mu$Jy beam^{-1}.

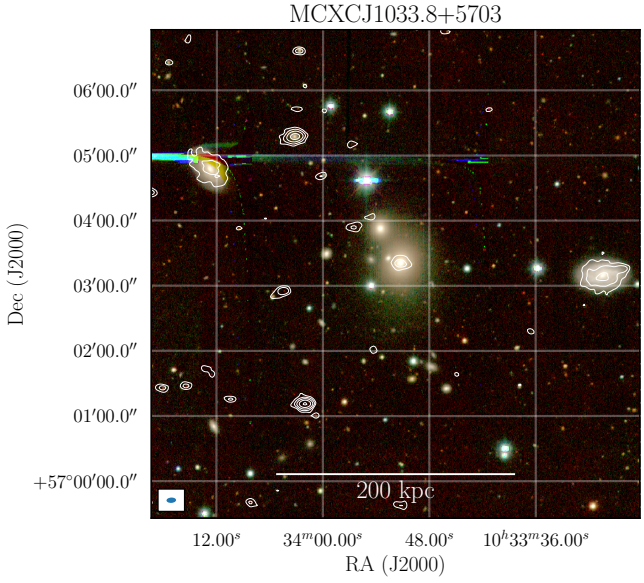

Figure 3.15: Optical (*grz* filters) image from the Legacy survey with high-resolution ($9'' \times 5''$) LOFAR radio contours overlaid for the cluster MCXCJ1033.8+5703. Contours are spaced at $[3, 6, 12, ..]\sigma$ where $\sigma = 48\mu$Jy beam^{-1}.

3.6 Discussion

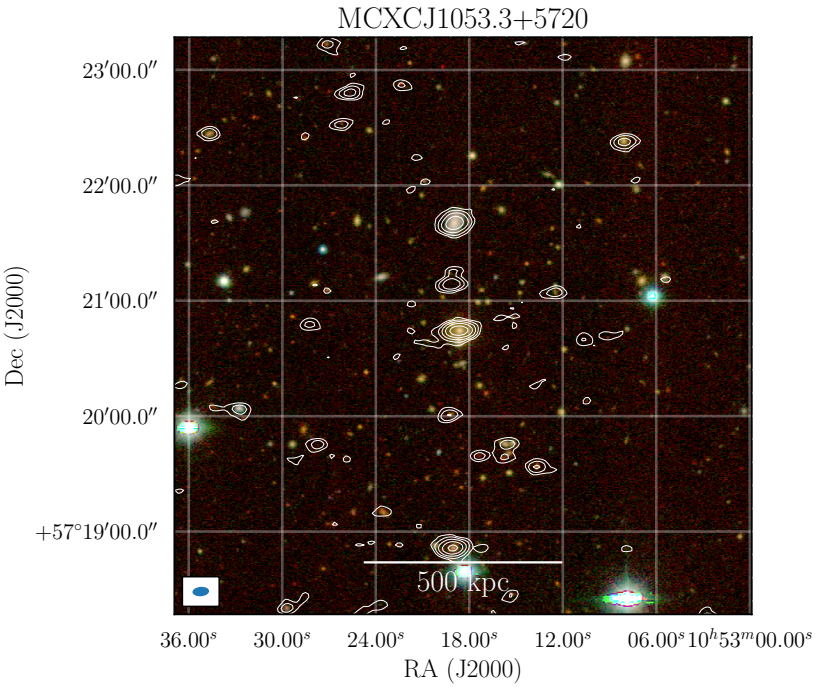

Figure 3.16: Optical (*grz* filters) image from the Legacy survey with high-resolution ($9'' \times 5''$) LOFAR radio contours overlaid for the cluster MCXCJ1053.3+5720. Contours are spaced at $[3, 6, 12, ..]\sigma$ where $\sigma = 32\mu$Jy beam^{-1}.

To quantify the robustness of the fitting procedure used to estimate the flux density of the diffuse emission in this study, we compare the fitted flux densities to flux densities measured in various other ways. Table 3.3 shows the best-fit values of I_0 and r_e, as well as a comparison with the flux density measured within 3σ contours ($S_\nu^{3\sigma}$) and the flux density measured in a spherical region with a radius of $2.6r_e$ ($S_\nu^{2.6r_e}$). We find generally good agreement of the flux density measured within 3σ contours and the flux density from integrating the best-fit model, indicating that setting $d = 2.6$ and using a circular model are reasonable choices for the clusters presented here. The only outlier is the source MCXCJ1036.1+5713, where the 3σ contours extend beyond $2.6e$-folding radii, and the actual flux density of the diffuse emission is thus slightly larger than the value of 9.8 ± 1.1 that is found by integration of the best-fit model. Integrating the model up to the value of $d = 3.6$ results in a flux density of 11.7 ± 1.3 mJy.

We have found diffuse emission from three galaxy clusters in this study. One cluster hosts a new high-redshift radio halo, PSZ2G084.69+42.28, and two have been observed previously with shallower LOFAR observations, PSZ2 G147.88+53.24 and PSZ2 G149.22+54.18. We tentatively detect diffuse emission from the cluster PSZ2G084.69+42.28, but this has to be confirmed with upcoming deeper data releases. Upper limits have been put on

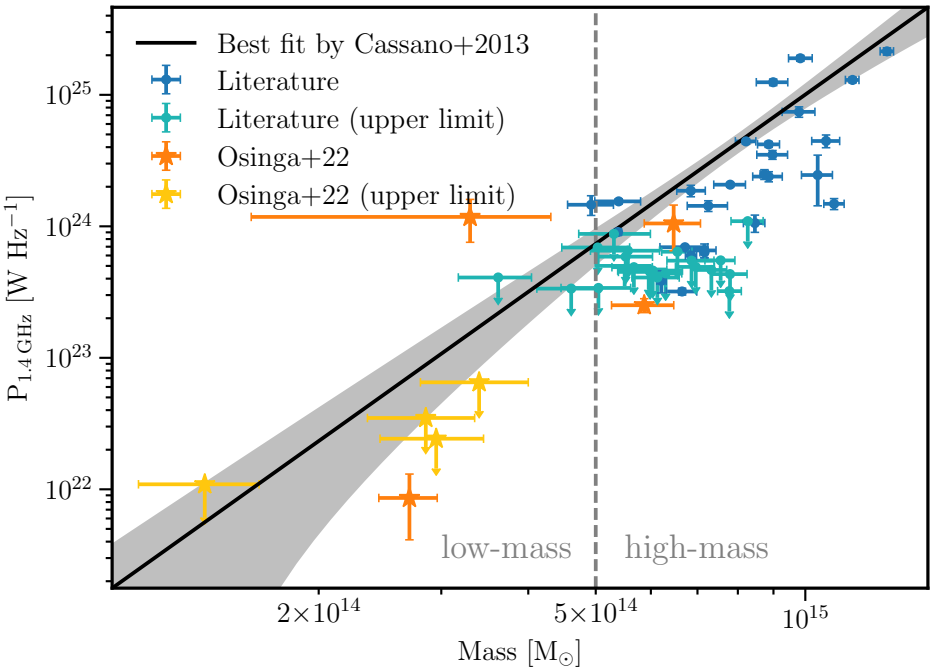

Figure 3.17: The radio halo power vs cluster mass diagram for the clusters in this work and a sample of clusters from Fig. 9 of van Weeren et al. (2019) and references therein. The best-fit relation for radio halos, with the shaded 95% confidence region, from Cassano et al. (2013) is shown in grey. We note that individual halos can easily scatter outside of the shaded region due to the intrinsic scatter of host cluster properties. For the sources in this work where the spectral index is unknown, we have assumed $\alpha = -1.5 \pm 0.2$.

the clusters PSZRX G084.01+46.28, WHL J160439.5+543139, WHL J161135.9+541635 and WHL J161420.1+544254. These results are compared to the well-known scaling relation between radio halo power and cluster mass from Cassano et al. (2013) derived for massive ($M_{500} > 5\times10^{14}$) clusters. This is shown in Figure 3.17. We find that the radio power of the diffuse emission in the low mass clusters PSZ2G084.69+42.28 and MCXCJ1036.1+5713 are inconsistent with the statistical error on the best fit radio halo power - cluster mass correlation observed for higher mass systems. However, given the fact that radio halos are expected to scatter intrinsically around the correlation due to the different intrinsic properties of galaxy clusters and the different properties of mergers (Brunetti et al., 2009), two data points are not yet enough to conclude a significant deviation.

The turbulent re-acceleration model states that radio halos are caused by merger-induced turbulence in the intra-cluster medium (ICM) which re-accelerates relativistic electrons. A key prediction of this model is that lower mass clusters have less energetic merger events and thus less turbulent energy is being transferred to accelerate particles, leading to less powerful and steeper spectra radio halos (Brunetti & Jones, 2014). These halos can only be picked up by sensitive low-frequency instruments. Calculations based on the turbulent re-acceleration model predict 1000-3000 halos with an integrated flux density

at 150 MHz of 10 mJy in the whole sky (Cassano et al., 2006b; Li et al., 2019). The three fields considered in this work cover an area of about 60 deg^2, thus we would expect about 3 radio halo detections above an integrated flux density of 10 mJy. The results presented in this work are in line with these predictions.

Our study shows the potential of deep LOFAR observations to detect diffuse emission from galaxy clusters with masses below $5\times10^{14}M_{\odot}$, thus entering a poorly explored territory. In the 8 hour LOFAR observations from the LOFAR Two Metre Sky Survey (Shimwell et al., 2019), the diffuse emission in PSZ2G084.69+42.28 is undetected and the diffuse emission in MCXCJ1036.1+5713 is barely detectable. Diffuse emission in a few other low mass clusters have been detected previously with LOFAR (e.g. Shimwell et al., 2016; Hoang et al., 2019; Botteon et al., 2019; Mandal et al., 2020). The diffuse emission found in PSZ2G084.69+42.28 and MCXCJ1036.1+5713 are important additions to the sparse sample of low mass ($< 5\times10^{14}M_{\odot}$) clusters.

Theoretically, due to the lower turbulent energy budget in these low mass systems, the secondary electrons from hadronic collisions may become the dominant source for powering radio halos (e.g. Cassano et al., 2012). The transition from re-acceleration to hadronic halos depends on several unknowns, such as the energy budget of cosmic-ray protons (CRp) in clusters and the extension of the regions where turbulent energy is dissipated into re-acceleration of particles. Models that assume that the energy budget of CRp is at the levels constrained by *Fermi-LAT* upper limits and that turbulence is dissipated in Mpc^3 regions (independent of cluster mass) predict a transition to hadronic halos at typical 150 MHz luminosities of $\sim 10^{24}$W Hz^{-1} (e.g. Cassano et al., 2012). This value is similar to the radio luminosity found in PSZ2G084.69+42.28 and the upper limits obtained in this study, showing that deep observations with LOFAR can potentially constrain this transition.

To investigate the possibility of a transition observationally, it is important to determine the dynamical state of the studied clusters. If radio halos in low mass clusters are still strongly connected to merger events, then that would suggest that the re-acceleration model still plays the dominant role, with implications on the extension of the turbulent regions and on the energy budget of CRp. The dynamical state of PSZ2G084.69+42.28 is also important to properly classify the diffuse emission.

Higher frequency follow-up observations are useful to differentiate between the two particle acceleration mechanisms. We have checked the ancillary 610 MHz GMRT observations of the ELAIS-N1 and Lockman Hole fields taken by Garn et al. (2008a,b), but unfortunately all PSZ2 and MCXC sources are just outside of the field-of-view of the GMRT observations. The WHL sources are observed, but show no sign of diffuse emission in the GMRT images. If, in future studies the spectral index of radio halos in low-mass sources is found to be very steep $\alpha \lessapprox -1.5$ a significant hadronic contribution will be ruled out (e.g. Pfrommer & Enßlin, 2004; Brunetti et al., 2008).

The discovery of a radio halo in MCXCJ1036.1+5713 is particularly intriguing due to the combination of relatively low mass ($M_{500} \sim 3.3\times10^{14}$) and high redshift ($z = 0.77$). Models predict a gradual decline of the fraction of clusters with radio halos at high redshift (e.g. Cassano et al., 2006b). The observed decline is less prominent at low frequencies due to the increasing population of very steep spectrum halos that are expected to be more common at high redshift. Depending on the clusters magnetic field strength, a fraction of halos

up to 10-25% in clusters with $M_{500} \sim (3-4)\times10^{14}M_{\odot}$ at a redshift of 0.7 is predicted to be observed with LOFAR (Cassano et al., 2019). Better X-ray data with modern telescopes are needed to obtain a good estimate of the cluster mass and dynamical state.

Finally, our deeper images confirm that PSZ2G149.22+54.18 (Abell 1132) is hosting an under-luminous and steep-spectrum radio halo, which supports the idea that Abell 1132 is in a late merger state with weak turbulence (Wilber et al., 2018). Due to the high sensitivity of the current data, we see the halo emission blending with the outer edge of the giant head-tail radio galaxy. The possibility has been raised that gently re-energised tails (GreETs; de Gasperin et al., 2017) can provide a seed population of relativistic electrons for the generation of the cluster-scale emission. The interplay between the giant head-tail radio galaxy and radio halo seems to corroborate this scenario, although observations at different frequencies are needed to properly map the spectral index over the western edge of the tail to identify whether gentle re-energisation is indeed powering the diffuse emission from the tail. This connection between head-tail radio galaxies and halo emission has been observed in a few other clusters as well (e.g. Rajpurohit et al., 2018; Mandal et al., 2019). We also identify a sharp front in the halo, annotated in Figure 3.4. This could be indicating a shock or shear motions in the ICM, although it is not visible in the X-ray image presented in Wilber et al. (2018). It might also be a magnetic filament or a region of higher turbulence seen in projection. Filamentary emission has been identified in halos before (e.g. in Abell 2255; Govoni et al., 2005; Botteon et al., 2020b). To investigate the possible polarisation of the filament, deep higher frequency observations are required.

3.7 Conclusion

This study presented a search for diffuse emission in the deepest LOFAR 144 MHz observations ever taken. All Planck Sunyaev-Zel'dovich detected clusters (PSZ2; ComPRASS; Planck Collaboration et al., 2016a; Tarrío et al., 2019) and clusters from the Meta Catalogue of X-ray detected Clusters (MCXC; Piffaretti et al., 2011) that overlap with the Deep Fields were inspected. The halos were systematically fitted with spherically symmetrical exponential profiles using Markov Chain Monte Carlo sampling to sample the likelihood function.

We have found a new radio halo in the low mass, high-redshift cluster MCXCJ1036.1+5713 ($z = 0.77$) and tentatively detect diffuse emission from the low mass cluster PSZ2G084.69+42.28 ($z = 0.13$). We have set deep upper limits on diffuse emission from clusters with a non-detection and for two clusters previously observed with LOFAR, PSZ2G147.88+53.24 and PSZ2G149.22+54.18, we confirm results in the literature.

This study has detected diffuse emission in a largely unexplored region of parameter space for galaxy clusters. The results were compared to the radio luminosity - cluster mass relation for radio halos found in the literature, and we found that this small sample of clusters is consistent with the correlation extrapolated to lower masses.

The results presented here underline the importance of deep low-frequency observations of galaxy clusters. As the LOFAR Deep Fields reach their final depths of 10-15 μJy beam^{-1}, we expect more low-mass clusters to show radio halos and to put more stringent upper limits on the radio luminosity of lower mass clusters, which will begin to allow a statistical study of a sample of radio halos in low mass clusters.

In the future, international baseline data will additionally be imaged, resulting in sub-arcsecond resolution images at the same depth. This will allow for better separation of AGN and diffuse emission, especially for mini-halos and high-redshift clusters.

ACKNOWLEDGEMENTS

We thank W. Williams for her plotting functions. EO, RJvW and AB acknowledge support from the VIDI research programme with project number 639.042.729, which is financed by the Netherlands Organisation for Scientific Research (NWO). GB, RC, FG, MR acknowledge support from INAF through mainstream program 'galaxy clusters science with LOFAR' 1.05.01.86.05. Ann.B. acknowledges support from the ERC-Stg DRANOEL n. 714245 and from the MIUR FARE grant "SMS". PNB is grateful for support from the UK STFC via grant ST/R000972/1. MBo acknowledges support from INAF under PRIN SKA/CTA FORECaST and from the Ministero degli Affari Esteri della Cooperazione Internazionale - Direzione Generale per la Promozione del Sistema Paese Progetto di Grande Rilevanza ZA18GR02. GDG acknowledges support from the ERC Starting Grant ClusterWeb 804208. MJH acknowledges support from the UK Science and Technology Facilities Council (ST/R000905/1). HR acknowledges support from the ERC Advanced Investigator programme NewClusters 321271. JS is grateful for support from the UK STFC via grant ST/R000972/1. LOFAR (van Haarlem et al., 2013) is the Low Frequency Array designed and constructed by ASTRON. It has observing, data processing, and data storage facilities in several countries, which are owned by various parties (each with their own funding sources), and that are collectively operated by the ILT foundation under a joint scientific policy. The ILT resources have benefited from the following recent major funding sources: CNRS-INSU, Observatoire de Paris and Université d'Orléans, France; BMBF, MIWF-NRW, MPG, Germany; Science Foundation Ireland (SFI), Department of Business, Enterprise and Innovation (DBEI), Ireland; NWO, The Netherlands; The Science and Technology Facilities Council, UK; Ministry of Science and Higher Education, Poland; The Istituto Nazionale di Astrofisica (INAF), Italy. This research made use of the Dutch national e-infrastructure with support of the SURF Cooperative (e-infra 180169) and the LOFAR e-infra group. The Jülich LOFAR Long Term Archive and the German LOFAR network are both coordinated and operated by the Jülich Supercomputing Centre (JSC), and computing resources on the supercomputer JUWELS at JSC were provided by the Gauss Centre for Supercomputing e.V. (grant CHTB00) through the John von Neumann Institute for Computing (NIC). This research made use of the University of Hertfordshire high-performance computing facility and the LOFAR-UK computing facility located at the University of Hertfordshire and supported by STFC [ST/P000096/1], and of the Italian LOFAR IT computing infrastructure supported and operated by INAF, and by the Physics Department of Turin university (under an agreement with Consorzio Interuniversitario per la Fisica Spaziale) at the C3S Supercomputing Centre, Italy. This research has made use of NASA's Astrophysics Data System.

Appendix I - Surface brightness fits

We show in this Appendix the azimuthally averaged surface brightness profiles, the best-fit model and the corner plots of the MCMC chain. To be clear, the fitting algorithm performs the fitting in the image plane, but because a spherically symmetrical model is assumed in this work the radial profiles contain all necessary information.

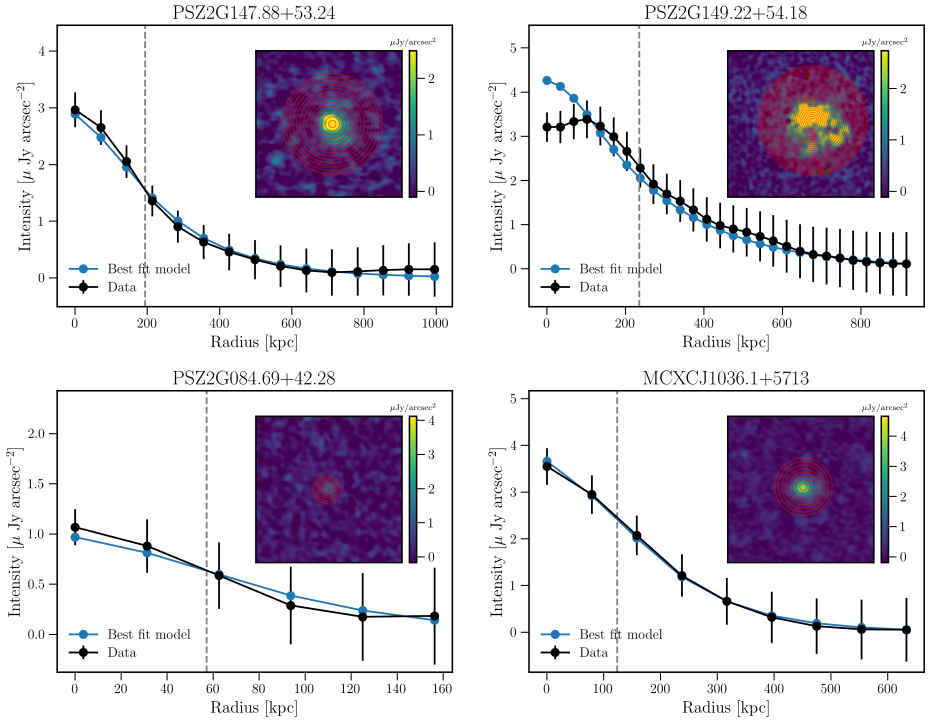

Figure 3.18: Azimuthally averaged surface brightness profiles for the clusters presented in this work. The inset images show the concentric annuli where the profile has been calculated, the width of the annuli is equal to the semi-major axis of the restoring beam. The dashed grey line indicates the best-fit *e*-folding radius.

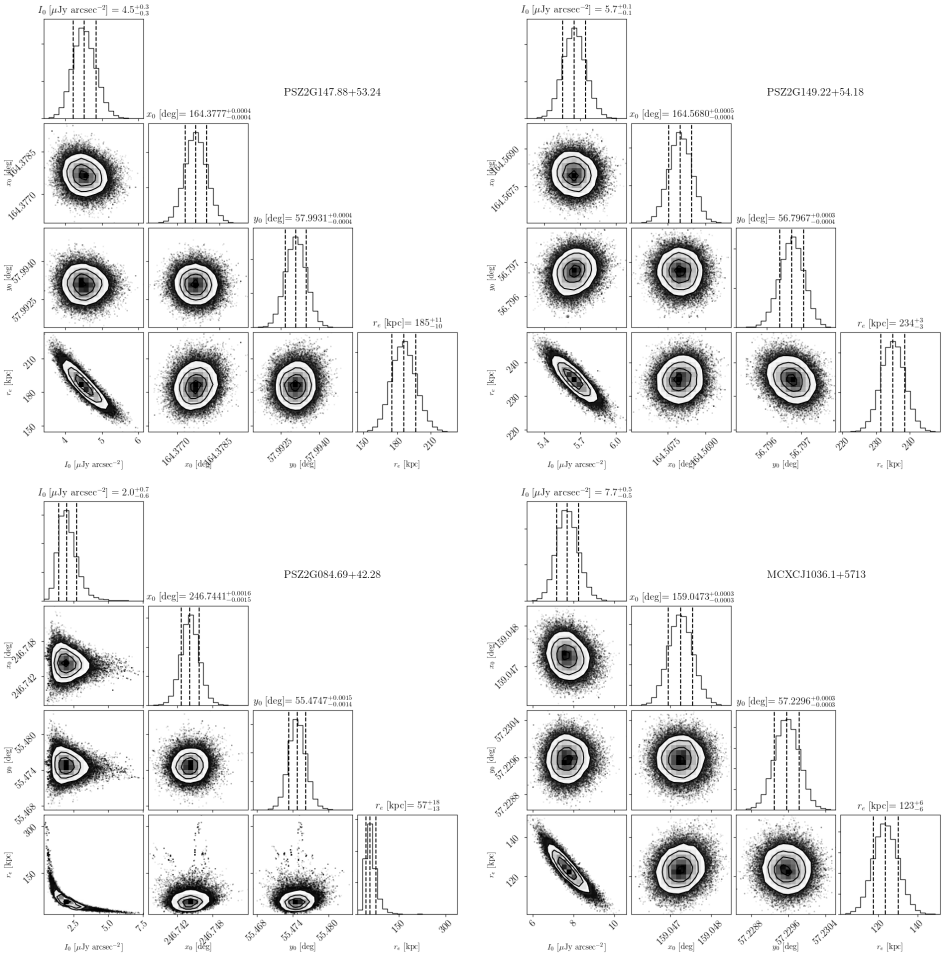

Figure 3.19: Corner plots of the fitted parameters given by the MCMC chain. The dashed lines indicate the 16, 50th and 84th percentiles of the chain.

Appendix II - Radio Optical overlays

This appendix shows the radio-optical overlays for all the clusters with non-detection of diffuse emission. Notes about these clusters can be found in Section 3.5.7.

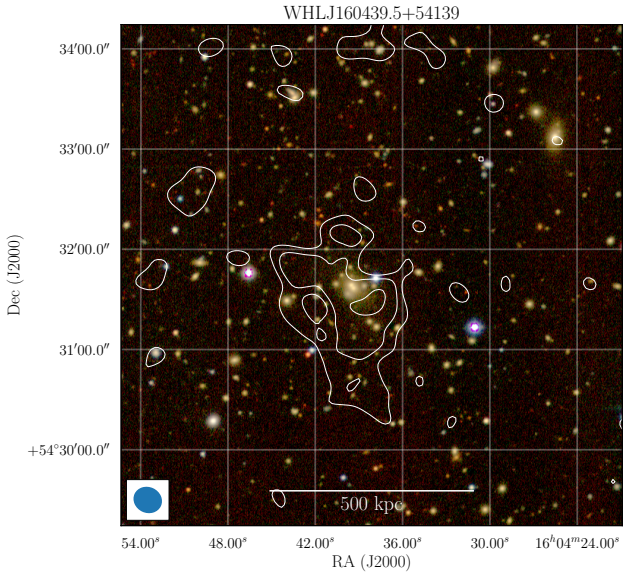

Figure 3.20: Optical (grz) image of WHLJ160439.5+54139 from the Legacy Survey with compact source subtracted low-resolution LOFAR contours overlaid. The beam size is $17'' \times 15''$. Contours at $[3, 6, 12, ..]\sigma$, where $\sigma = 72\mu$Jy beam^{-1}.

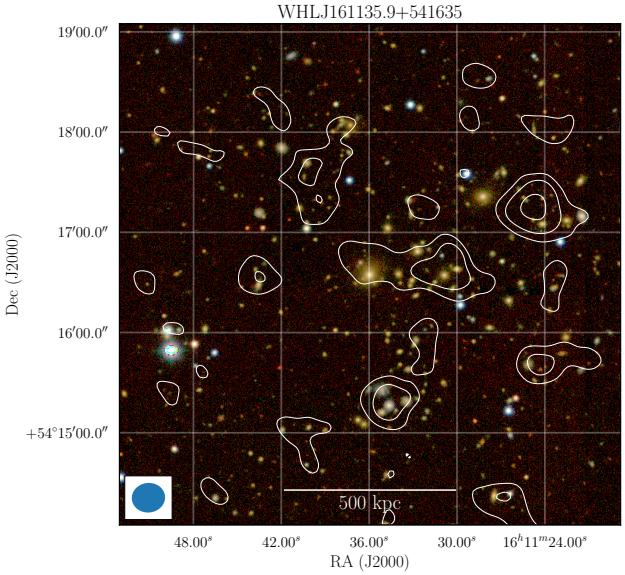

Figure 3.21: Optical (grz) image of WHLJ161135.9+541635 from the Legacy Survey with compact source subtracted low-resolution LOFAR contours overlaid. The beam size is $20'' \times 18''$. Contours at $[3, 6, 12, ..]\sigma$, where $\sigma = 62\mu$Jy beam^{-1}.

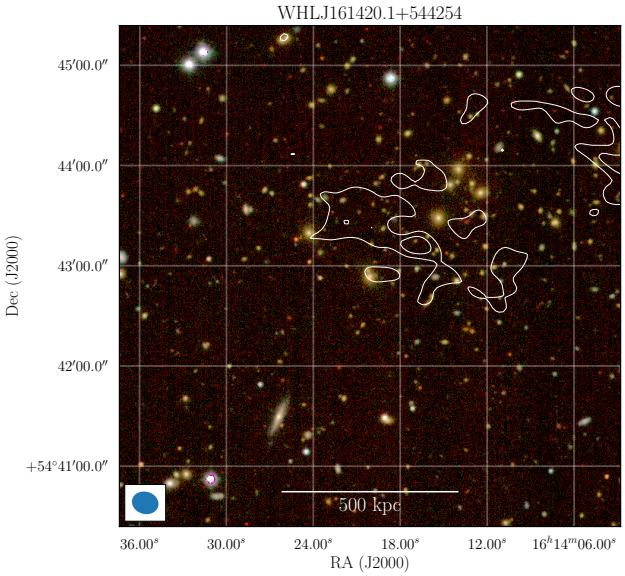

Figure 3.22: Optical (grz) image of WHLJ161420.1+544254 from the Legacy Survey with compact source subtracted low-resolution LOFAR contours overlaid. The beam size is $X16 \times 13''$. Contours at $[3, 6, 12, ..]\sigma$, where $\sigma = 66\mu$Jy beam^{-1}.

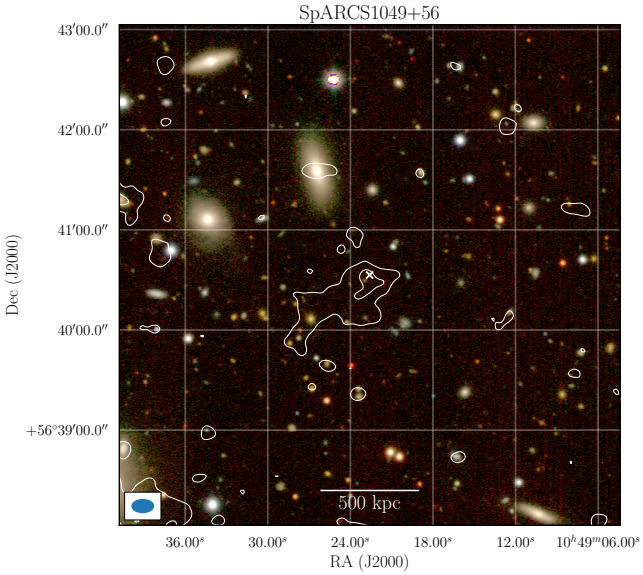

Figure 3.23: Optical (*grz*) image of SpARCS1049+56 from the Legacy Survey with compact source subtracted low-resolution LOFAR contours overlaid. The beam size is $14'' \times 9''$. Contours at $[3, 6]\sigma$, where $\sigma = 48\mu$Jy beam^{-1}.

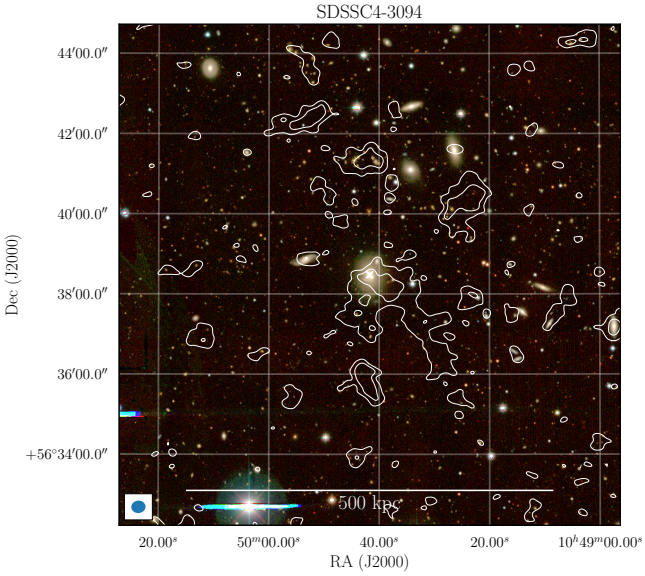

Figure 3.24: Optical (*grz*) image of SDSSC4-3094 from the Legacy Survey with compact source subtracted low-resolution LOFAR contours overlaid. The beam size is $21'' \times 19''$. Contours at $[3, 6, 12, ..]\sigma$, where $\sigma = 74\mu$Jy beam^{-1}.

4

Probing particle acceleration in Abell 2256: from to 16 MHz to gamma rays

Merging galaxy clusters often host spectacular diffuse radio synchrotron sources. These sources can be explained by a non-thermal pool of relativistic electrons that are accelerated by shocks and turbulence in the intracluster medium. The origin of the pool and details of the cosmic ray transport and acceleration mechanisms in clusters are still open questions. Due to the often extremely steep spectral indices of diffuse radio emission, it is best studied at low frequencies. However, the lowest frequency window available to ground-based telescopes (10-30 MHz) has remained largely unexplored, as radio frequency interference and calibration problems related to the ionosphere become severe. Here, we present LOFAR observations from 16 to 168 MHz targeting the famous cluster Abell 2256. In the deepest-ever images at decametre wavelengths, we detect and resolve the radio halo, radio shock and various steep spectrum sources. We measure standard single power-law behaviour for the radio halo and radio shock spectra, with spectral indices of $\alpha = -1.56 \pm 0.02$ *from 24 to 1500 MHz and* $\alpha = -1.00 \pm 0.02$ *from 24 to 3000 MHz, respectively. In contrast to the straight power-law spectra of the large-scale diffuse sources, the various AGN-related sources that we study often show extreme steepening towards higher frequencies and flattening towards low frequencies. We also discover a new fossil plasma source with a steep spectrum between 23 and 144 MHz, with* $\alpha = -1.9 \pm 0.1$*. Finally, by comparing radio and gamma-ray observations, we rule out purely hadronic models for the radio halo origin in Abell 2256, unless the magnetic field strength in the cluster is exceptionally high, which is unsupportable by energetic arguments and inconsistent with the knowledge of other cluster magnetic fields.*

Based on Osinga et al. (2023a): *E. Osinga, R. J. van Weeren, G. Brunetti, R. Adam, K. Rajpurohit, A. Botteon, J. R. Callingham, V. Cuciti, F. de Gasperin, G. K. Miley, H. J. A. Röttgering, T. W. Shimwell. A&A submitted.*

4.1 Introduction

Galaxy clusters provide a unique laboratory for studying the physics of particle acceleration in cosmic-scale dilute plasmas from the densest and hottest regions of the cosmic web. In these regions, the intracluster medium (ICM) shines brightly both in thermal bremsstrahlung observable with X-ray telescopes (Sarazin, 1986), and diffuse synchrotron radio emission due to ultra-relativistic electrons (see van Weeren et al., 2019, for a recent review). There is significant evidence that both types of emission are driven by the injection of energy through cluster mergers, which heat the ICM and accelerate charged particles through shocks and turbulence (e.g. Markevitch & Vikhlinin, 2007; Brunetti & Jones, 2014).

Because of the dynamic nature of the ICM, galaxy clusters host a panoply of interesting radio sources. Jets of active galactic nuclei (AGN) are found to be more bent closer to the centres of clusters (e.g. Garon et al., 2019) or possibly re-accelerated by interactions with the ICM (e.g. de Gasperin et al., 2017). On even larger (Mpc) scales, diffuse synchrotron radiation in the form of 'radio halos' and 'radio shocks' have been widely observed in merging galaxy clusters (e.g. Botteon et al., 2022a). In this work, we adopt the classification of the diffuse synchrotron radiation used in van Weeren et al. (2019), where radio halos are found in the centres of clusters with brightness profiles that generally follow the baryonic distribution of the ICM. In contrast, radio shocks are generally found on the outskirts of clusters and are thought to trace Fermi-I acceleration at shocks (Ensslin et al., 1998). Additionally, there exists another class of diffuse synchrotron sources that are believed to trace old plasma from AGN that has been re-energised by various processes in the ICM. For example, such diffuse emission could have been re-energised by adiabatic compression or internal turbulence. This class encompasses sources such as gently re-energized tails (de Gasperin et al., 2017) and radio phoenices (Mandal et al., 2020), which can be dubbed 'fossil plasma' sources. All classes of diffuse cluster radio emission typically show steep spectra with $\alpha < -1$, where α denotes the spectral index and the radio flux density follows $S_\nu \propto \nu^\alpha$, where ν denotes the frequency. This implies that the cluster diffuse emission is brighter, and sometimes easier to detect at high significance, at low frequencies.

There are various open questions related to the details of particle acceleration of different classes of diffuse cluster synchrotron sources. One major problem is that the acceleration seen in both the weak radio shocks in the ICM and the turbulent Fermi-II type acceleration in radio halos is not efficient enough to accelerate particles from the thermal pool (Brunetti & Jones, 2014). A 'seed' population of mildly relativistic electrons could alleviate this problem both in radio shocks (e.g. Markevitch et al., 2005; Kang et al., 2012; Botteon et al., 2020a) and radio halos (e.g. Brunetti et al., 2001; Cassano & Brunetti, 2005; Nishiwaki & Asano, 2022), although the origin of the seed population need not be the same. Possible scenarios for the origin of the seed population are the injection by AGN (e.g. van Weeren et al., 2017; ZuHone et al., 2021), multiple weak shocks (e.g. Kang, 2021), or secondary products of hadronic proton-proton collisions (e.g. Brunetti & Blasi, 2005; Brunetti & Lazarian, 2011; Pinzke et al., 2017).

The favoured scenario for the origin of radio halos is based on re-acceleration by merger-induced turbulence (Brunetti et al., 2001; Petrosian, 2001; Brunetti & Lazarian, 2007; Miniati & Beresnyak, 2015; Brunetti & Lazarian, 2016; Cassano et al., 2023). The role of secondary particles from hadronic interactions in the origin of radio halos is still unclear. A pure hadronic scenario is disfavoured by current radio data and their follow-up

(e.g. Brunetti et al., 2008; Cassano et al., 2010c; Bruno et al., 2021; Cuciti et al., 2021a; Di Gennaro et al., 2021b). However, the only direct limit to the presence of cosmic ray protons (CRp) and to their contribution to radio halos comes from gamma-ray observations. At the moment, the detection of gamma rays from clusters remains elusive, and the only direct constraints on CRp come from the Coma cluster (Brunetti et al., 2012, 2017; Xi et al., 2018; Adam et al., 2021; Baghmanyan et al., 2022).

Abell 2256 is one of the best laboratories for studying particle acceleration mechanisms. This is because of its large angular size and high flux density due to its proximity (z=0.058; Struble & Rood, 1991), coupled with the fact that it is undergoing a massive (M_{500} = $6.2\times10^{14}M_{\odot}$; Planck Collaboration et al. 2016a) and complex merger. The cluster hosts host clear well-characterised examples of all known classes of diffuse cluster radio emission. It also hosts the lowest redshift radio halo with an ultra-steep spectrum at low frequencies ($\alpha < -1.5$). It has therefore been studied extensively across the electromagnetic spectrum (Briel et al., 1991; Briel & Henry, 1994; Röttgering et al., 1994; Bridle & Fomalont, 1976; Bridle et al., 1979; Berrington et al., 2002; Sun et al., 2002; Miller et al., 2003; Clarke & Ensslin, 2006; Brentjens, 2008; van Weeren et al., 2009; Kale & Dwarakanath, 2010; Owen et al., 2014; Trasatti et al., 2015; Ge et al., 2020; Breuer et al., 2020; Rajpurohit et al., 2022c, 2023).

Until now, neither the ultra-low frequencies (< 100 MHz) nor the high-energy gamma-rays have been properly explored. No good quality data existed on Abell 2256 below 100 MHz due to calibration problems related to the ionosphere, although some ultra-low frequency observations were taken during the early phase of the LOFAR telescope when the calibration and imaging techniques were still in their infancy (van Weeren et al., 2012b). Those observations, combined with data up to $1.4GHz$, showed that the radio shock had an unusually flat spectrum of $\alpha = -0.81 \pm 0.03$, inconsistent with standard diffusive shock acceleration and that the radio halo showed unexpected flattening towards higher frequencies. These results were however not corroborated by recent higher frequency investigations (Rajpurohit et al., 2022c, 2023). A more thorough ultra-low frequency study of Abell 2256 is therefore warranted to accurately quantify and characterise the low-frequency emission.

Recent advances in calibration and imaging techniques have made routine LOFAR Low Band Antenna (LBA) observations at $\sim$ 50 MHz possible (e.g. de Gasperin et al., 2019, 2020; Biava et al., 2021; Edler et al., 2022; Botteon et al., 2022b; de Gasperin et al., 2023). In principle, the LOFAR LBA system works down to 10 MHz (van Haarlem et al., 2013), but no standard data reduction pipeline yet exists for observations in the 10-30 MHz range.

In this chapter, we present the deepest radio images made at the lowest radio window available to ground-based telescopes. We study particle acceleration in Abell 2256 by combining those data with higher-frequency data from the literature and gamma-ray upper limits from 13.5 years of Fermi-LAT observations. A flat concordance cosmology with $H_0 = 70$ kms^{-1}Mpc^{-1}, Ω_m=0.3 and $\Omega_\Lambda = 0.7$ is adapted, which means that at the cluster redshift, 1 arcsecond corresponds to 1.12 kpc.

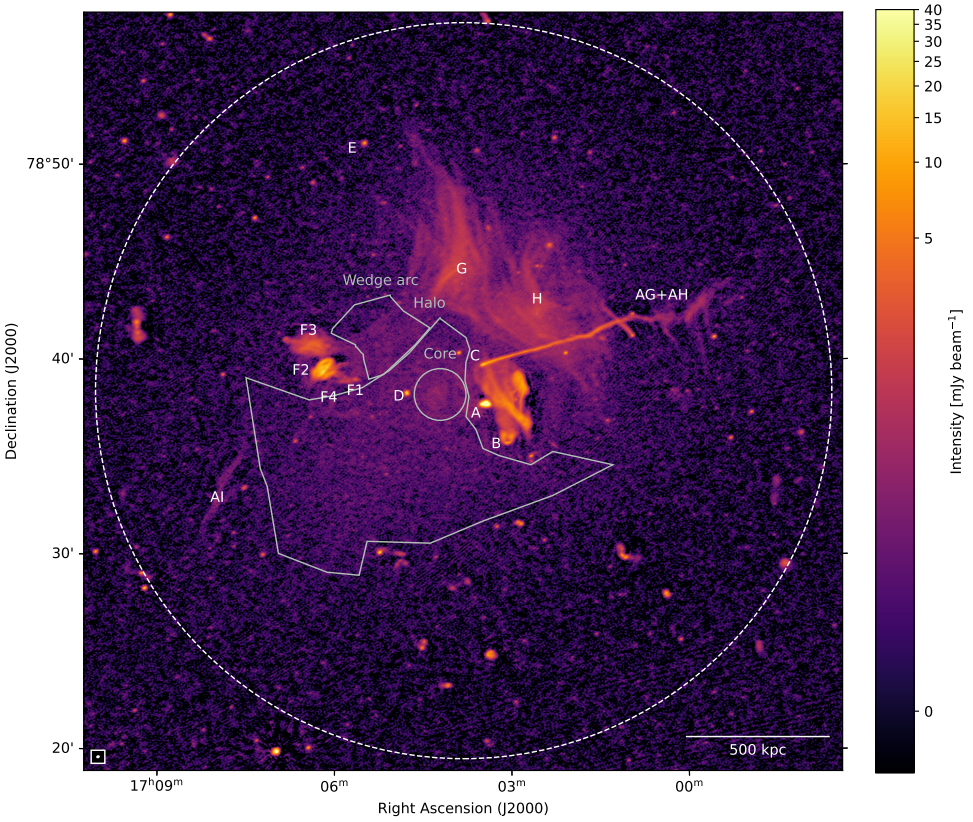

Figure 4.1: Full resolution LOFAR HBA (144 MHz) image of Abell 2256 with the $6'' \times 6''$ HPBW restoring beam, shown in the bottom left corner. The background rms noise is 90 μJy beam^{-1} and sources are labelled according to Röttgering et al. (1994). The dashed circle indicates the R_{500} radius.

Table 4.1: LOFAR radio observations used in this work.

Start date[a] [UT]	Frequency [MHz]	Integration time [hours]	Distance to pointing centre[b] [deg]	LOFAR Project code
2018-05-01 21:11	120-168	8	1.6	LC9_008
2019-05-31 19:20	120-168	8	1.0	LT10_010
2021-01-08 09:00	16-64	4	0.0	LC15_026
2021-01-10 08:00	16-64	8	0.0	LC15_026
2021-01-16 09:00	16-64	4	0.0	LC15_026

Notes. [(a)] Dates are given in the yy-mm-dd format [(b)] The distance from the cluster Abell 2256 to the pointing centre of the observations.

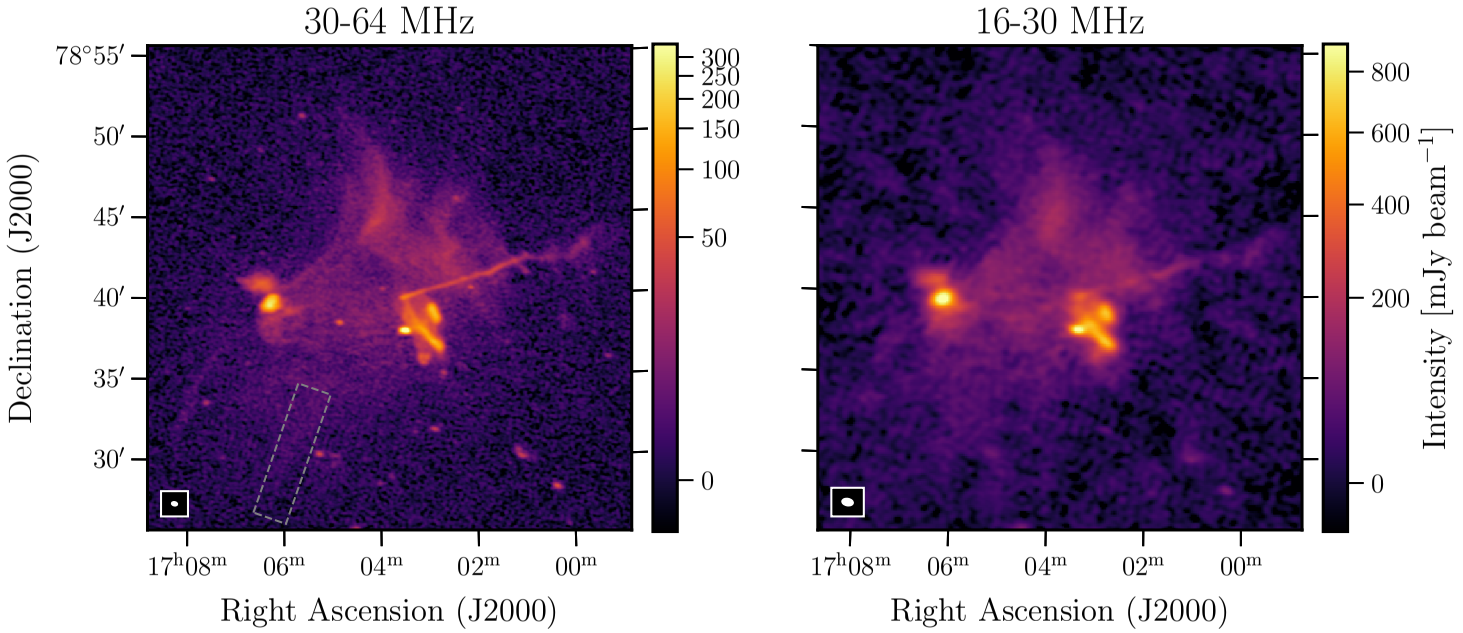

Figure 4.2: Full resolution LOFAR LBA (24 and 47 MHz) images of Abell 2256 at different frequencies with the restoring beam shown in the bottom left inset. The 46 and 23 MHz images, respectively, have resolutions (HPBW) of $19'' \times 12''$ and $39'' \times 24''$, and background noise levels of 1.4 mJy beam^{-1} and 9 mJy beam^{-1}. The tentative filamentary extension of the halo, parallel to source AI, is indicated by the grey dashed region.

4.2 Data

The radio observations used in this work are listed in Table 4.1. Abell 2256 was observed with both the LOFAR LBA and High Band Antenna (HBA) systems for 16 hours each. The observations and calibration process are detailed below, separately for the HBA and LBA. The flux density scale of both systems was verified with bright compact sources in the field using recent higher frequency data from Rajpurohit et al. (2022c), as shown in Appendix 4.6. We found that the LOFAR HBA maps were biased slightly high, and thus corrected those with a scaling factor of 0.83 (see also Rajpurohit et al., 2022c). Throughout this chapter, a 10% uncertainty will be assumed on all flux measurements, which is common for LOFAR observations (Shimwell et al., 2022). All images are made using Briggs weighting with a value of the robust parameter equal to -0.5 (Briggs, 1995).

4.2.1 LOFAR HBA

The LOFAR HBA (120-168 MHz) observations were taken in the `DUAL_INNER` configuration (i.e. the remote station collecting area is matched to the core stations) in two different observing sessions. Observations taken on 2018-05-01 include Abell 2256 at a distance of 1.6 degrees from the pointing centre as part of the LOFAR project with code *LC9_008*. Additionally, observations from the LOFAR Two-Metre sky survey (Shimwell et al., 2017, 2019, 2022) of the field P255+78, include Abell 2256 at a distance of 1.0 degree from the pointing centre. The total target observation time is 16 hours spread equally over the two observations and both observations were book-ended with 10-minute scans on the calibrator source 3C295.

We separately calibrated both observations using the standard LoTSS DR2 pipeline (full details in Tasse et al., 2021; Shimwell et al., 2022). First, direction-independent effects such as polarisation alignment, Faraday rotation, bandpass and delay terms were corrected in `prefactor`[1] using the calibrator observations (van Weeren et al., 2016a; Williams et al., 2016; de Gasperin et al., 2019). The solutions were applied to the target field after which several cycles of direction-dependent (self-) calibration were done.

After the complete direction-dependent calibrated image was created with the standard LoTSS DR2 pipeline, we extracted a region of $0.5^\circ \times 0.5^\circ$ around Abell 2256, using the extraction procedure detailed in van Weeren et al. (2021). This optimises the image quality of the main target of interest by removing sources away from the target and performing a direction-independent self-calibration towards the target with the full 16-hour dataset. The resulting image is shown in Figure 4.1. The final science image has a background RMS noise of 90 μJy beam^{-1} when imaged at the half-power beamwidth (HPBW) resolution of $6'' \times 6''$.

4.2.2 LOFAR LBA

Abell 2256 was observed with the LBA system as part of LOFAR project *LC15_026* from 16 to 64 MHz in three separate observing runs, detailed in Table 4.1. We employed a similar observing strategy to the LOFAR LBA sky survey (LoLSS; de Gasperin et al., 2021), observing a calibrator source (3C380) simultaneously during the entire run. Similar to the LoTSS DR2 pipeline and LoLSS pipelines, we first used `prefactor` over the full bandwidth

[1] `https://git.astron.nl/eosc/prefactor3-cwl`

to calculate the direction-independent corrections, which may vary over the time of the observation. These corrections include the polarisation alignment, bandpass and LOFAR beam model. Afterwards, calibration was performed separately for the frequency range 16-30 MHz and 30-64 MHz.

30-64 MHz

For the frequency range 30-64 MHz, we used the pipeline employed for LoLSS[2] (de Gasperin et al., 2019, 2020). This pipeline first solves for direction-independent effects (de Gasperin et al., 2019) in the target field by self-calibration, starting from a model from TGSS ADR1 (Intema et al., 2017) and then direction-dependent effects as described in de Gasperin et al. (2020). After successful calibration and imaging of the complete field-of-view, we extracted the target cluster using the method detailed in van Weeren et al. (2021). The final image integrated from 30-64 MHz has a resolution of $19'' \times 12''$ and an rms noise of 1.4 mJy beam^{-1}. It is shown in the left panel of Figure 4.2.

16-30 MHz

For the lower part of the LBA sub-band, from 16 to 30 MHz, no standard pipeline is yet available, although Groeneveld et al. (subm.) presents a calibration strategy for the decametre band that is shown to work for a standard LOFAR observation of an arbitrary field with typical observing conditions. We have used a similar method to calibrate the Abell 2256 field, proceeding as follows. We re-calculated phase calibration solutions in two steps using the calibrator source and solution intervals and smoothness constraints optimized for the frequency range. First, differential Faraday rotation was calibrated by converting the data to a circular basis and taking only the phase difference of the XX and YY correlations. This has the advantage that all scalar phase effects are removed from the data. Then, scalar phase effects (i.e. ionospheric dispersive delay and clock terms) were taken out by solving for a model of the calibrator source. For both of these calibrations, we constrained the solutions to be smooth by convolving them with a Gaussian kernel that has a width that is linearly proportional with the frequency, to follow the ν^{-1} dependence of ionospheric dispersive delays. The calibrator phase solutions were then applied to the target field, which concluded the data pre-processing. The first direction-independent image was then made by means of self-calibration using a bright calibrator in the target field, that dominates the flux density. We phase shifted to the brightest source in the target field, 3C390.3, and used the same calibration strategy as for the calibrator field, which solves for differential Faraday rotation and residual phase effects, but now in the direction of the target field. We used again the TGSS-ADR1 survey as the starting model. Finally, for direction-dependent calibration of the target field, we manually extracted $\sim 1^\circ \times 1^\circ$ regions around the 13 brightest sources in the field. Those were self-calibrated to correct for ionospheric distortions by calibrating for total electron content (TEC) and phase simultaneously (`tecandphase` in DP3; van Diepen et al. 2018), again using the TGSS-ADR1 survey as a starting model. The final direction-dependent calibrated image was made by combining the solutions from different directions to a smooth screen.

The full field-of-view of the LBA image is shown in the appendix (Fig. 4.16), where the imaging was done in WSclean using multi-scale clean (Offringa et al., 2014; Offringa

[2] `https://github.com/revoltek/LiLF`

& Smirnov, 2017) and the image-domain gridder (van der Tol et al., 2018). Then, as was similarly done for the higher frequency data, we manually extracted the direction of the target and performed additional rounds of self-calibration to optimise the calibration quality in the direction of Abell 2256 (van Weeren et al., 2021). The right panel of Figure 4.2 shows the resulting image of Abell 2256. We achieved unprecedentedly low Gaussian noise levels (< 10 mJy beam^{-1}) in the frequency range 16-30 MHz. This presents not only the deepest-ever image of Abell 2256 at such low frequencies but also of any celestial target.

4.2.3 Gamma-ray data

For comparison with gamma-ray observations, we have made use of publicly available data from the Fermi Large Area Telescope. The event selection and analysis follow the work presented in Adam et al. (2021).

We used 13.5 years of Pass 8 data (P8R3), collected from August 4, 2008, to February 7, 2022. They were extracted within a radius of 10 degrees from the cluster centre. We selected events with energies from 200 MeV to 300 GeV and we applied the `P8R3_SOURCE_V2` selection (event class 128) and selected `FRONT` + `BACK` converting photons (event type 3). Data from zenith angles less than 90 degrees were filtered out to remove the Earth limb photons. Time selection and rocking angle cuts were applied following recommendation: `DATA_QUAL` > 0 && `LAT_CONFIG` $== 1$, and (`ABS(ROCK_ANGLE)` < 52).

Here, we focus mainly on the gamma-ray spectral constraints, to be combined with radio synchrotron data. In order to extract the cluster SED, we performed a joint likelihood fit of both the background components and the cluster using the *fermipy* package (Wood et al., 2017). The data were binned both in energy and space, with 8 energy bins per decade and 0.1x0.1 deg^2 pixels. The region of interest (ROI) width was set to 12 degrees. We model the ROI using the 4FGL-DR2 catalog (`gll_psc_v20.fit`; Abdollahi et al. 2020; Ballet et al. 2020) together with the isotropic diffuse background (`iso_P8R3_SOURCE_V2_v1.txt`) and the galactic interstellar emission (`gll_iem_v07.fits`). The cluster gamma-ray template was modelled using the MINOT package (Adam et al., 2020). MINOT requires a thermal gas model and a cosmic ray proton (CRp) spatial and spectral distribution to compute gamma-ray templates from hadronic interactions. The thermal model was fixed to the one discussed in Section 4.4. When fitting the sky model to extract the SED, the photon spectral index is allowed to vary within the bins so that the final results are insensitive to the CRp spectrum. Given the fact that Abell 2256 is barely resolved by the Fermi-LAT, the SED constraints are only weakly sensitive to the assumptions made about the CRp spatial distribution with the cluster (see Section 4.4 for the modelling). We performed the spectral extraction using different assumptions about the spatial modelling and concluded that the results remained stable. In the end, we obtained, in each energy bin, the likelihood scan for the normalization of the flux that is either used to constrain the cluster CRp normalisation and spectrum independently from other wavelengths, or used jointly with radio data for testing acceleration models (Section 4.4).

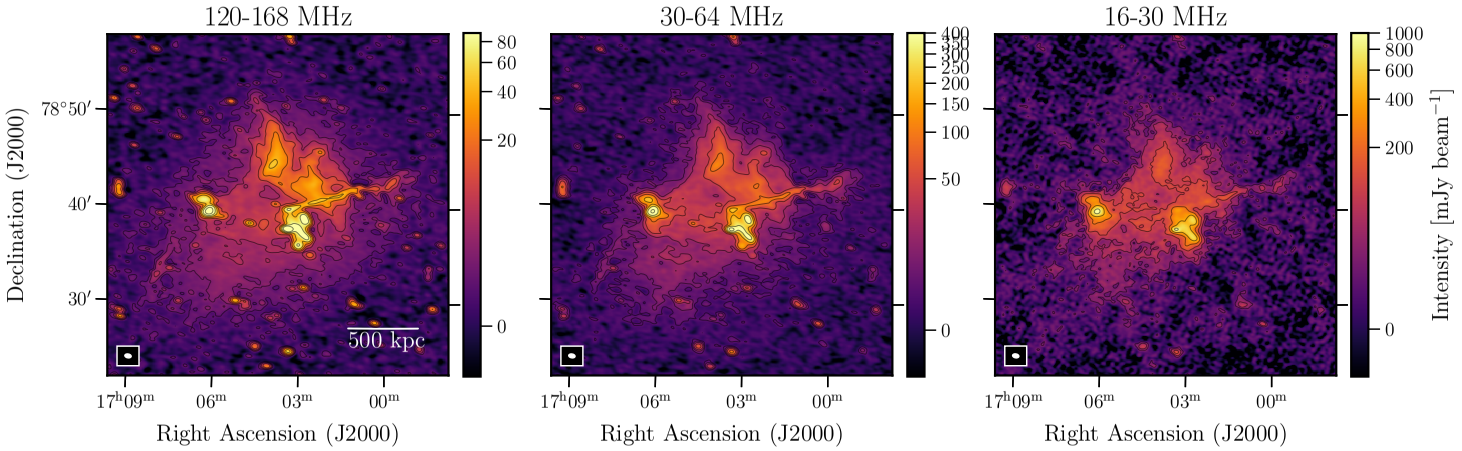

Figure 4.3: Common resolution (39″ ×24″) LOFAR images of Abell 2256 at different frequencies with the restoring beam shown in the bottom left inset. The background noise levels are σ =0.4, 1.7 and 9 mJy beam^{-1} respectively. Contours are drawn at [3,6,12,...,384]σ.

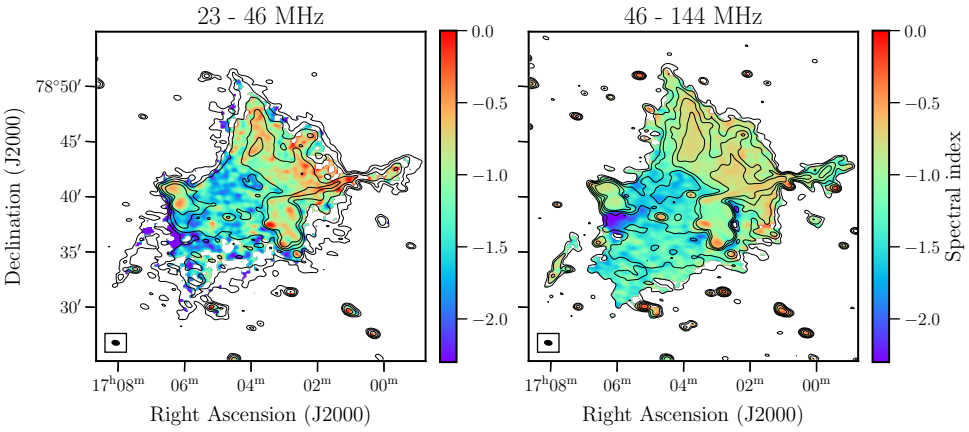

Figure 4.4: Spectral index maps of Abell 2256 at different frequencies with the restoring beam shown in the bottom left inset. Both maps have been smoothed to a common resolution of $39'' \times 24''$ and were made with an inner uv cut of 100λ. The contours show the higher frequency [3, 6, 12, 24, 48]σ levels where σ denotes the background rms noise level.

4.3 Results - Radio analysis

The full-resolution LOFAR images are shown in Figures 4.1 and 4.2, where no uv baseline filtering is applied. Although the resolution is low in the 16-30 MHz band, we can still clearly distinguish the distinct sources of radio emission in the cluster. The radio halo and radio shock are clearly resolved, and the brightest AGN-related sources can still be separated from the diffuse radio emission.

To emphasise the low surface brightness emission in the cluster, we plot the three frequency bands all convolved to the same resolution of $39'' \times 24''$ in Figure 4.3. We note that at the matched resolution, the 30-64 MHz and 16-30 MHz images have a similar sensitivity to the HBA system for sources with a spectral index of $\alpha = -1.3$ and $\alpha = -1.7$, implying that the HBA image is more sensitive than the two LBA images for sources that have $\alpha > -1.3$ and $\alpha > -1.7$, respectively.

We also made two spectral index maps, between 16-46 and 46-144 MHz, at a common resolution of $39'' \times 24''$. For these maps, we set the robust parameter to -0.5 and employed an inner uv baseline cut at 100 times the observing wavelength (i.e. 100λ), to ensure short baselines are similarly sampled at all frequencies. Additionally, only pixels with a flux density greater than three times the RMS noise in all three images were used. Figure 4.4 shows the spectral index maps, with contours representing the total intensity of the higher-frequency image. The spatial distributions of uncertainties are shown in the appendix (Fig. 4.17), including the flux density scale offset and statistical uncertainty. The median spectral index uncertainty is 0.31 for the lower part of the LBA band and 0.19 for the LBA-HBA map. In the following sections, we present the analysis of the radio halo, radio shock and AGN-related sources separately.

4.3.1 Radio halo

In the low-resolution images shown in Figure 4.3, the halo appears largest at 144 MHz, owing to the high sensitivity of the HBA system. In fact, with the low-resolution image bringing out the low surface-brightness emission, the radio halo is larger than reported in the recent work by Rajpurohit et al. (2023), with a largest-linear size (LLS) of 0.40°, corresponding to 1.6 Mpc at the cluster redshift. This is due to the fact that the halo LLS was measured in 20″ images with a uv cut of 100λ by Rajpurohit et al. (2023), but these full uv plane lower resolution images show that low surface-brightness emission extends further. The halo encompasses the radio shock, extending out to about 60% of the $R_{500} = 1273$ kpc radius. The halo emission appears to become filamentary in the south-east region, which is best visible in the high-resolution 120-168 and 30-64 MHz images in Figures 4.1 and 4.2, where the latter has been marked to indicate the location of the possible filament. We note that the filamentary emission is oriented approximately parallel to the source AI, but also underline that their detection remains tentative.

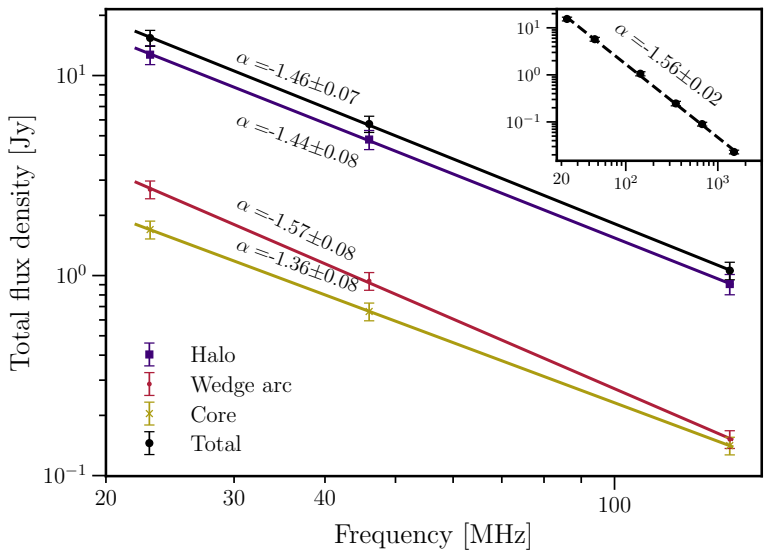

Figure 4.5: Integrated spectrum of the radio halo between 23 and 144 MHz. The three regions used to compute the spectrum are shown in Figure 4.1. The inset in the top-right corner shows the integrated spectrum with the addition of higher-frequency data from the recent study by Rajpurohit et al. (2023) and has the same axis labels as the main plot.

We calculated the integrated spectral index of the radio halo between 23 and 144 MHz using the same regions from the recent higher frequency study from Rajpurohit et al. (2023) for both the subtraction of compact sources and the integration of the halo flux density, as well as the definition of the sub-regions 'core' and 'wedge' (see Fig 4.1). The resultant integrated spectrum is shown in Figure 4.5, where the inset shows our data together with the higher frequency measurements, where for a correct comparison accounting for the different baseline coverages, we filtered out baselines below 100λ when measuring the

halo flux. The resultant halo flux measurements are given in Table 4.4. The integrated spectral index follows a power-law of -1.56 ± 0.02 over almost two orders of magnitude in frequency, from 24 to 1500 MHz. However, the spectral index of the core region is flatter than the overall radio halo, with $\alpha = -1.36 \pm 0.08$, while the spectral index of the 'wedge' is slightly steeper at low frequencies.

The integrated spectral index agrees within two standard deviations with the spectrum measured at higher frequencies ($\alpha = -1.63 \pm 0.03$; Rajpurohit et al. 2023), with no evidence for spectral curvature. This differs from the curved spectra observed in the radio halos of other clusters with wide frequency coverage, such as the Coma cluster, MACS J0717.5+3745 or Abell S1063 (Thierbach et al., 2003; Rajpurohit et al., 2021a; Xie et al., 2020). We note that for our measurements we have ensured a consistent *uv*-min in wavelength units for all datasets when imaging. This is highly important, as for example the halo is significantly brighter, by a factor of ~ 2, at LOFAR frequencies in images without inner *uv* cuts, indicating the presence of large-scale emission that is only detected with the shortest LOFAR baselines. Whilst our measurements integrated the pixels within a given region, we note that if we repeat the exercise but using the flux from the best-fit spherical models of the radio halo surface brightness (see Section 4.4.2 and Appendix 4.6) we find consistent results for the spectral index measurements.

To investigate the spatial distribution of the spectral index, we calculated the standard deviation from the halo region of the spectral index maps of the 23-46 and 46-144 MHz bands. These are 0.43 and 0.25, respectively. These standard deviations are significantly larger than what we would expect from the uncertainty in the spectral index maps. Across the radio halo, the median uncertainty was found to be 0.36 and 0.21 respectively. We can calculate the probability of observing the values for the sample standard deviations, given the null hypothesis that the scatter should be set by the uncertainty in the spectral index (i.e. that the scatter is consistent with the uncertainty). A chi-squared test of variance with $n \approx 160$ independent beams sampled across the radio halo returns $p < 0.001$, even without taking into account the spatial correlation of the uncertainty in the spectral index. We can thus reject the null hypothesis that the variance of the measurements is equal to the variance expected from the uncertainty of the measurements. This implies that the distribution of spectral indices in the radio halo has a significant spatial scatter. We note that this is a lower limit on the intrinsic scatter of the spectral index because we are only able to measure the projected spectrum.

Higher frequency data on Abell 2256 has shown that the spectral index also has a radial trend, with steeper spectra towards the outskirts (Rajpurohit et al., 2023). The low-frequency spectral index maps in Figure 4.4 do not show a clear radial trend when analysed in a comparable way. To quantify this, we calculated the spectral index by fitting the 23, 46 and 144 MHz flux densities in radial bins using concentric annuli. The best-fit spectral index, with the one-sigma uncertainty, is shown as a function of radius in Figure 4.6. Although there is a hint of steepening in the last radial bin and flattening in the core, the data are consistent with a constant spectral index as a function of radius, given the large error bars.

A superposition of curved spectra could result in a single power-law spectrum when integrated over the entire radio halo, as observed for example in Abell 2744 (Rajpurohit et al., 2021b). To investigate possible spatial variation of the curvature, we computed the

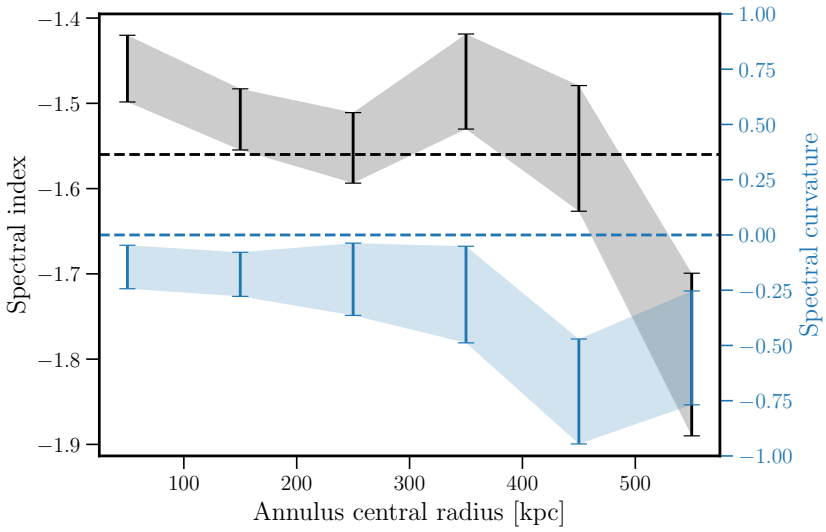

Figure 4.6: Spectral index (black) and curvature (blue) profile as a function of radius from the halo centre, computed in concentric annuli from a least-square fit to the 23, 46 and 144 MHz data. The value of the integrated spectral index and curvature of the radio halo is indicated by the dashed lines.

spectral curvature map from the spectral index maps as follows

$$\alpha_{23\mathrm{MHz}}^{46\mathrm{MHz}} - \alpha_{46\mathrm{MHz}}^{144\mathrm{MHz}}. \tag{4.1}$$

This spatial distribution of spectral curvature is shown in Figure 4.7, and the corresponding uncertainty map in Figure 4.18. The median uncertainty across the radio halo is 0.39 while the standard deviation of the measured curvature across the radio halo is 0.52. Using a chi-squared test of variance, the null hypothesis that the observed variance is equal to the variance expected from the uncertainties is rejected with $p < 0.001$, indicating that the spectrum locally exhibits a convex or concave shape in different regions of the radio halo. The spectral curvature variations also seem to have no radial dependence as the curvature profile, shown in Figure 4.6, is consistent with a straight line.

In summary, the radio analysis of the halo in Abell 2256 reveals that the integrated spectrum of the halo is consistent with a steep power-law. However, we also find evidence of spectral index and curvature variations that do not follow a radial profile, indicating a complex and inhomogeneous environment.

4.3.2 Radio shock

Abell 2256 hosts one of the clearest examples of filamentary radio emission inside a radio shock (Clarke & Ensslin, 2006; Brentjens, 2008; Owen et al., 2014). Usually, such filaments are observed at gigahertz frequencies only due to the high resolution required but here we present the first case where filamentary radio emission is observed in a radio shock down to at least 23 MHz. In the total intensity images shown in Figures 4.1 and 4.2 the well-known filaments inside the radio shock (source G and H) are still clearly seen at 144 and 46 MHz, while the 23 MHz image shows only the brightest larger filaments.

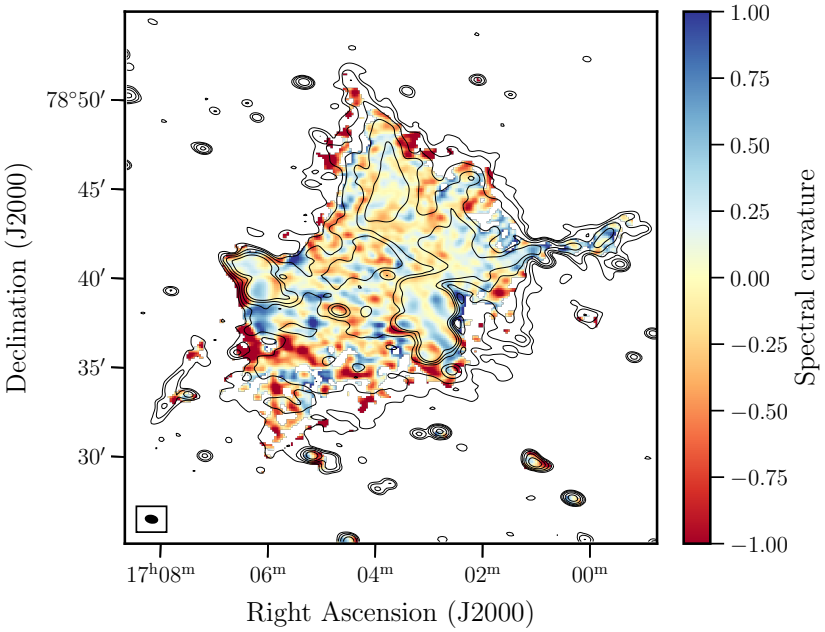

Figure 4.7: Spectral index curvature map of Abell 2256, calculated as $\alpha^{46\mathrm{MHz}}_{23\mathrm{MHz}} - \alpha^{144\mathrm{MHz}}_{46\mathrm{MHz}}$, where both spectral index maps are made with a common resolution of $39'' \times 24''$. Blue regions indicate spectral steepening towards higher frequencies and red regions indicate flattening at higher frequencies. The background contours show the 144 MHz intensity smoothed to the same resolution.

The integrated spectrum of the radio shock between 23 and 144 MHz is plotted in Figure 4.8, where we have divided the shock into three sub-regions (shown in Figure 4.9) to allow us to study the spectral steepening from west to east across the radio shock that was noticed at higher frequencies by Clarke & Ensslin (2006) and Rajpurohit et al. (2022c). The radio shock flux measurements are given in Table 4.4. In agreement with these previous studies, Figure 4.8 shows that the westernmost region R1 has a steeper spectrum than regions R2 and R3, with R1 showing $\alpha = -1.08 \pm 0.07$ and R2 and R3 showing $\alpha = -0.84 \pm 0.07$ and $\alpha = -0.83 \pm 0.08$, respectively. We note that the uncertainties on the spectral index measurements are dominated by the systematic uncertainty in the flux density scale, and thus have a strong spatial correlation while the statistical uncertainty is on the order of 0.02. The total integrated spectrum, when combined with higher frequency data from the recent study by Rajpurohit et al. (2022c), agrees with a straight power-law with $\alpha = -1.00 \pm 0.01$ from 24 to 3000 MHz. However, at low frequencies, the contribution of the radio halo flux to the region of the radio shock might become significant and cannot be easily separated in the images. We can estimate the contribution using the spherical halo models that were fit in Appendix 4.6. Assuming the radio halo is spherically symmetric, we find that the halo contributes 10%, 26% and 39% of the total radio shock flux in the 144, 46 and 23 MHz images respectively. However, subtracting this contribution only flattens the spectrum marginally. With the subtraction of the estimated radio halo flux from the radio shock region, we find that the radio shock spectrum between 24 and 3000 MHz still

follows a power-law with $\alpha = -0.95 \pm 0.01$.

The spectral index trend across the radio shock can also be seen in the spectral index map at $20''$ between 46 and 144 MHz, shown in Figure 4.9. This spectral index map indicates steepening from the southwest towards the northeast side of the radio shock, where we see preferentially emission with $\alpha < -1$. In contrast, the west side of the radio shock shows flatter spectrum emission, with $\alpha > -1$.

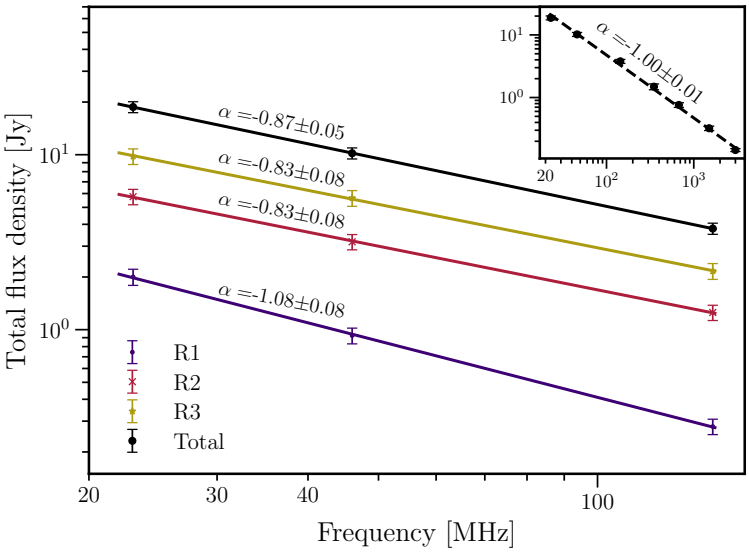

Figure 4.8: Integrated spectrum of the radio shock between 23 and 144 MHz. The three regions used to compute the spectrum are shown in Figure 4.9. The inset in the top-right corner shows the integrated spectrum with the addition of higher-frequency data from the recent study by Rajpurohit et al. (2022c) and has the same axis labels as the main plot.

4.3.3 AGN related emission

Abell 2256 also hosts a large number of complex radio sources, that appear to be either directly related to AGN or associated with (revived) fossil AGN plasma (van Weeren et al., 2009). Fossil plasma sources typically show very steep spectra that are often curved at high (GHz) frequencies (e.g. Mandal et al., 2020). In the case of Abell 2256, there are various (candidate) fossil plasma sources.

First, the sources labelled AG+AH and AI were discovered in van Weeren et al. (2009), where they showed spectral indices at frequencies higher than 140 MHz of $\alpha < -1.95$ and $\alpha < -1.45$ respectively. The possibility was raised that both sources are revived fossil plasma sources, although AG+AH might also simply be old AGN emission from the long, tailed radio galaxy. This scenario is supported by the high-resolution radio images of Figures 4.1 and 4.2, where AG+AH seems to be connected to the long Mpc-sized tailed radio source C. In the high-resolution HBA image, we also clearly observe for the first time

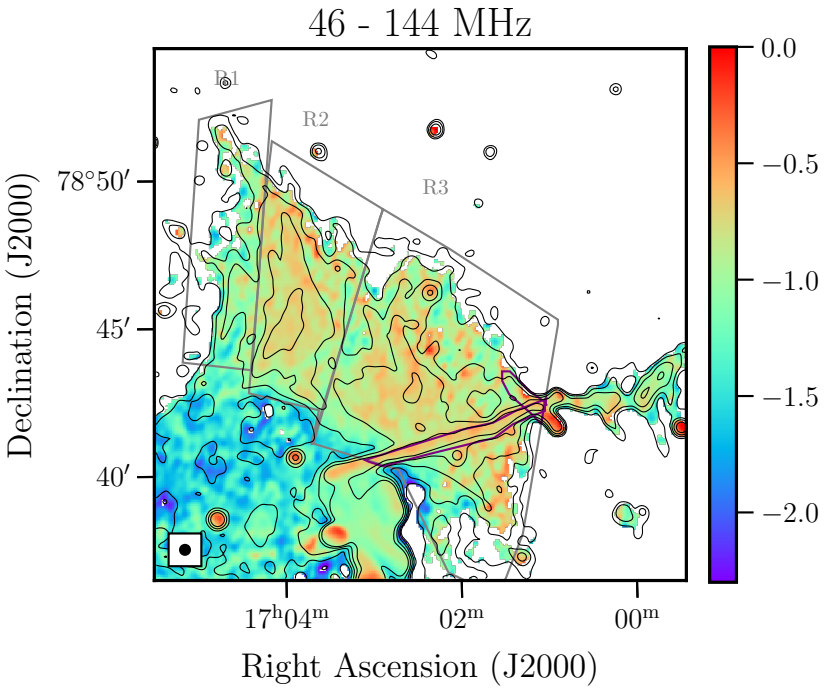

Figure 4.9: Spectral index map of the radio shock between 46 and 144 MHz made at a common resolution of $20'' \times 20''$. The three regions used to compute the integrated spectral index of the shock are shown in grey, where the contribution from the bright narrow-angle-tailed sources is subtracted, shown in purple. The contours indicate the LOFAR 144 MHz total intensity at [3,6,12,24,48] times the background noise.

'ribs' coming off the source AG+AH. These are reminiscent of the ribs seen in the radio tail dubbed T3266 in Abell 3266 as observed with the MeerKAT telescope (Knowles et al., 2022; Riseley et al., 2022; Rudnick et al., 2021)

Second, there is the F complex of sources, also discussed by Bridle & Fomalont (1976); Bridle et al. (1979); Röttgering et al. (1994); Brentjens (2008) and Owen et al. (2014). The F complex of sources is located on the west side of the radio halo, and consists of three components, F1, F2 and F3. The narrow-angle tailed source F3 is clearly associated with a cluster member (Fabricant et al. (1989) galaxy 122), situated at the eastern tip of the radio source (Owen et al., 2014), as shown in Figure 4.10. However, the nature and origin of the other two sources are still unclear. One possibility is that F1 and F2 are also related to the same galaxy as F3, but another possibility is that F1 and F2 consist of fossil radio plasma from previous episodes of AGN activity (possibly from F3) that is compressed somehow by interactions in the ICM (van Weeren et al., 2012b).

The 23 MHz data shows that F2 and F3 are more extended than previously reported at higher frequencies (Brentjens, 2008; Owen et al., 2014). The radio emission of F3 seems to fade into the wedge arc of the radio halo, indicating a possible connection between the tailed radio source and the halo arc. Interestingly, we observe no clear spectral index gradient across F1-F3. Additionally, we detect a new, very steep, region just below the F

complex, co-spatial with the radio halo. It is clearly seen as a bright region in the 46 MHz contours shown in Figure 4.10 and shows a spectral index of $\alpha < -2$ in the 46-144 MHz spectral index map (Fig. 4.4). This seems like a fossil plasma source due to the extreme steepness of the spectrum, and could possibly be associated with the F complex as well. We, therefore, label it F4 in this study. The optical overlay, Figure 4.10, shows that the 46 MHz contours seem to originate from the cluster galaxy MCG+13-12-020 at 17h05m39.5s +78d37m34.2s the south-west, which agrees with the spectrum flattening spatially towards this galaxy, implying a possible optical host.

As lower energy electrons cool less efficiently through synchrotron and inverse Compton radiation, our low-frequency data allows us to probe the aging of the observed emission. By fitting their spectra (see Fig 4.11) with simple synchrotron ageing models, we estimated the ages of AG, AH, AI and F1-F4, adding high-frequency data from the literature where possible. All sources except F1 and F4 show spectral flattening towards lower frequencies, indicating that we do not observe the break frequencies of F1 and F4, which are likely below 23 MHz.

We used *synchrofit*[3] (Quici et al., 2022) to fit standard synchrotron models to the various AGN-related sources in Abell 2256. We fit a continuous injection (KGJP; Komissarov & Gubanov, 1994) model to the curved spectrum sources. The model has three free parameters: the injection index $s = 1 - 2\alpha_{\rm inj}$, where $\alpha_{\rm inj}$ is the radio spectral index upon injection, the break frequency after which the spectrum steepens, and the remnant fraction (i.e. the fraction of time the source is 'off'). Following the minimum energy condition as calculated in Brentjens (2008) which follows the Beck & Krause (2005) formula, we assume a tangled magnetic field with a strength of 7 μG for the F complex. Doing the calculation for AG+AH and AI gives lower values of the minimum energy magnetic field strength around ~3 μG, but we assume 7μG as well to give a conservative age estimate. We note that the maximum age estimate is obtained for $B = B_{\rm CMB}/\sqrt{3}$ (e.g. Stroe et al., 2014), which results in 1.8μG at the redshift of Abell 2256. The resulting spectral ages, best-fit injection indices and break frequencies for the AGN-related sources are given in Table 4.2.

The straight spectrum of F1 over multiple decades in frequency indicates the source is likely still being energised and we are observing the spectrum above the break frequency. For a simple continuous injection model, the spectrum would consist of two power-laws with $\alpha = \alpha_{\rm inj} - 0.5$ after the break frequency (Pacholczyk, 1970). The best-fit spectral index of F1 was found to be $\alpha = -1.36 \pm 0.03$, implying a radio injection index of $\alpha_{\rm inj} = -0.86 \pm 0.03$. For source F4 the simple continuous injection model does not fully work, because it would imply an injection index of $\alpha_{\rm inj} = 0.5 - 1.9 \pm 0.1 = -1.4 \pm 0.1$, which is much steeper than typical injection indices (> -1). Thus we are likely observing the exponential steepening of the spectrum of F4, implying relativistic particles are not continuously injected.

[3] https://github.com/synchrofit

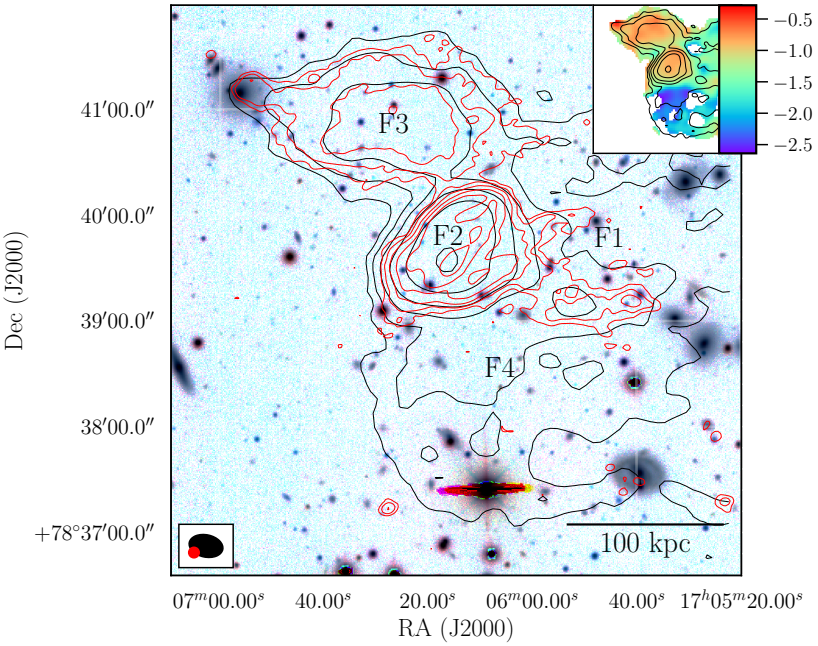

Figure 4.10: The F-complex in Abell 2256, shown as the overlay of LOFAR 144 MHz 6″ (red) and LOFAR 46 MHz 19″ (black) contours on the *grz* optical filters from the Legacy Survey (Dey et al., 2019), with inverted colours for visibility. The restoring beams are indicated in the lower left corner, and contours are drawn at [5,10,20,40] times the background noise level σ. The inset plot shows the spectral index map between 46 and 144 MHz at the common 19″ resolution with the same LOFAR 46 MHz contours, where F4 is visible as the blue steep region of emission.

Table 4.2: Flux density measurements and best-fit synchrotron model parameters of the AGN-related sources in Abell 2256.

Source	$S_{144\mathrm{MHz}}$[Jy]	$S_{46\mathrm{MHz}}$[Jy]	$S_{23\mathrm{MHz}}$[Jy]	Model	α_{inj} [a]	Break frequency[a] [MHz]	Remnant Fraction[a]	Age[b] [Myr]
AG+AH	0.13 ± 0.01	0.47 ± 0.05	0.64±0.08	KGJP	0.55±0.02	113±12	0.57±0.05	197±10
AI	0.04 ± 0.01	0.15 ± 0.02	0.38±0.06	KGJP	0.91±0.02	242±82	0.33±0.04	135±30
F1	0.05 ± 0.01	0.26 ± 0.03	0.64±0.07	CI[c]	0.86±0.02	< 23	-	> 437
F2	0.69 ± 0.07	1.96 ± 0.20	2.62±0.26	KGJP	0.53±0.01	129±22	0.24±0.05	185±15
F3	0.36 ± 0.04	1.06 ± 0.11	1.97±0.20	KGJP	0.66±0.02	145±24	0.25±0.05	174±14
F4	0.06 ± 0.01	0.56 ± 0.06	1.91±0.19	CI[c]	-1.4±0.1	< 23	-	> 437

Notes. [(a)] The error bars only reflect the statistical uncertainties from the fit. [(b)] For the age estimate, a conservative magnetic field value of 7μG was assumed, following Brentjens (2008). For a lower magnetic field strength, the age would increase. [(c)] F1 and F4 are consistent with a simple power-law spectrum without a break frequency observed.

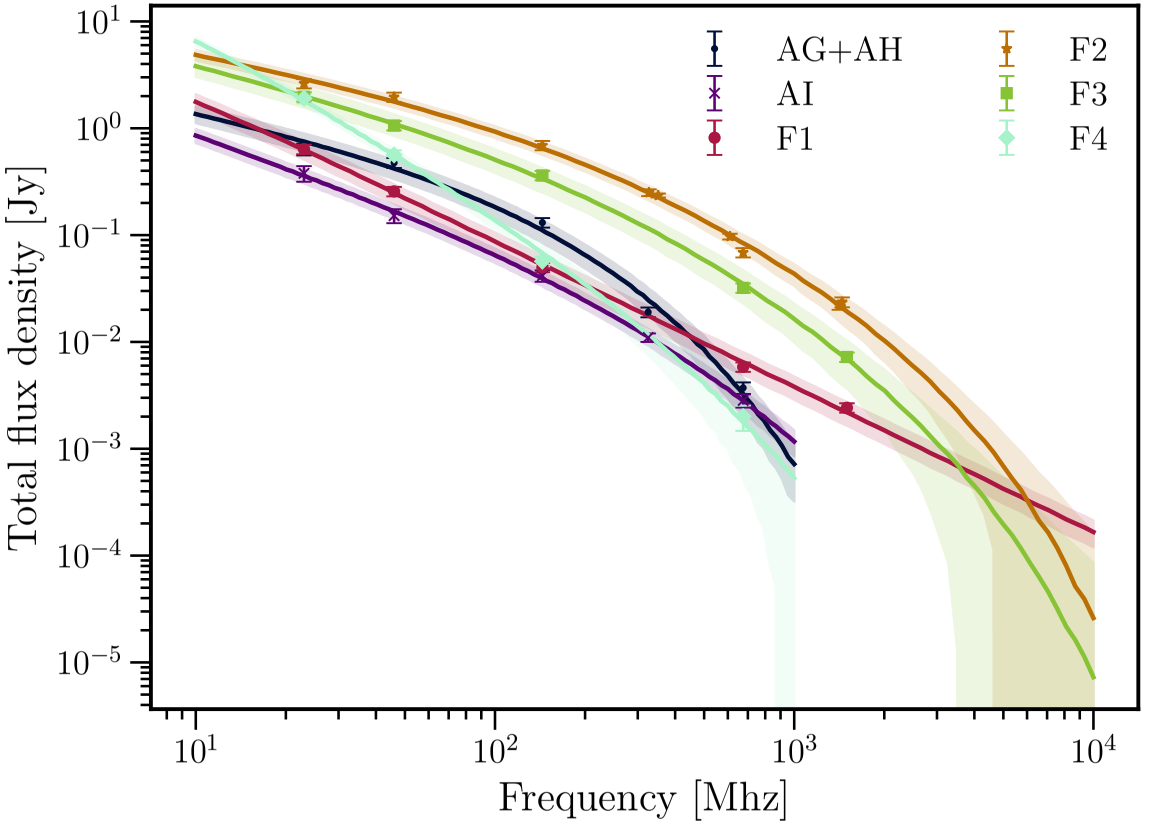

Figure 4.11: Spectra of fossil plasma sources down to 23 MHz adding literature data above 150 MHz where available. The flux density measurements and best-fit parameters of the synchrotron ageing models are given in Table 4.2.

4.4 Radio - Gamma-ray comparison

Nearby clusters such as Abell 2256, whose radio halo exhibits an ultra-steep spectrum, are expected to generate gamma-ray flux in the Fermi-LAT energy band if the halo is generated by secondary particles from hadronic interactions (Brunetti et al., 2009). They are therefore ideal candidates to constrain the contribution of secondary electrons from hadronic interactions to the cosmic ray electron population. In this section, we combine our LOFAR data with upper limits from Fermi-LAT data to test a purely hadronic origin of the halo.

4.4.1 Theoretical framework

Assuming purely hadronic models, we calculated the expected synchrotron intensity and gamma-ray flux density from the interactions of cosmic ray protons with thermal ions. We first assumed a power-law distribution of cosmic-ray proton density that follows the thermal plasma distribution n_{th} as follows;

$$\frac{dN_{CRp}(p,R)}{dpdV} = C_p n_{th}(R)^a kT(R) p^{-s}, \tag{4.2}$$

where C_p is a constant, n_{th} and kT denote the thermal gas density and temperature as functions of radius R, and p denotes the momentum of the protons, following a power-law distribution with index s. The proportionality between the cosmic ray proton energy density and the thermal plasma energy density ($W_{\rm CRp} \propto W_{\rm th}{}^a$) is left as an unknown and parameterised by a.

The collisions between CRp and thermal protons create pions (denoted by π) that decay into γ-rays, electrons/positrons and neutrinos (e.g. Blasi & Colafrancesco, 1999). The spectrum of secondary electrons is calculated as in Brunetti et al. (2017), assuming stationary conditions. First, the injection spectrum of electrons and positrons is given by

$$\begin{aligned} Q_e^{\pm}(p,t) = & \frac{8\beta'_\mu m_\pi^2 n_{\rm th} c^2}{m_\pi^2 - m_\mu^2} \int_{E_{\rm min}} \int_{p_*} \frac{{\rm d}E_\pi {\rm d}p}{E_\pi \bar{\beta}_\mu} \beta_p N_{CRp}(p,t) \\ & \times \frac{{\rm d}\sigma^{\pm,0}}{{\rm d}E}\left(E_\pi, E_p\right) F_e(E_e, E_\pi), \end{aligned} \tag{4.3}$$

where $\bar{\beta}_\mu = \sqrt{1 - m_\mu^2/\bar{E}_\mu^2}$, $\bar{E}_\mu = 1/2E_\pi(m_\pi^2 - m_\mu^2)/(\beta'_\mu m_\pi^2)$, $\beta'_\mu = 0.2714$, $d\sigma^{\pm,0}/dE$ is the differential inclusive cross-section for the production of neutral and charged pions from Brunetti et al. (2017) and $F_e(E_e, E_\pi)$ is given in Brunetti & Blasi (2005) below Eq. 36. The resulting steady-state distribution of the secondary electrons is then calculated as

$$N_e^{\pm}(p) = \frac{1}{\left|\frac{{\rm d}p}{{\rm d}t}\right|_{\rm rad} + \left|\frac{{\rm d}p}{{\rm d}t}\right|_{\rm C}} \int_p Q_e^{\pm}(p,t) p dt, \tag{4.4}$$

where $|{\rm d}p/{\rm d}t|_{\rm i}$ denotes radiative (i=rad) and Coulomb (i=C) losses.

These electrons will give rise to a synchrotron intensity spectrum $I_\nu \propto \nu^\alpha$ with $\alpha \simeq (1-s)/2$. From Equation 4.4, we can write the synchrotron intensity at a distance r on the

sky plane as the following integral along the line of sight.

$$I_{\rm syn}(\nu,r) = C\nu^{\alpha}kT\int_{\rm LOS}\frac{RdR}{\sqrt{R^2-r^2}}n_{\rm th}^2(R)\mathcal{F}(R)\frac{B(R)^{1+\alpha}}{B^2(R)+B_{\rm CMB}^2}, \tag{4.5}$$

where the constants have been absorbed into C and can be calculated following Brunetti et al. (2017) and we defined $\mathcal{F}(R) = \frac{W_{\rm CRp}(R)}{W_{\rm thp}(R)}$.

The gamma-ray intensity from the decay of pions was then computed following Brunetti et al. (2017, and ref. therein), with the injection rate of pions given by

$$Q_{\pi}^{\pm,0}(E,t) = n_{\rm th}c\int_{p_*}dpN_{CRp}(p,t)\beta_p\frac{d\sigma^{\pm,0}}{dE}(E_{\pi},E_{CRp}), \tag{4.6}$$

where $\pm$ and 0 refer to charged and neutral pions, respectively, and $d\sigma^{\pm,0}/dE$ is the differential inclusive cross section for their production, which is calculated in four different energy ranges of E_{CRp} as in Brunetti et al. (2017). The decay of neutral pions then generates gamma-ray emission with a spectrum

$$Q_{\gamma}(E_{\gamma},t) = 2\int_{E_{min}}^{E_{CRp,max}}\frac{Q_{\pi}^0(E_{\pi},t)\sqrt{E_{\pi}^2-m_{\pi}^2c^4}}{d}E_{\pi} \tag{4.7}$$

where $E_{min} = E_{\gamma} + m_{\pi}^2c^4/(4E_{\gamma})$. The final gamma-ray spectrum is then proportional to

$$I_{\gamma}(R) \propto \mathcal{F}(R)n_{\rm th}^2(R). \tag{4.8}$$

The ratio of the synchrotron to gamma-ray luminosity is thus governed by the magnetic field profile as

$$\frac{L_{\rm syn}}{L_{\gamma}} \propto \left\langle\frac{B(R)^{1+\alpha}}{B^2(R)+B_{\rm CMB}^2}\right\rangle, \tag{4.9}$$

where the brackets denote a volume-average weighted for the distribution of CRp (Brunetti et al., 2017).

The cluster magnetic field was assumed to follow the commonly used profile where the magnetic field energy density is proportional to the thermal gas energy density, as found for example for the Coma cluster (Bonafede et al., 2010)

$$B(r) = B_0\left(\frac{n_{\rm th}(r)}{n_{\rm th}(0)}\right)^{0.5}, \tag{4.10}$$

where $n_{\rm th}(r)$ denotes the thermal electron density at radius r. The central magnetic field strength B_0 is not well-constrained for Abell 2256 (e.g. Ge et al., 2020), so was left as a free parameter.

The thermal properties of Abell 2256 were obtained from the X-ray data from ACCEPT, ROSAT (Truemper, 1993; Eckert et al., 2012, 2013a,b), and the Sunyaev-Zel'dovich data from Planck (Planck Collaboration et al., 2016a). We fit a gNFW profile (Nagai et al., 2007) for the pressure and a simple β-model for the gas density. The best-fit parameters for

the beta model were found to be $n_{\rm th}(0) = 3\times10^{-3}$ cm^{-3}, r_c = 341 kpc, and $\beta = 0.77$ in the standard β-model given by

$$n(r) = n_{\rm th}(0)\left[1+\left(\frac{r}{r_c}\right)^2\right]^{-3\beta/2} \tag{4.11}$$

We verified that the fits also closely match the X-ray data from the Archive of Chandra Cluster Entropy Profile Tables (ACCEPT; Donahue et al., 2006; Cavagnolo et al., 2009) out to R_{500}. In summary, with reasonable assumptions on the magnetic field and measurements of the cluster thermal density, temperature profile, and synchrotron luminosity, we can estimate the expected gamma-ray luminosity from hadronic interactions in Abell 2256.

4.4.2 Gamma-ray upper limits

The LOFAR observations of the radio halo in Abell 2256 constrain the spatial distribution (i.e. a) and number density of cosmic ray protons of the purely hadronic model. We obtained the spatial distribution CRp from the brightness profile of the radio halo, which should follow Equation 4.5. We modelled the radio surface brightness using an MCMC halo-fitting code (Boxelaar et al., 2021). We masked the regions where the halo is seen in projection with either AGN or the large radio shock, as shown in Figure 4.19. We assumed a simple spherically symmetrical model commonly used for radio halos where $I(r) = I_0\exp(-r/r_e)$ (e.g. Osinga et al., 2021; van Weeren et al., 2021; Edler et al., 2022). The resulting fits are shown in Appendix 4.6 with the best-fit model parameters given in Table 4.5. We found similar values for the e-folding radius of $\sim$ 200 kpc at the three different frequencies, which is consistent with the finding in Section 4.3.1 that the spectral index is constant as a function of radius.

The observed surface brightness profiles of the radio halo at the three different frequency bands show very similar behaviour as a function of radius, as indicated in Figure 4.12 where the normalised profiles are shown for comparison. These profiles are flatter than expected from models that assume a constant CRp density (or a declining CRp density, with positive values of a). Such a tendency was also observed in other radio halos such as the Coma Cluster (Brunetti, 2003). Assuming a value of $a = -0.5$ approximately reproduces the flatness of the observed profile as a function of radius, so we set this as a reference value in the following calculations.

To match the total synchrotron luminosity of the radio halo for $B_0 = [3, 5, 10, 20, 30]\,\mu$G, hadronic models require an energy budget of CRp that is equal to $[15, 4.9, 1.4, 0.6, 0.4]$ times the thermal energy density averaged over the cluster volume within R_{500} respectively. This energy budget is large, because of the combination of the flat radio profile and steep synchrotron spectrum and improbable given the fact that the integrated CRp energy density is expected to be on the order of a few per cent of the total energy density in clusters (Pinzke & Pfrommer, 2010). Figure 4.13 shows that for all models, the radial profile of the cosmic ray energy density would exceed the thermal energy density within R_{500}. Such energy budgets of CRp should result in a detectable gamma-ray luminosity and flux.

To calculate the integrated synchrotron luminosity and gamma-ray luminosity from the hadronic model, we integrated out to $R_{500} = 1273$ kpc, although this cutoff is not sharp in practice. Therefore, this results in a conservative estimate for the expected gamma-ray

radiation from the hadronic model. We also note that for $a = -0.5$ although the cosmic ray fraction increases away from the cluster centre, the gamma-ray luminosity still declines as function of radius for $a > -1$, as can be derived from Equation 4.8. We show the expected gamma-ray flux derived from purely hadronic models that match the radio observations in Figure 4.14, where the overlay shows the current observational limits from Fermi-LAT. It is clear that for typical magnetic field values of $B_0 = 1\text{–}10\,\mu$G, gamma-rays would be detected if the halo was purely hadronic. At a three-sigma confidence level, the purely hadronic model disagrees with $B_0 < 17\,\mu$G.

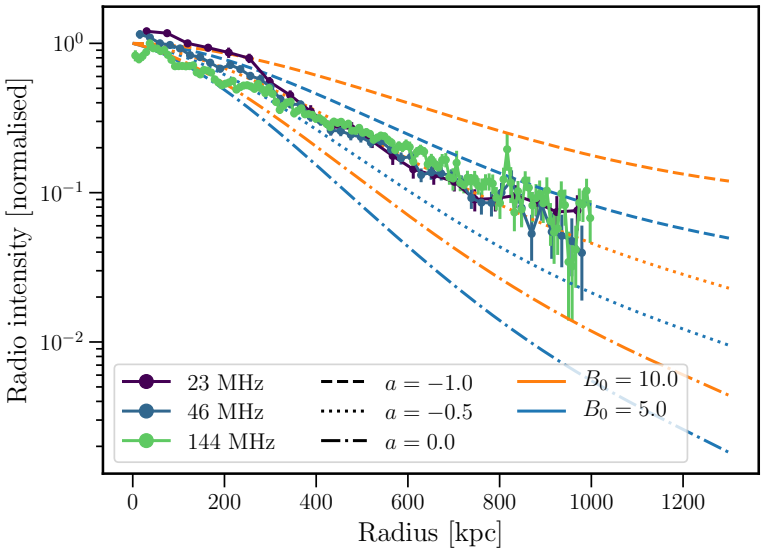

Figure 4.12: Observed (points) and modelled (lines) radio halo synchrotron intensity profiles in Abell 2256. The parameter B_0 denotes the central magnetic field strength, and a the proportionality between cosmic ray energy density and thermal energy density. The details of the models are explained in Section 4.4.1.

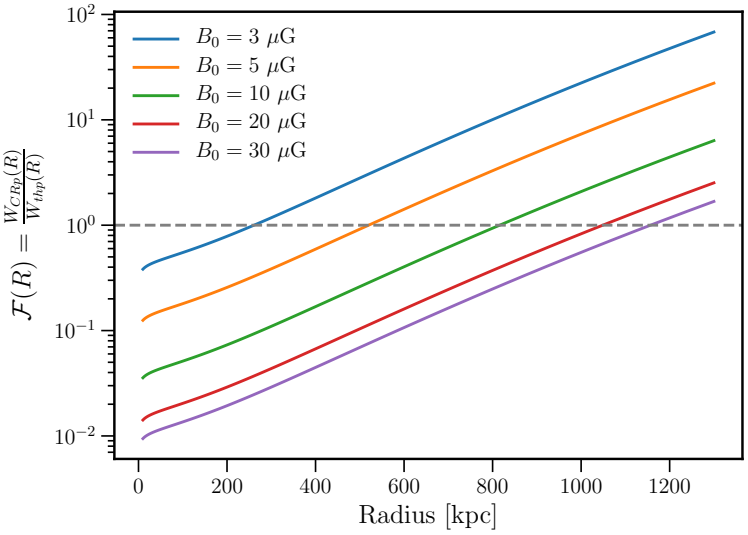

Figure 4.13: Required fractional energy density of cosmic ray protons with respect to the thermal protons as a function of radius to match the radio observations of the radio halo in Abell 2256 with hadronic models that have different central magnetic field strengths.

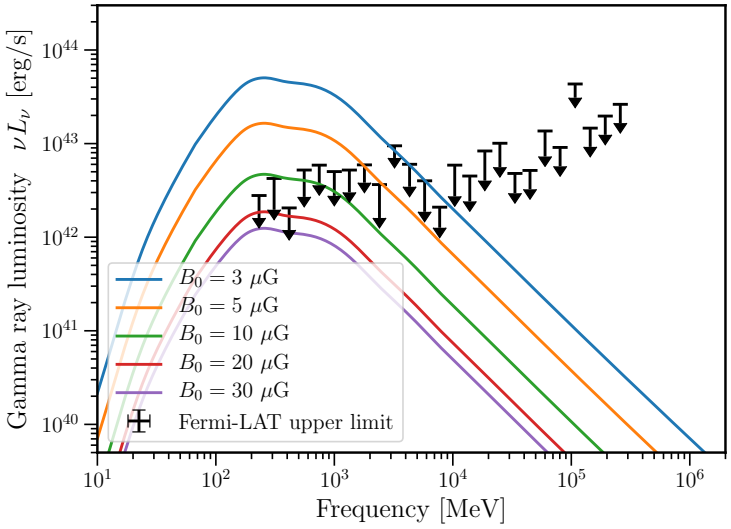

Figure 4.14: Expected gamma-ray luminosity from hadronic models that match the observed radio luminosity and brightness profile of the radio halo. Upper limits on the gamma-ray luminosity in Abell 2256 from Fermi-LAT observations are shown in black at 95% confidence.

4.5 Discussion

The radio halo in Abell 2256 was among the first radio halos to be discovered (Bridle & Fomalont, 1976), with deeper follow-up data uncovering its progressively larger extent (e.g. Clarke & Ensslin, 2006; Brentjens, 2008; Owen et al., 2014). The most recent estimate from Rajpurohit et al. (2023) shows that the largest linear size of the radio halo is at least 900 kpc.

In this work, we find the radio halo to be significantly larger than these previous estimates, with an observed size at 144 MHz of 1.6 Mpc. This significant increase in observed size can be attributed to the unparalleled sensitivity of LOFAR at low frequencies, particularly to large-scale emission because of the many short baselines. The large size of the radio halo implies that a large fraction of the cluster volume is occupied by relativistic electrons and magnetic fields, which is in line with recent works that have also found that radio halos extend out to large radii when observed with high sensitivities at low frequencies (Shweta et al., 2020; Cuciti et al., 2022; Botteon et al., 2022b). In fact, it is likely that the observed size of the radio halo is still limited by missing short baselines, as data imaged without 100λ baseline cuts shows a significantly larger and brighter radio halo (approximately 20%) than data imaged without short uv spacings. This was also found in previous works by injection of large mock radio halos into LOFAR data (Bruno et al., 2023). With the anticipated LOFAR2.0 upgrade to the LBA system, which can probe larger angular scales than the HBA system, observations will become more sensitive allowing the detection of even larger scale emission in nearby clusters.

Table 4.3: Radio halos detected over a large frequency range.

Name	Frequency [MHz]	Spectral index[a]	Curvature	σ_{2D} [b]	Mass $[10^{14} M_\odot]$	Reference
Abell 2256	23-1500	$\alpha_{23}^{1500} = -1.56 \pm 0.02$	no	≈ 0.2	6.2 ± 0.1	This work
Bullet cluster	1100-3100	$\alpha_{1100}^{3100} - 1.1 \pm 0.2$	no	-	13.1 ± 0.29	(Shimwell et al., 2014; Sikhosana et al., 2023)
Toothbrush cluster	147-4900	$\alpha_{147}^{4900} - 1.15 \pm 0.06$	no	< 0.04	10.8 ± 0.45	(van Weeren et al., 2012a)
Abell 2744	325-1500	$\alpha_{325}^{1500} - 1.32 \pm 0.14$	no	-	9.8 ± 0.4	(Pearce et al., 2017)
Abell S1063	325-3000	$\alpha_{325}^{1500} = -0.94 \pm 0.08$	yes	-	11.4 ± 0.34	(Xie et al., 2020)
Coma cluster	30-5000	$\alpha_{144}^{342} = -1.0 \pm 0.2$	yes	-	7.2 ± 0.1	(Bonafede et al., 2022)
MACS J0717.5+3745	144-1500	$\alpha_{144}^{1500} = -1.39 \pm 0.04$	yes	≈ 0.3	11.5 ± 0.5	(Rajpurohit et al., 2021a)

Notes. [(a)] In case the spectrum is curved, only the spectral index measured below the break frequency, is given. [(b)] Observed spatial scatter in the spectral index.

4.5.1 Spectral properties of the halo

The integrated spectrum of the radio halo in Abell 2256 is classified as ultra-steep and shows no indication of curvature (Figs. 4.5, 4.6). It is one of the few radio halos that are detected over a large frequency range, with other examples being the Bullet cluster (Liang et al., 2000; Shimwell et al., 2014; Sikhosana et al., 2023), the Toothbrush cluster (van Weeren et al., 2012a; de Gasperin et al., 2020), Abell 2744 (Pearce et al., 2017), Abell S1063 (Xie et al., 2020), Coma (Bonafede et al., 2022) and MACS J0717.5+3745 (Rajpurohit et al., 2021a). We compiled the properties of these clusters in Table 4.3. It is interesting that the first three of these other radio halos do not show any indication of spectral curvature, with relatively flat spectra $\alpha < -1.3$ up to GHz frequencies, while the last three halos do show spectral

curvature, resulting in ultra-steep spectra ($\alpha < -1.5$), at frequencies above ~ 1 GHz. Abell 2256 thus presents a unique radio halo with an ultra-steep spectrum up to GHz frequencies, without spectral curvature.

Simple homogeneous turbulent re-acceleration models, with constant magnetic field and acceleration rate throughout the volume, have been successful in reproducing the observed counts and redshift distribution of radio halos in statistical samples (Cassano et al., 2023). In such models, ultra-steep spectra are expected above a cut-off frequency that scales with the acceleration efficiency in the ICM, which depends on the energetics (e.g. mass and mass ratio) of the merger (Cassano & Brunetti, 2005; Cassano et al., 2006b). It is therefore interesting that the integrated spectrum of the radio halo in Abell 2256 shows no curvature, while it is ultra-steep.

Variations in the magnetic field, turbulent energy and resulting acceleration efficiency throughout the emitting volume may complicate the apparent spectral behaviour. The superimposition of different regions can stretch the spectrum and generate a quasi-power-law spectrum when integrated over the full halo region. This effect has been observed in simulations (e.g. Donnert et al., 2013), although they are limited in resolution and do not capture the full complexity of the dynamics of the ICM and CRs. The observed significant curvature and spectral index variations across the radio halo volume (e.g. Fig. 4.7), which were also observed at higher frequencies (Rajpurohit et al., 2023), point to an inhomogeneous situation in the Abell 2256 halo volume. In such a scenario, the steep spectral slope measured for Abell 2256 implies that a significant fraction of the emission in the halo volume is generated at low frequencies, where the acceleration time is shorter than the cooling time.

The intrinsic 2D scatter of the spectral index can be estimated as $\sigma_{\rm 2D} = \sqrt{\sigma^2_{\rm obs} - \sigma^2_{\rm rms}}$, where $\sigma^2_{\rm obs}$ is the total observed scatter, and $\sigma^2_{\rm rms}$ is the scatter expected from the flux density uncertainties. Values of $\sigma_{\rm 2D}$ of 0.14 and 0.24 are obtained for the scatter measured between $46-144$ and $23-46$ MHz, respectively. These variations are found to be quite large with respect to the other non-curved radio halo in the Toothbrush cluster ($\sigma_{\rm 2D} < 0.04$; van Weeren et al., 2016a), as listed in Table 4.3. However, the variations are of the same magnitude and spatial scale as those observed in MACS J0717.5+3745 ($\sigma_{\rm 2D} \approx 0.3$ Rajpurohit et al., 2021a), where an inhomogeneous situation was also proposed. Furthermore, Table 4.3 indicates that MACS J0717.5+3745 has the steepest spectrum below the break frequency, implying that the level of inhomogeneity might be correlated with the steepness of the radio spectrum. It is also noteworthy that Abell 2256 is the least massive galaxy cluster in this sample, which implies that it has a smaller turbulent energy budget and will preferentially emit lower frequency radiation. However, this sample of clusters with radio halos detected over a large frequency range is small and the selection is not unbiased, thus additional data are required to draw definite conclusions.

An inhomogeneous turbulent scenario has also been explored in the case of radio bridges, where theoretical models based on second-order Fermi re-acceleration predict that the fraction of the synchrotron emitting volume increases at lower frequencies (Brunetti & Vazza, 2020). The spectrum of radio bridges is not well known over large frequency ranges due to their low surface brightness, but the conditions for generating synchrotron emission in the volume (i.e. the acceleration time is smaller or equal to the cooling time) are more likely to be matched at lower emitting frequencies. However, it is still an open

question how this process would result in a straight power-law for the integrated spectrum. Thus, explaining the combination of inhomogeneity in the halo volume and the perfect integrated power-law over multiple orders of magnitude in frequency as observed in Abell 2256 requires further theoretical studies.

4.5.2 Testing a hadronic origin

The radio halo in Abell 2256 is the nearest one in the universe that shows an ultra-steep spectrum below GHz frequencies. It is therefore one of the best candidates to put constraints on hadronic models from the combination of gamma-ray and radio data, as such a steep spectrum requires a large energy budget of cosmic ray protons which should result in observable gamma-ray emission. In Section 4.4.2, we have shown that secondary models may explain the levels of radio and gamma-ray emission in Abell 2256 only in the case that $B_0 > 17\mu$G. This is significantly higher than typical magnetic field values of $B_0 < 10\mu$G estimated from Faraday rotation measurements in clusters (e.g. Bonafede et al., 2010; Vacca et al., 2012; Govoni et al., 2017; Osinga et al., 2022). In fact, such strong magnetic fields are also unlikely for energetic reasons, since it would imply a magnetic pressure in the ICM that is $\geq 19\%$ of the thermal pressure, and a total non-thermal pressure (i.e. magnetic + CR) of the same order as the thermal pressure at $r = R_{500}$. This is significantly higher than the non-thermal pressure found observationally from the combination of X-ray and SZ observations (Eckert et al., 2019). Thus, in practice, assuming a hadronic origin of the halo, the combination of our LOFAR and gamma-ray data requires an untenable energy budget due to the combination of steep spectrum and flat radio brightness profile of the radio halo. We conclude that the purely hadronic model cannot explain the radio halo in Abell 2256.

This conclusion is quite robust, because of the conservative assumptions made in Section 4.4.2. Firstly, we limit the integration of the gamma-ray emission at $r = R_{500}$. The required energy budget for the non-thermal components would be even larger with a larger aperture radius. Secondly, similar to the case of the Coma cluster (e.g. Brunetti et al., 2012, 2017), a flatter profile of the magnetic field would help reduce the energy budget of cosmic ray protons, but would not solve the tension because the magnetic field in the outskirts would become a dominant source of pressure.

Additionally, we note that our models for the gamma-ray emission in Abell 2256 did not consider other possible sources of cosmic-ray protons. Shock (re)accelerated electrons that generate the bright radio shock in Abell 2256 may also generate gamma-rays via inverse Compton scattering off the CMB, provided that TeV electrons are accelerated at the shock. Additionally, protons should also be accelerated by the shock front, but the acceleration efficiency of cosmic ray protons at ICM shocks is poorly constrained (e.g. Vazza et al., 2015), making it difficult to include this in our models. In any case, this implies that the central magnetic field strength would need to be even higher than $B_0 = 21\mu$G to explain the non-detection of gamma rays, which we have argued cannot be the case due to energetic reasons. In fact, our models are also conservative due to the fact that the radio halo was significantly brighter (factor 2) in images without a 100λ uv cut, but we employed this cut to make a fair comparison between different frequencies. We note, however, that gamma-ray observations do not suffer from resolving out large-scale emission like radio observations do.

In the turbulent re-acceleration scenario, a mildly relativistic 'seed' population of

electrons is re-accelerated by turbulence, which produces the radio halo (Brunetti & Blasi, 2005; Brunetti & Lazarian, 2011; Pinzke et al., 2017; Nishiwaki & Asano, 2022). The origin of the seed electrons is still unconstrained, and hadronic interactions might produce the seeds for re-acceleration (e.g. Nishiwaki & Asano, 2022). Jointly modelling the seed population from hadronic interactions at a level consistent with the upper limits presented here and the re-acceleration of those seed particles through turbulent magneto-hydrodynamics can address this problem, although such modelling is beyond the scope of the current work. We can however make a qualitative assessment of this model. In the turbulent scenario, the emission is generated with a ratio of radio to gamma-rays that is typically a factor $3-10$ smaller than that in the case of purely hadronic models, thus allowing an energy budget of CRps that is up to one order of magnitude smaller than in the purely hadronic case. Current gamma-ray limits constrain the energy budget of the CRp (and magnetic field) to a level that is several times smaller than that obtained in Section 4.4.2. If the radio halo is indeed generated by turbulent re-acceleration, Brunetti et al. (2009) predicted that a gamma-ray detection would only be possible in the case that $B_0 < 1\,\mu$G. The non-detection is thus consistent with typical magnetic field strengths between $1-10\,\mu$G that are observed in clusters from Faraday rotation experiments (e.g. Osinga et al., 2022). The current Fermi-LAT limits do not rule out re-acceleration of secondary particles for the origin of the halo in Abell 2256, as was also concluded for the Coma cluster (Brunetti et al., 2017; Adam et al., 2021).

4.5.3 Diffusive shock acceleration in the radio shock

The diffusive shock acceleration (DSA) of fossil electrons is the most promising model for radio shocks in clusters (e.g. Pinzke et al., 2013; Vazza et al., 2015, 2016; Kang & Ryu, 2016). According to DSA, the integrated spectral index of radio shocks cannot be flatter than $\alpha = -1.0$. However, this constraint was violated in the radio shock in Abell 2256 with early LOFAR observations at low frequency, where a radio shock spectral index value of -0.85±0.01 was found (van Weeren et al., 2012a).

In this work, we found that the low-frequency spectral index of $\alpha_{23}^{146} = -0.87 \pm 0.11$ does agree with DSA within the error margins. When combining our data with higher frequency data up to 3 GHz, we obtained a consistent value of $\alpha_{23}^{3000} = -1.00 \pm 0.02$. This implies that the integrated spectrum for the radio shock is a simple power-law up to the lowest frequencies, without any low-frequency flattening of the spectrum.

Similar to other radio shocks that are mapped over wide frequency ranges, such as the Toothbrush and Sausage radio shock (Rajpurohit et al., 2020; Loi et al., 2020), our findings suggest that there is no deviation from a power-law over multiple orders of magnitude, indicating no inconsistency with the standard DSA scenario in Abell 2256. The radio shock interpretation is also consistent with the X-ray detection of a nearby shock in Abell 2256 by Ge et al. (2020). However, while the DSA interpretation seems to be supported by observations, some problems remain to be understood. In the case of standard DSA, an integrated spectrum with a spectral index close to $\alpha = -1$ requires a large Mach number (Blandford & Eichler, 1987), which is inconsistent with what has been measured for the Mach number of the X-ray detected shock in Abell 2256 (SF1 in Ge et al., 2020). This might be resolved by considering that the radio shock region consists of an ensemble of shocks, and the radio and X-ray observations trace different parts of this distribution, with

projection effects also playing a significant role (e.g. Wittor et al., 2021).

4.5.4 Origin of AGN related sources

The physical interpretation and age estimation of the various smaller ultra-steep spectrum sources in Abell 2256 have been complicated by the inability of previous studies to fit their spectra with simple synchrotron models, due to the strong curvature implying low break frequencies (e.g. Brentjens, 2008; van Weeren et al., 2012b; Owen et al., 2014). The new ultra-low frequency data show that we can now observe many of the radio source spectra flatten towards lower frequencies (Fig. 4.11).

The question of whether the F-complex should be considered a radio shock was raised by Owen et al. (2014), because of its steep spectrum, polarisation and elongated structure. However, unlike the large radio shock of Abell 2256, the spectrum of this source is strongly curved, resembling a typical aged AGN spectrum. As raised already by Bridle et al. (1979), sources F1 and F2 might all be part of the tail of source F3. We propose that sources F2 and F1 are related to the Fabricant Galaxy 122 (FG122) at the location of F3. The synchrotron modelling implied that the radiative age of the sources is approximately 200 Myr, which is consistent with the time it would take FG122 to travel the distance between its current location and the location of the F complex, given the typical velocity dispersion in the cluster (Brentjens, 2008). If the magnetic field strength is lower than our assumed 7μG (Brentjens, 2008), then the age estimates would increase further and this picture would remain consistent with observations, unless the magnetic field is significantly weaker than $B = 1.8\mu$G, in which case inverse Compton losses would quickly dominate. Furthermore, we observe no spectral index gradient across sources F1 to F3 in the low-frequency spectral index map (Fig. 4.4), which is expected in the standard spectral ageing scenario (e.g. Myers & Spangler, 1985), for a constant magnetic field when observing sources below the break frequency.

Interestingly, a new source was detected below the F complex which complicates the scenario once more. We have named this source F4. The spectrum of F4 remains curved below 100 MHz, with a spectral index of $\alpha_{23}^{144} = -1.9 \pm 0.1$, indicating that we have not yet found the break frequency of this source, but constrain it to be < 23 MHz. Whether the source is physically related to the F1-F3 complex is difficult to say. However, the sudden steepening in the spatial spectrum, with no gradient in the spectral index map between F2 and F4 makes a physical relation unlikely. Multiple cluster members are located in the region co-spatial with F4, so an optical association is difficult to make correctly, given the diffuse morphology of the source. However, the morphology of the radio emission and the spectral index map shown in Figure 4.10 indicate a possible host galaxy (MCG+13-12-020). Given the steep spectrum of the source at such low frequencies, it is likely that source F4 is a very old remnant radio galaxy with an age of > 400 Myr. The dense and turbulent intracluster medium possibly quenched the expansion of source F4, limiting adiabatic losses and allowing the low-frequency detection of such an old source (Murgia et al., 2011).

The source AG+AH is located at approximately 800 kpc from the head of the tailed source C and shows a curved spectrum where $\alpha_{144}^{351} = -2.05$ (van Weeren et al., 2012b) while we observe $\alpha_{23}^{144} = -0.91 \pm 0.07$. In previous LOFAR observations, van Weeren et al. (2012b) noted that if the break frequency of the spectrum is below 50 MHz, the radiative age of the source would be old enough to link it to source C. However, we observed the break

frequency at 113 ± 12 MHz, implying AG+AH can only be related if the fossil plasma is re-accelerated. Processes such as the gentle re-energisation process (e.g. de Gasperin et al., 2017) or a shock wave that is also responsible for the radio shock can increase the age of the source substantially, (e.g. Kale & Dwarakanath, 2012), allowing a physical relation between the sources. Such processes could also explain the filamentary 'ribs' coming off the radio source, which are likely caused by complex interactions of the fossil plasma with the environment (Rudnick et al., 2021). Interestingly, like the first ribbed source detected in Abell 3266, AG+AH is also related to an apparently one-sided tail. There are multiple sources now found in clusters that show such one-sided tails with such rib-like features, including IC1711 in Abell 1314 (Wilber et al., 2018), and SDSS J105851.01+564308.5 in Abell 1132 (Wilber et al., 2019). These observations may provide insights into the origin of these phenomena.

Finally, source AI was discovered by van Weeren et al. (2009), where it was suggested to be either a radio shock or a radio phoenix. It was recently classified as a radio phoenix based on the morphology, location and curved spectrum by (Rajpurohit et al., 2023). This is corroborated by the ultra-low frequency results here, where the spectrum indeed approaches a typical AGN spectrum with $\alpha_{23}^{46} = -1.18$ which significantly steepens towards higher frequencies.

4.6 Conclusion

We have investigated particle acceleration in Abell 2256 by studying the lowest energy electrons observable by ground-based telescopes. This study presented the first high-quality LOFAR observations down to 16 MHz of Abell 2256, proving the potential for new cluster science with LOFAR ultra-low frequency observations. The radio halo, radio shock, and most prominent fossil plasma sources in Abell 2256 were all detected clearly at 144, 46 and 23 MHz. The ultra-low frequency data paint a consistent picture with respect to what was found at higher frequencies, where both the radio halo and radio shock show straight power-law spectra over multiple orders of frequency, while the fossil plasma sources show relatively flat spectra at low frequencies that can curve extremely towards higher frequencies. This dichotomy, where spectral shapes are powerfully distinguished, that starts to show at low frequencies could help in the classification of diffuse cluster sources, which is becoming increasingly challenging as cluster radio emission is more ubiquitously detected.

We summarise the main results of this work as follows:

1. The combination of low-frequency radio and gamma-ray data places some of the strongest direct constraints on the purely hadronic model for radio halos. The data are only consistent with the purely hadronic model for central magnetic field strengths $> 17\,\mu$G, which are improbably high given non-thermal pressure and magnetic field constraints that exist for comparable clusters. This is only the second cluster for which such a direct constraint was produced, with the only other cluster being the Coma cluster, where data also disfavours a purely hadronic model.

2. The sensitive LOFAR HBA image shows that the radio halo has a largest linear size of 24 arcminutes at 144 MHz, corresponding to a linear size of 1.6 Mpc at the cluster redshift. This is larger than previously measured.

3. The integrated radio halo spectrum follows a straight power-law with a spectral index of -1.56 ± 0.02 over a wide frequency range from 24 to 1500 MHz. The core region emits flatter spectrum emission ($\alpha = -1.36$) than the overall radio halo, and the wedge arc between the radio shock and the F-complex shows somewhat steeper emission.

4. Although the integrated spectrum follows a straight power-law, we found significant spatial variations in the spectral index and curvature across the radio halo on the order of $\sigma(\alpha_{2D}) = 0.2$. This implies that the emitting volume is strongly inhomogeneous, which is difficult to reconcile with the perfect power-law of the integrated spectrum by current theories.

5. The radio shock spectrum also agrees with a straight power-law, but is significantly flatter than the radio halo, with $\alpha = -1.00 \pm 0.02$ between 24 and 3000 MHz. The spectral index map at low frequencies also shows steepening from the southwest side to the northeast side, indicating the direction of the shock as electrons age in the downstream region.

6. Abell 2256 hosts six complex radio sources with mostly curved spectra, of which five were known previously. We have detected a new ultra-steep spectrum source just below the F-complex, which we have named F4. While we see the spectra of the other complex radio sources flatten significantly towards 23 MHz, F4 still shows an ultra-steep spectral index of $\alpha_{23}^{144} = -1.9 \pm 0.1$, and we suspect it is unrelated to sources F1-F3 based on the sudden discontinuity in the spectral index map.

7. We have modelled the synchrotron emission of these complex radio sources, finding typically curved spectra that agree well with simple ageing models, and finding radiative ages around 200 Myr. These findings are consistent with the interpretation that these are fossil plasma sources.

Most of the understanding about the origin and formation of diffuse radio emission in clusters has been derived from studies of relatively massive galaxy clusters that could be detected at GHz frequencies. However, turbulent re-acceleration models predict that an increasing fraction of halos in lower mass clusters should have a steep spectrum (e.g. Cassano et al., 2010c), implying they are missed at high frequencies. To constrain model parameters, a large lever arm is needed for precise spectral index determination. Observations down to about 16 MHz can provide a similar lever arm when combined with ~ 150 MHz to the lever arm historically used by combining 150 and 1500 MHz observations. The successful observations made in the lowest radio window available to ground-based telescopes thus open up exciting possibilities for future research on particle acceleration mechanisms in clusters.

ACKNOWLEDGEMENTS

EO and RJvW acknowledge support from the VIDI research programme with project number 639.042.729, which is financed by the Netherlands Organisation for Scientific Research (NWO). FdG acknowledges the support of the ERC CoG grant number 101086378 LOFAR (van Haarlem et al., 2013) is the Low-Frequency Array designed and constructed by ASTRON. It has observing, data processing, and data storage facilities in several countries, which

are owned by various parties (each with their own funding sources), and that are collectively operated by the ILT foundation under a joint scientific policy. The ILT resources have benefited from the following recent major funding sources: CNRS-INSU, Observatoire de Paris and Université d'Orléans, France; BMBF, MIWF-NRW MPG, Germany; Science Foundation Ireland (SFI), Department of Business, Enterprise and Innovation (DBEI), Ireland; NWO, The Netherlands; The Science and Technology Facilities Council, UK; Ministry of Science and Higher Education, Poland; The Istituto Nazionale di Astrofisica (INAF), Italy. This research made use of the LOFAR-UK computing facility located at the University of Hertfordshire and supported by STFC [ST/P000096/1], and of the LOFAR-IT computing infrastructure supported and operated by INAF, and by the Physics Dept. of Turin University (under the agreement with Consorzio Interuniversitario per la Fisica Spaziale) at the C3S Supercomputing Centre, Italy. We thank the staff of the GMRT that made TGSS possible. GMRT is run by the National Centre for Radio Astrophysics of the Tata Institute of Fundamental Research. EO thanks Jonah Wagenveld and Roland Timmerman for supplying useful Python scripts and the Istituto di Radioastronomia at CRN Bologna for the hospitality during the spring of 2022, where helpful discussions took place.

Appendix I: Flux measurements and decametre sky field-of view

To verify the flux density scale of the LOFAR LBA and HBA images in the direction of Abell 2256, we have compared our data with deep upgraded Giant Metrewave Radio Telescope (uGMRT) data at 675 MHz from Rajpurohit et al. (2022c). We have identified eight compact bright sources around Abell 2256 which are visible in the LOFAR 24 MHz, 46 MHz, HBA and uGMRT images. The 24 MHz flux was calculated in a 90-arcsecond resolution map to make sure all flux was captured for point sources which may still suffer from residual ionospheric errors. We decided not to compare to ancillary VLA 1-4 GHz data, as the field of view of those data is too small to make comparisons for many sources around Abell 2256. The results are shown in Figure 4.15, where the HBA flux is corrected by a scaling factor of 0.83, and the LBA flux is not adjusted. The results show that the fluxes are in line with simple polynomial fits in log space to the data, implying that there is no significant bias in the flux density scale.

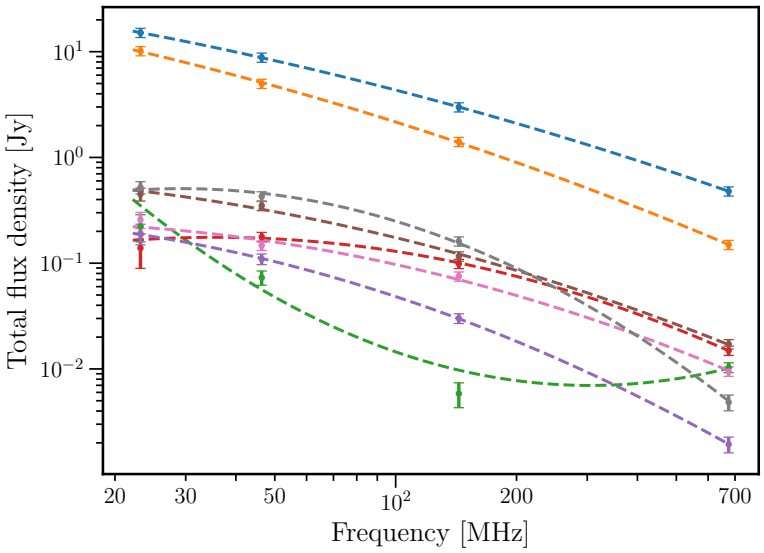

Figure 4.15: Flux density measurements at LOFAR LBA, HBA and uGMRT (675 MHz) frequencies with a best-fit polynomial in logspace shown. Most error bars are dominated by the assumed 10% absolute flux density scale error.

For completeness, the flux measurements of the radio halo and radio shock regions defined in Sections 4.3.1 and 4.3.2 are given in Table 4.4. The full field of view of the LBA observations in the 16-30 MHz range is shown in Figure 4.16.

Table 4.4: Flux density measurements and best-fit spectral index of the radio halo and radio shock regions as measured in Figures 4.5 and 4.8.

Source	$S_{23\mathrm{MHz}}$ [Jy]	$S_{46\mathrm{MHz}}$ [Jy]	$S_{144\mathrm{MHz}}$ [Jy]	α
Halo	12.72±1.38	4.79±0.52	0.91±0.11	-1.44±0.08
Wedge arc	2.69±0.27	0.94±0.10	0.15±0.02	-1.57±0.08
Halo core[a]	1.70±0.17	0.66±0.07	0.14±0.01	-1.36±0.08
Halo total	15.41±1.40	5.73±0.53	1.06±0.11	-1.46±0.07
Shock R1	2.00±0.21	0.92±0.10	0.28±0.03	-1.08±0.08
Shock R2	5.75±0.58	3.18±0.32	1.25±0.13	-0.83±0.08
Shock R3	9.79±1.00	5.65±0.58	2.16±0.22	-0.83±0.08
Shock total	18.73±1.35	10.19±0.74	3.78±0.28	-0.87±0.05

Notes. [(a)] We note that the 'halo core' region is a subset of the 'halo' region

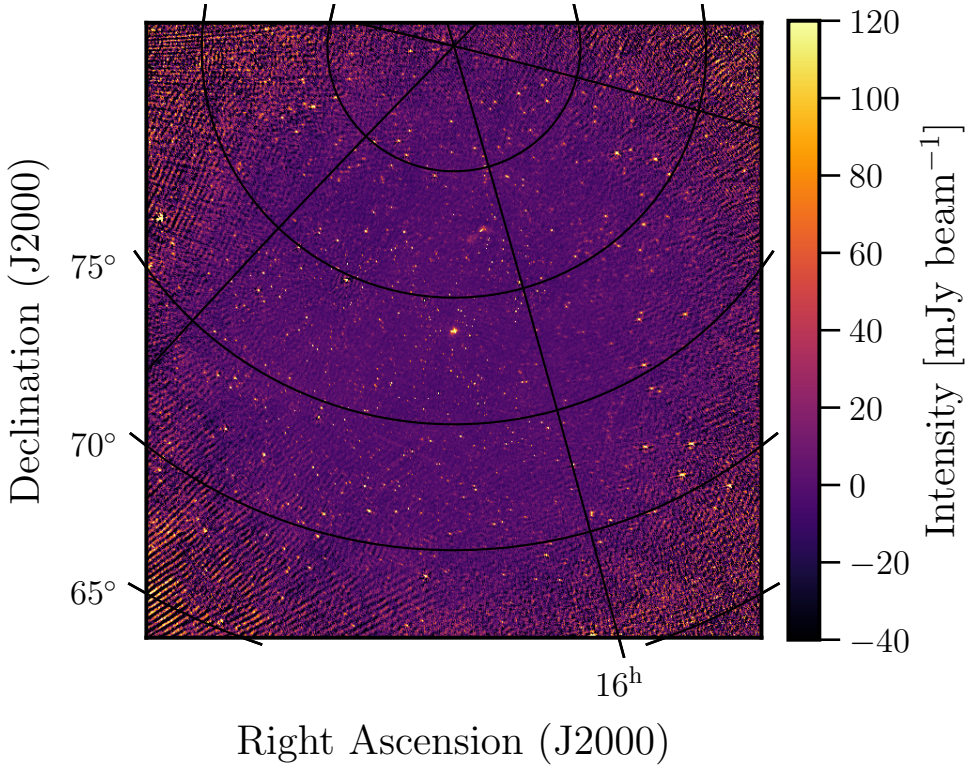

Figure 4.16: Full field-of-view image of the decametre sky from the LBA observations between 16-30 MHz. This image covers about 200 deg^2 and is centred on Abell 2256. The primary beam half-power beam-width is ~9 degrees at 30 MHz and the restoring beam is $39'' \times 24''$.

Appendix II: Uncertainty maps

We show in Figures 4.17 and 4.18 the uncertainty maps for the spectral index and spectral curvature respectively. The uncertainty on the spectral index was calculated as

$$\Delta\alpha = \frac{1}{\ln(\nu_1/\nu_2)}\left[\left(\frac{\Delta S_1}{S_1}\right)^2 + \left(\frac{\Delta S_2}{S_2}\right)^2\right] \tag{4.12}$$

where ν refers to the frequency of the observation, S to the corresponding observed flux, and ΔS to the uncertainty on the flux. The uncertainty on the curvature map was computed from the uncertainties on the spectral index maps using standard error propagation.

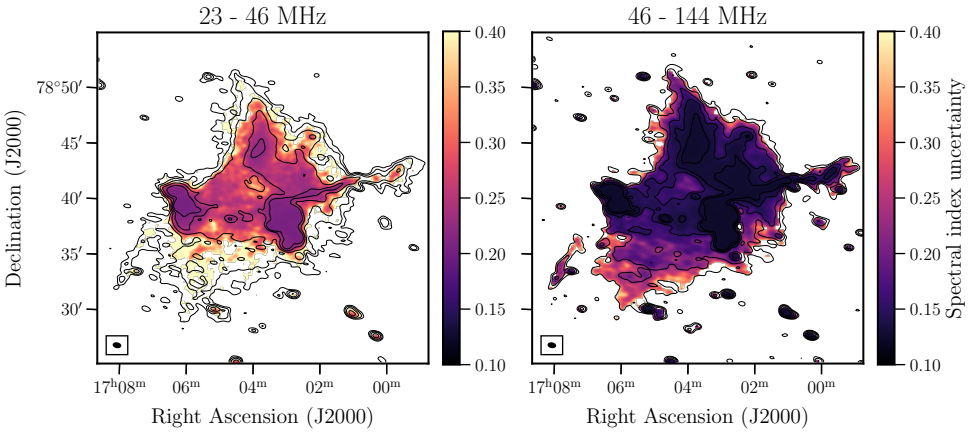

Figure 4.17: Spectral index uncertainty maps of Abell 2256 at different frequencies with the restoring beam shown in the bottom left inset. Both maps have been smoothed to a common resolution of $39'' \times 24''$. The median uncertainties are 0.31 and 0.19 in the left and right image, respectively. The contours show higher frequency [3, 6, 12, 24, 48]σ levels where σ denotes the background rms noise level.

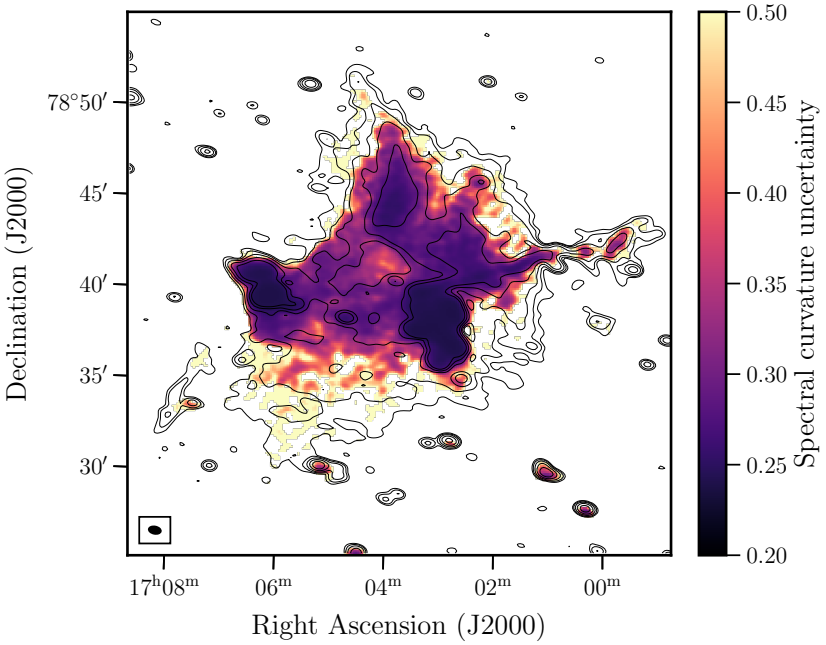

Figure 4.18: Curvature uncertainty map of Abell 2256 with the restoring beam of $39'' \times 24''$ shown in the bottom left inset. The median uncertainty is 0.33. The contours show 144 MHz frequency [3, 6, 12, 24, 48]σ levels where σ denotes the background rms noise level.

Appendix III: Halo fitting

Figure 4.19 shows the results of the Halo-Flux Density CAlculator (Halo-FDCA; Boxelaar et al., 2021), a Markov-chain Monte Carlo code that fits a simple surface brightness model,

$$I(r) = I_0 \exp(-r/r_e), \tag{4.13}$$

to a radio halo. We have indicated the region used for the fitting, and the regions used to mask the compact AGNs in the leftmost panel. The resulting best-fit parameters are given in Table 4.5.

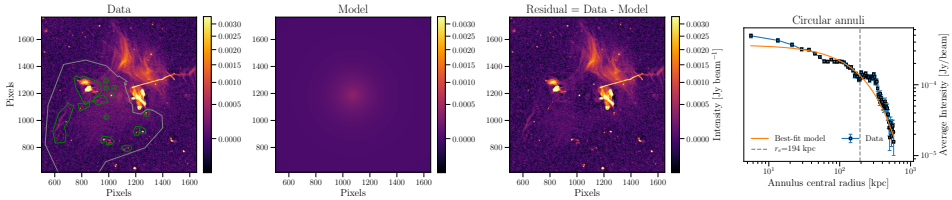

(a) 144 MHz

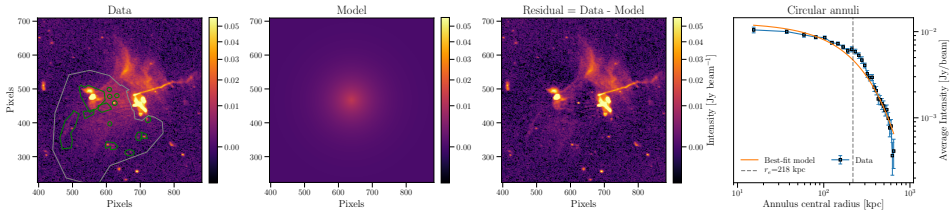

(b) 46 MHz

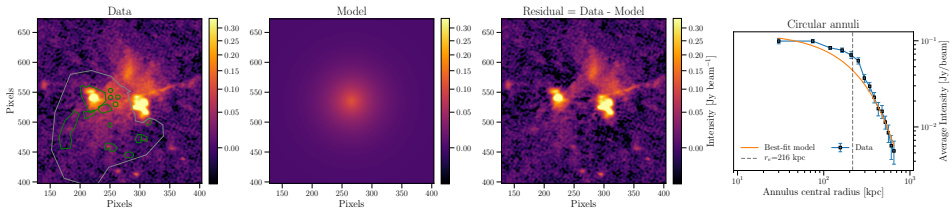

(c) 23 MHz

Figure 4.19: Halo fit results for various frequencies. The first panel shows the data, with masked sources indicated by the green regions and the fitting region indicated by the grey region. The second panel shows the best-fit halo model (Eq. 4.13) and the third panel the residual image. The last panel shows the same fit visualised in one dimension calculated from concentric annuli.

Table 4.5: Results of the 2D halo-fitting. The uncertainties indicate statistical uncertainties only, computed from the 16th and 84th percentile of the Markov chain.

Frequency [MHz]	I_0 [Jy arcsec^{-2}]	RA [deg]	DEC [deg]	r_e [kpc]	χ^2_{red}
144	$(9.878 \pm 0.007) \times 10^{-6}$	-103.9181 ± 0.0002	78.64251 ± 0.00003	193.6 ± 0.1	1.1
46	$(4.574 \pm 0.004) \times 10^{-5}$	-103.8822 ± 0.0003	78.64905 ± 0.00004	218.2 ± 0.2	1.5
23	$(1.130 \pm 0.001) \times 10^{-4}$	-103.8626 ± 0.0002	78.64970 ± 0.00004	216.1 ± 0.2	3.7

5

The detection of cluster magnetic fields via radio source depolarisation

It has been well-established that galaxy clusters have magnetic fields. The exact properties and origin of these magnetic fields are still uncertain even though these fields play a key role in many astrophysical processes. Various attempts have been made to derive the magnetic field strength and structure of nearby galaxy clusters using Faraday rotation of extended cluster radio sources. This approach needs to make various assumptions that could be circumvented when using background radio sources. However, because the number of polarised radio sources behind clusters is low, at the moment such a study can only be done statistically. In this chapter, we investigate the depolarisation of radio sources inside and behind clusters in a sample of 124 massive clusters at $z < 0.35$ observed with the Karl G. Jansky Very Large Array. We detect a clear depolarisation trend with the cluster impact parameter, with sources at smaller projected distances to the cluster centre showing more depolarisation. By combining the radio observations with ancillary X-ray data from Chandra, we compare the observed depolarisation with expectations from cluster magnetic field models using individual cluster density profiles. The best-fitting models have a central magnetic field strength of $5-10\,\mu G$ with power-law indices between $n = 1$ and $n = 4$. We find no strong difference in the depolarisation trend between sources embedded in clusters and background sources located at similar projected radii, although the central region of clusters is still poorly probed by background sources. Our findings show that the statistical depolarisation of radio sources is a good probe of cluster magnetic field parameters. Cluster members can be used for this purpose as well as background sources because the local interaction between the radio galaxies and the intracluster medium does not strongly affect the observed depolarisation trend.

Based on Osinga et al. (2022): *E. Osinga, R. J. van Weeren, F. Andrade-Santos, L. Rudnick, A. Bonafede, T. Clarke, K. Duncan, S. Giacintucci, Tony Mroczkowski, H. J. A. Röttgering, A&A, 665, A71 (2022)*

5.1 Introduction

Through observations of diffuse synchrotron emission such as radio halos (e.g. van Weeren et al., 2019, for a recent review) and Faraday rotation measures (RMs) of polarised radio sources (e.g. Akahori et al., 2018, for a recent review), it has been proven that galaxy clusters have magnetic fields. These fields play a key role in many astrophysical processes such as heat conduction, gas mixing, and cosmic ray propagation, but the exact properties and origin of these magnetic fields are still uncertain (see Carilli & Taylor, 2002; Donnert et al., 2018, for reviews on magnetic fields in galaxy clusters). Estimates of the magnetic field strength from observations of diffuse synchrotron emission (i.e. radio halos) place the magnetic field strengths of galaxy clusters around the μG level (Ferrari et al., 2008). Recently, observations of high-redshift radio halos have revealed that clusters at $z > 0.6$ might have similar magnetic field strengths to local galaxy clusters (Di Gennaro et al., 2021a), implying that magnetic field amplification should happen fast during cluster formation. However, estimates of the magnetic field strength from diffuse synchrotron emission require various assumptions as to the energy spectrum and distribution of relativistic particles (e.g. equipartition or minimum energy; Beck & Krause, 2005).

The most promising method to derive magnetic field properties in clusters is through Faraday rotation of polarised radio emission (see Govoni & Feretti, 2004, for a review). Various studies have constrained the magnetic field strength and structure of nearby galaxy clusters using the RM of extended radio sources (e.g. Murgia et al., 2004; Govoni et al., 2006; Guidetti et al., 2008; Laing et al., 2008; Bonafede et al., 2010; Guidetti et al., 2010; Vacca et al., 2012; Govoni et al., 2017). These studies have found central magnetic field strengths of the order of 1-10 μG, and a magnetic field power spectrum index between $n = 2$ and $n = 4$.

The depolarising effect of Faraday rotation can also be used to constrain magnetic field properties (e.g. Taylor et al., 2006; Bonafede et al., 2011; O'Sullivan et al., 2019; Stuardi et al., 2020; Sebokolodi et al., 2020; Di Gennaro et al., 2021c; de Gasperin et al., 2022; Rajpurohit et al., 2022b). Since we observe radio sources with a finite spatial resolution, the differential Faraday rotation between different lines of sight within a single beam reduces the observed degree of polarisation. This beam depolarisation effect depends on the correlation scales of the magnetic field and the magnetic field strength. In this way, the average properties of magnetic fields in clusters can be investigated, and differences can be studied between various cluster properties, such as the presence or absence of a cool core (Bonafede et al., 2011). The advantage of using fractional polarisation over the RM of radio sources is that unpolarised sources can also be taken into account, as upper limits on the polarisation fraction can be estimated.

A drawback in most studies of Faraday rotation and the resulting depolarisation is that the polarised radio sources are often cluster members. This introduces a small uncertainty because the location of the radio sources inside the cluster cannot be determined accurately, but a larger uncertainty is introduced by the gas in the intracluster medium (ICM), whose properties are usually not known in detail. Often, it is assumed that the interaction between the ICM gas around the radio source and the radio plasma is negligible. However, it is debated to what extent this assumption is true, with some studies showing evidence for local Faraday rotation being induced in radio lobes (e.g. Rudnick & Blundell, 2003) and other studies finding no evidence for this (e.g. Ensslin et al., 2003). The ICM could be

locally compressed around cluster radio sources, causing higher densities and thus also higher depolarisation, potentially biasing results. Additionally, bent-tailed radio galaxies which are often seen in clusters might not have the same intrinsic polarisation as classic double-lobed radio galaxies (Feretti et al., 1998).

In this chapter, we aim to alleviate these problems through a study of the polarisation properties of sources inside and behind clusters. Because the number of polarised radio sources (behind clusters) is typically low (e.g. Rudnick & Owen, 2014), such a study will be most often statistical. Although polarisation properties of sources behind clusters have been investigated for some single clusters (e.g. Bonafede et al., 2010), this has not yet been studied thoroughly in a sample of clusters. This chapter focuses on the beam depolarisation effect and considers only the implications of the fractional polarisation measurements of the radio sources. In the next chapter, we extensively study the Faraday RM of the polarised sources.

Samples of galaxy clusters can be selected relatively unbiased through the thermal Sunyaev-Zel'dovich effect, which imprints a redshift-independent distortion on the spectrum of the cosmic microwave background (Sunyaev & Zeldovich, 1970, 1972). The sample we use as a starting point for this work is the Planck Early Sunyaev Zel'dovich sample (Planck Collaboration et al., 2011). This provides mass-selected samples of galaxy clusters up to high redshifts. We obtained observations with the Karl G. Jansky Very Large Array (VLA), which are detailed in Section 5.2, to study the linear polarisation properties of radio sources located inside and behind ESZ clusters. The source finding, determination of the polarisation properties, host galaxy identification and redshift estimation process is explained in Section 5.3. Theoretical depolarisation expectations are derived through modelling of the magnetic fields as Gaussian random fields in Section 5.4 and results are shown in Sections 5.5 and 5.6. Finally, we conclude with a discussion and summary in Sections 5.7 and 5.8. Possible biases are discussed in Appendix 5.8. Throughout this chapter, we assume a flat ΛCDM model with $H_0 = 70$ kms^{-1}Mpc^{-1}, $\Omega_m = 0.3$ and $\Omega_\Lambda = 0.7$. We refer to the intensity of linearly polarised light simply as the polarised intensity.

5.2 Data

5.2.1 Chandra-Planck ESZ sample

The Planck Early Sunyaev-Zel'dovich (ESZ) results presented 189 cluster candidates all-sky (Planck Collaboration et al., 2011), of which 163 clusters are at a redshift of $z < 0.35$. The Chandra-Planck Legacy Program for Massive Clusters of Galaxies[1] observed all 163 clusters with sufficient exposure time to collect at least 10,000 source counts per cluster. This makes it (one of) the largest relatively unbiased samples of galaxy clusters with high-quality X-ray data available. The Chandra observations of 147 clusters from the ESZ sample are presented in Andrade-Santos et al. (2017, 2021), where the sample has been reduced by 16 because six clusters are too close to point sources, nine clusters are classed as multiple objects and one system was too large to allow for a reliable background estimate in the Chandra field of view. High-quality X-ray data is particularly important for polarisation studies to be able to break the degeneracy between electron density and magnetic field. In

[1] http://hea-www.cfa.harvard.edu/CHANDRA_PLANCK_CLUSTERS/

this chapter, we used the thermal electron density profiles which were calculated from the fitting procedure detailed in Andrade-Santos et al. (2017).

5.2.2 Observations and data reduction

We have obtained VLA L-band (1-2 GHz) observations of 126 Planck clusters at $z < 0.35$ and DEC>-40° (VLA project code 15A-270). The redshift cut is made because the angular size of higher redshift clusters on the sky becomes too small to find a significant number of polarised background sources. Out of these 126 clusters, 102 are from the ESZ catalogue and 24 clusters are new detections in the PSZ1 (Planck Collaboration et al., 2015) and PSZ2 (Planck Collaboration et al., 2016a) catalogues that have been added to the sample. The observations were taken in the B(nA) array configuration, with the BnA configuration employed for targets located at DEC < -15° or DEC > +75° to match the resolution of targets observed in favourable declination ranges. Targets are observed for ∼ 40 minutes each. The full L-band comprises 16 spectral windows, each consisting of 64 channels before frequency averaging.

The calibration of the radio data was done using the Common Astronomy Software Application (`CASA`; McMullin et al. 2007) and proceeded in the following fashion. For each observing run, the initial data calibration was done per spectral window, such that bad spectral windows could be identified and flagged. We Hanning smoothed the spectral axis to reduce the effect of Gibbs ringing due to strong radio frequency interference (RFI) in the L-band. Shadowed antennas were flagged and the initial flagging of RFI was done with the `CASA` *TFCrop* algorithm. The effect of the elevation on the antenna gain and efficiency was calculated and antenna position corrections were applied. The flux scale was set to the Perley & Butler (2017) scale. We calculated initial-bandpass calibration solutions using a large solution interval and initially calibrated the complex gains with the central channels of the spectral window. The antenna delay terms were then calculated and applied, after which the final-bandpass solutions could be calculated. A polarised calibrator (either 3C138 or 3C286) was used to solve for a global cross-hand delay and an unpolarised calibrator (3C147) was used to calibrate on-axis polarisation leakage. Subsequently, the polarised calibrator was then used to calibrate the polarisation angle. Off-axis polarisation leakage due to a time, frequency, and polarisation-dependent primary beam becomes important as the distance from the pointing centre increases but is known to be less important in Stokes Q and U than in Stokes V (Uson & Cotton, 2008). Typically for VLA L-band observations, the leakage from Stokes I into Q and U is around 1% at the primary beam full-width half maximum (Jagannathan et al., 2017). While this effect can mimic depolarisation due to the frequency dependence of the primary beam, we do not consider it to be a major issue for this study because all clusters are observed near the pointing centre. We discuss off-axis leakage in more detail in Section 5.7.4. Finally, the antenna-based complex gain solutions were calculated using the calibrator sources, and another round of automatic flagging was performed using the `CASA` *TFcrop* and *Rflag* algorithms. All spectral windows were then combined and the resulting data were averaged to 8 MHz channels and 6-second timesteps. Leftover RFI was then flagged with the *AOflagger* (Offringa et al., 2012) and a custom strategy to flag RFI in the cross-hand correlation (rl,lr) plane was employed. Spectral window 8 was fully lost to RFI in every observing run, resulting in a total of 90 frequency channels after initial calibration.

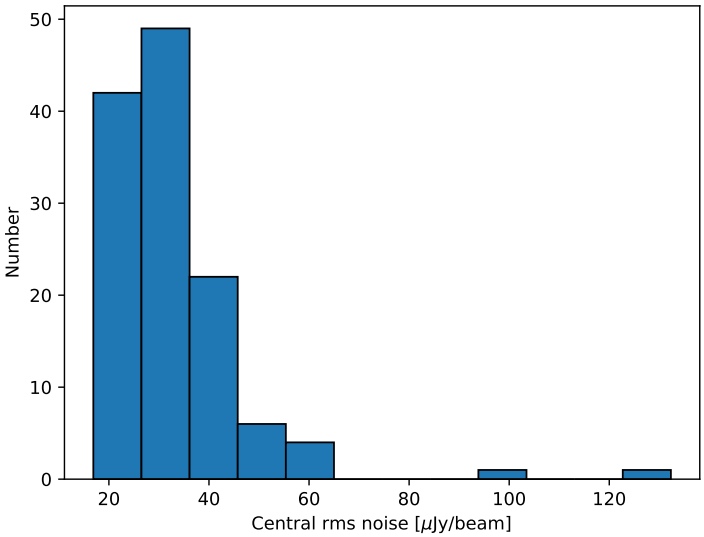

Figure 5.1: Central RMS noise in Stokes I in the 124 observed target fields.

To remove residual amplitude and phase errors in the direction of the target fields and increase the quality of the final images, we further performed six rounds of self-calibration, automatically calculating the solution interval based on the mean flux density in each field. This was done to ensure enough signal-to-noise during the calibration steps, with larger solution intervals used for fields with fainter sources. The imaging and cleaning were done using `WSclean` version 2.7.3 with the options *-join-polarizations* and *-squared-channel-joining* for Stokes Q and U imaging (Offringa et al., 2014). The six rounds of self-calibration involve three phase-only calibration rounds and three amplitude and phase rounds, decreasing the solution interval each round. For the majority of targets, this automatic self-calibration pipeline proved sufficient to obtain high-quality images of the target fields. A small number of target fields needed manual tweaking of parameters or flagging of RFI. For those clusters, one or two additional rounds of self-calibration were performed after the pipeline.

Each 8 MHz channel was corrected for the VLA primary beam attenuation, and all channels were smoothed to a circular Gaussian restoring beam at the resolution of the lowest frequency channel, to ensure that all channels have the same angular resolution. This resulted typically in a synthesised beam size of 6-7 arcseconds. The distribution of central root-mean-square (RMS) noise in the full-band Stokes I images is given in Figure 5.1. Most targets have an RMS noise of around 20-30 μJy/beam in the centre of the field. Two clusters, G033.46-48.43 and G226.17-21.91, have been removed from the sample. Calibration artefacts from a bright radio source were completely dominating the G033.46-48.43 field and during observations of G226.17-21.91 most of the data was lost to interference by a thunderstorm.

We found significant flux density variations between the spectral windows in all observations, also noted by Di Gennaro et al. (2021c), probably related to bandpass calibration or deconvolution uncertainties. To mitigate this problem as much as possible, we aligned the flux scale per observing run by fitting a simple power-law model to all bright Stokes I sources with at least a signal-to-noise ratio of 100,

$$I_\nu = I_0 \nu^\alpha, \tag{5.1}$$

where α represents the spectral index and I_ν is the Stokes I intensity. Correction factors for each spectral window were determined per observing run by averaging the correction factors of individual sources. These correction factors were usually of the order of 5-10%. The corrections were applied to the Stokes I, Q and U fluxes.

The final 124 calibrated radio images are shown as a mosaic in Figure 5.2. The five fields with RMS noise higher than 60 μJy/beam in Figure 5.1 are caused by calibration artefacts from bright sources at the edge of the fields, and in one case in the centre of the field. Direction-dependent calibration (e.g. Tasse, 2014) could improve the quality of the images affected by bright off-axis sources, but these few fields should not significantly affect the results presented here. We decided to keep all 124 fields for our analysis because even in the five fields with bright artefacts 27 polarised radio sources were still relatively unaffected by those artefacts and could be used in the analysis.

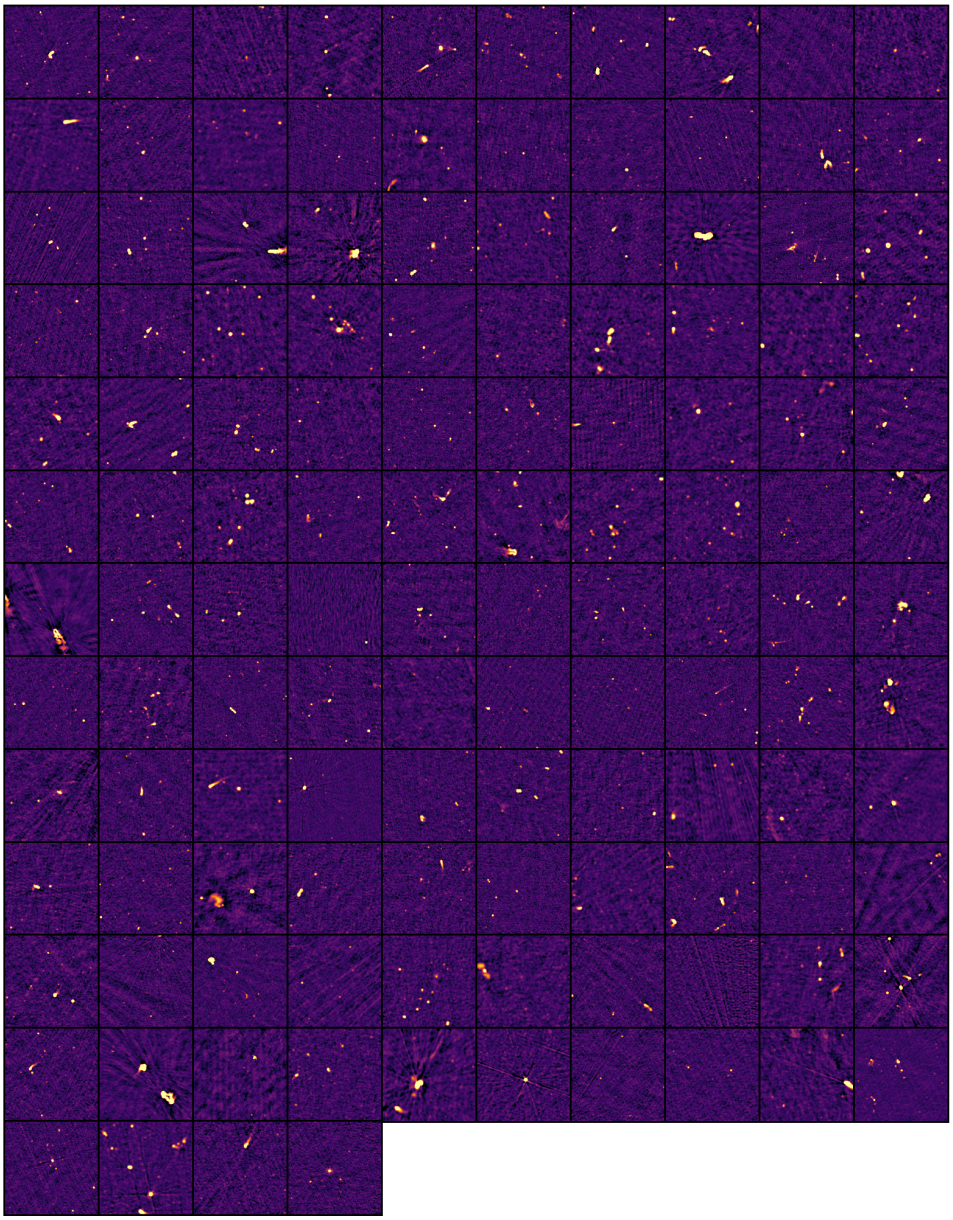

Figure 5.2: VLA 1-2 GHz primary beam corrected total intensity images of the 124 Planck clusters. The images are smoothed to the resolution of the lowest frequency channel (typically 6″) and the size is equal to the field-of-view at 2 GHz (0.35×0.35 deg^2). The colour scale is logarithmic with the scale range determined individually per cluster for visualisation purposes. The order of clusters follows the order in Table H.1, in row-major order.

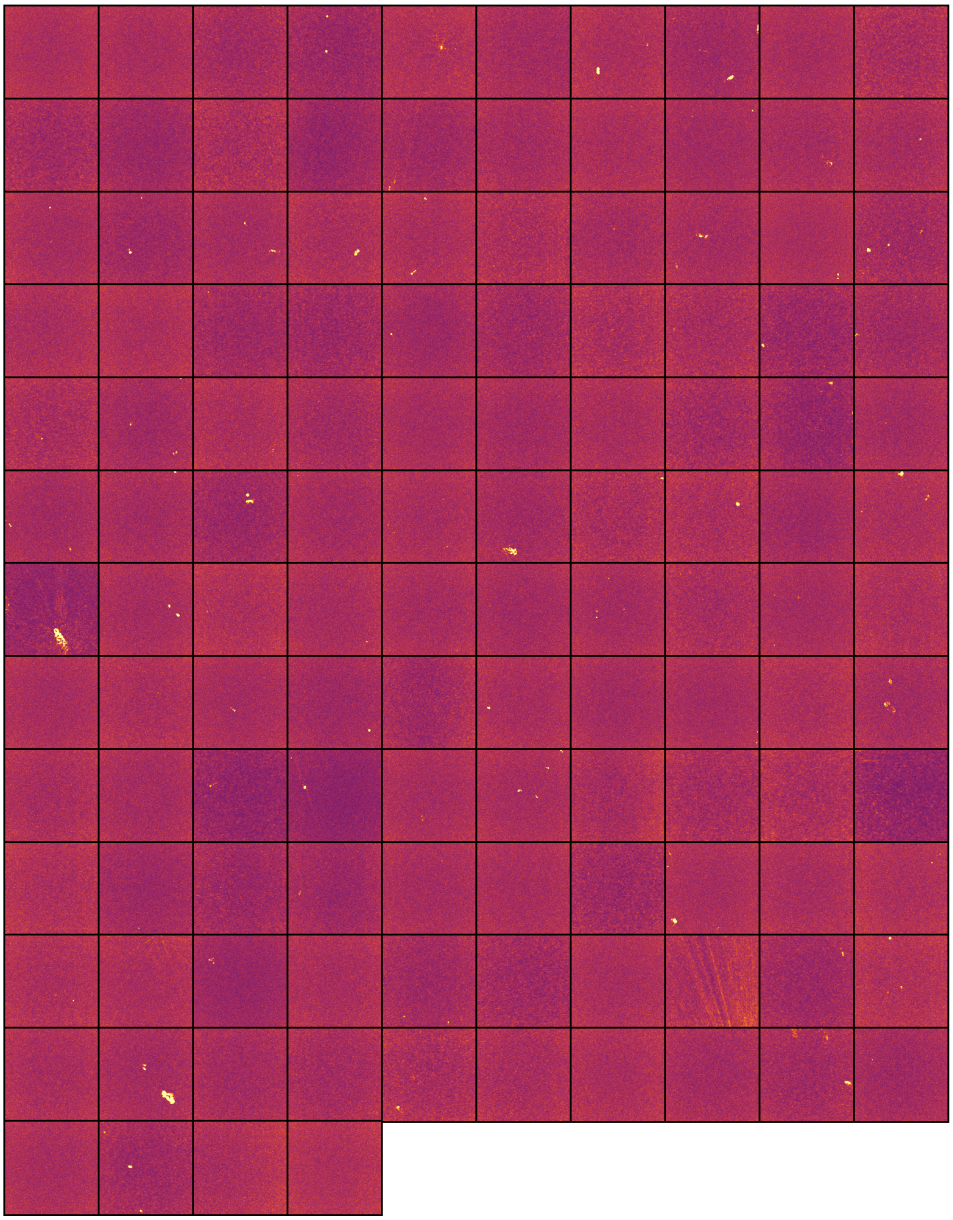

Figure 5.3: Same as Figure 5.2, but for peak polarisation intensity. The colour scale used here is `arcsinh`. We note that the calibration artefacts visible in cluster position 107 (zero-based row-major index [10,7]) were not used in the analysis, but the field was kept as two polarised sources at the edge of the primary beam were relatively unaffected by the artefacts.

5.3 Methods

This section details the source finding of both polarised and unpolarised radio sources and the determination of their polarisation properties. Thereafter, we explain the optical counterpart identification and estimation of the redshift of the sources, such that we can classify the host galaxies as background sources, cluster members or foreground sources.

5.3.1 Polarised source finding

Linear polarisation can be expressed as a complex quantity by a combination of Stokes Q and Stokes U or written as a complex vector

$$P(\lambda^2) = Q + iU = p_0 I \exp(2i\chi), \tag{5.2}$$

where λ indicates the observed wavelength, p_0 the polarisation fraction, I refers to the Stokes I intensity and

$$\chi(\lambda^2) = \frac{1}{2}\arctan\left(\frac{U}{Q}\right) \tag{5.3}$$

is the polarisation angle. Faraday rotation introduces a wavelength-dependent rotation of the polarisation angle χ. In the general case, the Faraday depth of a source is defined as (Burn, 1966; Brentjens & de Bruyn, 2005)

$$\phi(\mathbf{r}) = 0.81 \int n_e \mathbf{B} \cdot d\mathbf{r} \quad \left[\mathrm{rad\,m^{-2}}\right], \tag{5.4}$$

where n_e is the electron density in parts per cm^{-3}, $\mathbf{B}$ is the magnetic field in μGauss and d$\mathbf{r}$ the infinitesimal path length increment along the line of sight in parsecs. We adhere to the definition that $\phi(\mathbf{r}) > 0$ implies that the magnetic field is pointing towards the observer.

In the simplest case, where only one source is present along the line of sight without internal Faraday rotation, the Faraday depth ϕ is equal to the RM of a source, and the observed rotation can be expressed as

$$\chi(\lambda^2) = \chi_0 + \phi\lambda^2. \tag{5.5}$$

Faraday rotation may cause polarised sources to be undetected in the wide-band Stokes Q and U images or in the linearly polarised intensity ($\sqrt{Q^2+U^2}$) images. This is because the Stokes Q and U intensities can be both positive and negative, resulting in averaging out the frequency integrated signal if the RM is significant. To solve this problem, we used the Faraday RM-synthesis (Brentjens & de Bruyn, 2005) technique. RM-synthesis aims to approximate the Faraday dispersion function $F(\phi)$ by Fourier inversion of the following equation

$$P(\lambda^2) = \int_{-\infty}^{+\infty} F(\phi) e^{2i\phi\lambda^2} d\phi, \tag{5.6}$$

where $P(\lambda^2)$ is the complex polarised surface brightness (Eq. 5.2) as a function of the observing wavelength (squared) and ϕ is the Faraday depth of the source (Eq. 5.4). Calculating the Faraday dispersion function $F(\phi)$ essentially corresponds to de-rotating polarisation vectors to their position at an arbitrary wavelength λ_0^2. However, we note that RM-synthesis only approximates the Faraday dispersion function because we cannot sample all wavelengths.

The limitations of our frequency setup can be expressed with the three following quantities (Brentjens & de Bruyn, 2005). The maximum Faraday depth to which we have more than 50% sensitivity is given by the channel width: $\delta\lambda^2$

$$\|\phi_{max}\| \approx \frac{\sqrt{3}}{\delta\lambda^2} \approx 1200 \quad \left[\mathrm{rad\,m^{-2}}\right]. \tag{5.7}$$

The resolution in ϕ space is determined by our wavelength coverage, with the full-width half-maximum given by

$$\delta\phi \approx \frac{2\sqrt{3}}{\Delta\lambda^2} \approx 52 \quad \left[\mathrm{rad\,m^{-2}}\right]. \tag{5.8}$$

The maximum scale we can resolve in ϕ space (analogous to resolving-out extended radio sources in synthesis imaging) is given by the shortest observable wavelength

$$\text{maximum scale} \approx \frac{\pi}{\lambda^2_{min}} \approx 140 \quad \left[\mathrm{rad\,m^{-2}}\right]. \tag{5.9}$$

5

Because the resolution in ϕ space is smaller than the maximum scale we can resolve, we are technically able to detect slightly extended sources in Faraday space (i.e. Faraday thick sources). Typical values of RM found in clusters are usually of the order of 10^2 rad m^{-2}, going up to 10^3 rad m^{-2} in dense cool-core clusters (e.g. Abell 780 and Cygnus A; Taylor et al., 1990; Sebokolodi et al., 2020). Thus with the current frequency setup, we are sensitive to the typical amount of Faraday rotation in clusters.

We performed RM-synthesis using the `pyrmsynth`[2] module, weighting by the inverse RMS noise of the channels and ignoring bad channels. The result is an 'RM-cube' with two spatial axes and a Faraday depth ϕ axis, that contains the polarised intensity at each pixel location as a function of the Faraday depth, sampled from $\phi = -2000$ to $\phi = 2000$ rad m^{-2} in steps of 10 rad m^{-2}. The peak polarised intensity map is then made by taking the maximum value along the ϕ axis. The peak polarised intensity map for all clusters is shown as a mosaic in Figure 5.3.

To find polarised source candidates automatically, we used the source finder program PyBDSF (Mohan & Rafferty, 2015) on both the Stokes I images and the peak polarised intensity maps after RM-synthesis. We set the parameters `thresh_pix` = 5.0 and `thresh_isl` = 3.0, meaning that a five-sigma threshold was used for the source detection and a three-sigma threshold was used during the fitting of the total intensity source properties. The background noise was calculated over the image in a box with a size of 3 arcminutes in steps of 1 arcminute to account for the varying background noise to the primary beam.

We found that PyBDSF performed better when de-correcting the peak polarised intensity maps for the primary beam, such that an approximately flat-noise image was used for the source finding. More involved methods for polarised source finding were considered (e.g. moment analysis; Farnes et al., 2018), but our simple method was found to be sufficient given the still relatively small data size which allowed for visual inspection of the polarised source candidates. All polarised source candidates were cross-matched with sources found in the Stokes I images and source candidates that lie inside the extent of the Stokes I source

[2] `http://www.github.com/mrbell/pyrmsynth`

were retained as real polarised sources. We defined the extent of the sources in the Stokes I map as twice the full width at half maximum (FWHM) of the fitted Gaussian, which is empirically found to be a good estimate of source sizes (e.g. Hardcastle et al., 2019). This source finding process proved successful in most of the observations, but all fields were also visually inspected and some manual intervention was needed for rare cases, such as clear polarised source candidates that were positioned just outside of the extent of the source in the Stokes I map. In total, PyBDSF found 6 807 source candidates in Stokes I and 819 source candidates in polarisation over the 124 target fields.

5.3.2 Fractional polarisation measurement

To determine the polarisation properties such as the intrinsic polarisation fraction p_0 and the Faraday depth ϕ of polarised source candidates, we can model the polarised emission as

$$P(\lambda^2) = p_0 I \exp\left[2i(\chi_0 + \phi\lambda^2)\right]. \tag{5.10}$$

However, if a source emits at different Faraday depths along the same line of sight it suffers from depolarisation due to the differential Faraday rotation causing the emission from the far side of the source to be rotated more than emission from the nearby side of the source. This internal depolarisation can be modelled as (see Sokoloff et al., 1998, for details)

$$P = p_0 I \left[\frac{1-\exp(-2\Sigma_{\mathrm{RM}}^2\lambda^4)}{2\Sigma_{\mathrm{RM}}^2\lambda^4}\right] \exp[2i(\chi_0 + \phi\lambda^2)], \tag{5.11}$$

where Σ_{RM}^2 represents the amount of depolarisation. A similar effect happens because we observe the sources with a finite spatial resolution. If the magnetic field in an external Faraday screen (e.g. the ICM) changes on scales smaller than the restoring beam sources are partly depolarised by beam depolarisation. This is an external depolarisation effect and can be modelled as (see Sokoloff et al., 1998, for details)

$$P = p_0 I \exp(-2\sigma_{\mathrm{RM}}^2\lambda^4) \exp[2i(\chi_0 + \phi\lambda^2)], \tag{5.12}$$

where σ_{RM}^2 models the amount of depolarisation. Finally, if the polarisation angle rotates significantly in a single frequency channel, bandwidth depolarisation occurs. This limits the maximum observable RM, as is given in Equation 5.7.

Distinguishing between internal and external depolarisation effects can be done by measuring the spectral index of the polarised emission at lower frequencies with high resolution because external depolarisation effects are stronger at low frequencies (Arshakian & Beck, 2011). In reality, there are probably both internal and external Faraday effects at play and a combination of the models could be used to fit the data. However, for this study distinguishing exactly between polarisation mechanisms is not important, as we are only interested in the polarisation fraction trend. The internal depolarisation of radio sources should not affect the general trend and can be found from the depolarisation ratio of sources at cluster outskirts (see Sec. 5.5.) Therefore we decided to fit only the external depolarisation model given by Equation 5.12. We fitted this model to the Stokes Q and U channels simultaneously and the total intensity (Stokes I) spectrum was modelled as a simple power-law (Eq. 5.1). Fitting the Stokes I, Q and U channels directly has the advantage that we can assume Gaussian likelihoods because these channels have Gaussian

noise properties, unlike the polarised intensity maps, whose distribution is Ricean. We fitted the integrated Q and U flux densities of each polarised source candidate, where the integration was performed over the extent of the polarised source as defined in Section 5.3.1. This means that separate polarised components of the same physical source (e.g. two polarised lobes of a single radio galaxy) were treated as separate sources during fitting. The uncertainty in the integrated flux density per channel was calculated as

$$\sigma_i = \sqrt{(\sigma_{\mathrm{rms}} \times \sqrt{N})^2 + (\delta_{\mathrm{cal}} \times f_i)^2}, \tag{5.13}$$

where N is the number of beams covered by the source and σ_{rms} the background RMS noise in the corresponding channel. The second term accounts for the flux density variations explained in Section 5.2 by assuming a $\delta_{\mathrm{cal}} = 5\%$ error on the measured flux densities per channel, denoted by f_i.

The fitting was done using a Monte Carlo Markov Chain (MCMC) fitting code developed by Di Gennaro et al. (2021c) to sample the posterior probability. The following uniform priors were assumed:

$$\begin{cases} I_0 \sim \mathcal{U}(0, \infty) \\ \alpha \sim \mathcal{U}(-\infty, \infty) \\ p_0 \sim \mathcal{U}(0, 1) \\ \chi_0 \sim \mathcal{U}(0, \pi) \\ \phi \sim \mathcal{U}(-2000, 2000) \\ \sigma^2_{\mathrm{RM}} \sim \mathcal{U}(0, \infty), \end{cases} \tag{5.14}$$

The initial values for the parameters were found through a least-square fit, using the ϕ as obtained from the RM-synthesis method as the initial guess for the Faraday depth. The posterior was sampled with 200 walkers for 1 000 steps and a burn-in period of 200 steps was removed from each chain. The one-sigma uncertainties on the best-fit parameters are given by the 16th and 84th percentile of the chain. An example of the results on a polarised source with a good signal-to-noise ratio is shown in Figure 5.4.

To judge whether the model m, given by Equation 5.12, is a good fit to the data points y_i (i.e. the Stokes Q and U flux densities), we inspected the normalised residuals,

$$R_i = \frac{y_i - m(\lambda^2, \theta)}{\sigma_i}, \tag{5.15}$$

where σ_i is the uncertainty on the polarised flux. It is not possible to determine analytically the number of degrees of freedom k in the external depolarisation model because it is a non-linear model, which is why we are not able to determine the reduced chi-squared value. In Figure 5.5 we plot the distribution of the sum of the squared residuals (i.e. the χ^2 value) of the best fitting external depolarisation model to each polarised component. Most polarised sources have around 84 to 89 data points (i.e. channels) after masking the bad channels. This would give 80 to 85 degrees of freedom if the model was linear with 4 parameters. For comparison, we show also the theoretical χ^2 distribution with 80 degrees of freedom. The main peak of the sum of the squared residuals shows good agreement with the theoretical χ^2 distribution, indicating that most sources have acceptable fits. There is however a long

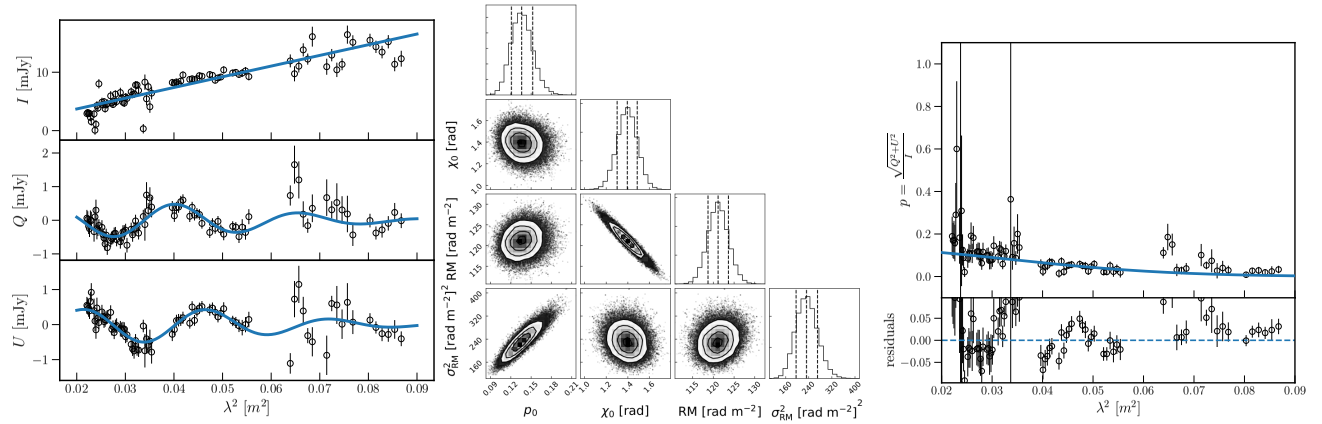

(a) (b) (c)

Figure 5.4: Results of the MCMC fitting of the external depolarisation model on the Stokes I, Q and U channels to a polarised source with good signal-to-noise ratio. Figure (a) shows the measured flux densities per channel in black and the best-fit model in blue. Figure (b) shows the posterior distribution of the model parameters visualised as one and two-dimensional projections in a corner plot. Figure (c) shows the inferred polarisation fraction from the data and the best-fit model together with the residuals.

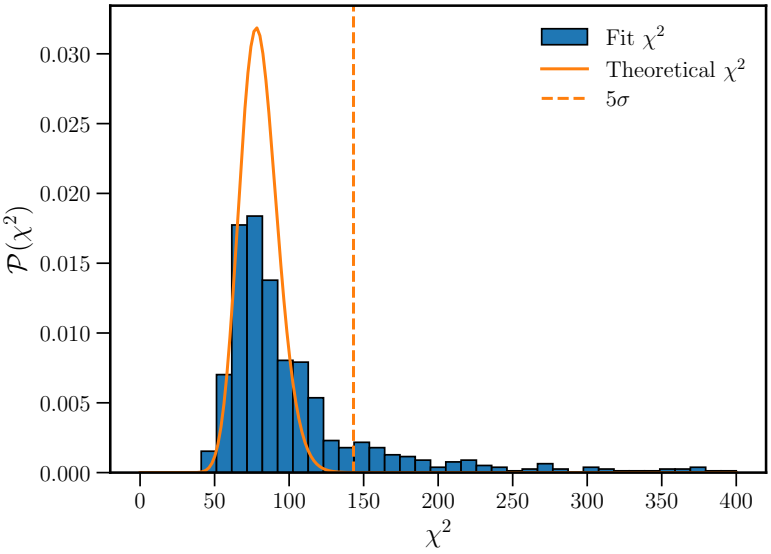

Figure 5.5: Distribution of the sum of the squared residuals (χ^2) of the model fits to all polarised components. The plot is truncated at $\chi^2 = 400$ for visibility.

tail of large χ^2 values, mainly caused by bright Stokes I sources, where residual calibration artefacts are more noticeable. To automatically discard bad fits, we decided to cut all fits with a χ^2 value that is 5σ away from the theoretical distribution, indicated by the dashed line in the Figure. This cut removed 148 polarised components. A few of these components are possibly Faraday complex sources, for which the simple model with a single RM component is not sufficient. We note that there are no apparent correlations between the χ^2 parameter and the derived best-fitting parameters $p_0, \chi 0, \phi, \sigma^2_{\rm RM}$, or the projected radius to the cluster centre, so we are not biasing our analysis by removing these sources. Additionally, for sources with low signal-to-noise polarised emission, a good fit (according to the χ^2 parameter) can be found by artificially large values of $\sigma_{\rm RM}$. For these sources, the best-fit $\sigma_{\rm RM}$ is basically unconstrained, with large error bars. Therefore we decided to also cut sources where the fractional uncertainty on the best-fit $\sigma_{\rm RM}$ is larger than two. This cuts 45 additional sources, so in total 193 polarised components have bad fits. These components are indicated in the polarised source Table H.1 by the column 'Flagged', where we have also flagged 11 components that are part of a radio relic.

To calculate the upper limit on the fractional polarisation of sources detected only in Stokes I, we followed a method similar to Bonafede et al. (2011). We randomly sampled empty regions with a size of 10″, a bit larger than the synthesised beam. For these 'noise sources' we computed the polarised surface brightness and compared the distribution of the polarised surface brightness of the 'noise sources' to the distribution of real sources, taking into account the varying background noise level due to the primary beam of the VLA. We put the noise-dependent threshold of the surface brightness where noise sources

constitute 10% of the real sources. The resulting threshold (P_t) as a function of the RMS noise is 0.04, 0.05, 0.06 and 0.08 mJy beam^{-1} for sources with background RMS values 0-29, 29-36, 36-46 and 46+ μJy/beam respectively, where the background noise bins are chosen such that in each bin there are an equal amount of simulated noise sources. For comparison, the threshold P_t calculated independently of the background noise level gives a value of $P_t = 0.06$ mJy beam^{-1}. The one-sigma upper limit on the fractional polarisation value is then calculated as

$$F_p \leq \sqrt{\frac{P_t^2}{I^2 - \sigma_I^2}}, \tag{5.16}$$

where I is the surface brightness of the unpolarised source and σ_I is the background RMS noise. This method gives conservative upper limits for extended unpolarised sources because the Stokes I surface brightness is computed over the entire extent of the source (rather than e.g. per lobe).

5.3.3 Optical counterparts

To determine the redshift of the radio sources, each radio source needs to be associated with an optical counterpart. PyBDSF is known to occasionally split up components of a single physical radio source (e.g. Williams et al., 2019). This particularly happens for large and extended sources, and often when the source has multiple disconnected patches of emission. To group PyBDSF Stokes I source candidates into single physical sources and to identify the optical counterpart, radio-optical overlays were created and every source was visually inspected. We used the g, r, z filters from the Legacy Survey (Dey et al., 2019) where available and used the Pan-STARRS survey (Chambers et al., 2016) for the 32 fields outside of the Legacy survey sky coverage.

As a first guess of the optical host galaxy, the nearest optical neighbour to the radio source was marked. This proved a good guess in 5 806 out of 6 807 total intensity source candidates. For the remaining 1 001 sources, the best candidate optical counterpart position was manually marked from visual inspection of radio-optical overlays.

The source association was done in the same visual inspection step as the host galaxy identification. Out of the 6 807 total intensity source candidates, 411 candidates were components of another source, leaving 6 396 physical sources detected in total intensity. This indicates that PyBDSF in most cases correctly identified the total extent of the Stokes I source. We did not perform the source association step for the polarised components. Because different parts of a radio source can have different RM determinations and thus polarised intensities, we decided to treat separate polarised components as separate polarised sources, as for example was also done in Böhringer et al. (2016).

5.3.4 Redshift estimation

With the best-estimated location of the host galaxies determined, we employed different methods to estimate the source redshift. First, we checked whether a source has a spectroscopic redshift measurement available by cross-matching the host galaxy positions to the *NASA/IPAC Extragalactic Database* (NED[3]) and the Sloan Digital Sky Survey (SDSS DR16; Ahumada et al., 2020) with a matching radius of 0.5 and 3 arcseconds respectively. If a

[3] https://ned.ipac.caltech.edu/

spectroscopic redshift was found, but no uncertainty was quoted the redshift uncertainty is set to 0 in the catalogue.

If no spectroscopic redshift was found, a photometric redshift estimation was done from the Legacy Imaging Surveys Data Release 8 (Dey et al., 2019), which is the most sensitive optical survey covering the majority of our clusters. This approach is detailed fully in Duncan (2022) and provides high quality redshifts for galaxies at $z < 1$. For sources outside of the Legacy Survey, we calculated the photometric redshift using the Pan-STARRS *grizy* bands. We followed the method and used the code provided by Tarrío & Zarattini (2020), which estimates redshifts through local linear regression in a five-dimensional colour and magnitude space. The five-dimensional space consists of (r, g-r, r-i, i-z, z-y) where the letters indicate the extinction corrected Kron magnitudes (Kron, 1980) of galaxies in the PanSTARRS *grizy* bands. The correction for interstellar extinction used the maps from Schlegel et al. (1998) and is described in detail in Section 2.3 of Tarrío & Zarattini (2020). To compute the photometric redshifts from the Pan-STARRS band, we found the 100 nearest neighbours in the five-dimensional space for each source, from a training set composed of 2 313 724 galaxies with spectroscopic redshifts, constructed by Tarrío & Zarattini (2020). The redshift was computed for all sources where at least four out of five colours were available. We note that missing features most often occur in very faint galaxies, which makes it likely that the sources are at a redshift $z > 0.35$, and are thus background sources. The quality of the Pan-STARRS photometric redshifts was checked by comparing to spectroscopic redshifts for sources where spectroscopic redshifts were available. Using standard literature metrics for the robust scatter $\sigma_{\rm NMAD}$ and outlier fraction OLF (cf. Dahlen et al., 2013; Duncan, 2022) we find that the photometric redshifts have good quality, with $\sigma_{\rm NMAD} = 0.025$ and OLF= 0.075.

The combination of all methods resulted in a redshift estimate for 77% (632/819) of the polarised sources and 67% (4 544/6 807) of the unpolarised sources. The distribution of redshifts estimates is given in Table 5.1. The final catalogues of polarised and unpolarised radio sources are provided in Tables H.1 and H.1 respectively. These tables contain the polarised and unpolarised source properties, the best estimate for the redshift of the sources and the method used to get this estimate.

Table 5.1: Redshift estimates of all polarised ($N_{\rm pol}$) and unpolarised sources ($N_{\rm I}$).

$z_{\rm best}$ source[a]	Source	$N_{\rm pol}$	$N_{\rm I}$
0	NED/Literature (spectroscopic)	248	1059
1	SDSS (spectroscopic)	21	208
2	Legacy (photometric)	260	2097
3	PANSTARRS (photometric)	101	1131
4	SDSS (photometric)	2	49
-	No redshift available	187	2263
Total		819	6807

Notes. [(a)] The '$z_{\rm best}$ source' key is used in the catalogue presented in Table H.1 to indicate the origin of the redshift estimate.

5.4 Magnetic field modelling

To compare observations with theoretical expectations, we modelled the magnetic field as a three-dimensional Gaussian random field, characterised by a single power-law spectrum. We followed the approach proposed by Tribble (1991), used in various works in the literature (e.g. Murgia et al., 2004; Guidetti et al., 2008; Bonafede et al., 2011, 2013; Vacca et al., 2012; Govoni et al., 2017; Stuardi et al., 2021). This approach starts with generating the vector potential of the magnetic field, A, in Fourier space, denoted by $\tilde{A}$. The amplitude and phase of the components of the vector potential were generated such that the phases are randomly distributed between 0 and 2π and the amplitudes follow a power-law given by

$$|A_k|^2 \propto k^{-\xi}, \tag{5.17}$$

where k denotes the magnitude of the three-dimensional wave-vector $\vec{k}$. The wave numbers k are related to the spatial scales Λ as $k = 0.5 \cdot \frac{2\pi}{\Lambda}$, where Λ refers to the reversal scale of the magnetic field, following the definition used by Murgia et al. (2004) Because the vector potential and magnetic field are real quantities, we made sure that the matrix $\tilde{A}$ is Hermitian (i.e. equal to its conjugate transpose). The components of the Fourier transform of the magnetic field are then given by the following cross product

$$\tilde{B}(k) = ik \times \tilde{A}(k). \tag{5.18}$$

This results in the magnetic field B, which is simply calculated by (fast) Fourier transform, being divergence-free, isotropic and component-wise Gaussian random, with a power-law spectrum

$$|B_k|^2 \propto k^{-n}, \tag{5.19}$$

where $n = \xi - 2$. A power-law spectral index of $n = 3$ implies that the magnetic field energy density is scale-invariant, for $n < 3$ the energy density is larger on smaller scales and for $n > 3$ the energy density is mostly in the larger scales (Murgia et al., 2004). The range of spatial scales Λ that can be explored is given by the size of the computational grid. The simulated maximum scale on which the magnetic field reverses is equal to $\Lambda_{\rm max} = \pi/k$ while the minimum scale $\Lambda_{\rm min}$ that can be probed is determined by the cell size.

The normalisation of the magnetic field was set after the Fourier transform such that the magnetic field strength approximately follows an assumed magnetic field profile. Like previous literature, we assumed that the magnetic field profile is proportional to the gas density profile, which is expected to happen during cluster formation from simulations (Dolag et al., 2008),

$$B(r) = B_0 \left(\frac{n_e(r)}{n_e(0)} \right)^{\eta}, \tag{5.20}$$

where B_0 is the average magnetic field strength at the cluster centre, n_e is the thermal electron gas density profile and η denotes the proportionality between the magnetic field strength and electron density. For $\eta = 0.5$, the magnetic field energy density is linearly proportional to the thermal gas density. The thermal electron density profile is available for every cluster in the Chandra-Planck sample, from the X-ray observations presented in Andrade-Santos et al. (2017), where the fitted profile was assumed to follow a modified double β model (see Vikhlinin et al. (2006) for more details):

$$n_e n_p = n_0^2 \frac{(r/r_c)^{-\alpha}}{(1+r^2/r_c^2)^{3\beta-\alpha/2}} \frac{1}{(1+r^\gamma/r_s^\gamma)^{\epsilon/\gamma}} + \frac{n_{02}^2}{(1+r^2/r_{c2}^2)^{3\beta_2}}, \quad (5.21)$$

Given the modelled magnetic field and observed electron density profile, we calculated the expected Faraday rotation in the clusters by numerical integration of Equation 5.4. Then, assuming an intrinsic polarisation p_0, and a single polarisation angle χ_0 for a polarised background screen, we computed the polarisation angle of the radio emission at 1.5 GHz at the cluster redshift (χ_{obs}) with Equation 5.5. The predicted Stokes Q and U intensities were then obtained by inversion of $P = \sqrt{Q^2+U^2}$ and Equation 5.3:

$$Q = \pm \sqrt{\frac{p_0^2}{1+\tan^2(2\chi_{obs})}} U = \pm \sqrt{p_0^2 - Q^2}. \quad (5.22)$$

Using the convention that Stokes Q is positive for $-\pi/2 \leq \chi_{obs} \leq \pi/2$ and Stokes U is positive for $0 \leq \chi_{obs} < \pi$. Finally, the images were convolved with a beam corresponding to a 6″ FWHM at the cluster redshift. From the convolved Stokes Q and U images, we calculated the expected depolarisation fraction at 1.5 GHz in the cluster rest-frame.

5.5 Results - Observations

The intrinsic polarisation fraction of radio sources is often assumed to be the same for sources irrespective of their projected distance from the cluster centre. To test whether this is a good assumption, we plot in Figure 5.6 the intrinsic polarisation fraction p_0 (see Eq. 5.12) as a function of projected radius to the cluster centre. As the figure shows, there is a relatively large scatter in the intrinsic polarisation fraction of radio sources. This indicates that the assumption does not hold for this dataset and that the intrinsic polarisation fraction should be taken into account when estimating the amount of depolarisation.

To minimise the effect of the scatter introduced by source-dependent intrinsic polarisation, we calculated for every source the depolarisation ratio DP. We defined this as the ratio of the polarisation fraction at 1.5 GHz in the cluster rest-frame $p_{1.5GHz}$ to the intrinsic polarisation fraction p_0, using the best-fit model (Eq. 5.12). In this way, we do not assume the same intrinsic polarisation fraction for all radio sources and take into account the cosmological redshift.

We combined the information from the upper limits (unpolarised sources) with the depolarisation ratio of polarised sources using the Kaplan-Meier (KM) estimator (Feigelson & Nelson 1985; see also Bonafede et al. 2011). The KM estimator is a non-parametric statistic used to estimate the complement of the cumulative distribution function, called the survival function. With $x_1 < x_2 < .. < x_r$ denoting distinct, ordered, observed values, the survival function is given by:

$$S_{KM}(x) = P(X \geq x) = 1 - F(x), \quad (5.23)$$

where F(x) denotes the cumulative distribution function of the random variable x, in our case the random variable is the depolarisation ratio measured in the centre of the band (i.e.

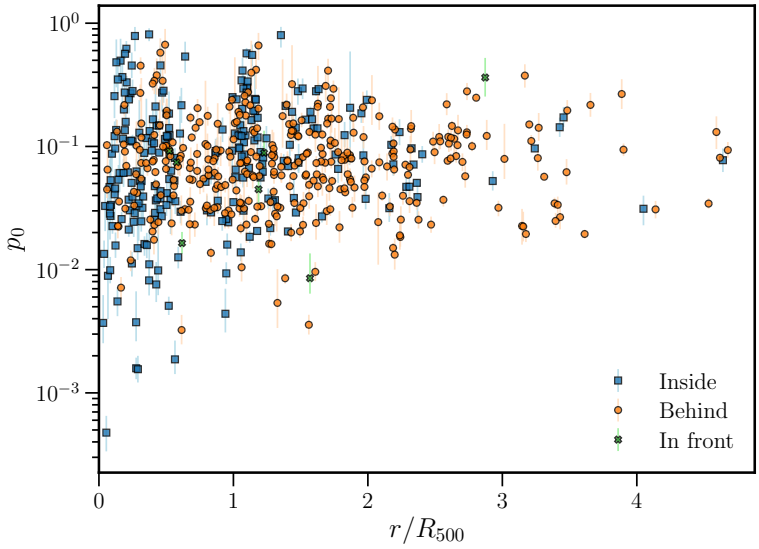

Figure 5.6: Best-fit intrinsic polarisation fraction against the projected distance to the cluster centre, normalised by the cluster R_{500}. Polarised sources are coloured based on their position along the line-of-sight with respect to the nearest cluster, defined in Section 5.5.2.

DP). The KM estimator of the survival function is given by

$$\hat{S}_{KM}(x) = \begin{cases} =\Pi_{i,x_i<x}\left(1-\frac{d_i}{n_i}\right)^{\delta_i} & \text{for x} > \text{x}_1 \\ =1 & \text{for x} \leq \text{x}_1, \end{cases} \tag{5.24}$$

with x_i the observed or censored depolarisation fraction of source i, d_i the number of sources with fractional polarisation equal to x_i, n_i the number of sources with (upper limits on) fractional polarisation $\geq x_i$ and $\delta_i = (1, 0)$ if x_i is polarised or unpolarised, respectively. The KM estimator is here expressed in the case of a right-censored sample, and most algorithms indeed only support right-censored data. Thus, we transformed our left-censored data to right-censored data by subtracting the data from a constant, following Feigelson & Nelson (1985).

For unpolarised sources, we calculated upper limits on $p_{1.5\text{GHz}}$ as explained in Section 5.3.2, so an assumption on the intrinsic polarisation fraction must be made to translate this upper limit on the fractional polarisation to an upper limit on the depolarisation ratio. Thus, for these sources we calculated the depolarisation ratio assuming $p_0 = 0.022$, which is the median of the Kaplan-Meier estimator of all polarised radio sources detected at $r > 1.5R_{500}$. All KM estimates were calculated using the `lifelines`[4] package (Davidson-Pilon, 2019).

[4] `https://github.com/CamDavidsonPilon/lifelines/`

5.5.1 Full sample

Figure 5.7 shows in the left panel the depolarisation fraction for all sources in our sample, including upper limits that are below $DP = 1$. The right panel shows the median depolarisation fraction, calculated using the KM estimator by splitting the sample into bins of projected radius to the cluster centre. Each bin was chosen such that it contains an equal number of sources. The error bars reflect the 68% confidence interval of the KM estimator, added in quadrature with the uncertainty introduced by the fitting procedure. The uncertainty introduced by the fitting was estimated using a Monte Carlo method. For every source, we draw 1 000 samples from a Gaussian distribution with a standard deviation equal to the one-sigma uncertainty on the depolarisation ratio given by the MCMC chain. We note that the error is dominated by the confidence interval of the KM estimator, thus that the effect of the uncertainty in the best-fit polarisation parameters is small. This means that we are limited by the number of polarised radio sources, and not by the quality of the data.

Figure 5.7 shows a clear trend of sources being more depolarised as they move towards the cluster centre, where the magnetic field strength and the line-of-sight column densities increase. The depolarisation ratio is around 0.92 beyond $2R_{500}$, which is likely not an external, but an internal depolarisation effect because at these distances the column density and magnetic field strength of the intracluster medium would be too low to result in significant external depolarisation.

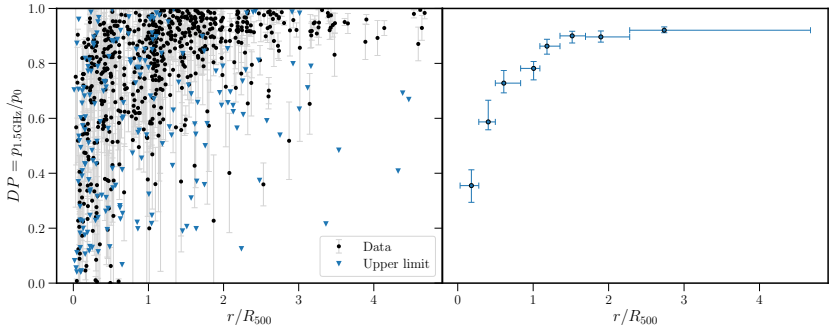

Figure 5.7: Depolarisation against normalised projected radius. *Left panel:* Full sample of sources and relevant upper limits. The error bars reflect the 68% confidence interval from the MCMC fitting procedure. *Right panel:* median of the Kaplan-Meier estimate of the depolarisation ratio survival function in different bins of projected radius to the cluster centre. The bin width is chosen such that each bin contains an equal number of polarised sources and is denoted by the horizontal lines (i.e. 0th and 100th percentile). The points are plotted at the median radius in each bin.

5.5.2 Background versus cluster members

To investigate whether there is a difference between depolarisation of cluster members and depolarisation of background radio sources, we classified each radio source according to the following definitions. We defined a source to be in front of a cluster if it lies at least

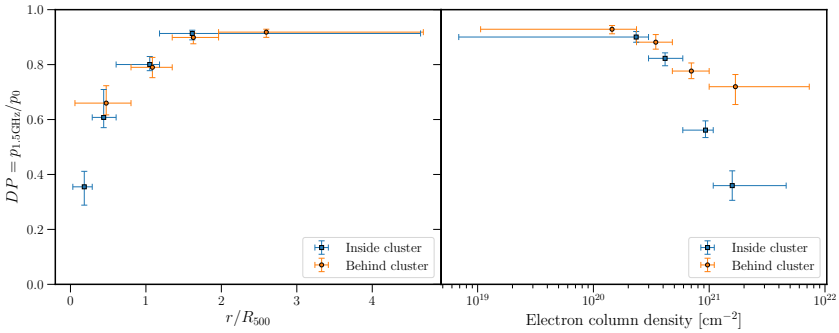

Figure 5.8: Median of the Kaplan-Meier estimate of the depolarisation ratio survival function in different bins of radius and electron column density. Sources inside clusters are shown in green and sources behind clusters are shown in red. The bin width is chosen such that each bin contains an equal number of polarised sources and is denoted by the horizontal lines. The points are plotted at the median radius or column density in each bin.

5

$1\sigma_z$ away from a chosen boundary (Δz) around the cluster redshift

$$z_{\mathrm{cluster}} - (z_{\mathrm{source}} + \sigma_z) > \Delta z, \tag{5.25}$$

where z_{cluster} is the cluster redshift, z_{source} the source redshift and $\sigma_{\mathrm{zsource}}$ the one-sigma uncertainty on the source redshift. The values of z_{source} and $\sigma_{\mathrm{zsource}}$ are given in Tables H.1 and H.1 in the column 'z_{best}' for every source. Similarly, a source was defined to be behind a cluster if

$$(z_{\mathrm{source}} - \sigma_z) - z_{\mathrm{cluster}} > \Delta z. \tag{5.26}$$

All other sources were defined as inside the cluster. We have set $\Delta z = 0.04(1+z)$, following the definition of cluster membership used by Wen & Han (2015). Sources without an optical counterpart are likely faint sources at redshifts higher than $z = 0.35$, particularly because radio galaxies are often hosted by massive elliptical galaxies which should be easily detectable at $z < 0.35$ at the depth of Legacy and PanSTARRS. Therefore, sources without an optical counterpart were also defined as background sources. We verified, through a two-sample KS test, that the measured polarisation fraction of the sample of sources without an optical counterpart does not significantly differ from the sample of sources with an optical counterpart (p-value 0.14), implying that they pass similar Faraday screens.

We investigated the depolarisation effect as a function of radius and electron column density to partially split the degeneracy between magnetic field strength and electron column density, which are both a function of radius, and both increase the amount of depolarisation (Eq. 5.4). To determine the electron column density for sources inside the clusters we integrated the best-fit electron density profile along the line-of-sight, from the centre of the cluster out to R_{500}, thus effectively integrating over half the sphere. For sources located behind the cluster, this column density was multiplied by two because we assumed spherical symmetry in the electron profiles.

In Figure 5.8 we show the depolarisation ratio calculated in different bins of normalised projected distance or electron column densities, for cluster members and background sources separately. Firstly, the figure shows the difficulty of detecting background sources

close to the cluster centre, which means larger bins need to be used for background sources than for cluster members. For completeness, the full sample of data points is plotted in Figure 5.30.

Secondly, we detect a significant difference between cluster members and background sources in the highest column density bin (right panel). This could arise because at similar column densities background sources are projected further away from the cluster centre than cluster members and thus probe smaller magnetic field strengths, causing less depolarisation. Additionally, because cluster members are easier to detect near the cluster centre, the largest column density bin also samples preferentially higher column densities for cluster members.

Conversely, we expect that at similar radii, background sources probe higher column densities and are thus more depolarised. However, we do not significantly detect this difference given the uncertainties and the large bin size of background sources near the centre of the cluster.

Thirdly, at radii where we have similar sampling (i.e. $r > 0.5R_{500}$), we do not see a significant difference between cluster members and background sources. To statistically confirm this, we used the non-parametric log-rank test (Feigelson & Nelson, 1985), used frequently with other astronomical works dealing with survival analysis (e.g. Bonafede et al., 2011; Kang et al., 2020; van Terwisga et al., 2022). The resulting survival curves of cluster members and background sources are shown in Figure 5.9, and according to the log-rank test with p-value 0.89 we cannot reject the null hypothesis that there is no difference between background sources and cluster members.

Lastly, at the inner radii ($r < 0.5R_{500}$) where we do not have a similar sampling of background sources and cluster members, we see a hint of more depolarisation detected in the cluster member population. However, the log-rank test returns $p = 0.13$, indicating that with the current sampling, this result is not statistically significant.

5.5.3 Dynamical state

The magnetic field evolution of galaxy clusters remains poorly constrained. During the lifetime of clusters, mergers with other clusters or smaller substructures can alter the structure and strength of the magnetic field significantly. This section focuses on possible differences between merging and relaxed systems.

Generally, relaxed clusters show strongly peaked, symmetrical X-ray emission that has a radiative cooling time much shorter than the Hubble time (e.g. Fabian, 1994). These clusters show the shortest cooling times in their cores and are therefore often referred to as cool-core clusters. Cluster mergers can destroy the cool core and significantly disturb the observed X-ray morphology (Burns et al., 2008). Thus, X-ray morphological parameters such as the concentration or cuspiness of the gas density profile can be used to determine whether a system has a cool core (e.g. Andrade-Santos et al., 2017).

We use the X-ray morphology parameters derived from the Chandra observations of 93 clusters in our sample in Andrade-Santos et al. (2017) to determine the presence or absence of a cool core. We note that this split does not perfectly correspond to a split in the dynamical state, as there are rare examples of merging clusters that still show a cool core (e.g. Somboonpanyakul et al., 2021). However, this split is sufficient to generally divide the sample into merging and relaxed systems. Using the concentration parameter calculated in

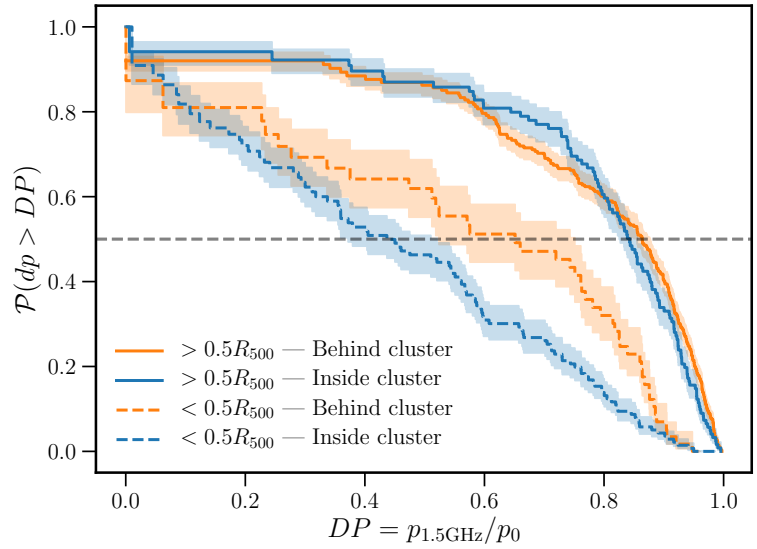

Figure 5.9: Survival function (i.e. 1-CDF) inferred from the Kaplan-Meier estimator for all sources located at $r/R_{500} > 0.5$, and $r/R_{500} < 0.5$. Background sources and cluster members are indicated by red and green, respectively. The grey dashed line shows the location of the 50th percentile, indicating the median for both populations.

the 0.15–1.0 R_{500} range (C_{SB}) by Andrade-Santos et al. (2017) to classify clusters as cool-core or non-cool-core, we found that 65% (60/93) of the clusters in our sample are non-cool-core (NCC) and 35% (33/93) are cool-core (CC) clusters.

Figure 5.10 shows the depolarisation effect separately for CC and NCC clusters in equal frequency bins, the full sample is plotted in Figure 5.31. We see a hint in the first radius bin of detecting more depolarisation in NCC clusters than in CC clusters.

To separate the effect of the central cooling core region in CC clusters, we have manually defined bins of projected radius in the right panel of Figure 5.10. We have chosen an inner radius bin of $0.0 - 0.2R_{500}$ because the effect of the cooling core is significant only in the inner $\sim 0.2R_{500}$ of CC clusters (e.g. Vogt & Enßlin, 2006; Eckert et al., 2011). The right panel shows that the larger depolarisation fraction in NCC is dominated by sources detected at $r > 0.2R_{500}$. In fact, sources detected at $r < 0.2R_{500}$ show a hint that there is more depolarisation in the central cooling core region of CC clusters, although the uncertainties are large due to the low number of sources detected near the centre of CC clusters. At $r < 0.2R_{200}$, we have detected only 9 sources and 16 upper limits in CC clusters, and 36 sources and 14 upper limits in NCC clusters. The significance of these results was determined by comparing the survival functions of sources detected in the $0.0 - 0.2R_{500}$ and $0.2 - 1.0R_{500}$ bins. The survival functions are shown in Figure 5.11 and the log-rank test yields p-values of 0.22 and 0.001 for the $0.0 - 0.2R_{500}$ and $0.2 - 1.0R_{500}$ bins, respectively. This implies that the hint is statistically significant, with less depolarisation in CC clusters than in NCC clusters outside the core region. Conversely, inside the core region we do not

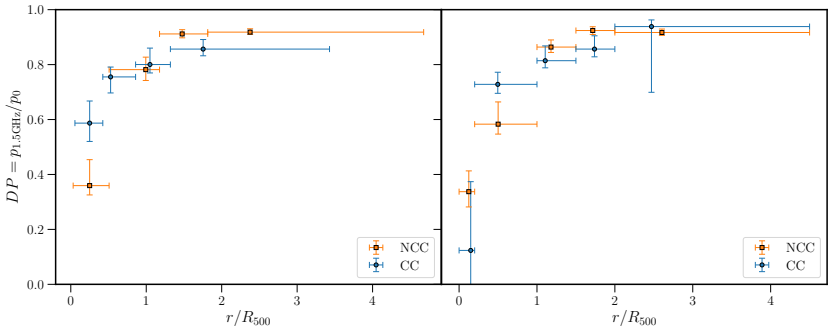

Figure 5.10: Median of the Kaplan-Meier estimate of the depolarisation ratio survival function in different bins of radius. Cool-core clusters are shown in blue and non-cool-core clusters are shown in orange. The left panel shows bin widths (denoted by horizontal lines) chosen such that each bin contains an equal number of sources detected in polarisation and the right panel shows manually selected bins. The points are plotted at the median radius in each bin.

have enough sources to significantly detect a difference between the two samples.

To examine to what extent the results of the CC/NCC split are affected by the position along the line-of-sight of the sources, we repeat this analysis separately for background sources and cluster members. Figure 5.12 shows that we do not detect a difference between NCC and CC clusters in either sub-sample. This is likely because of the low number of sources left in each sub-sample. We are mainly limited by the number of polarised sources detected near the centre of CC clusters. Comparing the survival curves of the NCC and CC sample for sources detected below $0.5R_{500}$, the log-rank test returns p-values of 0.07 and 0.24, for the sources inside clusters and behind clusters, respectively. Thus, we cannot significantly detect differences between NCC and CC clusters when splitting the sample into background and cluster members due to the limited amount of data points. We do see that most of the depolarisation found at small radii is from cluster members, although the uncertainties become quite large due to the small sample sizes.

5.5.4 Cluster mass and redshift

Although the sample of clusters is constrained to a relatively low redshift range ($z < 0.35$), we can attempt to trace the evolution of the magnetic field of clusters, by splitting the sample based on cluster redshift. We note that the redshift of the host cluster should correlate with the amount of beam depolarisation because the same telescope resolution corresponds to larger physical areas probed at higher redshifts. This means that we effectively average over larger magnetic field scales, and thus expect more beam depolarisation. Another effect that we have to take into account is the selection function of the Planck cluster sample. There is a strong correlation between cluster mass and redshift, with the most massive clusters preferentially being detected at high redshift (see Fig. 26 in Planck Collaboration et al., 2016a). This means that a cut in redshift effectively also corresponds to a mass cut, as shown in Figure 5.13. As the figure shows, it is not possible to separate the effects of cluster

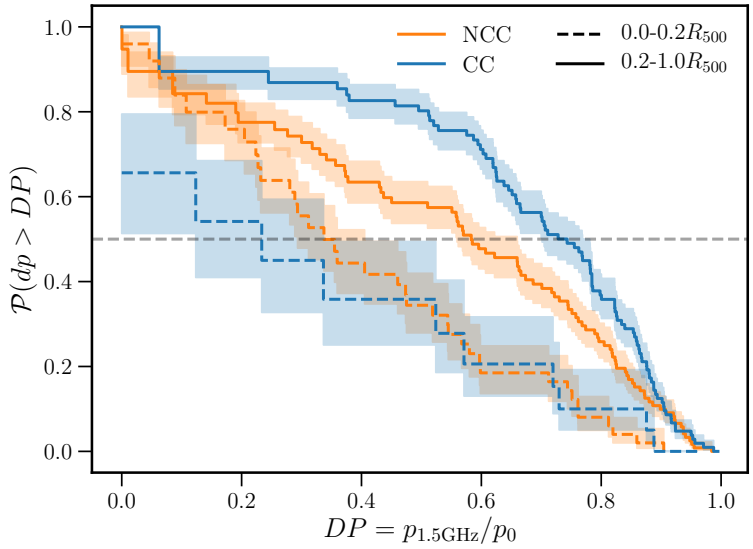

Figure 5.11: Survival functions (i.e. 1-CDF) inferred from the Kaplan-Meier estimator for all sources in the $0.0-0.2R_{500}$ and $0.2-1.0R_{500}$ bins, separately for sources detected around CC and NCC clusters. The grey dashed line shows the location of the 50th percentile, indicating the median for both populations.

redshift and cluster mass because there is almost no overlap in the same mass range.

Figure 5.14 shows the depolarisation trend for low- and high-redshift clusters separately, and the full sample is shown in Figure 5.32. The low-redshift sample contains clusters with $z < 0.175$ and the high-redshift sample contains clusters with $0.175 < z < 0.35$. The first thing to note is that we detect significantly more sources at lower projected radii through the low-redshift clusters. Each projected radius bin has 78 detected sources through low-redshift clusters, while the high-redshift clusters have only 43 detected sources per bin. This is expected because the larger angular size of low-redshift clusters makes it easier to detect polarised sources, especially in the centre of the cluster. The low number of polarised sources detected at low projected radii in the high-redshift sample makes it difficult to compare the two populations. Therefore, we performed a bootstrap re-sampling to enforce that we have a similar sampling of radius in both low- and high-redshift clusters. This was repeated 1000 times, with one realisation of the re-sampled values shown in Figure 5.15. Out of 1000 log-rank tests comparing the high-redshift sample to the sub-sampled low-redshift sample, 4% (43/1000) of the tests returned $p < 0.05$, indicating that we cannot distinguish a difference in depolarisation in the low- and high-redshift sample of clusters. However, this is likely due to the low number of sources in the high-redshift sample.

5.5.5 Presence of a radio halo

There is an apparent dichotomy in clusters regarding the presence of a radio halo, where clusters that show a radio halo are almost always found to be dynamically disturbed, while

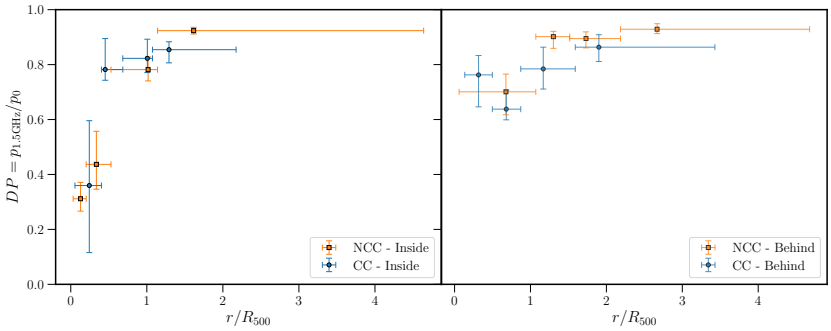

Figure 5.12: Same as the left panel of Figure 5.10, but separately for cluster members (left panel) and background sources (right panel).

clusters without a radio halo are more relaxed (Cuciti et al., 2021a). However, there are some cases of merging clusters without radio halos or with much fainter radio halos than usual (e.g. Cuciti et al., 2018; Russell et al., 2011). While these might be special cases, it is interesting to investigate whether there are differences between the magnetic fields in merging clusters that show a radio halo and those that do not.

We searched the literature for every cluster in our sample and found that out of the 60 clusters classified as merging, 26 have a radio halo detection, also incorporating the results of the second Data Release of the LOFAR Two-meter Sky Survey (Botteon et al., 2022a). This thus splits the sample in about half, allowing for the same bins to be used. The resulting depolarisation curves are very similar, as shown in Figure 5.16, and the log-rank test for similarity returned a p-value of 0.79. It is thus clear that with the current sample size, we see no evidence of a difference in depolarisation between clusters with radio halos and clusters without radio halos.

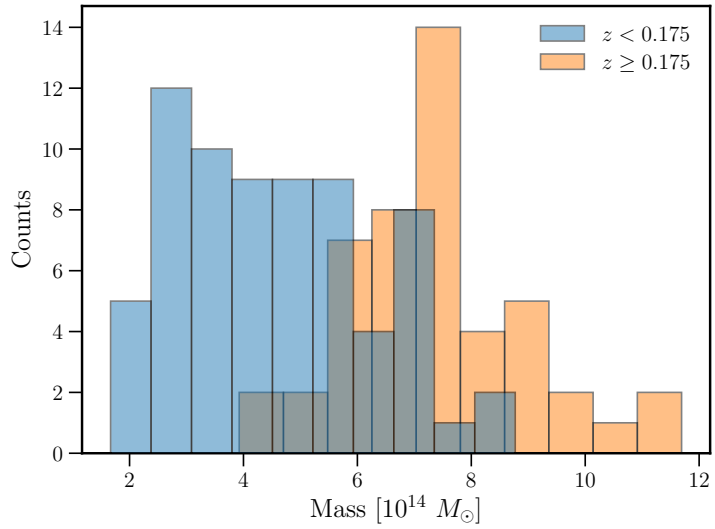

Figure 5.13: Distribution of cluster mass in the low- and high-redshift samples.

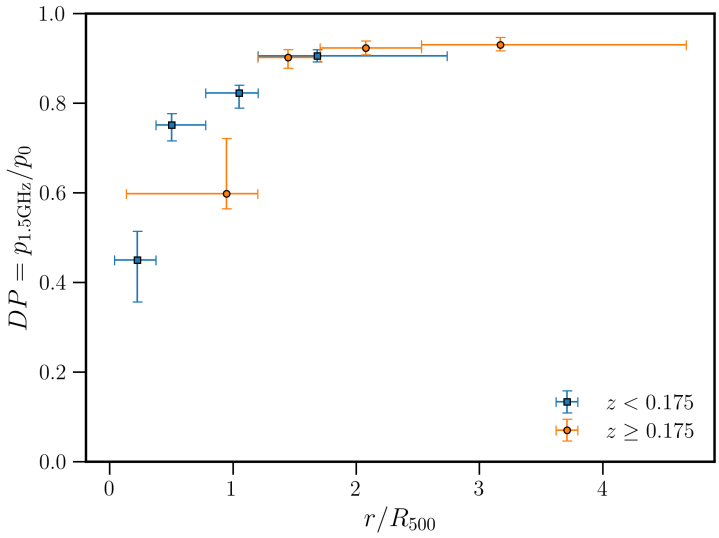

Figure 5.14: Median of the Kaplan-Meier estimate of the depolarisation ratio survival function in bins of projected radii and column density, for the low- and high-redshift clusters. The bin width is chosen such that each bin contains an equal number of sources detected in polarisation and is denoted by the horizontal lines. The points are plotted at the median projected radius.

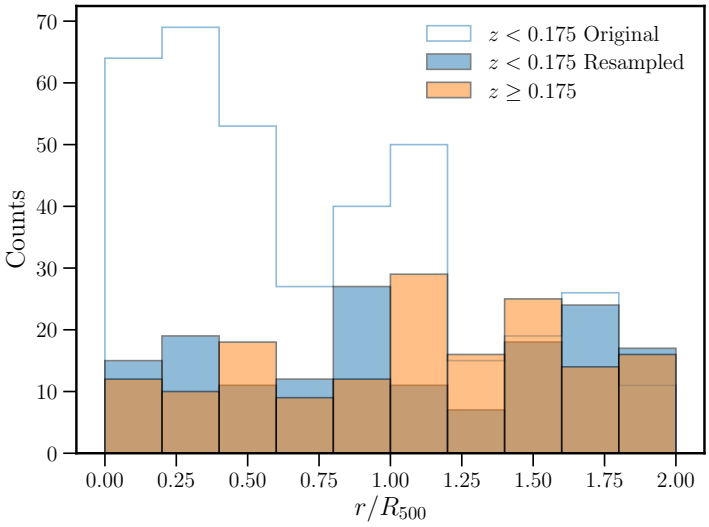

Figure 5.15: Distribution of the projected radius of sources detected in the low and high-redshift cluster samples. The solid blue histogram shows the result of one realisation of randomly sub-sampling sources in the low-redshift cluster sample to match the distribution of sources in the high-redshift sample.

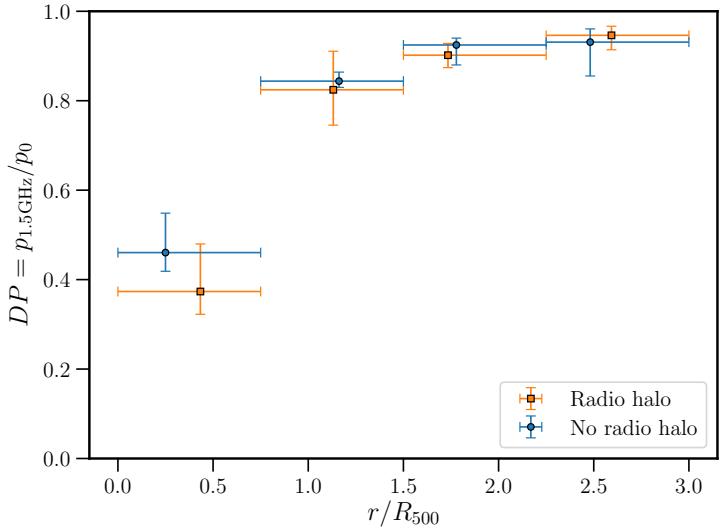

Figure 5.16: Comparison of the median observed depolarisation ratio against the projected distance between the merging clusters with and without detected radio halos.

5.6 Results - Modelling

This section details the results of the modelling, and the comparison of theory with observations. We simulated magnetic fields following the approach laid out in Section 5.4. We used the density profiles presented in Andrade-Santos et al. (2017), which were fitted to the modified double β model shown in Equation 5.21. Profiles were only available for the 102 clusters from the ESZ catalogue, so we could not model the depolarisation in the 24 new clusters from the PSZ1 (Planck Collaboration et al., 2015) and PSZ2 (Planck Collaboration et al., 2016a) catalogues.

5.6.1 Effect of density profiles

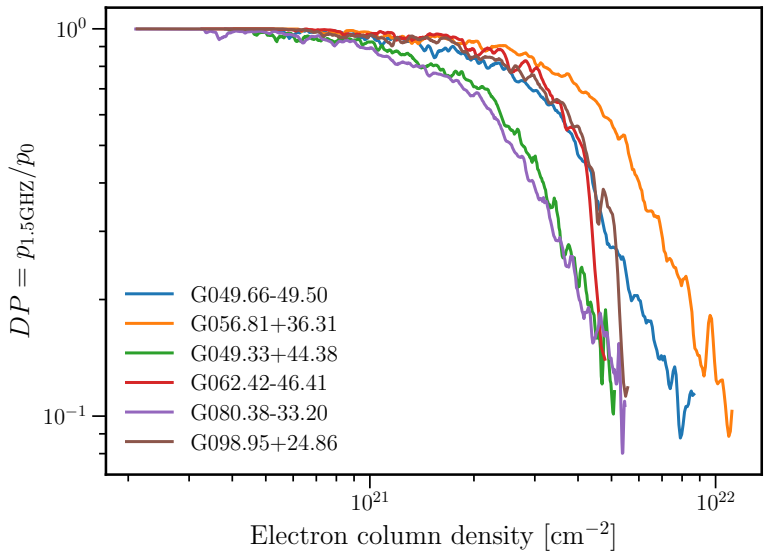

Figure 5.17: Modelled depolarisation ratio as a function electron column density for six different clusters around $z = 0.1$. The assumed parameters for the magnetic field are $B_0 = 5.0\,\mu$G, $n = 11/3$ and $\eta = 0.5$, with $\Lambda_{\mathrm{min}} = 4$ kpc and $\Lambda_{\mathrm{max}} = 1024$ kpc.

In previous works, when clusters were stacked often a mean profile was assumed (e.g. Murgia et al., 2004; Bonafede et al., 2011). We first investigated the effect of the different electron density profiles. We used a subset of six arbitrarily chosen clusters around the same redshift $z = 0.1$, such that we probe about the same physical scales. The modelled magnetic field parameters for this experiment are $B_0 = 5.0\,\mu$G, $n = 11/3$ and $\eta = 0.5$ with a box-size of 1024^3 pixels, where each pixel represents 2 kpc. The minimum magnetic field reversal scale Λ_{min} is thus 4 kpc, and the maximum reversal length scale, $\Lambda_{\mathrm{max}} = 1024$ kpc. At the redshift of 0.1, the $6''$ beam corresponds to a physical scale of 11 kpc. All models start from the same random initialisation of the magnetic field vector potential A, meaning that the only difference between the simulated clusters is the assumed electron density profile. The properties of the clusters are given in Table 5.2.

Table 5.2: Properties of the six clusters that were modelled in Figure 5.17.

Cluster	Redshift	Dynamical state[a]	Mass $[10^{14} M_\odot]$	n_e ($r = 10$ kpc)[a] $[\mathrm{cm}^{-3}]$
G049.66-49.50	0.098	CC	$3.63^{+0.30}_{-0.30}$	0.01
G056.81+36.31	0.095	CC	$4.38^{+0.19}_{-0.21}$	0.02
G049.33+44.38	0.097	NCC	$3.67^{+0.26}_{-0.26}$	0.004
G062.42-46.41	0.090	NCC	$3.47^{+0.28}_{-0.27}$	0.02
G080.38-33.20	0.11	NCC	$3.77^{+0.27}_{-0.28}$	0.004
G098.95+24.86	0.092	NCC	$2.58^{+0.16}_{-0.18}$	0.01

Notes. [(a)] The X-ray properties are taken from Andrade-Santos et al. (2017).

The resulting depolarisation ratio as a function of electron column density is shown in Figure 5.17. From this figure it is clear that even at the same electron column densities, the amount of depolarisation can be quite different in different clusters, depending on the electron density profile. This is because at the same electron column densities, the local electron density profile along the line of sight can still differ quite a lot between clusters. This also influences the magnetic field strength along the line of sight because we assumed a relation between the magnetic field strength and the electron density profile. This means that it is important to take into account the different electron density profiles of the clusters, rather than define a mean electron density profile to stack the clusters.

5.6.2 Effect of the magnetic field strength and fluctuation scales

We have chosen an arbitrary cluster, PLCKESZ G039.85-39.98, located at $z = 0.176$, to investigate the qualitative effect on the depolarisation profiles of changing the scales on which the magnetic field fluctuations and the central magnetic field strength B_0. The effect of increasing the magnetic field is easily understood to result in more depolarisation because the scatter in RM increases (e.g. Murgia et al., 2004). To understand the effects of changing the fluctuation scales, we must consider two different competing effects. First, as more power is put into larger scale fluctuations (i.e. increasing n), the scatter in RM over the entire cluster increases because one is integrating coherently over longer path lengths (cf. Eq. 5.4). At the same time, because the fluctuations on smaller scales are reduced, the scatter in RM over the region probed by each individual observing beam decreases. Thus, depending on the size of the observing beam, this will either increase or decrease the amount of depolarisation as n changes.

We plot the modelled depolarisation profiles in Figure 5.18 as a function of different parameters. As expected, the amount of depolarisation increases with increasing magnetic field strength. When the magnetic field energy density is mostly on large scales (i.e. $n = 4$), the depolarisation profile becomes quite flat as a function of projected radius because the magnetic field becomes correlated on scales larger than the beam. As the magnetic field becomes more correlated on smaller scales (i.e. from $n = 4$ to $n = 2$, green lines), the amount of depolarisation increases. However, as we put even more power on smaller scales (i.e. from $n = 2$ to $n = 1$) we reach the turn-over point where the effect of decreasing the RM scatter over the entire cluster dominates increasing the RM scatter on regions probed by

the beam, resulting in less depolarisation. The exact turn-over point in the slope n depends on the size of the sampling region (i.e. the observing beam size) that the simulated radio images are smoothed with and can be different for different locations in the cluster, which have different magnetic field strengths.

The degeneracy between a steep and strong magnetic field (e.g. $B_0 = 10\,\mu$G, $n = 4$) and a shallower and weaker magnetic field (e.g. $B_0 = 5\,\mu$G, $n = 2$) is also clear from this figure. This implies that using depolarisation alone makes it difficult to disentangle between a weaker magnetic field with a steep power-law index, or a shallower magnetic field with a flatter power-law index. The effect of setting a maximum fluctuation scale of $\Lambda = 16$ kpc does not strongly influence the depolarisation ratio except somewhat at the cluster outskirts. This can be explained by the fact that the observing resolution (FWHM of 18 kpc at the cluster redshift) is comparable to the maximum fluctuation scale. However, the amount of depolarisation does decrease slightly because the scatter in RM over the entire cluster will be smaller due to the magnetic field being less correlated along the line of sight.

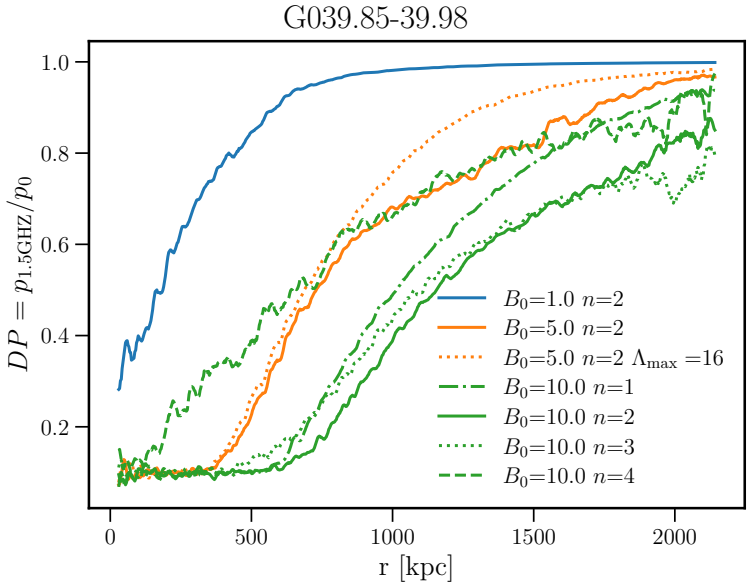

Figure 5.18: Effect of the magnetic field parameters on the depolarisation profile of the cluster G039.85-39.98, with $R_{500} = 1.2$ Mpc. The varied parameters are the central magnetic field strength B_0 in units of μG, the magnetic field power-law index n and the maximum correlation scale Λ_{max} in kpc. For all but one model, the maximum correlation scale was set to the maximum allowed by the image.

5.6.3 Comparison with observations

To compare the models to the data, we modelled the depolarisation ratio as a function of projected radius for every cluster for which a Chandra observation and thus electron density profile was available. Given the computational intensity (which scales as N^3 where N is the number of pixels) of generating many magnetic field cubes out to typical values of

Table 5.3: Model parameters used for comparison to observations.

Cluster redshift bin	Observed beam FWHM (kpc)	Model resolution (kpc pixel^{-1})	Model grid size (pixels)	N^a
0.05 - 0.09	6-10	1	2048^3	22
0.09 - 0.16	10-17	2	1024^3	23
0.16 - 0.35	17-30	3	1024^3	40

Notes. $^{(a)}$ N denotes the amount of clusters with X-ray observations available such that models could be generated.

R_{500}, we decided to simulate different clusters with different resolution depending on the cluster redshift. To simulate the depolarisation effect, the model resolution should be at least a few times the physical resolution given by the synthesised beam of the radio observations. The resolution of the synthesised beam is given in Table 5.3 with the accompanying model resolution and model grid sizes used. For clusters below $z = 0.05$ it was not feasible to generate simulations, since the physical resolution (FWHM) of the $6''$ synthesised beam corresponds to less than 6 kpc, and thus the resolution of the models should be higher than 1 kpc pixel^{-1}, which made the cube size unfeasibly big to generate. All modelled depolarisation profiles are shown in Figure 5.34 for completeness.

One final effect that we have to take into account when comparing the model to the data is internal depolarisation. Figure 5.8 showed that the depolarisation ratio is around 0.92 at the cluster outskirts. The fact that this is not 1.0 is likely caused by internal depolarisation effects. This internal depolarisation effect should not affect the trend, and therefore we multiply the simulated depolarisation ratio by the depolarisation ratio measured in the cluster outskirts to incorporate this effect.

Background versus cluster members

We can model the expected difference between the depolarisation of cluster members and background sources assuming that this difference can be fully attributed to the larger path length of background sources through the cluster. We assume that the radio emission from cluster members on average intersects about half the ICM column density and that emission from background sources travels through the full column. Theoretically, this is expected to give on average a factor of two larger Faraday depth for background sources (cf. Eq. 5.4) and a factor $\sqrt{2}$ in $\sigma_{\rm RM}$, which theoretically should not result in more than a factor two in depolarisation (cf. Eq. 5.12) for the wavelength range that we are probing. Indeed, when modelling the depolarisation profiles occurring as a result of a Faraday screen halfway inside the cluster versus a Faraday screen behind the cluster, Figure 5.19 shows that the location of the Faraday screen only has a marginal effect on the resulting depolarisation. This is in agreement with the results shown in Figure 5.8, where no clear difference between background sources and cluster members was found.

Average magnetic field properties

As shown in Section 5.5.2, we did not detect a significant difference in the depolarisation of cluster members and sources located behind the clusters. This is consistent with a picture

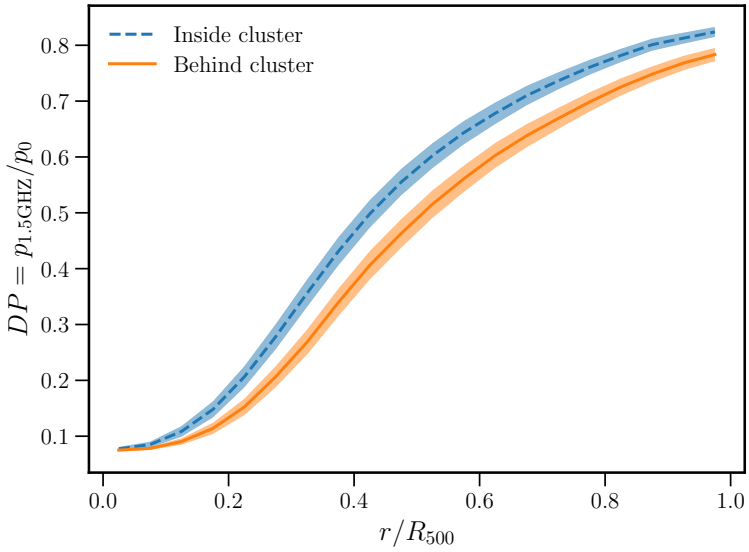

Figure 5.19: Average depolarisation ratio profile over all simulated clusters using a Faraday screen located behind (blue dashed line) or inside (orange solid line) the cluster. The uncertainty interval indicates the standard error on the mean of the simulated profiles.

where only the difference in path length between background radio emission and radio emission from the cluster medium affects the depolarisation of radio sources. To estimate the average properties of magnetic fields in galaxy clusters we can therefore compare our models with the depolarisation calculated over all sources (background and cluster members) to maximise the signal-to-noise ratio.

Although η is an important parameter that can influence the magnetic field estimates and the dependence on the fluctuation power-law slope n (Johnson et al., 2020), we fixed $\eta = 0.5$ to reduce the number of free parameters. This value is chosen such that the magnetic field energy density follows the thermal gas density (as found in e.g. Coma and Abell 2382 Bonafede et al., 2010; Guidetti et al., 2008). We then varied $B_0 = [1, 5, 10]\,\mu$G and $n = [1, 2, 3, 4]$. The maximum and minimum correlation scales are also fixed to the minimum and maximum size allowed by the computational grid.

The observed depolarisation trend was re-calculated in five equal-width bins between $0 - 1R_{500}$ using only sources detected in clusters that are part of the modelling, to make a fair comparison. The results of the comparison of the data with the modelled profiles are shown in Figure 5.20. Because of the degeneracy between n and B_0 (shown in Section 5.6.1) and the fact that we are averaging over many individual clusters with different electron density profiles, there is a large overlap between the different models. Still, it is clear that $B_0 = 1\,\mu$G does not fit the data for all values of n. For values of n between 1 and 4, the best fitting average central magnetic field strength is between $5 - 10, \mu$G, but due to the degeneracy it is not possible to distinguish between these models.

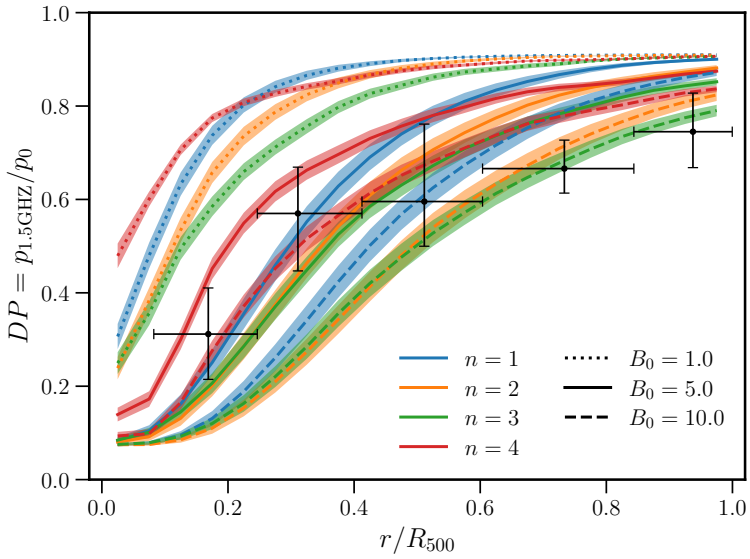

Figure 5.20: Comparison of the median observed depolarisation ratio in bins of projected radius, denoted by the horizontal lines, with the modelled depolarisation ratio profile for models with different magnetic field strengths (in μG) with $\eta = 0.5$. The model uncertainty interval indicates the standard error on the mean of the simulated profiles.

Dynamical state

Section 5.5.3 showed that NCC clusters appear to cause significantly more depolarisation than CC clusters outside $0.2R_{500}$. To investigate in more detail to what degree this is caused by a difference in the magnetic field properties, we average the CC and NCC clusters separately. This allows us to quantify the effect of the different electron density profiles of the two cluster samples. If the thermal gas profiles are the only cause of the discrepancy in depolarisation between NCC and CC, then the same magnetic field parameters would fit both samples.

Figure 5.21 shows that we indeed expect more depolarisation outside the core region from NCC clusters than from CC clusters when they have the same magnetic field properties. This can be understood from the assumption that was made in Eq. 5.20, where the magnetic field energy density was assumed to follow the thermal gas density, normalised by the central electron density of the cluster. Because CC clusters generally have denser cores than NCC clusters, the magnetic field strength a few hundred kiloparsec away from the central cooling core declines faster than in NCC systems, where the denominator of Eq. 5.20 is smaller. Indeed the models also show that the amount of depolarisation increases more steeply towards the centre of cooling cores than in non-cool cores, which is in line with the observations shown in the right panel of Figure 5.10.

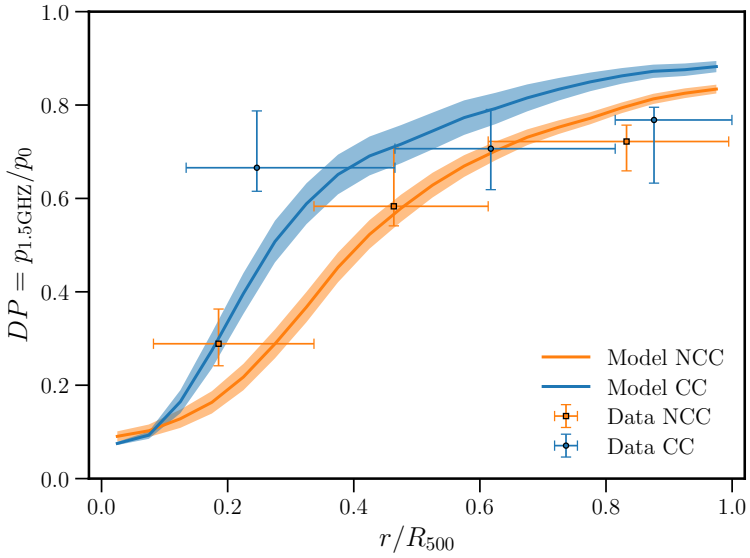

Figure 5.21: Comparison of the median observed depolarisation ratio with the modelled depolarisation ratio profile separately for the cool-core (CC) and non-cool-core (NCC) cluster sample. The modelled magnetic field parameters are $B_0 = 5\mu$G, $\eta = 0.5$ and $n = 3$ for both samples. The model uncertainty interval indicates the standard error on the mean of the simulated profiles.

Mass and redshift

Due to the low number of sources detected in the high-redshift sample, it was not possible to detect differences as a function of mass or redshift. Similar to the previous section, we can investigate to what extent we would expect a difference simply from the fact that we are probing a larger physical region at high redshift. However, in this case, the number of polarised sources detected in high-redshift clusters was already low due to the smaller angular size of the clusters and is even lower for the sample of clusters for which we also have density profiles available.

Within $1.0R_{500}$, we have detected only 26 polarised sources in the high-redshift cluster sample, and 132 in the low-redshift sample with density profiles available. This causes large uncertainties for the high-redshift sample, particularly closest to the cluster centre. Figure 5.22 shows that, for similar magnetic field parameters, we would expect slightly more depolarisation from the high-redshift sample than the low-redshift sample, although again this effect is not strong enough to be observed in our data. We thus do not find evidence for a difference between the magnetic field properties of the high-redshift, high-mass and low-redshift, low-mass sample of clusters.

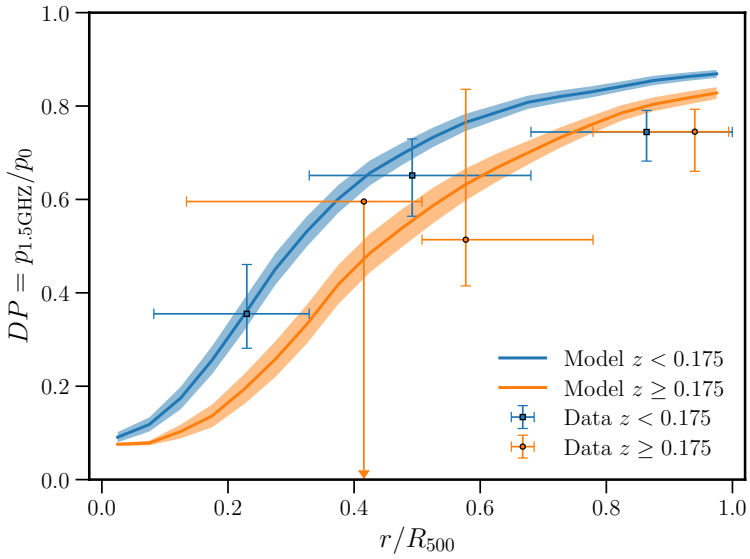

Figure 5.22: Comparison of the median observed depolarisation ratio with the modelled depolarisation ratio profile separately for the low- and high-redshift cluster sample. The modelled magnetic field parameters are $B_0 = 5\mu$G, $\eta = 0.5$ and $n = 3$ for both samples. The model uncertainty interval indicates the standard error on the mean of the simulated profiles.

5.7 Discussion

We investigated the magnetic field properties in a sample of galaxy clusters through the effect of beam depolarisation. We confirm the hint of the depolarisation trend with cluster projected radius seen in previous studies (Bonafede et al., 2011; Stuardi et al., 2020) with a highly statistically significant result, as shown in Figure 5.7. In this section, we discuss the implications of the results and the possible limitations of this study.

5.7.1 Cluster members versus background sources

One of the main questions that this work addressed is whether there is a difference between using cluster radio galaxies and background radio sources to probe the magnetic fields in galaxy clusters. One could expect such a difference because cluster radio galaxies might locally reshape the magnetic field and density structure, causing a bias in the RM and amount of depolarisation. Interactions with surrounding gas have been suggested to affect observed RM distributions in various powerful radio sources (e.g. 3C75, 3C465, 3C270 and 3C353; Rudnick & Blundell, 2003; Guidetti et al., 2011, 2012). However, this has not yet been shown in a statistical study.

Figure 5.8 and the log-rank comparison of the survival curves shown in Figure 5.9 demonstrated that, although near the cluster centres (i.e. $r < 0.5R_{500}$) it is difficult to have similar sampling of cluster members and background sources, at radii where we have similar sampling (i.e. $r > 0.5R_{500}$) the depolarisation of cluster members and background

radio sources is similar.

In Section 5.6.3 we modelled the difference between the amount of depolarisation expected for cluster members and background sources based on the different locations of the Faraday screens. We showed that this difference is minimal, and this difference is in line with the observed depolarisation trend for background sources and cluster members. This implies that there is no significant difference between using the depolarisation properties of cluster members or background sources as a probe of the cluster magnetic field.

Our results are in line with the findings by Bonafede et al. (2011) that used source angular size as a proxy of cluster membership and by Ensslin et al. (2003) that found that the biases from cluster members are not statistically significant. We note the caveat that the central region is still not well constrained with background sources.

When splitting the sample into NCC and CC clusters, there does seem to be a hint that there is a difference between background sources and cluster members near the cluster centres (Figure 5.12), although only a few sources were detected near the central regions in these splits. A possible explanation for this is that there might be a pronounced effect on the cluster ICM from a select number of powerful cluster radio galaxies, which is averaged out when using a larger sample of sources. This means that when only a few cluster members are used to probe the magnetic field strength, the results may still be biased.

We thus did not find any strong differences between the depolarisation of cluster members and background sources in the full sample. However, larger samples might be able to pick up more subtle effects.

5.7.2 Magnetic field parameters

The average magnetic field properties of the cluster sample were explored by combining the depolarisation of all detected sources, irrespective of their redshift. The results in Figure 5.20 showed that for all power spectrum indices, a central magnetic field strength higher than $B_0 = 1\,\mu$G is needed to explain the observed depolarisation trend. For models with power-law indices between $n = 1$ and $n = 4$, an average central magnetic field strength between 5 and $10\,\mu$G proved to be the best fit, although it was not possible to distinguish between these models. Our results agree with previous radio observations that have shown that clusters have central magnetic field strengths between 1 and $10\,\mu$G with power spectrum indices between $n = 2$ and $n = 4$ (Murgia et al., 2004; Govoni et al., 2006; Guidetti et al., 2008; Laing et al., 2008; Bonafede et al., 2010; Guidetti et al., 2010; Vacca et al., 2012; Govoni et al., 2017; Vacca et al., 2018) and values from magneto-hydrodynamic simulations of clusters (Domínguez-Fernández et al., 2019).

With larger cluster samples or deeper cluster surveys with polarisation information, such as the MeerKAT Galaxy Cluster Legacy Survey (MGCLS; Knowles et al., 2022), it might be possible to group clusters with similar density profiles together. This would reduce the scatter in the modelled depolarisation trend and allow for a more accurate determination of magnetic field parameters.

5.7.3 Cluster properties

We investigated possible differences in observed depolarisation as a function of various cluster properties, such as whether a cluster is undergoing a merger. The magnetic field might be altered by cluster mergers, during which a massive amount of energy is released

(up to 10^{64} ergs on a few Gigayear timescales; Sarazin 2002). It is expected that this energy is injected on large spatial scales and released to smaller and smaller scales through turbulent cascades (Vacca et al., 2018; Domínguez-Fernández et al., 2019). Observations find central magnetic field strengths of around $\sim 1\,\mu$G and fluctuation scales up to a few hundreds of kpc in merging systems, while relaxed systems show higher central field strengths of around $\sim 10\,\mu$G and much smaller fluctuation scales (less than a few tens of kpc) (Taylor et al., 2002; Clarke et al., 2001; Vacca et al., 2018). This implies that, theoretically, we would expect a stronger depolarisation effect in CC clusters.

We investigated whether there are differences in the depolarisation found in CC and NCC clusters in Figure 5.10. Surprisingly, we found that NCC clusters show more depolarisation than CC clusters outside the cooling-core region defined as $r > 0.2R_{500}$ (Figure 5.11). When modelling (Fig. 5.21), it was found that the same central magnetic field strength in CC clusters results in less depolarisation outside the core than in NCC clusters because the magnetic field was assumed to scale with the electron density normalised by the central electron density, which is generally higher in CC clusters than in NCC clusters. Hence, the observed differences could be explained by the same magnetic field parameters in the CC and NCC sample.

To investigate to what extent this result is dependent on the cluster classification method, we also checked different morphological parameters, splitting the sample using the cuspiness and central gas density parameters from Andrade-Santos et al. (2017). In these splits, NCC clusters still showed more depolarisation than CC clusters outside the core region. We note that we could not use the entire sample of clusters in this analysis because only 93 out of 124 clusters are observed with Chandra in Andrade-Santos et al. (2017). A literature search resulted in the dynamical states for 9 more galaxy clusters, which also does not change the observed depolarisation trends significantly.

Thus, we found no strong evidence that CC clusters have significantly higher magnetic field strengths or smaller fluctuations scales than NCC clusters in the central regions, although the uncertainties were large as shown in Figure 5.10. However, there is a hint that CC clusters indeed show more depolarisation inside the core region, as also found tentatively in Bonafede et al. (2011). Unfortunately, the typical size of the cooling cores in galaxy clusters is only 50-100 kpc, which is a region that is still poorly constrained in this study. The potential difference between the depolarisation in CC clusters and NCC clusters both inside and outside the core region should be investigated further because the sample size is still relatively small when splitting into multiple bins.

We also checked whether there is a correlation between magnetic field parameters and cluster mass or redshift. A positive correlation between magnetic field strength and cluster mass might be expected, as the observed radio power of giant radio halos is found to correlate with cluster mass, which can be reproduced by turbulent re-acceleration models with a positive scaling of the magnetic field strength with the cluster mass (Cassano et al., 2006a). However, the number of polarised sources detected in the high-redshift and high-mass cluster sample was too low to investigate a trend or differences between the low-mass and high-mass samples. A deeper survey such as MGCLS might be able to overcome this problem, although the sample of clusters should be large enough or carefully selected to break the redshift-mass selection bias discussed in Section 5.5.4.

Finally, we checked whether the presence of a radio halo in merging systems influences

the observed depolarisation trend. Models based on the turbulent re-acceleration scenario usually define a radio halo as observable if the break frequency of the radio halo spectrum is above the observing frequency. In these models, the break frequency of the spectrum depends on the magnetic field strength, the cluster mass and the merging state (Cassano et al., 2006b). To investigate whether the magnetic field properties of clusters with a radio halo are different, we split the merging cluster sample based on the detection of a radio halo. No significant differences were observed between the depolarisation of clusters with radio halos and without radio halos, suggesting that they have similar magnetic field parameters. We checked that the cluster mass and redshift distributions are similar, (with a KS-test resulting in p-values of 0.2 and 0.8, respectively,) so the results are not biased by this. While these clusters are all classified as merging clusters according to the X-ray morphological parameters, a more in-depth study of their merging state might reveal that the clusters without radio halos are only minor merging systems where less turbulence is generated than in major mergers, which would be in line with the findings by Cuciti et al. (2021a).

5.7.4 Possible caveats

In this section, we focus on the possible shortcomings of this work. Firstly, a single component external depolarisation model was used to fit the data. In reality, multiple interfering RM components can produce behaviour that is not proportional to λ^2 and even cause re-polarisation with decreasing frequencies (e.g. Pasetto et al., 2016). Observations of bright polarised sources observed at two different GHz frequencies have found that more than 25% of sources can show re-polarisation behaviour (Lamee et al., 2016). We have found in Section 5.3.2 that about 25% (193/819) polarised sources detected in this work are not well-fitted by the single component external depolarisation model. While fitting these sources with more complicated models (e.g. Brown et al., 2019) is beyond the scope of this work, we can briefly investigate how many sources show evidence of re-polarisation by allowing $\sigma_{\rm RM}$ to take negative values. This test resulted in 61 sources out of 819 that show a better fit with negative values of $\sigma_{\rm RM}$. However, most of these sources do not show strong evidence for re-polarisation and could be fit almost equally well with a value of $\sigma_{\rm RM}$ that is around 0, and as such do not change the resulting depolarisation curve significantly. Additionally, the resulting median depolarisation as a function of radius is similar when incorporating the sources with bad fits, which reinforces the fact that we are not biasing the results by omitting these sources. The difference between the number of re-polarising sources found here and in the literature could be caused by the fact we measure the polarisation over the entire bandwidth, where almost always some depolarisation occurs, rather than at only two points in frequency points where multiple components might interfere and show re-polarisation.

Secondly, to derive upper limits an assumption on the intrinsic polarisation p_0 had to be made. For these sources we assumed $p_0 = 0.022$, which was the median intrinsic polarisation fraction of sources detected at $r > 1.5R_{500}$. If this assumption was too high, we are biasing the results through the inclusion of the upper limits by calculating too much depolarisation. However, not including upper limits would cause a bias in the opposite direction by omitting preferentially the most depolarised sources. While it is impossible to determine the intrinsic polarisation value for unpolarised sources, we can show that the depolarisation curve is not dominated by upper limits. Because the upper limits were

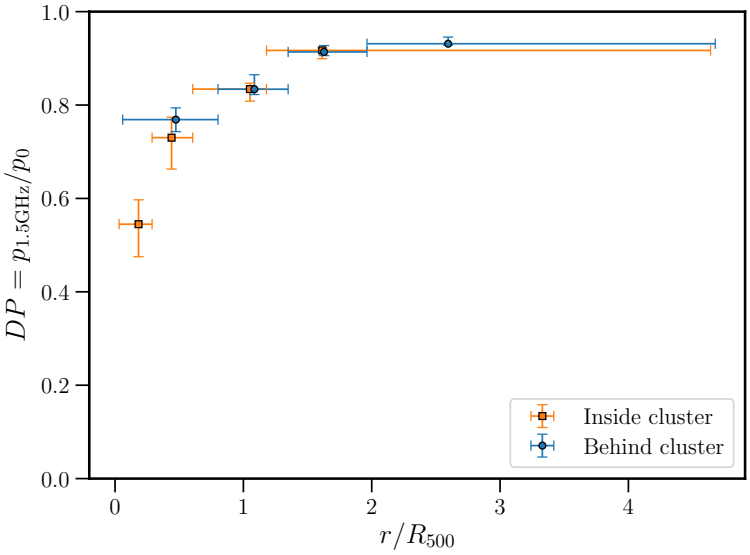

Figure 5.23: Median depolarisation ratio in different bins of radius without incorporating upper limits from unpolarised sources. Sources inside clusters are shown in green and sources behind clusters are shown in red. Compared to Figure 5.8, there is significantly less depolarisation in the lowest radius bin.

computed conservatively over the entire extent of the total intensity sources, only 196 out of the 6 807 unpolarised sources have an upper limit on the 1.5 GHz polarisation fraction that is below the assumed $p_0 = 0.022$. Thus, in terms of the number of sources, the upper limits are not dominating the results. The depolarisation trend with radius when omitting upper limits entirely is shown in Figure 5.23. Cluster members now show less depolarisation in the centre of the cluster because the most constraining upper limits on the depolarisation fraction are found near the cluster centres, where the brightest sources are detected. However, it is clear that even without the inclusion of the upper limits, the depolarisation trend with radius is still clearly detected.

Thirdly, for the upper limits, we computed a polarised flux threshold as described in Section 5.3.2, which was dependent on the varying background noise level. This introduces a bias because all clusters are observed approximately in the pointing centre, so the upper limits are generally higher at larger projected radii. This means we are underestimating the amount of depolarisation more strongly at the edges of the field. Section 5.8 investigates trends with angular distance from the pointing centre in detail and shows that this bias is very small compared to the observed depolarisation trend. Because the clusters are all observed near the pointing centre, other trends with projected distance from the cluster centre could also (partially) be due to instrumental or observational trends with angular distance from the pointing centre. These biases are also investigated in detail in Appendix 5.8, where we present that there are indeed sources of bias, but through a Monte Carlo experiment we show that the effect of these biases is minimal compared to the observed

depolarisation effect.

Fourthly, the effect of off-axis polarisation leakage can also mimic depolarisation because of the frequency dependence of the primary beam at a fixed angular distance from the pointing centre. This effect is expected to be at the order of the 1% level for VLA L-band observations (Jagannathan et al., 2017). To correct for this effect, full direction-dependent primary beam corrections need to be made (a-term corrections), which is possible for example with IDG (van der Tol et al., 2018), but is computationally expensive for large sample sizes and beyond the scope of this work. However, the leakage effect is in the opposite direction from the observed trend because polarisation leakage effects are stronger near the periphery of the fields, while the observed depolarisation effect is stronger near the centre of the field. Additionally, we can see in Figure 5.6 and Figure 5.25c that there is no significant increase in the measured intrinsic polarisation fraction of radio sources as a function of angular separation to the pointing centre. This implies that off-axis leakage effects are negligible for this study.

Lastly, electron density profiles were not available for all clusters studied in this work, with the 24 new clusters from the PSZ1 and PSZ2 catalogues not having Chandra observations. However, all clusters have been observed through the Sunyaev-Zel'dovich effect, which probes the integrated pressure along the line of sight. It has been shown that the pressure profile of galaxy clusters follows a relatively universal shape, called the universal pressure profile (UPP; Nagai et al., 2007; Arnaud et al., 2010a). This profile scales in terms of the cluster properties M_{500}, R_{500} and P_{500}, where P_{500} is the characteristic pressure at an overdensity of 500. With an assumption on the cluster temperature, we can thus calculate a general electron density profile from the UPP to include these 24 clusters in our modelling. To derive the electron density profiles, we use the best-fit parameters for the UPP fit on Planck ESZ clusters from Planck Collaboration et al. (2013) combined with the best-fit mass-temperature relation on ESZ clusters from Lovisari et al. (2020). Including these 24 additional clusters in our modelling results in slightly more average depolarisation as a function of radius, but the final results do not change significantly, as shown in Figure 5.24. Thus, assuming a universal pressure profile might be useful for future studies of larger, or higher redshift samples of clusters where X-ray observations are not available.

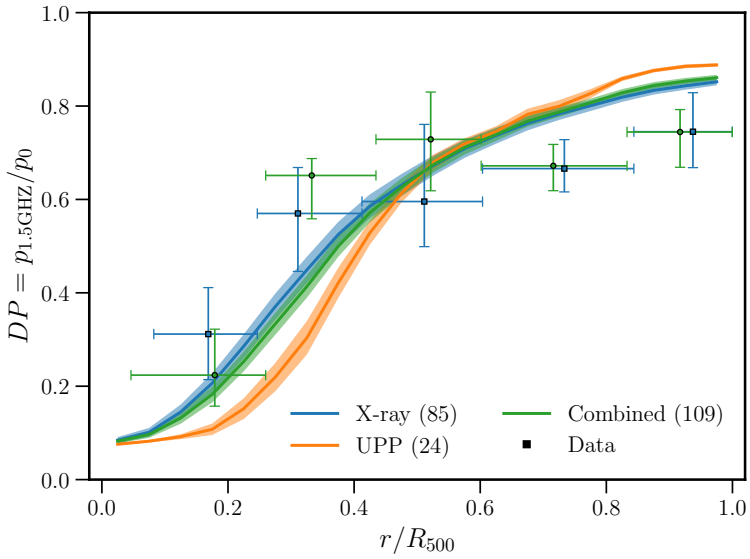

Figure 5.24: Comparison of the median observed depolarisation ratio with the modelled depolarisation ratio profile using only clusters that have X-ray observations (blue) and all clusters (green) by calculating electron density profiles from a universal pressure profile (orange). The model uncertainty interval indicates the standard error on the mean of the simulated profiles.

5.8 Conclusion

In this work, we have utilised VLA L-band polarisation observations of a sample of 124 clusters from the Chandra-Planck Legacy Program for Massive Clusters of Galaxies to measure the depolarisation properties of radio sources inside and behind clusters. The main aims of this work were to use the depolarisation ratio to i) determine the average magnetic field properties in clusters, ii) investigate whether there is a difference between using cluster members and background sources as probes and iii) quantify the dependence of the magnetic field with cluster properties such as mass and dynamical state. We compared the data with modelled depolarisation trends by assuming the magnetic field is a Gaussian random field that follows the thermal electron density profile of the cluster. For the first time in a statistical polarisation study, we took into account the individual electron density profiles of different clusters when modelling the depolarisation ratio. We showed that the depolarisation ratio is a good probe of the magnetic fields in galaxy clusters. Our main results can be summarised as follows:

1. We clearly detect a trend of radio sources becoming more depolarised as they move (in projection) towards the cluster centre. This trend can be explained by models with a central magnetic field strength of $5-10\,\mu$G with power-law indices between $n=1$ and $n=4$ and cannot be easily attributed to observational or other systematic biases in the analysis.

2. The individual thermal electron density profiles of the clusters should be taken into account when modelling multiple clusters, as the theoretical depolarisation in separate clusters can be significantly different, even at similar electron column densities. This scatter might be overcome with larger samples when clusters with similar density profiles are grouped together.

3. The relation between the simulated beam depolarisation and fluctuation scale spectral slope is not monotonic. We found that simulated beam depolarisation can increase or decrease with increasing fluctuation scale spectral slope n depending on the size of the observing beam and the location in the cluster.

4. We found no statistically significant difference between the depolarisation properties of background and cluster sources, although background sources were rare to detect near the cluster centre, where cluster members were most often detected. The fact that we see no strong difference implies that the interaction between the radio sources in clusters and their local surrounding medium generally does not strongly influence their polarisation properties. Thus, in statistical studies, both in-cluster and background sources can be used as a probe of the magnetic fields.

5. Disturbed (non-cool-core) clusters showed more depolarisation in the $0.2-1.0R_{500}$ region than cool-core clusters. After modelling, this effect was not strong enough to warrant different magnetic field parameters for disturbed or relaxed systems. While literature suggests that cool-core clusters have stronger magnetic fields inside the core region and should thus show more depolarisation, we did not significantly detect different polarisation fractions inside $0.2R500$ in cool-core and non-cool-core clusters. However, the uncertainties were large due to the low number of sources, and the most central (~100 kpc) cooling core region is even more unconstrained in this study and should be investigated further.

6. The observed depolarisation in merging clusters that show a radio halo and merging galaxy clusters that do not show a radio halo is similar. This implies that the presence or absence of a radio halo in merging clusters is likely not dominated by the cluster magnetic field properties.

The biggest limitation of the study of magnetic fields in clusters through depolarisation is currently the number of polarised sources that are detected. With deeper cluster surveys and the advent of the SKA, depolarisation of radio sources will be a promising tool to study cluster magnetic fields.

ACKNOWLEDGEMENTS

The authors would like to thank the anonymous referee for the comments and suggestions that improved the quality of the manuscript. EO and RJvW acknowledge support from the VIDI research programme with project number 639.042.729, which is financed by the Netherlands Organisation for Scientific Research (NWO). LR acknowledges partial support from U.S. National Science Foundation grant AST17-14205 to the University of

Minnesota. AB acknowledges support from the ERC Starting Grant 'DRANOEL', number 714245 and from the from Italian MIUR grant FARE 'SMS'. KJD acknowledges funding from the European Union's Horizon 2020 research and innovation programme under the Marie Skłodowska-Curie grant agreement No. 892117 (HIZRAD). Basic research in radio astronomy at the Naval Research Laboratory is supported by 6.1 Base funding. This work was performed using the compute resources from the Academic Leiden Interdisciplinary Cluster Environment (ALICE) provided by Leiden University. This paper has made use of observational material taken with an NRAO instrument. The National Radio Astronomy Observatory is a facility of the National Science Foundation operated under cooperative agreement by Associated Universities, Inc. The Pan-STARRS1 Surveys (PS1) and the PS1 public science archive have been made possible through contributions by the Institute for Astronomy, the University of Hawaii, the Pan-STARRS Project Office, the Max-Planck Society and its participating institutes, the Max Planck Institute for Astronomy, Heidelberg and the Max Planck Institute for Extraterrestrial Physics, Garching, The Johns Hopkins University, Durham University, the University of Edinburgh, the Queen's University Belfast, the Harvard-Smithsonian Center for Astrophysics, the Las Cumbres Observatory Global Telescope Network Incorporated, the National Central University of Taiwan, the Space Telescope Science Institute, the National Aeronautics and Space Administration under Grant No. NNX08AR22G issued through the Planetary Science Division of the NASA Science Mission Directorate, the National Science Foundation Grant No. AST-1238877, the University of Maryland, Eotvos Lorand University (ELTE), the Los Alamos National Laboratory, and the Gordon and Betty Moore Foundation. The Legacy Surveys consist of three individual and complementary projects: the Dark Energy Camera Legacy Survey (DECaLS; Proposal ID 2014B-0404; PIs: David Schlegel and Arjun Dey), the Beijing-Arizona Sky Survey (BASS; NOAO Prop. ID 2015A-0801; PIs: Zhou Xu and Xiaohui Fan), and the Mayall z-band Legacy Survey (MzLS; Prop. ID 2016A-0453; PI: Arjun Dey). DECaLS, BASS and MzLS together include data obtained, respectively, at the Blanco telescope, Cerro Tololo Inter-American Observatory, NSF's NOIRLab; the Bok telescope, Steward Observatory, University of Arizona; and the Mayall telescope, Kitt Peak National Observatory, NOIRLab. The Legacy Surveys project is honoured to be permitted to conduct astronomical research on Iolkam Du'ag (Kitt Peak), a mountain with particular significance to the Tohono O'odham Nation. SDSS-IV is managed by the Astrophysical Research Consortium for the Participating Institutions of the SDSS Collaboration including the Brazilian Participation Group, the Carnegie Institution for Science, Carnegie Mellon University, Center for Astrophysics | Harvard & Smithsonian, the Chilean Participation Group, the French Participation Group, Instituto de Astrofísica de Canarias, The Johns Hopkins University, Kavli Institute for the Physics and Mathematics of the Universe (IPMU) / University of Tokyo, the Korean Participation Group, Lawrence Berkeley National Laboratory, Leibniz Institut für Astrophysik Potsdam (AIP), Max-Planck-Institut für Astronomie (MPIA Heidelberg), Max-Planck-Institut für Astrophysik (MPA Garching), Max-Planck-Institut für Extraterrestrische Physik (MPE), National Astronomical Observatories of China, New Mexico State University, New York University, University of Notre Dame, Observatário Nacional / MCTI, The Ohio State University, Pennsylvania State University, Shanghai Astronomical Observatory, United Kingdom Participation Group, Universidad Nacional Autónoma de México, University of Arizona, University of Colorado Boulder, University of Oxford, University of Portsmouth, University of Utah, University of Virginia, University of Washington, University of Wisconsin, Vanderbilt University, and Yale University This research has made use of the NASA/IPAC Extragalactic Database (NED), which is operated by the Jet Propulsion Laboratory, California Institute of Technology, under contract with the National Aeronautics and Space Administration. This research has made use of NASA's Astrophysics Data System (ADS).

Appendix I: Possible biases

This appendix aims to investigate possible biases that might affect the analysis. The polarisation properties of radio sources might be influenced by other source properties such as size, total intensity, and whether the source is a single or multi-component source. If, for example, multi-component sources are easier to detect near the pointing centre and have different polarisation properties than single-component sources, the observed depolarisation effect with projected radius might be biased. This is because all clusters have been observed approximately in the pointing centre. As mentioned in Section 5.7.4, this also introduces a bias through the inclusion of the upper limits because the upper limits on the fractional polarisation are generally higher at larger projected radii due to the primary beam response. In the first section of this appendix, we check whether biases because of source properties are present, and in the second section we quantify the biases through a Monte Carlo experiment.

Source properties

To investigate whether there is a dependence between observed source properties and polarisation, taking into account the distance to the pointing centre, we plot running medians of various quantities versus the angular distance to the pointing centre. The uncertainty, $\sigma_{\pm}$, on the running median M is calculated as in Lamee et al. (2016),

$$\sigma_{\pm} = |M - [p_{16}, p_{84}]/\ \sqrt{N}, \tag{5.27}$$

where p_x denotes the x-th percentile of the distribution, and N is the number of points in a bin. The amount of correlation is quantified by the Pearson (Pearson, 1895) and Spearman (Spearman, 1904) coefficients, shown in Table 5.4. We define weak correlation for values of Pearson $|r| \leq 0.3$, moderate correlation for $0.3 < |r| \leq 0.7$ and strong correlation for $r > 0.7$, using the common cutoff p-value of 0.05 for statistical significance. Because the Pearson coefficient only measures the linear relationship we also report the Spearman coefficient. The monotonicity of the correlation is given by the Spearman coefficient, where an absolute value of 1 indicates a perfectly monotonic relationship.

We plot in Figure 5.25a the running median of the observed polarised source major axis versus the angular distance to the pointing centre. As the figure shows, there is some dependence of polarised source size on angular separation. Cluster members show an increase in median source size around 5 arcminutes from the pointing centre, while for background sources there is no significant correlation. The median source size is larger for cluster members than for background sources, which is expected simply because they are nearby sources.

The total flux density versus angular separation is shown in Figure 5.25b. The background population clearly shows the effect of the primary beam response. Cluster members are less affected by this, possibly because they are all low redshift ($z < 0.35$) sources for which we are already sensitive enough to probe the majority of the cluster population. There is an excess of bright cluster members in the centre of the image, indicated by the peak at low angular separation. This means that we are detecting the brightest cluster members preferentially in the centre of the images. This is not unexpected because the centres of the clusters lie near the centres of the images, but it might bias the results if the total flux density is correlated with polarisation properties.

Although we are mainly interested in the depolarisation of radio sources, it is important to investigate the best-fit intrinsic polarisation fraction as a function of angular distance. Because of the chosen model and finite amount of bandwidth, there is a degeneracy between p_0 and $\sigma_{\rm RM}$ (see Fig. 5.4). While this degeneracy is simply a result of the fitting, real correlations between p_0 and $\sigma_{\rm RM}$ have been claimed before in the literature (e.g. Lamee et al., 2016). It is therefore important to inspect trends of p_0 with angular separation because that could create biases in the depolarisation trend. In Figure 5.25c we plot the best-fit intrinsic polarisation fraction. Here we see that there is a weak correlation with angular distance for cluster members and no significant correlation for background sources. The fact that the median p_0 is lower near the centre of the image is likely (at least partly) caused by the fact that the brightest cluster members often lie in the centre of the cluster (Fig.5.25b), where it is thus possible to detect smaller polarisation fractions.

Lastly, there might be a difference in polarisation properties of single and multi-component sources, so we also plot this separation in Figure 5.25d. We note that multi-component sources are often, but not always, cluster members. Both populations show no evidence for a strong correlation of the intrinsic polarisation with angular separation, and both populations have similar distributions of intrinsic polarisation, so it is unlikely that this is biasing the results significantly.

Now that we have established that the cluster population has a higher median flux density in the centre of the images and that the intrinsic polarisation fraction of cluster members is generally lower in the centre of the images, it is important to know whether these variables correlate with the depolarisation parameter $\sigma_{\rm RM}$. Figures 5.26 and 5.27 show the trend of total flux density and intrinsic polarisation fraction with $\sigma_{\rm RM}$. We see for background sources no clear correlation between total flux density and depolarisation. Cluster members do show that the brightest sources show more depolarisation. However, this is to be expected in the case of a magnetised depolarising intracluster medium (ICM) in the cluster centre if the brightest cluster members are also found preferentially in the cluster centre, which is indeed the case as shown by Figure 5.25b. The question remains how much of this effect is a real effect and how much is caused by biases such as only picking up the most depolarised sources near the centre of the cluster. This is addressed in the next section. Figure 5.27 shows the degeneracy between p_0 and $\sigma_{\rm RM}$, particularly for large values of $\sigma_{\rm RM}$. It is interesting that this trend implies that more depolarised sources have larger p_0, while Figure 5.25c showed that smaller values of p_0 are generally found more towards the cluster centre. This trend would therefore cause a bias in the direction opposite to the trend expected from a depolarising ICM.

Monte Carlo experiment

The previous section showed that there are no strong trends detected between source properties and polarisation properties or angular radius to the pointing centre, but there are weak trends in the data that possibly bias the results. Most notably, we have seen that the brightest cluster members are preferentially detected in the centre of the images and it is this class of sources that shows the most depolarisation. To quantify the bias introduced by selection effects and the fitting procedure, we took a Monte Carlo approach, simulating polarised radio sources with random properties that are taken from distributions that are representative of the data. If, through the effect of the choices made during the

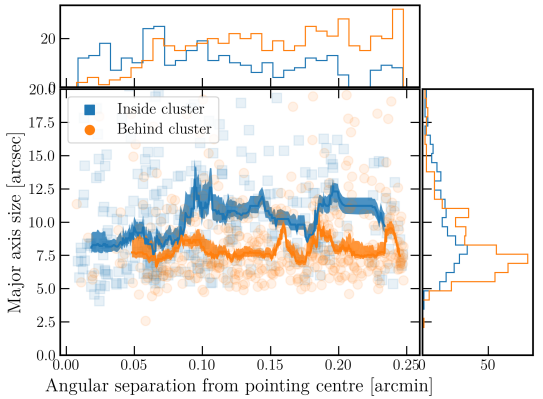

(a) Polarised source sizes

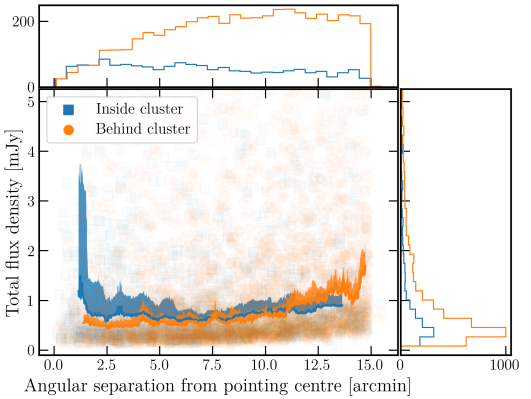

(b) Total Stokes I flux density

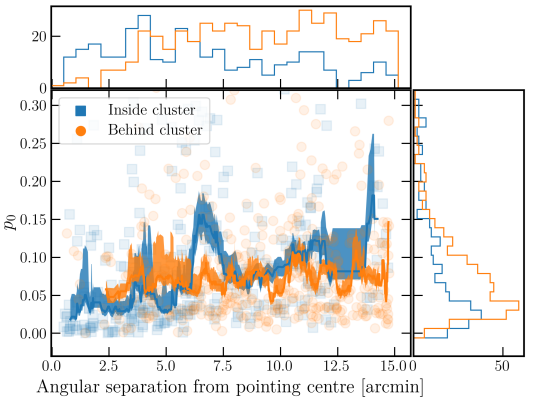

(c) Intrinsic polarisation fraction

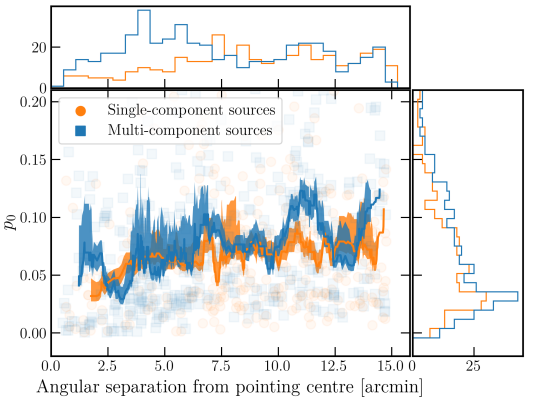

(d) Intrinsic polarisation fraction for single- and multi-component sources

Figure 5.25: Various quantities against angular separation separately for cluster members and background sources. The running median is shown with uncertainties in the shaded region. Histograms show the projected distributions along the axes.

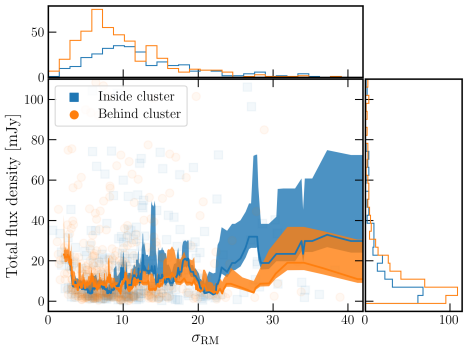

Figure 5.26: Same as Figure 5.25, but for total Stokes I flux density against depolarisation parameter $\sigma_{\rm RM}$ in units of rad m^{-2}.

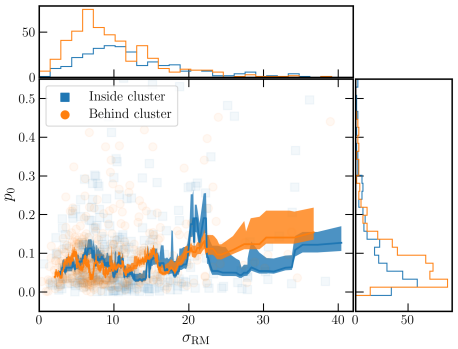

Figure 5.27: Same as Figure 5.25, but for intrinsic polarisation fraction against depolarisation parameter $\sigma_{\rm RM}$ in units of rad m^{-2}.

Table 5.4: Pearson and Spearman correlation coefficients and accompanying p-values for various combinations of parameters shown in Figures 5.25, 5.26 and 5.27.

Population	Pearson (r, p-value)	Spearman (r, p-value)	Conclusion[a]
Major axis size - θ_p cluster members	(0.15, 7.4×10^{-3})	(0.22, 8.5×10^{-5})	weak correlation
Major axis size - θ_p background sources	(0.018, 6.9×10^{-1})	(0.070, 1.2×10^{-1})	no significant correlation
Total Flux - θ_p cluster members	(-0.087, 6.6×10^{-4})	(0.0080, 7.5×10^{-1})	weak correlation
Total Flux - θ_p background sources	(-0.021, 1.4×10^{-1})	(0.26, 8.3×10^{-79})	non-monotonic correlation
p_0 - θ_p cluster members	(0.15, 7.7×10^{-3})	(0.33, 1.6×10^{-9})	weak correlation
p_0 - θ_p background sources	(-0.041, 3.7×10^{-1})	(0.0020, 9.7×10^{-1})	no significant correlation
p_0 - θ_p multi-component sources	(0.083, 1.28×10^{-1})	(0.116, 3.35×10^{-2})	no significant correlation
p_0 - θ_p single-component sources	(0.001, 9.87×10^{-1})	(0.183, 6.62×10^{-5})	no significant correlation
Total Flux - $\sigma_{\rm RM}$ cluster members	(-0.19, 1.0×10^{-3})	(-0.15, 8.1×10^{-3})	weak correlation
Total Flux - $\sigma_{\rm RM}$ background sources	(0.0060, 9.0×10^{-1})	(0.062, 1.8×10^{-1})	no significant correlation
p_0 - $\sigma_{\rm RM}$ cluster members	(0.097, 8.8×10^{-2})	(0.045, 4.3×10^{-1})	no significant correlation
p_0 - $\sigma_{\rm RM}$ background sources	(0.25, 5.2×10^{-8})	(0.19, 4.0×10^{-5})	weak correlation

Notes. [(a)] A cutoff p-value of 0.05 is used for statistical significance, and the correlation is defined as weak for values of Pearson $|r| \leq 0.3$.

analysis or because of the radio source properties such as size and flux density a bias is introduced in the depolarisation curve, we should find that bias when employing the same methods on a sample of completely randomly (de)polarised sources. The distributions used to generate random polarised sources for this experiment are shown in Figure 5.28, where we have fit gamma distributions to the strictly positive values p_0 and $\sigma_{\rm RM}$ and used a Cauchy distribution for RM to account for the large peak around RM=0. The initial polarisation angle χ_0 was simply drawn from a uniform distribution between 0 and π. The steps taken in the Monte Carlo experiment were as follows. First, we calculated the total flux density per channel of all detected total intensity sources. Then, for each total intensity source, we randomly drew a value of p_0, RM, $\sigma_{\rm RM}$ and χ_0 from the representative probability distribution functions. Third, we computed simulated Stokes Q and U emission using the external depolarisation model given in Eq. 5.12 with the randomly drawn parameters. Then, we determined which sources are detected in polarisation at a 5σ level given the

varying background noise due to the primary beam response. Finally, we fitted the detected sources with the MCMC IQU fitting code and calculated upper limits on the undetected sources as explained in Section 5.3.2. The resulting best-fit parameters and upper limits were again used to find the median depolarisation in bins of projected radius.

This approach resulted in 1050 simulated sources detected in polarisation. The resulting median depolarisation trend with projected distance to the cluster centre is shown in Figure 5.29 for simulated sources. Figure 5.29 shows that there is indeed a very small bias from selection effects or fitting, with a minor trend showing slightly more depolarisation near the cluster centres than at the cluster outskirts. However, this trend is only a small fraction of the real detected trend in Figure 5.8. Thus, even though there are significant correlations as shown in Table 5.4, they cause only a minimal bias because they have small correlation coefficients. This means that if the observed sources were a population with random polarisation parameters, there would not be a strongly detected depolarisation trend with radius. The striking difference between Figure 5.29 and the depolarisation trend detected in the real data shown in Figure 5.8 makes a strong case that the observed depolarisation trend cannot be explained only by selection effects or biases.

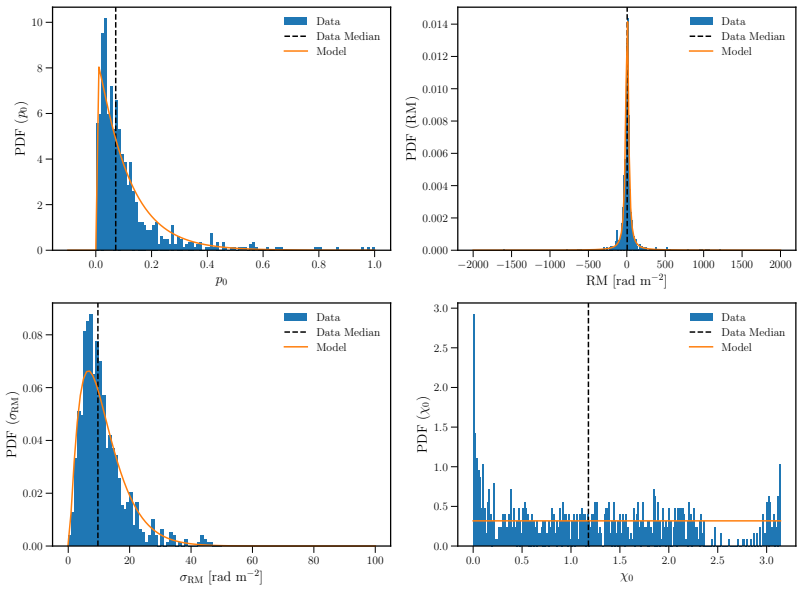

Figure 5.28: Probability distribution functions used to generate polarised radio sources during the Monte Carlo analysis shown in orange. The distribution of the real data is shown in blue.

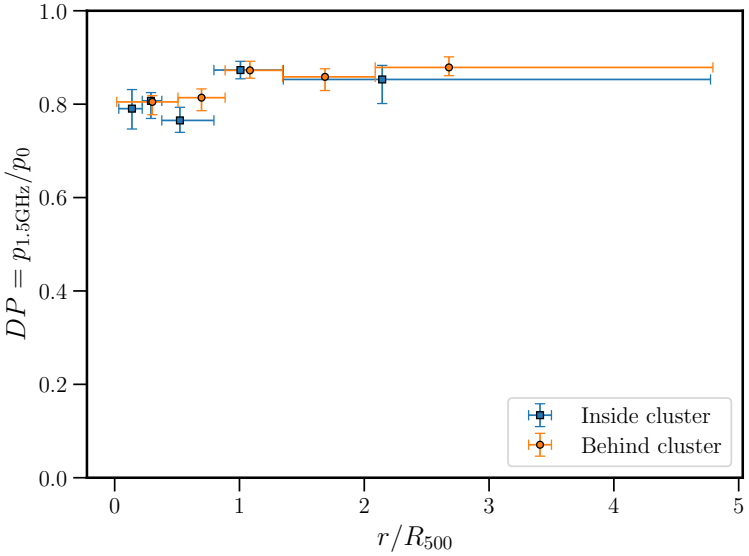

Figure 5.29: Median of the Kaplan-Meier estimate of the depolarisation ratio survival function in different bins of radius for simulated data. The bin width is chosen such that each bin contains an equal number of polarised sources and is denoted by the horizontal lines. The points are plotted at the median radius in each bin

Appendix II: Full sample plots

For completeness, we plot in Figures 5.30 to 5.32 the full sample of data-points that have been summarised with the KM estimator in Figures 5.8 to 5.14. Figure 5.33 shows an alternative visualisation of the full sample of data points, which also clearly shows the trend of sources becoming more depolarised as the projected radius and column densities increase. Finally, Figure 5.34 shows the modelled depolarisation profiles for all clusters where X-ray data was available, for a single set of magnetic field parameters.

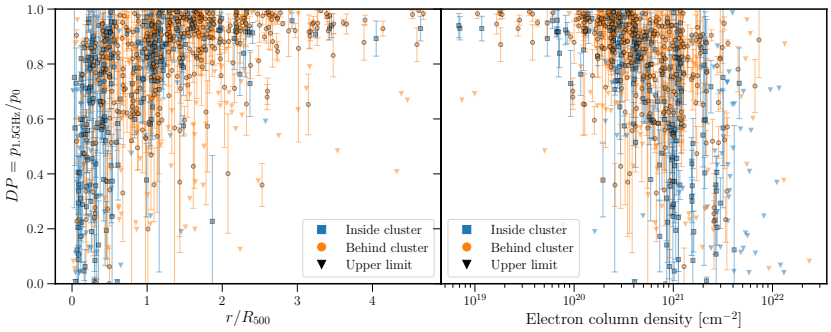

Figure 5.30: Depolarisation ratio and relevant upper limits for all sources as a function of projected radius and column density. Points are coloured by their position along the line-of-sight with respect to the nearest cluster.

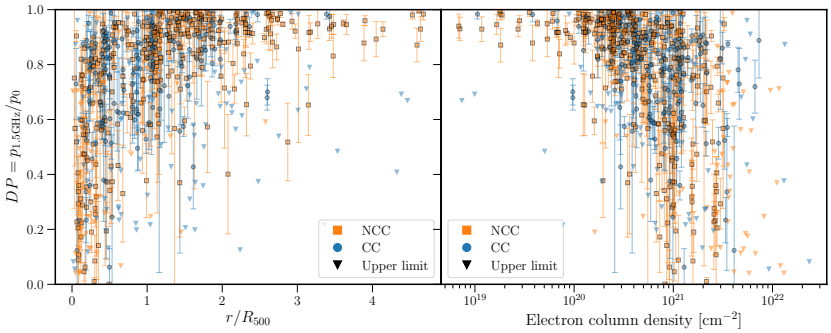

Figure 5.31: Depolarisation ratio and relevant upper limits for all sources as a function of projected radius and column density. Points are coloured by the dynamic state of the cluster, indicated by non-cool-core (NCC) and cool-core (CC).

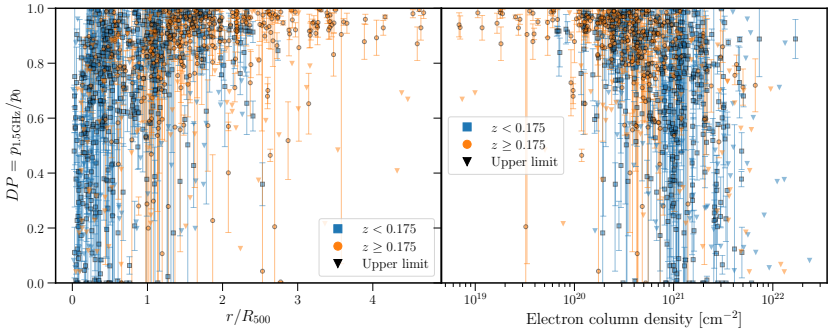

Figure 5.32: Depolarisation ratio and relevant upper limits for all sources as a function of projected radius and column density. Points are coloured according to the redshift of the cluster.

5

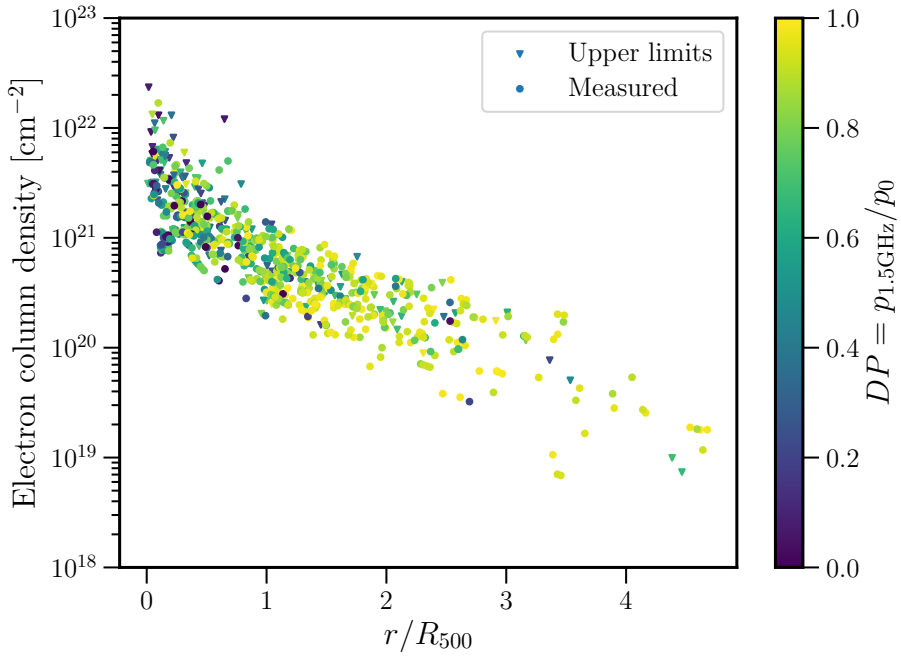

Figure 5.33: Full sample of measured values and upper limits on the depolarisation of radio sources as a function of both electron column density and projected radius. The points are coloured by the depolarisation value.

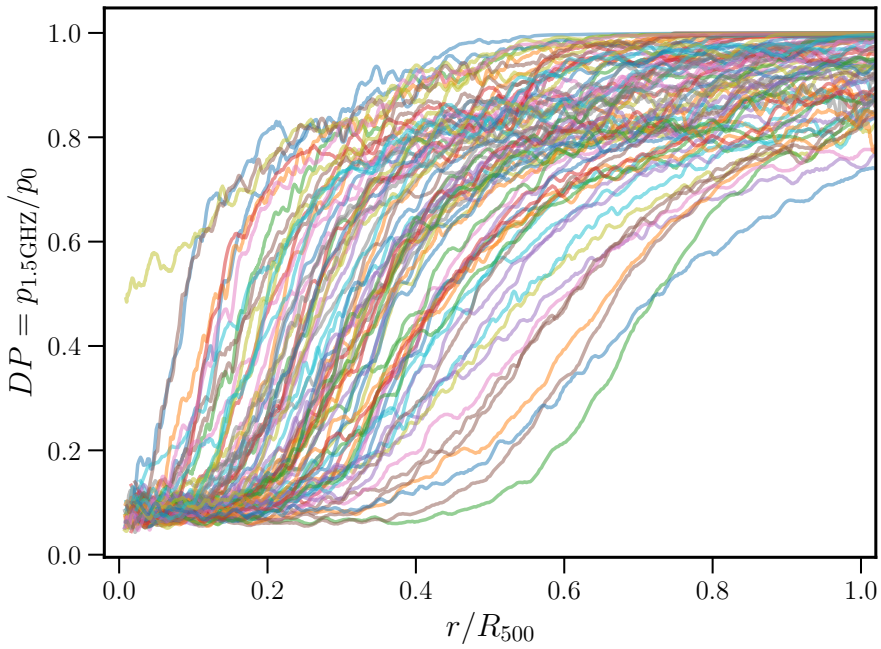

Figure 5.34: All simulated depolarisation ratio profiles for the full sample of simulated clusters. The assumed parameters for the magnetic field are $B_0 = 5.0\,\mu$G, $n = 3$ and $\eta = 0.5$.

Appendix III: Polarised source catalogue

Table H.1: First 30 rows of the catalogue of 819 polarised radio sources that were detected in this work. The full table is available at the CDS via anonymous ftp to `cdsarc.u-strasbg.fr` (130.79.128.5) or via `http://cdsarc.u-strasbg.fr/viz-bin/cat/J/A+A/665/A71`.

RA [deg]	DEC [deg]	Maj [']	Min [']	PA [deg]	p_0	χ_0 [rad]	RM [rad m^{-2}]	$\sigma_{\rm RM}$ [rad m^{-2}]	I_0 [mJy]	α	$\chi^2_{\rm QU}$	$z_{\rm best}$	$z_{\rm best}$ source	θ_P [arcmin]	r/R_{500}	Cluster	RA$_{\rm opt}$ [deg]	DEC$_{\rm opt}$ [deg]	Multi component	Flagged	Note
-132.2610	5.6140	8.2	5.8	90	$0.102^{+0.005}_{-0.005}$	$0.911^{+0.036}_{-0.036}$	-137^{+1}_{-1}	10^{+0}_{-0}	$25.0^{+0.3}_{-0.3}$	$-0.81^{+0.03}_{-0.03}$	171	0.584 ± 0.040	2	8.06	0.6	G006.47+50.54	227.7304	5.6153	True	True	
-132.2780	5.6184	4.9	4.0	52	$0.040^{+0.010}_{-0.008}$	$3.030^{+0.080}_{-0.137}$	-68^{+1}_{-2}	7^{+1}_{-2}	$5.6^{+0.1}_{-0.1}$	$-0.95^{+0.05}_{-0.05}$	56	0.584 ± 0.040	2	7.80	0.6	G006.47+50.54	227.7304	5.6153	True	False	
-132.2767	5.6172	5.4	3.8	68	$0.048^{+0.015}_{-0.012}$	$0.091^{+0.131}_{-0.067}$	-113^{+3}_{-4}	13^{+4}_{-3}	$7.3^{+0.1}_{-0.1}$	$-0.98^{+0.04}_{-0.04}$	66	0.584 ± 0.040	2	7.87	0.6	G006.47+50.54	227.7304	5.6153	True	False	
-111.9212	5.5698	6.2	5.7	59	$0.058^{+0.010}_{-0.009}$	$1.943^{+0.125}_{-0.130}$	8^{+4}_{-3}	17^{+2}_{-2}	$20.2^{+0.2}_{-0.2}$	$-1.20^{+0.03}_{-0.03}$	75	0.581 ± 1.268	2	6.10	0.8	G021.09+33.25	248.0775	5.5694	False	False	Counterpart unsure
-111.9898	5.4658	7.8	5.9	41	$0.033^{+0.003}_{-0.003}$	$2.209^{+0.092}_{-0.124}$	4^{+2}_{-2}	3^{+2}_{-1}	$25.8^{+0.3}_{-0.3}$	$-0.86^{+0.03}_{-0.03}$	104	1.675 ± 0.611	2	12.44	1.7	G021.09+33.25	248.0106	5.4644	True	True	
-111.7294	5.5442	12.0	6.5	76	$0.561^{+0.300}_{-0.091}$	$2.254^{+0.442}_{-2.220}$	-36^{+10}_{-8}	15^{+1}_{-1}	$3.2^{+0.2}_{-0.2}$	$-2.30^{+0.17}_{-0.18}$	151	-	-	6.00	0.8	G021.09+33.25	-	-	False	True	No optical counterpart.
-111.9211	5.4755	7.1	6.3	39	$0.039^{+0.003}_{-0.003}$	$0.458^{+0.078}_{-0.080}$	28^{+2}_{-2}	14^{+1}_{-1}	$38.0^{+0.4}_{-0.4}$	$-0.43^{+0.03}_{-0.03}$	131	2.389 ± 0.208	2	8.98	1.2	G021.09+33.25	-	-	False	True	No optical counterpart.
-111.9888	5.4639	7.7	6.2	49	$0.033^{+0.002}_{-0.002}$	$0.015^{+0.023}_{-0.011}$	-2^{+0}_{-1}	3^{+2}_{-1}	$27.8^{+0.3}_{-0.3}$	$-0.77^{+0.03}_{-0.03}$	152	1.675 ± 0.611	2	12.46	1.7	G021.09+33.25	248.0106	5.4644	True	True	
-48.0417	-17.7068	7.7	7.1	111	$0.053^{+0.014}_{-0.011}$	$0.914^{+0.302}_{-0.303}$	-31^{+6}_{-6}	7^{+3}_{-2}	$5.5^{+0.2}_{-0.1}$	$-1.63^{+0.07}_{-0.07}$	57	-	-	8.50	1.4	G028.77-33.56	-	-	False	True	No optical counterpart.
-47.9835	-17.7248	7.2	7.2	103	$0.093^{+0.028}_{-0.023}$	$0.961^{+0.354}_{-0.364}$	-24^{+9}_{-8}	14^{+3}_{-2}	$4.6^{+0.1}_{-0.1}$	$-2.04^{+0.09}_{-0.09}$	73	-	-	5.66	0.9	G028.77-33.56	-	-	False	False	No optical counterpart.
-48.0167	-17.7220	7.8	6.5	89	$0.023^{+0.008}_{-0.007}$	$1.854^{+0.389}_{-0.437}$	-42^{+9}_{-9}	11^{+3}_{-3}	$11.9^{+0.2}_{-0.2}$	$-1.51^{+0.04}_{-0.04}$	59	-	-	6.87	1.1	G028.77-33.56	-	-	False	False	No optical counterpart.
-119.4219	16.0547	8.8	8.5	27	$0.108^{+0.004}_{-0.003}$	$1.829^{+0.031}_{-0.030}$	-136^{+1}_{-1}	14^{+0}_{-0}	$40.2^{+0.6}_{-0.6}$	$-0.78^{+0.03}_{-0.03}$	215	0.282 ± 0.077	2	0.95	0.0	G029.00+44.56	240.5791	16.0553	False	True	Counterpart unsure
-119.3140	16.1258	7.9	5.5	74	$0.020^{+0.335}_{-0.006}$	$1.718^{+0.472}_{-0.568}$	-100^{+24}_{-12}	8^{+2997}_{-3}	$11.3^{+0.3}_{-0.2}$	$-0.96^{+0.05}_{-0.05}$	68	-	-	8.37	0.3	G029.00+44.56	-	-	False	True	No optical counterpart.
-119.6253	16.0712	8.4	8.0	94	$0.073^{+0.010}_{-0.007}$	$0.012^{+2.539}_{-0.010}$	4^{+10}_{-1}	4^{+2}_{-1}	$14.1^{+0.3}_{-0.3}$	$-0.77^{+0.06}_{-0.06}$	235	1.285 ± 0.435	2	10.83	0.4	G029.00+44.56	-	-	False	True	No optical counterpart.
-119.4438	15.8343	7.9	6.2	40	$0.024^{+0.007}_{-0.005}$	$1.497^{+0.249}_{-0.236}$	34^{+4}_{-4}	6^{+4}_{-2}	$16.7^{+0.3}_{-0.4}$	$-1.07^{+0.06}_{-0.05}$	61	-	-	13.16	0.5	G029.00+44.56	-	-	False	False	No optical counterpart.
-119.4234	16.1195	8.5	8.3	66	$0.050^{+0.004}_{-0.005}$	$2.229^{+0.056}_{-0.111}$	141^{+1}_{-1}	10^{+1}_{-1}	$32.6^{+0.5}_{-0.5}$	$-0.86^{+0.03}_{-0.03}$	163	0.385 ± 0.000	0	4.05	0.2	G029.00+44.56	240.5783	16.1194	False	True	
-152.5871	26.5863	6.1	5.3	137	$0.084^{+0.023}_{-0.018}$	$0.840^{+0.217}_{-0.220}$	-26^{+4}_{-4}	8^{+3}_{-2}	$3.8^{+0.1}_{-0.1}$	$-1.17^{+0.11}_{-0.11}$	57	-	-	9.07	0.6	G033.78+77.16	-	-	False	False	No optical counterpart.
-152.7815	26.5929	18.0	9.2	176	$0.001^{+0.000}_{-0.000}$	$1.239^{+0.108}_{-0.109}$	21^{+2}_{-2}	7^{+2}_{-2}	$1238.8^{+14.5}_{-14.5}$	$-0.99^{+0.03}_{-0.03}$	733	0.250 ± 0.114	2	1.45	0.1	G033.78+77.16	207.2186	26.5931	False	True	
-152.6178	26.5824	6.1	6.0	176	$0.098^{+0.062}_{-0.034}$	$0.941^{+0.557}_{-0.519}$	54^{+19}_{-26}	33^{+6}_{-4}	$24.2^{+0.3}_{-0.3}$	$-0.51^{+0.03}_{-0.03}$	107	0.793 ± 0.078	2	7.43	0.5	G033.78+77.16	207.3823	26.5824	False	False	
-152.5220	26.5313	7.0	6.1	82	$0.045^{+0.006}_{-0.006}$	$1.807^{+0.117}_{-0.117}$	2^{+3}_{-3}	14^{+1}_{-1}	$34.8^{+0.5}_{-0.4}$	$-0.86^{+0.03}_{-0.03}$	80	1.187 ± 0.378	2	12.97	0.9	G033.78+77.16	-	-	False	False	No optical counterpart.
-152.8105	26.5899	5.4	5.0	68	$0.031^{+0.008}_{-0.006}$	$2.863^{+0.177}_{-0.222}$	1024^{+5}_{-4}	7^{+4}_{-2}	$3.7^{+0.1}_{-0.1}$	$0.02^{+0.05}_{0.06}$	71	0.570 ± 0.000	0	2.93	0.2	G033.78+77.16	207.1893	26.5903	False	False	
-152.5875	26.6306	7.5	6.9	62	$0.046^{+0.003}_{-0.003}$	$0.003^{+0.005}_{-0.002}$	-43^{+0}_{-0}	4^{+1}_{-1}	$31.4^{+0.4}_{-0.4}$	$-0.89^{+0.03}_{-0.03}$	160	-	-	9.46	0.6	G033.78+77.16	-	-	False	False	No optical counterpart.
-2.0992	-25.9382	7.7	5.8	102	$0.038^{+0.009}_{-0.007}$	$3.073^{+0.054}_{-2.581}$	-18^{+2}_{-9}	7^{+3}_{-2}	$16.5^{+0.2}_{-0.2}$	$-0.55^{+0.04}_{-0.03}$	68	0.187 ± 0.133	3	8.47	2.0	G034.03-76.59	357.9006	-25.9388	False	False	
-89.0409	10.0803	7.5	4.7	66	$0.030^{+0.011}_{-0.007}$	$0.713^{+0.215}_{-0.213}$	58^{+4}_{-4}	8^{+5}_{-2}	$11.6^{+0.2}_{-0.2}$	$-0.93^{+0.04}_{-0.05}$	82	0.559 ± 0.089	3	10.82	1.7	G036.72+14.92	-	-	False	False	No optical counterpart.
-88.7551	10.1938	7.6	5.5	150	$0.022^{+0.008}_{-0.006}$	$0.267^{+2.351}_{-0.200}$	-1^{+8}_{-5}	7^{+5}_{-2}	$13.1^{+0.2}_{-0.2}$	$-0.80^{+0.05}_{-0.05}$	70	0.416 ± 0.214	3	11.41	1.8	G036.72+14.92	271.2446	10.1943	False	False	
-88.8378	9.9030	6.4	5.3	59	$0.022^{+0.003}_{-0.003}$	$0.453^{+0.154}_{-0.153}$	47^{+3}_{-3}	5^{+3}_{-2}	$11.3^{+0.2}_{-0.2}$	$-0.05^{+0.04}_{-0.04}$	77	0.186 ± 0.073	3	8.13	1.3	G036.72+14.92	271.1620	9.9031	False	False	
-88.7312	9.9649	8.3	4.7	48	$0.218^{+0.059}_{-0.057}$	$2.139^{+0.308}_{-2.081}$	19^{+5}_{-12}	4^{+3}_{-2}	$1.2^{+0.2}_{-0.2}$	$-1.02^{+0.35}_{-0.35}$	81	-	-	8.90	1.4	G036.72+14.92	271.2703	9.9618	True	False	
-88.7910	10.1261	13.6	7.3	57	$0.108^{+0.023}_{-0.020}$	$2.184^{+0.132}_{-2.099}$	13^{+3}_{-17}	11^{+2}_{-1}	$13.5^{+0.3}_{-0.3}$	$-1.63^{+0.06}_{-0.06}$	108	0.130 ± 0.032	3	6.88	1.1	G036.72+14.92	271.2022	10.1263	True	False	
-88.7946	10.1282	13.6	6.4	67	$0.030^{+0.005}_{-0.005}$	$0.098^{+0.106}_{-0.069}$	-16^{+2}_{-2}	9^{+2}_{-2}	$29.6^{+0.4}_{-0.4}$	$-1.30^{+0.03}_{-0.03}$	99	0.130 ± 0.032	3	6.85	1.1	G036.72+14.92	271.2022	10.1263	True	False	
-88.8257	10.0041	14.9	8.0	172	$0.018^{+0.000}_{-0.000}$	$0.988^{+0.006}_{-0.006}$	-23^{+0}_{-0}	3^{+0}_{-0}	$836.2^{+9.5}_{-9.4}$	$-0.81^{+0.03}_{-0.03}$	10001	-	-	2.94	0.5	G036.72+14.92	271.1741	10.0012	True	True	

Notes. The columns 'Maj' and 'Min' indicate the major and minor axis of the polarised sources and 'PA' the position angle. The results of the fitting as described in Section 5.3.2 are given in the columns p_0 to $\chi^2_{\rm QU}$ with uncertainties given by the 16th and 84th percentile of the MCMC chains. The columns starting with z are the results of the redshift estimates as detailed in Section 5.3.4. The angular distance to the pointing centre and projected radius to the cluster centre are given by the θ_p and r/R_{500} columns respectively. The 'Flagged' column indicates True when the source was omitted for the final analysis, for example because it was a bad fit.

Appendix IV: Full source catalogue

Table H.1: First 30 rows of the catalogue of 6 807 total intensity sources that were detected in this work. The full table is available at the CDS via anonymous ftp to `cdsarc.u-strasbg.fr` (130.79.128.5) or via `http://cdsarc.u-strasbg.fr/viz-bin/cat/J/A+A/665/A71`.

RA [deg]	DEC [deg]	Maj [″]	Min [″]	PA [deg]	Total flux [mJy]	Peak Flux [mJy beam^{-1}]	$p_{1.5\mathrm{GHz}}$ uplim	z_{best}	z_{best} source	θ_p [arcmin]	r/R_{500}	Cluster	$\mathrm{RA_{opt}}$ [deg]	$\mathrm{DEC_{opt}}$ [deg]	Visual counterpart id	Multi component	Note
19.7206	-26.9792	13.6	10.0	142	1.059±0.206	0.587±0.078	0.48	-	-	9.39	2.1	G212.97-84.04	-	-	False	False	
19.6823	-27.0611	9.7	6.8	99	0.328±0.100	0.376±0.062	0.87	-	-	8.99	2.2	G212.97-84.04	19.6824	-27.0613	False	False	
19.6530	-26.9383	8.4	7.9	73	0.721±0.090	0.814±0.056	0.32	-	-	6.17	1.3	G212.97-84.04	19.6528	-26.9385	False	False	
19.6515	-26.9198	9.4	8.8	113	1.106±0.109	1.008±0.059	0.24	-	-	6.57	1.4	G212.97-84.04	-	-	False	False	
19.6284	-27.0460	9.2	9.0	178	3.411±0.108	3.120±0.059	0.08	0.871±0.162	3	6.19	1.6	G212.97-84.04	19.6285	-27.0461	False	False	
19.6115	-27.0112	9.8	8.7	106	0.401±0.100	0.357±0.053	0.54	-	-	4.18	1.1	G212.97-84.04	19.6110	-27.0110	False	False	
19.6104	-27.0795	13.2	9.0	63	0.500±0.151	0.318±0.063	0.92	-	-	7.21	1.8	G212.97-84.04	-	-	False	False	
19.6064	-26.7558	9.9	8.6	112	1.004±0.194	0.891±0.103	0.28	-	-	13.52	2.9	G212.97-84.04	19.6062	-26.7559	False	False	
19.6056	-27.0319	9.8	8.9	10	0.881±0.102	0.757±0.053	0.23	-	-	4.73	1.2	G212.97-84.04	19.6054	-27.0319	False	False	
19.5740	-26.9712	24.0	10.2	69	44.649±0.373	16.358±0.073	0.01	-	-	1.57	0.4	G212.97-84.04	19.5700	-26.9724	True	False	
19.5825	-26.9747	15.9	11.9	176	1.901±0.261	0.757±0.077	0.20	-	-	2.01	0.5	G212.97-84.04	-	-	True	False	No optical counterpart.
19.5664	-27.1593	11.3	9.8	63	5.909±0.197	4.007±0.087	0.06	-	-	11.14	2.8	G212.97-84.04	19.5606	-27.1622	True	True	
19.5616	-27.1625	18.3	11.2	63	1.635±0.304	0.600±0.084	0.19	-	-	11.31	2.8	G212.97-84.04	19.5606	-27.1622	True	True	
19.5540	-27.1671	14.0	11.1	95	7.832±0.464	3.410±0.084	-	-	-	11.57	2.9	G212.97-84.04	19.5606	-27.1622	True	True	
19.5530	-26.8093	9.4	8.2	167	0.784±0.112	0.771±0.064	0.31	-	-	9.92	2.1	G212.97-84.04	19.5531	-26.8093	False	False	
19.5561	-26.8117	10.9	9.6	92	0.343±0.147	0.247±0.068	0.75	-	-	9.79	2.0	G212.97-84.04	-	-	False	False	
19.5467	-26.9700	9.8	8.8	118	7.547±0.102	6.596±0.054	0.03	0.173±0.000	0	0.29	0.2	G212.97-84.04	19.5463	-26.9700	False	False	
19.5359	-27.0165	8.8	8.0	90	0.519±0.093	0.554±0.056	0.34	-	-	2.56	0.8	G212.97-84.04	-	-	False	False	
19.5328	-27.0496	8.6	8.4	27	0.814±0.087	0.848±0.052	0.22	-	-	4.55	1.3	G212.97-84.04	19.5330	-27.0496	False	False	
19.5250	-26.7445	9.7	8.6	167	4.825±0.232	4.327±0.124	0.05	-	-	13.84	3.0	G212.97-84.04	19.5249	-26.7447	True	True	
19.5218	-26.7448	9.5	9.0	59	3.102±0.236	2.735±0.125	0.06	-	-	13.84	3.0	G212.97-84.04	19.5249	-26.7447	True	True	
19.5167	-26.9539	10.0	8.0	5	0.372±0.096	0.351±0.053	0.63	-	-	1.96	0.4	G212.97-84.04	19.5166	-26.9531	False	False	
19.4966	-27.0013	9.4	8.9	116	0.310±0.105	0.277±0.056	0.70	0.225±0.000	0	3.05	0.9	G212.97-84.04	19.4964	-27.0013	False	False	
19.4759	-26.8784	9.3	8.5	126	1.379±0.099	1.308±0.055	0.19	0.538±0.035	3	6.85	1.4	G212.97-84.04	19.4759	-26.8783	False	False	
19.4656	-26.8930	9.2	8.3	161	1.790±0.087	1.770±0.050	0.14	-	-	6.48	1.4	G212.97-84.04	19.4656	-26.8931	False	False	
19.4630	-26.9808	13.5	10.1	83	0.581±0.155	0.323±0.059	0.68	0.062±0.035	3	4.40	1.1	G212.97-84.04	19.4630	-26.9812	False	False	
19.4531	-26.7984	9.3	8.8	25	0.681±0.147	0.628±0.080	0.43	0.648±0.060	3	11.66	2.5	G212.97-84.04	19.4530	-26.7984	False	False	
19.4408	-27.0741	9.7	7.9	89	0.577±0.110	0.566±0.062	0.44	-	-	8.17	2.1	G212.97-84.04	-	-	False	False	
19.4236	-26.9546	9.1	8.8	167	2.697±0.110	2.515±0.061	0.09	-	-	6.60	1.5	G212.97-84.04	19.4236	-26.9547	False	False	
19.3981	-27.0851	8.9	7.8	160	0.608±0.115	0.664±0.070	0.41	-	-	10.28	2.5	G212.97-84.04	-	-	False	False	

Notes. The columns 'Maj' and 'Min' indicate the major and minor axis of the polarised sources and 'PA' the position angle. The upper limit on the polarisation fraction $p_{1.5\mathrm{GHz}}$ was determined for unpolarised radio sources as described in section 5.3.2. The columns starting with z are the results of the redshift estimates as detailed in Section 5.3.4. The angular distance to the pointing centre and projected radius to the cluster centre are given by the θ_p and r/R_{500} columns respectively. The 'Visual counterpart id' column indicates whether the source has undergone visual inspection to mark the optical counterpart or whether it was determined automatically as described in Section 5.3.3.

Appendix V: Cluster catalogue

Table H.1: First 30 rows of the catalogue of 124 clusters used in this work. The full table is available at the CDS via anonymous ftp to `cdsarc.u-strasbg.fr` (130.79.128.5) or via `http://cdsarc.u-strasbg.fr/viz-bin/cat/J/A+A/665/A71`.

Cluster	PSZ2 Name	cRA [deg]	cDEC [deg]	pRA [deg]	pDEC [deg]	cz	M_{500} [$10^{14} M_{\odot}$]	R_{500} [Mpc]	Dynamical state (C_{SB})	Radio Halo
G006.47+50.54	G006.49+50.56	227.7319	5.7481	-132.2679	5.7481	0.08	7.0	1.3	CC	False
G021.09+33.25	G021.10+33.24	248.1795	5.5866	-111.8204	5.5866	0.15	7.8	1.3	CC	False
G028.77-33.56	G028.77-33.56	312.0614	-17.8090	-47.9387	-17.8090	0.15	4.5	1.1	-	False
G029.00+44.56	G029.06+44.55	240.5617	16.0536	-119.4383	16.0536	0.04	3.5	1.1	NCC	False
G033.78+77.16	G033.81+77.18	207.2437	26.5846	-152.7562	26.5846	0.06	4.5	1.1	CC	False
G034.03-76.59	G033.97-76.61	357.9274	-26.0953	-2.0904	-26.0791	0.23	7.6	1.3	-	False
G036.72+14.92	G036.73+14.93	271.1365	10.0362	-88.8633	10.0362	0.15	5.3	1.2	CC	False
G039.85-39.98	G039.85-39.96	321.7764	-12.1686	-38.2238	-12.1686	0.18	5.9	1.2	NCC	False
G040.63+77.13	G040.58+77.12	207.3622	28.0946	-152.6517	28.1053	0.07	2.6	1.0	-	True
G042.82+56.61	G042.81+56.61	230.6103	27.7033	-129.3896	27.7033	0.07	4.1	1.1	NCC	False
G044.22+48.68	G044.20+48.66	239.5878	27.2290	-120.4121	27.2290	0.09	8.8	1.4	CC	False
G046.50-49.43	G046.47-49.44	332.5733	-12.1582	-27.4267	-12.1582	0.08	4.4	1.1	NCC	False
G046.88+56.49	G046.88+56.48	231.0292	29.9118	-128.9708	29.9118	0.11	5.3	1.2	NCC	True
G048.05+57.17	G048.10+57.16	230.2998	30.5986	-129.7000	30.5986	0.08	3.6	1.1	NCC	False
G049.20+30.86	G049.22+30.87	260.0316	26.6138	-99.9683	26.6138	0.16	5.9	1.2	CC	False
G049.33+44.38	G049.32+44.37	245.1297	29.9055	-114.8704	29.9055	0.10	3.7	1.1	NCC	True
G049.66-49.50	G049.69-49.46	333.6475	-10.3919	-26.3525	-10.3919	0.10	3.6	1.1	CC	False
G053.44-36.26	G053.44-36.25	323.8120	-1.0503	-36.1879	-1.0503	0.32	-	-	NCC	False
G053.52+59.54	G053.53+59.52	227.5341	33.4851	-132.4658	33.4851	0.11	5.9	1.2	NCC	False
G055.60+31.86	G055.59+31.85	260.6118	32.1431	-99.3883	32.1431	0.22	7.8	1.3	CC	True
G055.97-34.88	G055.95-34.89	323.8269	1.4312	-36.1729	1.4312	0.12	6.7	1.2	NCC	False
G056.81+36.31	G056.77+36.32	255.6779	34.0808	-104.3221	34.0808	0.10	4.4	1.1	CC	True
G057.33+88.01	G057.80+88.00	194.9093	27.9350	-165.0908	27.9350	0.02	7.2	1.4	NCC	False
G057.61+34.94	G057.61+34.93	257.4608	34.4586	-102.5392	34.4586	0.08	3.7	1.1	NCC	False
G057.92+27.64	G057.92+27.64	266.0695	33.0054	-93.9304	33.0054	0.08	2.7	1.0	CC	False
G058.28+18.59	G058.29+18.55	276.2835	30.4342	-83.7167	30.4342	0.06	3.9	1.1	NCC	False
G062.42-46.41	G062.44-46.43	335.9655	-1.6173	-24.0346	-1.6173	0.09	3.5	1.0	NCC	False
G062.92+43.70	G062.94+43.69	247.1383	39.5458	-112.8617	39.5458	0.03	2.9	1.0	CC	False
G067.23+67.46	G067.17+67.46	216.4929	37.8344	-143.5071	37.8344	0.17	7.2	1.3	CC	False
G068.23+15.20	G068.22+15.18	284.3945	38.0050	-75.6237	38.0223	0.06	2.2	0.9	-	False

Notes. The cluster centre coordinates from the X-ray profiles are given by *cRA* and *cDEC* and pointing coordinates are given by *pRA* and *pDEC*. The dynamical state was determined as described in Section 5.5.3 and the presence of a radio halo by a literature search.

6

Probing cluster magnetism with embedded and background radio sources in Planck clusters

Magnetic fields remain an enigmatic part of the non-thermal content of galaxy clusters. Faraday rotation and depolarisation of extragalactic radio sources are useful probes, but the limited availability of polarised radio sources necessitates the stacking of clusters to study average magnetic field profiles and correlation scales. In this study, we combine the information from depolarisation with the observed rotation measure (RM) and present an investigation into the average magnetic field properties of the most massive Planck clusters at low redshift ($z < 0.35$), using both background sources and sources embedded in clusters. As expected for randomly oriented magnetic fields, we find an average RM consistent with zero as a function of projected radius, but observe a significant increase in the RM scatter, $\sigma_{\rm RM}$, closer to the cluster centres. Averaging all 124 clusters, we find a scatter within R_{500} of $\sigma_{\rm RM} = 241 \pm 44$ rad m^{-2}. In the simple assumption of a uniform magnetic field with a single fluctuation scale Λ_c, this translates to an average magnetic field strength of $3\,(\Lambda_c/10{\rm kpc})^{-0.5}\,\mu G$. Because the highest RM sources near the centre of clusters are depolarised, the radial profile of $\sigma_{\rm RM}$ puts a lower limit on the scaling between the magnetic field and thermal gas density of $\eta > 0.15$. Combining depolarisation and RM in a full forward model, we find that the observations best agree with a magnetic field that fluctuates on a maximum scale $\Lambda_{\rm max} > 300$ kpc and follows a power spectrum with exponent $n = 3$ to $n = 4$, consistent with Kolmogorov turbulence injected on large scales. The best-fit average magnetic field profile is equal to $B_0 = 5\,\mu G$ in the centre, declining with radius as $B(r) \propto n_e(r)^{0.5}$.

Based on Osinga et al. (2023b): *E. Osinga, R. J. van Weeren, L. Rudnick, F. Andrade-Santos, A. Bonafede, T. Clarke, K. Duncan, S. Giacintucci, Tony Mroczkowski, H. J. A. Röttgering, A&A to be subm.*

6.1 Introduction

Galaxy clusters, the largest gravitationally bound structures in the Universe, harbour a rich variety of physical phenomena. Radio observations have revealed that clusters often show diffuse synchrotron emission that can span Mpc-sized regions, such as 'radio halos' (e.g. Bonafede et al., 2022) or 'mega-halos' (Cuciti et al., 2022), implying that clusters are filled with ultra-relativistic electrons and magnetic fields. The influence of the magnetic fields extends to particle acceleration models, radio synchrotron age estimates, the dynamics of the intracluster medium (ICM) and the transport of cosmic rays. Understanding the properties and origins of magnetic fields in clusters thus has broad importance (see Carilli & Taylor, 2002; Govoni & Feretti, 2004; Donnert et al., 2018, for reviews on magnetic fields in galaxy clusters).

The most promising tool to study magnetic fields is radio polarisation observations of Faraday rotation and depolarisation. A magnetised plasma such as the ICM causes a wavelength-dependent rotation of the polarisation angle. In general, the Faraday depth of a source is defined as (Burn, 1966; Brentjens & de Bruyn, 2005)

$$\phi(\mathbf{r}) = 812 \int n_e \mathbf{B} \cdot d\mathbf{r} \,\mathrm{rad\,m^{-2}}, \tag{6.1}$$

where n_e is the electron density in parts per cm^{-3}, $\mathbf{B}$ is the magnetic field in μGauss and d$\mathbf{r}$ the infinitesimal path length increment along the line of sight in kpc, and we define $\phi(\mathbf{r}) > 0$ for the magnetic field pointing towards the observer. In the simple case of just one radio-emitting source along the line of sight, the Faraday depth is equal to the rotation measure (RM). With a combination of radio and X-ray observations, it is thus possible to study the magnetic field properties of galaxy clusters.

Such studies are best done at low redshifts, due to the rarity of polarised radio sources (e.g. Rudnick & Owen, 2014). The most detailed analyses have been of the Coma Cluster (Bonafede et al., 2010) and Abell 2345 (Stuardi et al., 2021), where seven radio sources were detected per cluster. The Coma Cluster magnetic field was found to agree with a Kolmogorov power spectrum with a central strength of 5 μG and a scaling of magnetic field energy density linearly proportional to the thermal gas density ($B^2 \propto n_e$). The central magnetic field strength in Abell 2345 was found to be similar to the Coma Cluster, but with a magnetic field energy density that scales super-linear instead (i.e. $B^2 \propto n_e^2$). Several other low-redshift clusters have been analysed in polarisation (Murgia et al., 2004; Govoni et al., 2006; Guidetti et al., 2008; Govoni et al., 2010; Vacca et al., 2012; Govoni et al., 2017), with typically less than five polarised radio galaxies per study, resulting in large uncertainties on the magnetic field estimates (see e.g. Johnson et al., 2020, for a detailed discussion).

Because cluster magnetic fields are thought to be generally turbulent and disordered, the observed Faraday rotation is the result of a random walk process and thus a random variable. Accurate magnetic field estimates, therefore, require a statistical analysis probing many independent sight lines. Another potential problem is that polarised radio galaxies are often embedded in the cluster, and the degree to which the observed RM variations are caused by local interaction of the lobes with the ICM is debated (Laing et al., 2008; Guidetti et al., 2012; Osinga et al., 2022). Such problems can be overcome by stacking clusters to increase the number of polarised radio sources located behind clusters and thus independent sight lines through a cluster (Clarke et al., 2001; Bonafede et al., 2011;

Böhringer et al., 2016; Stasyszyn & de los Rios, 2019; Osinga et al., 2022). Although stacking experiments have limited ability to probe differences between clusters, they are useful for obtaining average cluster magnetic field properties, and are currently the only way to study clusters beyond the few nearest clusters.

We recently published, in Osinga et al. (2022), the largest homogeneous stacking experiment using Karl G. Jansky Very Large Array (VLA) observations of 124 galaxy clusters selected from the Planck 2nd Sunyaev-Zeldovich Source Catalog (PSZ2) (Planck Collaboration et al., 2016a). This study presented the first clear depolarisation trend tracing the radial profile of cluster magnetic fields using over 600 polarised radio sources. While depolarisation traces the smaller scale structure of the magnetic fields (i.e. few kpc), the larger scale structure can be inferred from the Faraday rotation of the radio sources. In this paper, we add the information from the Faraday rotation of the same sample of sources to study the large-scale properties of the magnetic fields in galaxy clusters. By jointly fitting both depolarisation and Faraday rotation, we aim to constrain the average magnetic field strength, scaling with density, and power spectrum. Cosmological calculations are performed assuming a flat ΛCDM model with $H_0 = 70$ kms^{-1}Mpc^{-1}, $\Omega_m = 0.3$ and $\Omega_\Lambda = 0.7$.

6.2 Chandra-Planck ESZ sample

The sample of galaxy clusters is a subset of 124 out of 165 clusters from the *Chandra-Planck Legacy Program for Massive Clusters of Galaxies*[1] (Andrade-Santos et al., 2021) that have VLA observations presented in Osinga et al. (2022). The full details on the data reduction, polarised source identification and association, and determination of the polarisation properties are presented in the aforementioned paper, but we briefly summarise the important points here and highlight some improvements to the catalogue.

Each of the 124 clusters was observed for ∼ 40 min each in the VLA L-band (1–2GHz), resulting in typically 20–30 μJy beam^{-1} noise levels at a resolution of 6–7″ after data reduction. Polarised sources were identified using RM-synthesis (Brentjens & de Bruyn, 2005) and matched to total intensity components and optical counterparts. In total 6,807 and 819 source components were detected in total and polarised intensity respectively. We have fit the following model to the polarised intensity as a function of wavelength λ, which accounts for rotation and depolarisation (see Sokoloff et al., 1998, for details),

$$P(\lambda^2) = p_0 I \exp(-2\sigma_{\rm RM}^2\lambda^4)\exp[2i(\chi_0 + \phi\lambda^2)], \tag{6.2}$$

where p_0 denotes the intrinsic polarisation and $\sigma_{\rm RM}^2$ the variance of the RM distribution which models the depolarisation as a function of wavelength. χ_0 is the intrinsic polarisation angle, and I denotes the total intensity model, which was assumed to be a simple power-law of the form $I(\nu) = I_0\nu^\alpha$.

We have improved the Monte Carlo Markov chain (MCMC) fitter used in Osinga et al. (2022) to now properly take into account the circular nature of χ_0 during the fitting. In Osinga et al. (2022), the prior on χ_0 was uniform $\sim \mathcal{U}(0,\pi)$, which would cause the sampler in some cases to get stuck around the boundary values. We removed this prior on χ_0 and fold the chain back into the range $[0,\pi)$ after the sampling is completed. We also calculate the mean and spread using circular statistics where we take into account the fact that the

[1] http://hea-www.cfa.harvard.edu/CHANDRA_PLANCK_CLUSTERS/

angles are distributed on the half-circle $\in [0, \pi)$. In this way, the mean denotes the angle of the average vector on the unit circle, and the standard deviation is the spread in angles around the average vector. This agrees with the definition of the simple arithmetic mean and standard deviation when the angles are distributed away from the edges of the domain.

This paper is thus accompanied by an updated table of polarised components, shown in Appendix 6.6. We note that this update mainly corrects the quoted mean and uncertainty of the intrinsic polarisation angle χ_0 and most sources have similar best-fit RM and depolarisation parameters. This thus does not significantly impact the results. Finally, we used the same criteria for identifying bad fits as Osinga et al. (2022). All sources with a best-fit χ^2 value that is $> 5\sigma$ away from the theoretical distribution, and sources with low signal-to-noise polarised emission resulting in artificially large values of $\sigma^2_{\rm RM}$ were flagged. This resulted in 196 bad fits out of 819 polarised sources. The following analysis is thus performed using the remaining 623 polarised radio sources detected in 124 galaxy clusters.

6.3 Methods

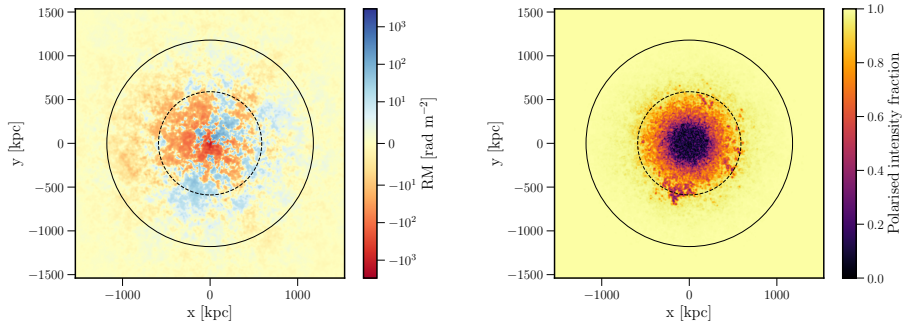

Figure 6.1: Simulated Faraday rotation (left) and depolarisation (right) screen for a random cluster from our sample as it would appear at 1.5 GHz with perfect sampling. The parameters are $B_0 = 5.0\,\mu$G, $n = 2$, $\eta = 0.5$ and the dashed and solid circles show $0.5R_{500}$ and $1.0R_{500}$, respectively.

The galactic contribution to the RM is expected to be small since the cluster sample is selected from the PSZ2 survey and thus avoids the galactic plane by design. While cluster induced RMs are often on the order of 10^3 rad m^{-2}, for comprehensiveness we subtracted the galactic contribution (on the order of 10^1 rad m^{-2}) to the sources using the recent map from Hutschenreuter et al. (2022), propagating the uncertainties as well. Afterwards, we corrected the RM to the cluster rest frame to account for cosmological redshift. This assumes that the RM, after subtraction of the galactic contribution, is dominated by the effect of the ICM and that the intrinsic RM of the source and the component from the intergalactic medium are both negligible in comparison. We thus defined the RM induced by the ICM as

$$\mathrm{RM}_{\rm cluster} = (\mathrm{RM}_{\rm obs} - \mathrm{RM}_{\rm gal})(1 + z_{\rm cluster})^2, \tag{6.3}$$

where $\mathrm{RM}_{\rm obs}$ refers to the best-fit RM in the observer frame, $\mathrm{RM}_{\rm gal}$ to the galactic contribution and $z_{\rm cluster}$ to the cluster redshift.

To infer magnetic field properties from the distribution of $RM_{cluster}$, we consider models of various levels of complexity. First, in the simple scenario of random magnetic field orientations in cells of size Λ_c kpc, which have uniform magnetic field strengths and electron densities, the observed RM is the result of a random walk process. Because of the central limit theorem, the distribution of RMs is then expected to be a Gaussian distribution with zero mean, and variance given by (e.g. Murgia et al., 2004)

$$\sigma^2_{\rm RM} = 812^2 \Lambda_c \int (n_e B_{\parallel})^2 dl, \tag{6.4}$$

where dl is the infinitesimal path length increment along the line of sight in kpc, n_e is measured in cm^{-3} and $B_{\parallel}$ is the magnetic field strength parallel to the line of sight in μG.

In reality, the magnetic field structure will more closely resemble a random field with fluctuations on many spatial scales, and both the magnetic field strength and electron density will scale with radius. Thus comparing observations to more realistic scenarios requires simulated magnetic fields. We followed the approach explained in Section 4 of Osinga et al. (2022) to generate mock rotation measure and depolarisation images for all clusters in our sample which have X-ray observations available (99/124). An example of a mock RM and depolarisation image is shown in Figure 6.1 for a random cluster in our sample. In these models, the magnetic field is assumed to be a three-dimensional Gaussian random field with a single-power law spectrum characterised by the following parameters: B_0, η, n, $\Lambda_{\rm min}$ and $\Lambda_{\rm max}$. The first two denote the variables that parameterise the magnetic field, assumed to follow (e.g. Bonafede et al., 2010)

$$B(r) = B_0 \left(\frac{n_{\rm th}(r)}{n_{\rm th}(0)} \right)^{\eta}, \tag{6.5}$$

and the last three parameters encode the power spectrum of the magnetic field:

$$|B_k|^2 \propto k^{-n}, \tag{6.6}$$

between minimum and maximum fluctuations scales that are denoted by $\Lambda_{\rm min}$ and $\Lambda_{\rm max}$ in image space, respectively. In the picture of Kolmogorov turbulence, $n = 11/3$, but this was found observationally to take values between $n = 1$ and $n = 4$ (Murgia et al., 2004; Govoni et al., 2006; Guidetti et al., 2008; Bonafede et al., 2010; Vacca et al., 2010, 2012; Govoni et al., 2017; Stuardi et al., 2021; Osinga et al., 2022). We have computed all models on 1024^3 pixel grids, to simulate all clusters in the same way. Here, one pixel represents 3 kpc, and clusters are thus simulated out to about $1.5R_{500}$, with a minimum fluctuation scale of $\Lambda_{\rm min} = 6$ kpc. These models will be compared to observations in various ways, as detailed in the next section.

6.4 Results

6.4.1 Average magnetic field strength

The cluster rotation measure with the uncertainty given by the 16th and 84th percentile of the MCMC is plotted as a function of distance to the nearest cluster centre in Figure 6.2. A clear trend is visible, with the scatter in the rotation measures decreasing with a

larger distance to the cluster centre. Taking all sources within $1.0R_{500}$, we find that the standard deviations of the RM of cluster members and background sources are similar[2], being 263 ± 56 and 216 ± 68 rad m^{-2}, respectively, as shown in Table 6.1. In reality, we expect that for a given magnetic field strength, the standard deviation of the RM of background sources is expected to be $\sqrt{2}$ times that of cluster members, as cluster members are on average located at the mid-plane of the cluster. However, cluster members are also found preferentially at smaller radii, where the scatter in RM is larger due to generally larger magnetic field strength and electron densities.

Table 6.1: Standard deviation of $\mathrm{RM_{cluster}}$ as defined in Eq. 6.3 for different subsets and projected radii.

	$< 0.5R_{500}$	$0.5 - 1.0R_{500}$	$< R_{500}$	$> R_{500}$
All	299 ± 61	120 ± 29	241 ± 44	38 ± 4
Inside[a]	288 ± 71	182 ± 48	263 ± 56	38 ± 7
Behind[b]	315 ± 103	57 ± 6	216 ± 68	37 ± 5
CC[c]	169 ± 67	85 ± 29	139 ± 49	27 ± 2
NCC[d]	236 ± 46	70 ± 9	192 ± 36	29 ± 6

Notes. [(a)] Sources located inside clusters [(b)] Sources located behind clusters [(c)] Only cool-core clusters [(d)] Only non-cool-core clusters

The mean value of the RMs is consistent with zero as a function of radius, as shown in Figure 6.3, consistent with random magnetic field orientations along the line of sight. Assuming the simple random walk scenario denoted by Equation 6.4, we find that the most rudimental estimate of the line-of-sight magnetic field strength is given by

$$\left(\frac{B_{\parallel}}{\mu G}\right) = 2.46 \left(\frac{\sigma_{\mathrm{RM}}/200}{\mathrm{rad\,m^{-2}}}\right) \left(\frac{n_e/10^{-3}}{\mathrm{cm^{-3}}}\right) \left(\frac{\Lambda_c/10}{\mathrm{kpc}}\right)^{-1/2} \left(\frac{L/1000}{\mathrm{kpc}}\right)^{-1/2} \tag{6.7}$$

where L indicates the line-of-sight column length, which will be on average twice as large for background sources as cluster members. If we assume that cells are ordered on scales of 10 kpc with an electron density of $10^{-3}\mathrm{cm}^{-3}$ (e.g. Böhringer et al., 2016), this reduces to

$$B_{\parallel} = \frac{\sigma_{\mathrm{RM}}}{2.57\ \sqrt{L}}. \tag{6.8}$$

If we assume approximately $L = 1000$ kpc for cluster members and twice as large for background sources, we find magnetic field strengths averaged within R_{500} equal to 2-3 μG. Although the simple scenario suffices to give an order of magnitude estimate for the average magnetic field in galaxy clusters, it is clear from Figure 6.2 that the product of the magnetic field strength and electron density is not constant as a function of radius.

To sample a more physical property, we plot in Figure 6.4 the observed rotation measures as a function of ICM electron column density. This plot is less populated, as we now only show sources that are detected within a projected radius $r < 2R_{500}$, where the Chandra-derived column density values are reliable. The increased scatter in rotation

[2]Uncertainties on σ_{RM} are calculated by 1 000 bootstraps.

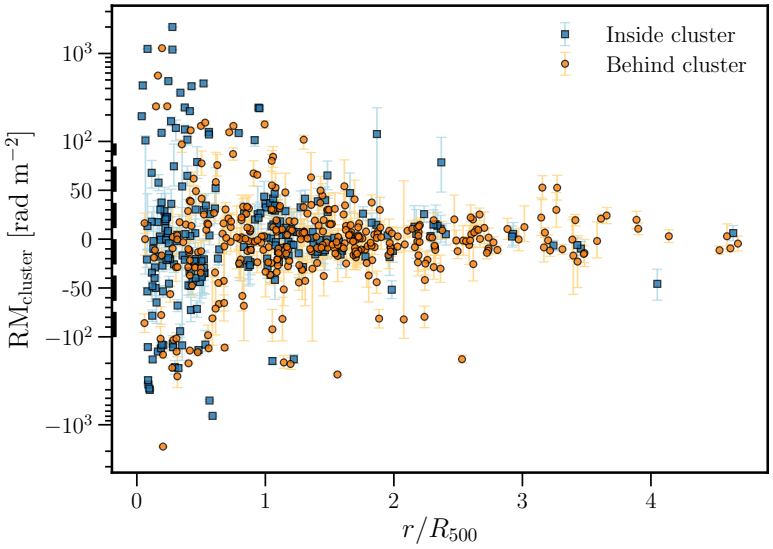

Figure 6.2: Cluster induced rotation measure as a function of normalised distance to the nearest cluster centre. The y-axis is partially linear and partially logarithmic for visibility. The region between -10^{-2} and 10^2 rad m^{-2}, indicated by the dashed axis, is shown on a linear scale and the scale is logarithmic outside of this region. The median uncertainty in RM is 13 and 11 rad m^{-2} in cluster members and background sources, respectively. The plot is shown on a linear scale in Appendix 6.6.

measure with increasing column density is still significant, and the preferential sampling of cluster members at high column densities (i.e. low radii) is clearly pronounced. Following Böhringer et al. (2016), we calculated the scatter in rotation measure in bins of column density, from which the average magnetic field strength along of the line of sight can be calculated as

$$\left(\frac{B_{\parallel}}{\mu G}\right) = 3.801 \times 10^{18} \left(\frac{\sigma_{\mathrm{RM}}}{\mathrm{rad\,m^{-2}}}\right) \left(\frac{N_e}{\mathrm{cm^{-2}}}\right) \left(\frac{L}{\Lambda_c}\right)^{1/2}. \tag{6.9}$$

The RM scatter as a function of column density is shown in Figure 6.5. The bottom panel of Figure 6.5 shows the resulting magnetic field estimate from Equation 6.9. We find that the average magnetic field strength is 0.3μG $\sqrt{L/\Lambda_c}$, resulting in around 3μG for typical values of $L = 1000$ kpc and $\Lambda_c = 10$ kpc (Böhringer et al., 2016). There is a hint of increasing average magnetic field strength towards lower column densities, although this is likely dominated by the scatter from the uncertainties in the RM, as will be discussed in the next section.

6.4.2 Radially declining magnetic field

In reality, cluster magnetic fields and electron densities show a radial decline. To investigate the (spherically averaged) magnetic field properties as a function of radius, we calculated the scatter in rotation measure as a function of radius. The data were binned into radial

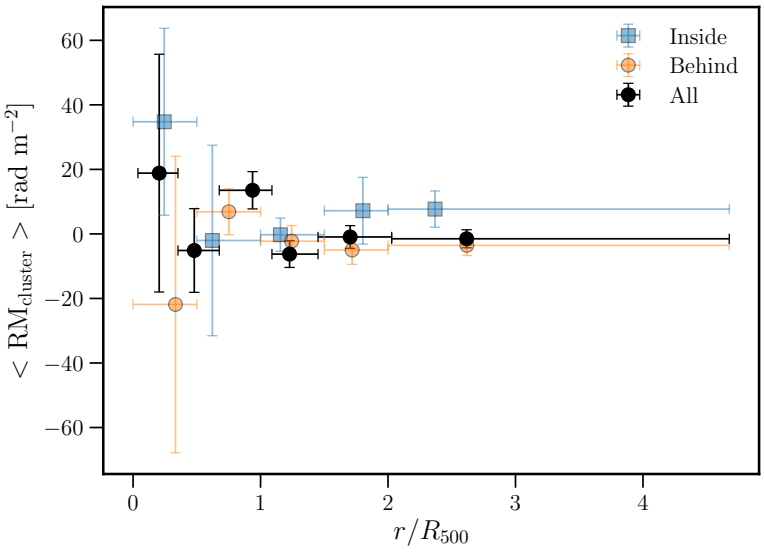

Figure 6.3: Mean of the cluster induced rotation measure in bins of projected normalised distance to the nearest cluster centre. The horizontal error bars indicate the bin edges. Cluster members are shown in blue, background sources in orange, and the combined bins in black.

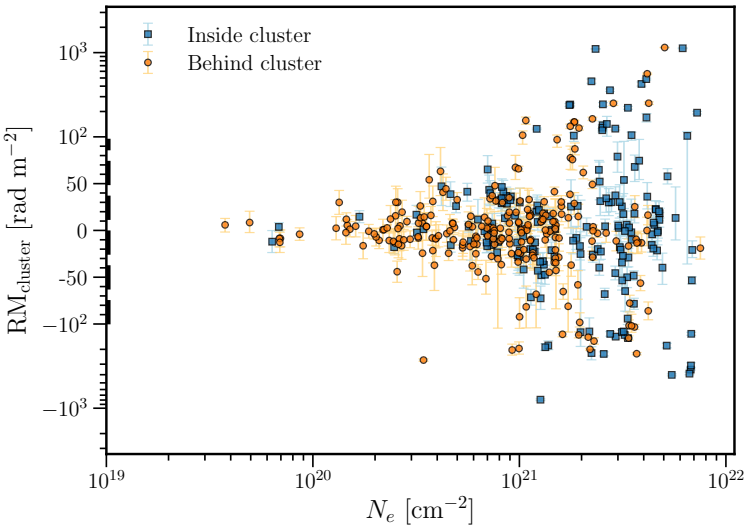

Figure 6.4: Cluster induced rotation measure as a function of electron column density, for sources detected at $r < 2R_{500}$. The y-axis is partially linear and partially logarithmic for visibility. The region between -10^{-2} and 10^2 rad m^{-2}, indicated by the dashed axis, is shown on a linear scale and the scale is logarithmic outside of this region. The plot is shown on a linear scale in Appendix 6.6.

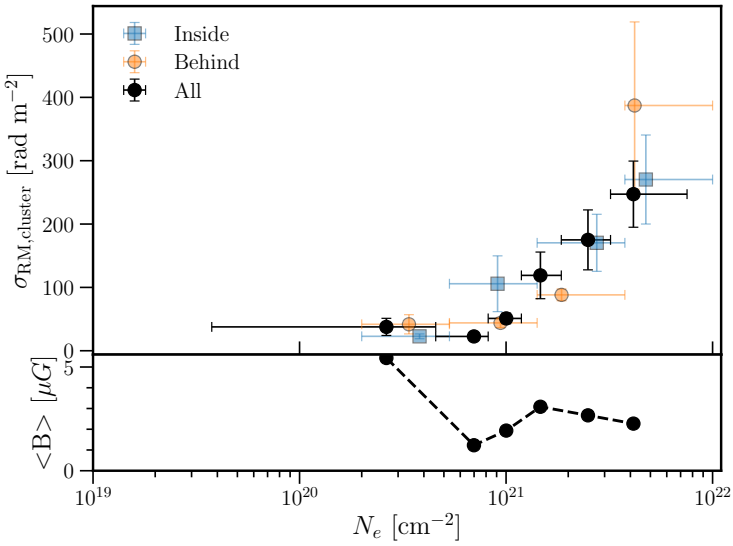

Figure 6.5: Standard deviation of the RMs in bins of electron column density, for sources detected at $r < 2R_{500}$. The bins for the full sample have equal frequency with 70 sources per bin, while the bins for the sub-samples are defined in logarithmically spaced bins to sample similar densities. The horizontal error bars indicate the bins, and points are plotted at the median N_e. The bottom panel shows the magnetic field estimate assuming Equation 6.9, with a correlation length that is a factor 100 smaller than the line-of-sight distance, resulting in a mean strength of 3μG.

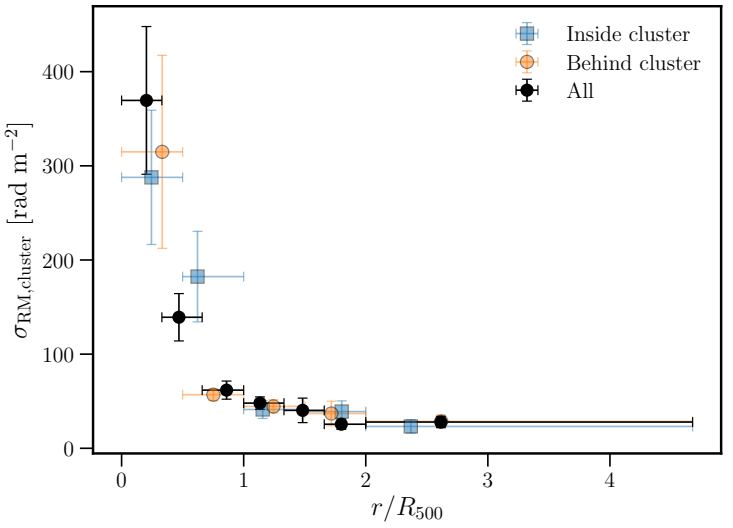

Figure 6.6: Standard deviation of the RMs in bins of projected distance to the nearest cluster centre. The horizontal error bar indicates the width of the bin, and the points are plotted at the median radius in the bin.

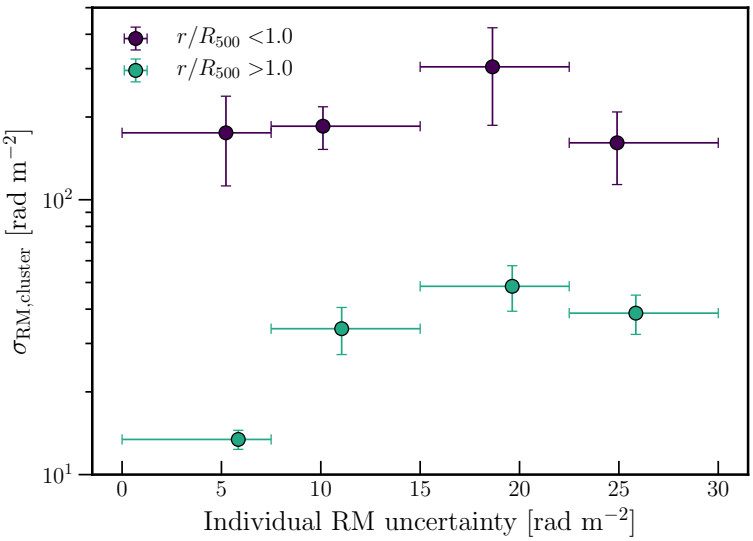

Figure 6.7: Scatter in rotation measure as a function of the RM uncertainty, separately for sources detected within R_{500} and outside R_{500}.

bins, and the standard deviation is shown as a function of radius in Figure 6.6. A strong trend of the RM scatter being significantly higher closer to the cluster centre is present.

The RM scatter at large radii (i.e. $r > 2R_{500}$) is still considerably above zero, with a value of $\sigma_{\mathrm{RM}} = 28 \pm 6$. It is likely that this value reflects the uncertainties in the RM determination. To verify this, we plot in Figure 6.7 the scatter σ_{RM} as a function of the individual RM uncertainty. The plot shows that the scatter outside $1R_{500}$ is already dominated by the uncertainties, with the observed σ_{RM} increasing with the RM uncertainty. For sources located within $1R_{500}$, we see no such trend, indicating that the scatter is dominated by the real physical scatter induced by the turbulent magnetic medium. However, the RM scatter near the centre of the clusters is likely underestimated, as sources with large RM values are depolarised, given that the 50% sensitivity Faraday depth is equal to only 1200 rad m^{-2} for the channel width of our observations (Osinga et al., 2022).

Assuming that the magnetic field fluctuates on a single scale Λ_c regardless of radius, we can determine the magnitude of the 3D magnetic field fluctuations and the scaling between magnetic field and thermal electron density from the σ_{RM} profile. In this assumption, the variance in rotation measure as a function of projected distance is proportional to the line-of-sight integral of Equation 6.4,

$$\sigma^2_{\mathrm{RM}}(r/R_{500}) = \sigma_{\mathrm{RM,0}} \int_{\mathrm{LOS}} n_e^{2(1+\eta)}(\mathbf{r})\,\mathrm{d}L, \tag{6.10}$$

where $\sigma_{\mathrm{RM,0}}$ denotes the theoretical central RM dispersion and η models the relationship between the magnetic field energy density and thermal energy density (i.e. $B^2 \propto n_e^{2\eta}$),

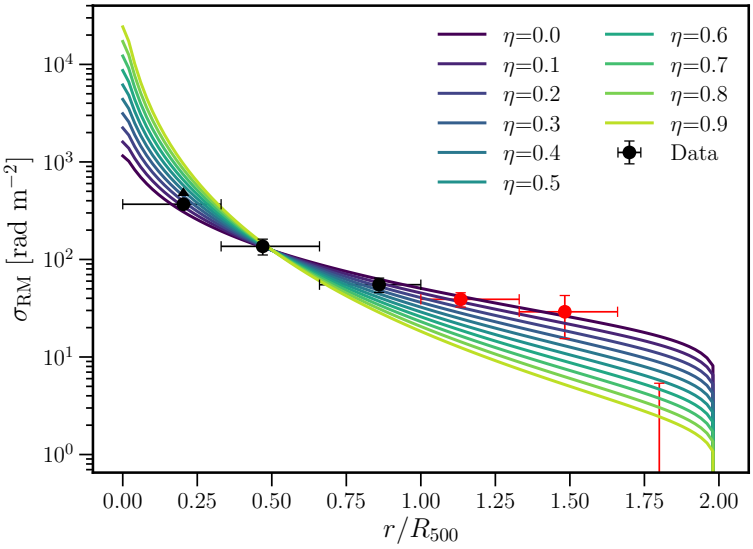

Figure 6.8: RM scatter as a function of projected distance. The data is corrected for a baseline value of $\sigma_{\rm RM} = 28$, meaning the last data point is consistent with zero. The first point is plotted as a lower limit, and points outside R_{500} (shown in red) are ignored in the fit, as Fig. 6.7 showed that the scatter is dominated by uncertainties for these points. The coloured lines show best-fit profiles computed for various values of η assuming Equation 6.10.

which was found to be 0.5 in the Coma Cluster (e.g. Bonafede et al., 2010). Because we are investigating a stacked sample of clusters this scaling might, in reality, be more complicated, but this can only be investigated in single clusters with next-generation polarisation data. At the moment, we determined an average cluster electron density profile by stacking all individual profiles, which are shown in Figure 6.19, which is on average a good assumption because clusters are relatively self-similar (e.g. Arnaud et al., 2010a).

Correcting for the scatter from measurement uncertainties, we compare in Figure 6.8 the observed RM scatter with the theoretical profile from integrating the mean density profile along the line-of-sight out to $2R_{500}$ for various values of η. This figure demonstrates that the observed RM scatter profile is relatively flat, with models requiring $\eta \leq 0.5$ to fit the observed RM scatter observed in the centre of clusters. The best-fit parameters are found to be $\sigma_{\rm RM,0} = 1538$ rad m^{-2} and $\eta = 0.15$, but we note that this value of eta likely presents a lower limit, because the observed RM scatter at small projected radii is a lower limit, as explained more in Section 6.5.

If we fit a β-model to the cluster density profile, we can de-project the profile and calculate the 3D central magnetic field dispersion $\sigma_{B,0}$ as (e.g. Johnson et al., 2020)

$$\sigma_{B,0} = \sigma_{\rm RM,0} \frac{\sqrt{3}}{812\,\pi^{1/4}}\, n_0^{-1}\, \Lambda_0^{-1/2}\, r_c^{-1/2} \sqrt{\frac{\Gamma(\alpha_1 + 1/2)}{\Gamma(\alpha_1)}}. \tag{6.11}$$

where Λ_0 is the unknown characteristic length scale of the magnetic field and $\alpha_1 = \frac{3}{2}(1+$

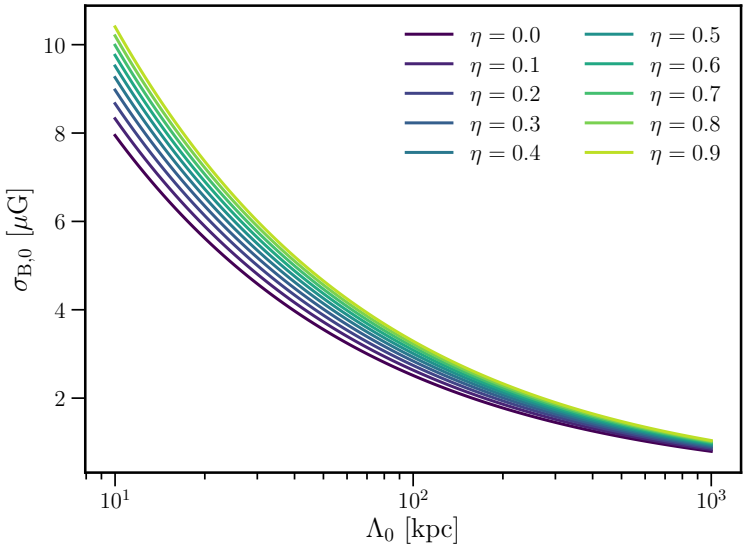

Figure 6.9: Central magnetic field dispersion, calculated from Eq. 6.11, as a function of the characteristic length scale Λ_0 and the magnetic field to thermal electron density scaling parameter η.

$\eta)\beta_c - \frac{1}{4}$. Figure 6.9 shows the value of $\sigma_{B,0}$ against Λ_0. For a reference value of $\Lambda_0 = 10$ kpc and $\eta = 0.15$, we find that $\sigma_{B,0} = 8\,\mu$G.

6.4.3 Cluster members vs background sources

Theoretically, since cluster members are on average located at the midplane of the cluster and polarised light thus travels through half the column that background sources probe, we would expect background sources to display a scatter in RM that is on average greater by a factor $\sqrt{2}$. However, from Figure 6.6 it becomes clear that such an effect is not observed. To investigate this in more detail, we calculated a more robust measure of scatter, the interquartile range. This is defined as the difference between the 75th and 25 percentiles of the data such that a few sources with large RM values do not dominate the scatter. The interquartile range is shown in Figure 6.10. The trend of increasing scatter with decreasing radius is still visible, but cluster members and background sources show similar scatter even when computed at similar radii.

To quantify this, we performed a z-test to test two null hypotheses in every bin: i) that the scatter of background sources and cluster members are the same, and ii) that the scatter of background sources is $\sqrt{2}$ times the scatter of cluster members. We found that we could reject neither of the null hypotheses with 95% confidence. This implies that the uncertainties are currently still too large to identify a statistically significant difference between the RM of background sources and cluster members. To increase the number statistics, we also tried binning all sources into a radial bin bounded by $[0, R_{500}]$, and found marginal evidence ($p = 0.02$) to reject the null hypothesis that $\mathrm{IQR}(\mathrm{RM}_{\mathrm{behind}}) = \sqrt{2}\cdot\mathrm{IQR}(\mathrm{RM}_{\mathrm{inside}})$. However,

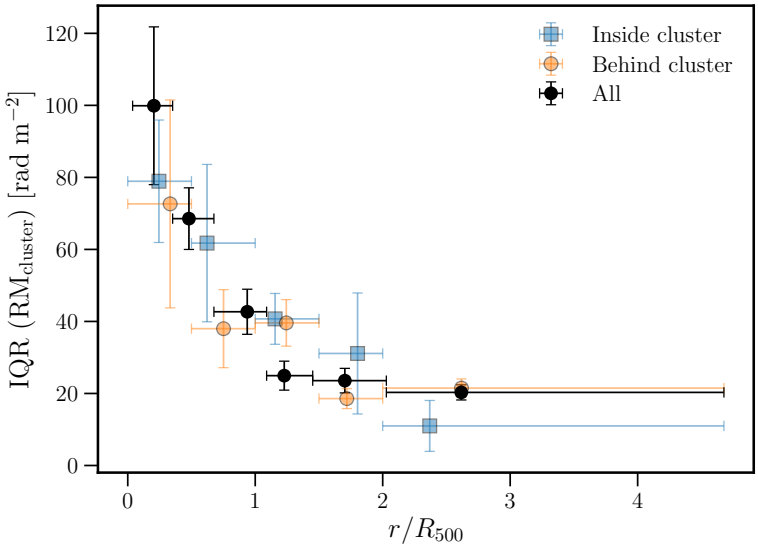

Figure 6.10: Interquartile range of the RMs in bins of projected distance to the nearest cluster centre. The bins for the full sample have equal frequency with 98 sources per bin, while the bins for the subsamples are defined in steps of $0.5R_{500}$ up to $2R_{500}$ to sample similar radii. The horizontal error bar indicates the width of the bin, and the points are plotted at the median radius in the bin. Uncertainties are calculated from 1 000 bootstraps.

this is likely caused by the fact that the cluster members are preferentially detected at smaller radii (median radius $0.34R_{500}$) than background sources (median radius $0.54R_{500}$), where the scatter is expected to be larger.

6.4.4 Merging vs relaxed clusters

Differences between the magnetic fields of relaxed and merging clusters have been tentatively observed in various studies (Bonafede et al., 2010; Stasyszyn & de los Rios, 2019; Osinga et al., 2022), but not yet clearly quantified. Following Osinga et al. (2022), we split our sample into merging and relaxed clusters based on the presence of a cool-core (CC) or absence of one (NCC). We defined the same bins as Osinga et al. (2022) to separate the central cooling core region ($r < 0.2R500$), as this is where the enhanced electron density of the cool-core clusters becomes noticeable, as also shown in Figure 6.19. The scatter in RM as a function of distance for the NCC and CC clusters is shown in Figure 6.11. We note that the central bin only has 7 sources in the CC sample (while the NCC sample has 37), which prevents using the IQR as a robust estimate of the scatter. There is a hint that CC clusters have higher $\sigma_{\rm RM}$ as expected from the increased electron density in the cooling core region, but the uncertainties are too large to reliably conclude such an effect. We do however see that merging clusters have significantly higher RM scatter in the region $0.2 < r/R_{500} < 1.0$ where 90 and 88 sources are detected respectively in both sub-samples.

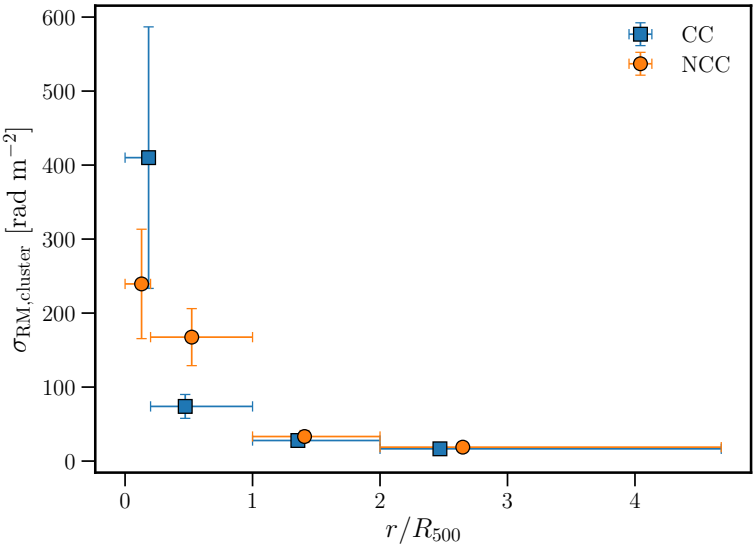

Figure 6.11: Standard deviation of RM as a function of projected distance to the nearest cluster centre, separately for CC and NCC clusters. The horizontal error bar indicates the width of the bin, and the points are plotted at the median radius in the bin.

6.4.5 Comparison to models

To compare the data to more involved models with a radial decline of magnetic field values and electron densities determined per cluster, and a power spectrum of magnetic field fluctuation scales, we follow the principle as laid out in Section 6.3, simulating magnetic fields with a 1024^3 pixel grid with a pixel size of 3 kpc. In the following section, we thus consider only sources that are detected at $\lesssim 1500$ kpc. This results in 303 polarised radio sources detected in 70 clusters for which X-ray information is available and simulations could be evaluated.

Constraining the magnetic field power spectrum

Both the RM and depolarisation of sources scale similarly (although not identically) with the magnetic field strength, but differently with n and Λ_{max}, and therefore the ratio can be used to constrain n and Λ_{max}, relatively independent of the other parameters (e.g. Bonafede et al., 2010). We defined the RM ratio as

$$\mathrm{RM\,ratio} = \frac{|\mathrm{RM}|}{1 - DP}. \tag{6.12}$$

This ratio is also relatively independent of radial distance, as the depolarisation will increase (i.e. take lower values of DP) as the RM increases towards the cluster centre. We verified this with both Spearman and Pearson tests, which showed no significant correlation.

The median observed RM ratio across all sources was found to be 139 ± 17, with the uncertainty calculated by 1 000 bootstraps. Figure 6.12 shows the median observed RM ratio

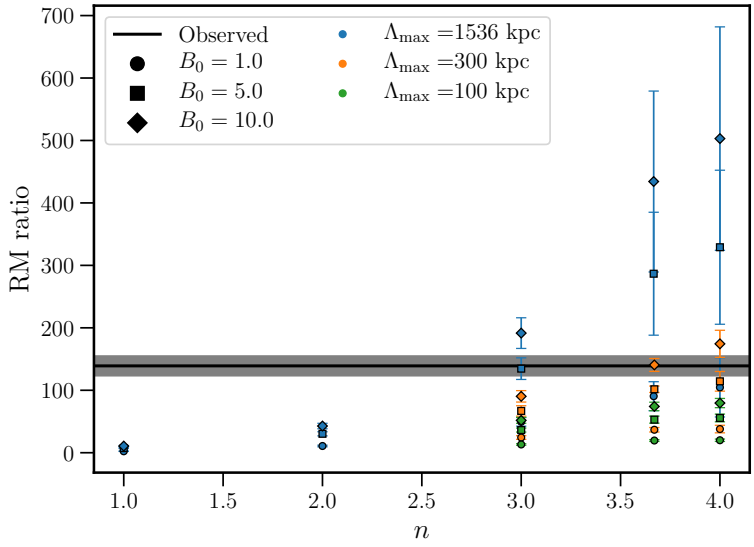

Figure 6.12: RM ratio, as defined in Equation 6.12, as a function of magnetic field power spectrum index n. The median observed value is indicated by the black line, while the simulated values are indicated by the coloured points, with different markers for different magnetic field strengths. The uncertainty on the simulated values reflect the 16th and 84th percentile of 10 random initialisations.

compared with simulated values for sources sampled at similar positions in the simulated RM and depolarisation images. It is clear from the figure that models with most of the magnetic field energy on small scales (i.e. $n < 3$) cannot reproduce the observed RM ratio, mainly because those models result in too low values of |RM| due to the rapidly fluctuating magnetic field along the line of sight. Instead, models with $n \geq 3$ provide a good fit for various values of the maximum correlation scale Λ_{max}. Lowering Λ_{max} has an analogous effect to lowering n, namely decreasing the coherence length of the magnetic field along the line of sight. This thus results in a smaller average |RM| while the effect on depolarisation is less significant, as this is measured on scales below the observing beam (less than typically 15 kpc, although dependent on cluster redshift). Thus, the observed data best matches $n \geq 3$.

For a Kolmogorov spectrum ($n = 3.67$) with typical values of the central magnetic field strength between $1 - 10\,\mu$G, the data is consistent with $\Lambda_{max} > 300$ kpc. Lower values of Λ_{max} would require significantly higher central magnetic field strengths.

Constraining the maximum correlation scale

To attempt to constrain the maximum projected correlation scale of the magnetic field, we computed the RM structure function[3]. The structure function is sensitive to fluctuations in rotation measure on varying scales. If the thermal electron density and magnetic field

[3]The structure function was computed using the framework from `https://github.com/AlecThomson/structurefunction`

strength are uniform, the structure function can be used to infer the power spectrum of the magnetic field (Ensslin et al., 2003). Although this is not the case across our cluster sample, the structure function is still a useful estimate to characterise RM fluctuations as a function of physical scales.

The (two point) structure function is defined as (e.g. Haverkorn et al., 2004)

$$\mathrm{SF}_{\mathrm{RM,obs}}(\Delta r) = \langle \mathrm{RM}(\mathbf{x}) - \mathrm{RM}(\mathbf{x}+\mathbf{r}) \rangle \,. \tag{6.13}$$

where the average is taken over all pairs at positions $\mathbf{x}$ and $\mathbf{x}+\mathbf{r}$ with similar distance Δr between the two components. Taking into account the offset added by the uncertainties on the RM, we computed the corrected structure function as

$$\mathrm{SF}_{\mathrm{RM}}(\Delta r) = \mathrm{SF}_{\mathrm{RM,obs}}(\Delta r) - \mathrm{SF}_{\sigma_{\mathrm{RM}}}(\Delta r), \tag{6.14}$$

where $\mathrm{SF}_{\sigma_{\mathrm{RM}}}$ denotes the offset correction, calculated by computing the structure function of the uncertainties. This correction was found to be on the order of $< 10\%$ of the observed structure function, as is shown in Figure 6.20.

The uncertainty on the observed structure function was computed numerically by bootstrapping the catalogue 100 times. Because we are interested in the structure function of the cluster magnetic field and not that of the intrinsic radio sources, we computed the projected distance between the radio source pairs by placing them at the cluster redshift, as that is the location of the Faraday screen. This assumes that the intrinsic RMs of source pairs are uncorrelated, which is a good assumption since they are almost exclusively unrelated sources. However, the fact that sources in a similar Δr bin can be located at different radial distances complicates the interpretation of the structure function, unless the form of the power spectrum is independent of radius, and only the amplitude scaling is affected.

The structure function is expected to approach zero for small values of Δr and $2\sigma^2_{\mathrm{RM}}$ for large values of Δr (Haverkorn et al., 2004; Johnson et al., 2020). In the Gaussian random field assumption, the amplitude of the structure function scales with B^2, because the scatter in RM scales linearly with B. We thus plot normalised structure functions, as we are not interested in the B^2 normalisation in this section.

The structure function is shown in Figure 6.13a, where the distance between pairs is normalised by the host cluster R_{500} to stack different clusters together and only sources detected at $r < R_{500}$ were used. The form of the structure function is relatively flat, showing no clear increase as a function of projected separation, indicating that it has already saturated. This would mean that the characteristic scale of RM fluctuations is below $0.05R_{500}$, or roughly 50 kpc. However, when we compare the observed structure function to the structure function calculated from simulated RM images with an equivalent sampling of sight lines, the simulated structure functions all show similar behaviour to the observed structure function, indicating the radial location of the sightline is dominating the form of the structure function. This is clearly seen when sources are not sampled at equivalent positions, as shown in Figure 6.13b. This means that current data do not allow us to distinguish different characteristic correlation scales through the structure function.

We can, however, compute the structure function in bins of projected radius, to investigate whether the magnetic field adheres to a similar power spectrum as a function of projected radius. The structure function computed in three different radial bins is shown

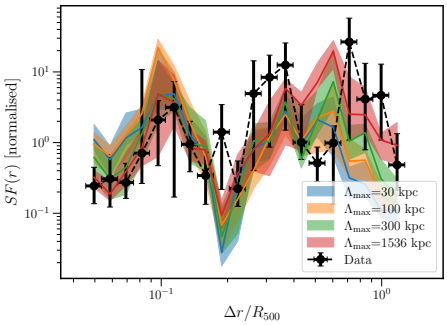

(a) Sampled at an equal number of equivalent sightlines.

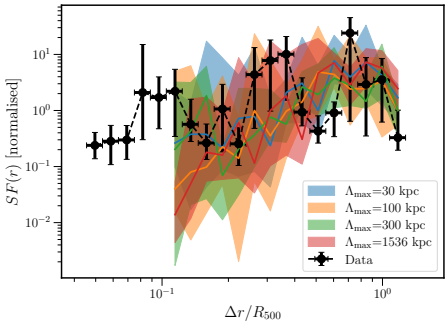

(b) Sampled at an equal number of randomly placed sightlines. Bins at small separations are now omitted as not enough source pairs were found in the simulations.

Figure 6.13: RM structure function as a function of normalised pair separation in 20 logarithmically spaced bins. The black points indicate the observed values, while the coloured points indicate simulated values for a Kolmogorov power spectrum. All functions are normalised to have a median amplitude equal to 1, as the amplitude is degenerate with B_0^2. The shaded regions show the 16th and 84th percentiles of 10 random initialisations.

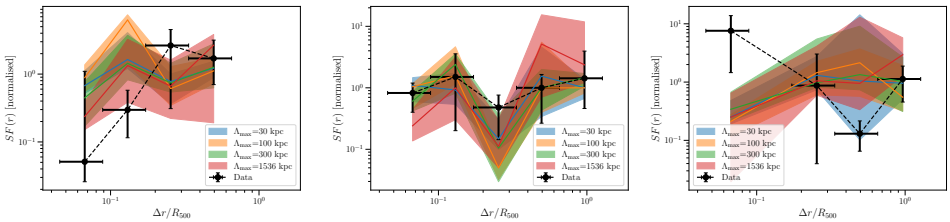

(a) $0.0 < r/R_{500} < 0.33$ (b) $0.33 < r/R_{500} < 0.66$ (c) $0.66 < r/R_{500} < 1.0$

Figure 6.14: Equivalent to Fig. 6.13a, but in bins of projected distance.

in Figure 6.14. From this figure, we see that the observed structure function is consistent with being constant for all three radial bins. We thus find no evidence that the structure of the magnetic field is different as a function of radius.

Full forward model

Finally, we find the best model that reproduces the data by following the approach used in previous works such as Murgia et al. (2004); Bonafede et al. (2010); Govoni et al. (2017); Stuardi et al. (2021), directly comparing the simulated RM and depolarisation images to the observed data. For every source, we sample an equivalent source from the simulated clusters, and compute the expected RM and depolarisation. We minimize the difference between the simulated and observed radial scatter in RMs, and the depolarisation as a

function of radius. We define the function to be minimized, q, as follows

$$q = q_{\rm depol} + q_{\rm RM} = \sum_r \left(\frac{{\rm DP}_{\rm obs}(r) - \langle {\rm DP}_{\rm sim}(r) \rangle}{{\rm err}({\rm DP}_{\rm obs})} \right)^2 + \left(\frac{\sigma_{\rm RM,obs}(r) - \langle \sigma_{\rm RM,sim}(r) \rangle}{{\rm err}(\sigma_{\rm RM,obs})} \right)^2, \quad (6.15)$$

where the observables are calculated in bins of projected radii (equivalent to Fig. 6.6), and the simulated observables, denoted by the angle brackets, are averaged over 10 different random initialisations. Because sources in this sample were found to be intrinsically depolarised with DP=0.92 at large radii (Osinga et al., 2022), we incorporated this into the simulated depolarisation. Similarly, we correct $\sigma_{\rm RM}$ for the contribution caused by the uncertainties by subtracting in quadrature the observed $\sigma_{\rm RM}$ in the last bin from the $\sigma_{\rm RM}$ profile. As Section 6.4.5 showed that the RM ratio is consistent only with models that have $n > 3$, we fix the power spectrum to the Kolmogorov value of $n = 3.67$ to reduce the computational burden.

First, we investigate the best-fit models when fixing the magnetic field to electron density scaling to the typical value of $\eta = 0.5$. Figures 6.15a and 6.15b show the values of $q_{\rm depol}$ and $q_{\rm RM}$ respectively, as a function of B_0 and $\Lambda_{\rm max}$. We find the best agreement for a model with $B_0 = 5.0\,\mu$G and a maximum correlation scale equal to either $\Lambda_{\rm max} = 1536$ kpc or $\Lambda_{\rm max} = 300$ kpc. These models have very similar total q values, but $\Lambda_{\rm max} = 1536$ kpc is preferred by the depolarisation profile, while $\Lambda_{\rm max} = 300$ kpc is preferred by the $\sigma_{\rm RM}$ profile. The measured and simulated radial profiles are shown in Figure 6.16 for both best-fit models. Both models ($\Lambda_{\rm max} = 300$ and 1536 kpc) are shown to fit the data very well, although the observed $\sigma_{\rm RM}$ at a low projected radius is in both cases lower than the simulated value. This is likely due to the selection effect that sources with high values of RM will be depolarised and thus missed, biasing our observed $\sigma_{\rm RM}$ low, as discussed more in the next section. This selection bias is less important for radial depolarisation because upper limits on DP can be calculated from unpolarised sources as well.

Section 6.4.2 showed that the radial profile of $\sigma_{\rm RM}$ preferred low values of $\eta \approx 0.1$. We thus also test the value of $\eta = 0.1$, although we stress again that this might be caused by missing preferably high RM sources at low radii. The plots are shown in Appendix 6.6, Figures 6.21 and 6.22. The modelled $\sigma_{\rm RM}$ curve does provide a better fit for $B_0 = 1.0\mu$G, $\Lambda_{\rm max} = 300$ kpc and $\eta = 0.1$, although the model now underestimates the central scatter, while in reality, the central scatter is likely higher than what we observed. Additionally, the depolarisation profile shows a worse fit to the data for this model, instead favouring $B_0 = 10\,\mu$G and $\Lambda_{\rm max} = 30$ kpc, which is rejected on the basis of the RM ratio analysis in Section 6.4.5. A model with $\eta = 0.5$ thus better explains both the depolarisation and RM scatter profile simultaneously.

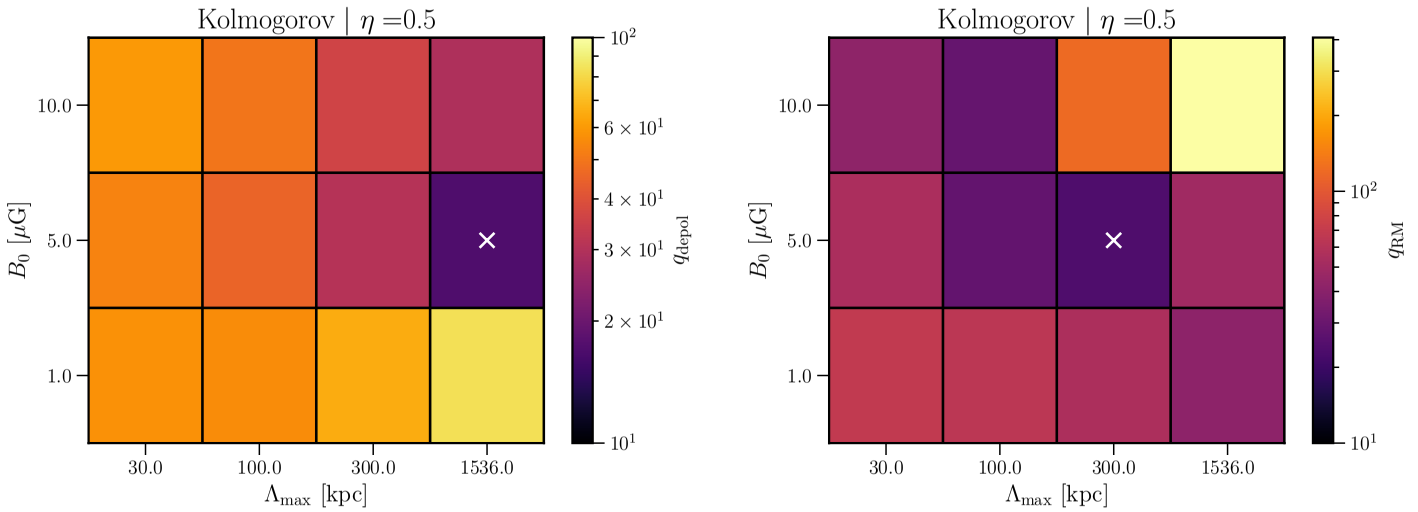

(a) (b)

Figure 6.15: Values of q_{depol} (a) and q_{RM} (b) as defined in Equation 6.15 for combinations of B_0 and Λ_{RM}. Models are simulated with a Kolmogorov power spectrum and $\eta = 0.5$. The best-fit model is marked by a cross.

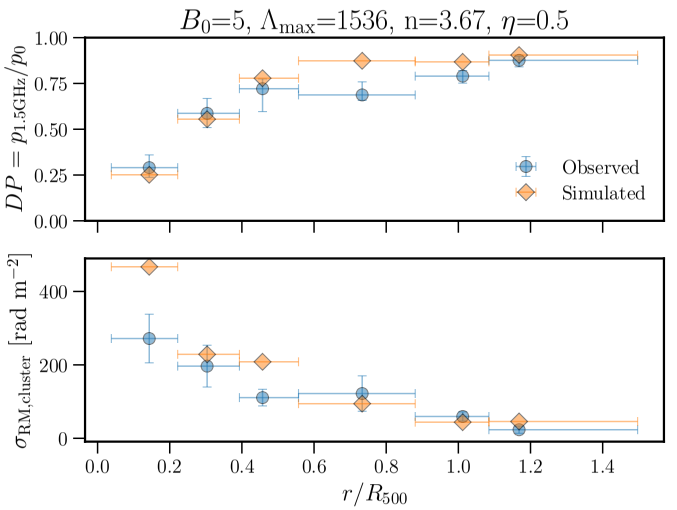

(a) Model that minimizes q_{depol}.

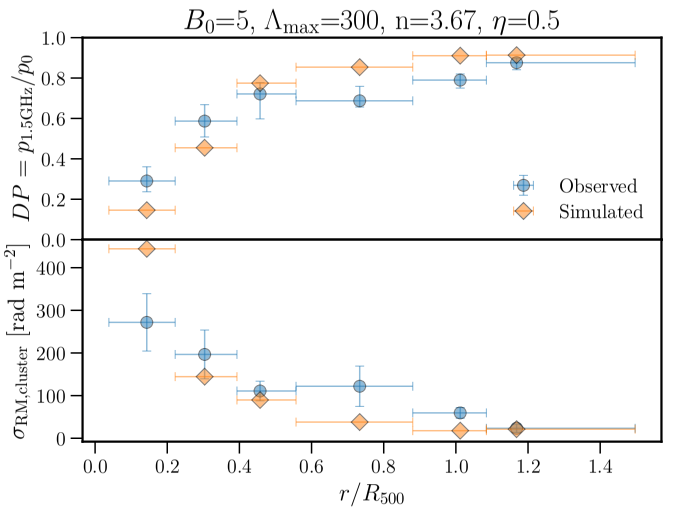

(b) Model that minimizes q_{RM}.

Figure 6.16: Comparison between observed and forward-simulated depolarisation and RM scatter for two models that minimize the q statistic as defined in Equation 6.15.

6.5 Discussion

Previous studies of samples of clusters have investigated either the statistical depolarisation (Bonafede et al., 2010; Osinga et al., 2022) or the rotation measure as a function of projected radius (Clarke et al., 2001; Böhringer et al., 2016; Stasyszyn & de los Rios, 2019). In this work, we have for the first time measured both the rotation measure and depolarisation in a consistent way for polarised radio sources along sight-lines of stacked galaxy clusters.

The previously largest statistical study was performed by Böhringer et al. (2016), who found 92 RM sight-lines within R_{500} by cross-matching 1773 clusters with the RM catalogue compiled by Kronberg & Newton-McGee (2011). We significantly increase the number statistics, detecting 261 radio sources with well-defined RM and depolarisation within R_{500} in only 124 clusters. Comparing Table 6.1 with Table 1 in Böhringer et al. (2016), we find significantly higher $\sigma_{\rm RM}$ in all radial bins, except outside R_{500}. The reason for this is likely twofold. First, there is a difference in the RM sensitivity as the Böhringer et al. (2016) is likely based on radio data with larger channel widths, preventing detection of high RMs (they find a maximum $|{\rm RM}| < 700$ rad m^{-2}). Second, the cluster samples are different, as Böhringer et al. (2016) quote a mean cluster mass of $3\times10^{14} M_{\odot}$, while only 15 out of our 124 clusters have a mass below this value, and the mean mass of our sample is $5.7\times10^{14} M_{\odot}$. Taking the different sampling into account by calculating the scatter as a function of electron column density in Section 6.4.1, we found an average magnetic field estimate of $3\,\mu$G in our sample of galaxy clusters, perfectly consistent with the findings of Böhringer et al. (2016).

The observed scatter of RMs was found to be dominated by the effect of the ICM inside R_{500}, but dominated by the uncertainties in the RM outside R_{500}, as shown in Figure 6.7. At large radii (i.e. $r > 2R_{500}$) we observed $\sigma_{\rm RM} = 28 \pm 6$, which is a combination of source to source RM scatter and measurement uncertainties. This is lower than the value of 56 ± 8 found by Böhringer et al. (2016), but significantly higher than the expected intrinsic variation in the radio sources of $5-7$ rad m^{-2} (Schnitzeler, 2010). We thus cannot determine the magnetic field properties on the outskirts of galaxy clusters, as we are dominated by the uncertainties in the RM determination. However, inside R_{500}, the radial profile of the scatter can be used to determine the magnetic field strength and radial profile, as shown in Figure 6.8.

The RM scatter inside R_{500} showed a flat radial profile compared to expectations from a simple scaling of the magnetic field with the electron density of clusters. Plasma theories generally predict $\eta > 0.5$, with flux freezing giving $\eta = \frac{2}{3}$, adiabatic compression giving $\eta = 1.0$ and dynamo models often predicting a constant magnetic energy density to thermal energy density ratio (i.e. $\eta = 0.5$). Observationally, the best determined magnetic field profile is that of the Coma cluster, for which $\eta = 0.4-0.7$ was found. Other studies using resolved (cluster) radio galaxies also find $\eta \geq 0.5$ (Murgia et al., 2004; Vacca et al., 2012; Govoni et al., 2017; Stuardi et al., 2021). In comparison, we found that the best-fit $\sigma_{\rm RM}(r)$ model preferred $\eta > 0.15$, which is below the other experimental and theoretical values. However, statistical studies such as this one that use RMs of unresolved radio sources to determine the RM scatter suffer from a significant observational bias as sources with high RM values near the centre of clusters are likely to be depolarised and thus missed. The observed electron density profiles, shown in Fig 6.19, illustrate the problem as the electron densities rise strongly towards the core of clusters. Using Eq. 6.10, we expect $\sigma_{\rm RM}$ to be

$\sim$ 10 times larger at $r = 0.25R_{500}$ than at $r = 0.5R_{500}$. Since the scatter observed at $0.5R_{500}$ is on the order of 10^2 rad m^{-2}, we expect a scatter on the order of 10^3 rad m^{-2} at $r = 0.25R_{500}$. Sources with such high RM scatter are quickly depolarised at L-band frequencies (Osinga et al., 2022), presenting a missing data problem. This artificially decreases the steepness of the $\sigma_{\rm RM}$ profile, requiring low values of η to match the data. In contrast, studies relying on resolved radio sources often probe $\sigma_{\rm RM}$ on smaller scales (i.e. the size of the radio source) where fluctuations are expected to be significantly smaller and thus if a polarised radio source is detected, the scatter can be determined more accurately (e.g. Bonafede et al., 2010).

Other statistical studies probing many unresolved sightlines such as Böhringer et al. (2016); Stasyszyn & de los Rios (2019) have also not observed a strong increase of $\sigma_{\rm RM}$ at low radii, implying the same observational bias. However, at higher frequencies, RM values as high as 10,000 have been observed in the centre of some clusters (e.g. Taylor & Perley, 1993). Higher frequency data that suffers less from depolarisation is thus needed to determine the value of η accurately, but the current value $\eta > 0.15$ can be interpreted as a lower limit.

Depolarisation does not suffer as strongly from this observational bias at low radii, as upper limits on depolarisation fractions can still be set on sources that are significantly depolarised. Thus, we finally fit both the $\sigma_{\rm RM}$ and depolarisation radial profile jointly by means of forward modelling. When fixing the magnetic field to electron density scaling to the observationally best-determined value of $\eta = 0.5$ (Bonafede et al., 2011). The best-fit model was found to have $B_0 = 5.0\mu$G and $\Lambda_{\rm max} \geq 300$ kpc. The central magnetic field strength is consistent with previous single object studies as well as statistical studies (Murgia et al., 2004; Govoni et al., 2006; Guidetti et al., 2008; Bonafede et al., 2010; Vacca et al., 2010, 2012; Govoni et al., 2017; Stuardi et al., 2021; Böhringer et al., 2016). However, the correlation scale is significantly larger than found in resolved cluster member studies that typically find values around 50 kpc (Guidetti et al., 2008; Bonafede et al., 2010; Vacca et al., 2012; Govoni et al., 2017), although the resolved sources are often limited in size to less than a few hundred kiloparsec. Studies that use the brightness fluctuations or possibly polarised emission of radio halos to constrain the magnetic field power spectrum found results consistent with outer magnetic field fluctuation scales of $\sim$ 400kpc (Govoni et al., 2005; Vacca et al., 2010), agreeing with our estimate. Fluctuations on scales of more than a few hundred kpc are also expected theoretically, as the turbulent dynamo process thought to be responsible for magnetic field amplification in galaxy clusters is expected to occur on various scales, from less than a kpc up to a Mpc (Donnert et al., 2018).

In our modelling, we have decided to combine the information from cluster members and background sources, as Osinga et al. (2022) showed that the depolarisation properties of cluster members and background sources were similar. We checked for a local contribution to $\sigma_{\rm RM}$ from cluster members in Section 6.4.3 but found that we could reject neither the null hypothesis that cluster members and background sources have similar scatter nor the null hypothesis that background sources show a scatter that is $\sqrt{2}$ times larger. This is in accordance with the interpretation from Osinga et al. (2022) that, at the moment, we do not have the number statistics to confidently assert that cluster members are a biased probe of the magnetised ICM.

Finally, we checked for qualitative differences between merging and relaxed clusters.

During cluster mergers, turbulence is injected on large scales, which can amplify magnetic fields, and drive large fluctuation scales (e.g. Vacca et al., 2018). Relaxed clusters, on the other hand, are expected to have smaller fluctuation scales, as the energy injected by a previous merger has dissipated through cascades to smaller and smaller scales. We found that merging clusters show higher values of $\sigma_{\rm RM}$ in the region $0.2 < r/R_{500}$, while relaxed clusters tentatively showed larger scatter inside the dense cooling core region (Fig. 6.11). The higher RM scatter in merging clusters was also observed by Stasyszyn & de los Rios (2019), although with larger radial bin sizes. If a scaling between B and n_e is assumed, then CC clusters would indeed show a steep radial profile in both $\sigma_{\rm RM}$ and depolarisation (which was observed in also in Osinga et al. 2022), while NCC clusters should show a flatter profile, as the thermal gas density follows a flatter profile. The observed difference between the radial RM scatter in CC and NCC clusters is thus consistent with the behaviour of the thermal plasma in galaxy clusters.

6.6 Conclusion

This work has presented the continuation of the study presented in Osinga et al. (2022), where VLA L-band polarisation observations of 124 massive Planck clusters were presented, and the depolarisation properties of polarised sources were investigated as a function of radius. We have incorporated the additional information from the best-fit RM and constrained cluster magnetic field properties by combining depolarisation and RM in a sample of clusters for the first time. We summarise the results of this work as follows:

1. We have clearly detected the increase of the scatter in rotation measure as a function of decreasing projected radius or increasing electron column density. Averaging all 124 clusters, we find a scatter within R_{500} of $\sigma_{\rm RM} = 241 \pm 44$ rad m^{-2}. The scatter outside of R_{500} was found to be 38 ± 4 rad m^{-2} and dominated by the uncertainties in the RM determination.

2. Assuming that magnetic fields fluctuate on a single characteristic length scale Λ_c with a constant strength, the observed RM scatter agrees with an average magnetic field strength within R_{500} of $3\,(\Lambda_c/10{\rm kpc})^{-0.5}\,\mu$G.

3. The profile of $\sigma_{\rm RM}$ as a function of projected radius requires a scaling of $B \propto n_e^{\eta}$ with $\eta > 0.15$. This value presents a lower limit, as sources with high RM values are missed near the centre of the clusters due to depolarisation. Higher frequency data is required to more accurately constrain η using RM scatter only.

4. Jointly modelling both the depolarisation and rotation measure of sources in a forward modelling approach, we find that the observations best agree with the following magnetic field parameters: $B_0 = 5.0\,\mu$G, $\Lambda_{\rm max} = 300 - 1536$ kpc, $\eta = 0.5$ for a fixed Kolmogorov power spectrum with $n = 3.67$. Models with $n < 3$ are strongly rejected by the RM data.

5. We could not reject the null hypothesis that cluster members sources show similar scatter in $\sigma_{\rm RM}$ as background sources, consistent with the result that background sources and cluster members also show similar depolarisation in the same sample of clusters (Osinga et al., 2022).

6. The radial $\sigma_{\rm RM}$ profile of cool-core and non-cool-core clusters follows the expected trend from the thermal gas density profiles, with CC clusters showing a hint of larger $\sigma_{\rm RM}$ in the core, which significantly drops below the observed $\sigma_{\rm RM}$ of NCC clusters outside of the core, as the thermal gas density also drops rapidly outside of the core.

In this work, we implicitly assumed that all clusters have the same magnetic field parameters, while in reality, this might be a function of dynamical state, mass, or redshift. The universality of cluster magnetic fields has not been thoroughly tested (e.g. Govoni et al., 2017). Future observations with more sensitive telescopes such as MeerKAT and the SKA could test this assumption by detecting enough polarised sightlines through single clusters such that stacking is not required.

ACKNOWLEDGEMENTS

EO and RJvW acknowledge support from the VIDI research programme with project number 639.042.729, which is financed by the Netherlands Organisation for Scientific Research (NWO). EO thanks both Wout Goesaert and Joppe Swart for the careful looks at his code. This paper has made use of observational material taken with an NRAO instrument. The National Radio Astronomy Observatory is a facility of the National Science Foundation operated under cooperative agreement by Associated Universities, Inc. The Pan-STARRS1 Surveys (PS1) and the PS1 public science archive have been made possible through contributions by the Institute for Astronomy, the University of Hawaii, the Pan-STARRS Project Office, the Max-Planck Society and its participating institutes, the Max Planck Institute for Astronomy, Heidelberg and the Max Planck Institute for Extraterrestrial Physics, Garching, The Johns Hopkins University, Durham University, the University of Edinburgh, the Queen's University Belfast, the Harvard-Smithsonian Center for Astrophysics, the Las Cumbres Observatory Global Telescope Network Incorporated, the National Central University of Taiwan, the Space Telescope Science Institute, the National Aeronautics and Space Administration under Grant No. NNX08AR22G issued through the Planetary Science Division of the NASA Science Mission Directorate, the National Science Foundation Grant No. AST-1238877, the University of Maryland, Eotvos Lorand University (ELTE), the Los Alamos National Laboratory, and the Gordon and Betty Moore Foundation. The Legacy Surveys consist of three individual and complementary projects: the Dark Energy Camera Legacy Survey (DECaLS; Proposal ID 2014B-0404; PIs: David Schlegel and Arjun Dey), the Beijing-Arizona Sky Survey (BASS; NOAO Prop. ID 2015A-0801; PIs: Zhou Xu and Xiaohui Fan), and the Mayall z-band Legacy Survey (MzLS; Prop. ID 2016A-0453; PI: Arjun Dey). DECaLS, BASS and MzLS together include data obtained, respectively, at the Blanco telescope, Cerro Tololo Inter-American Observatory, NSF's NOIRLab; the Bok telescope, Steward Observatory, University of Arizona; and the Mayall telescope, Kitt Peak National Observatory, NOIRLab. The Legacy Surveys project is honoured to be permitted to conduct astronomical research on Iolkam Du'ag (Kitt Peak), a mountain with particular significance to the Tohono O'odham Nation. SDSS-IV is managed by the Astrophysical Research Consortium for the Participating Institutions of the SDSS Collaboration including the Brazilian Participation Group, the Carnegie Institution for Science, Carnegie Mellon University, Center for Astrophysics | Harvard & Smithsonian, the Chilean Participation Group, the French Participation Group, Instituto de Astrofísica de Canarias, The Johns Hopkins University, Kavli Institute for the Physics and Mathematics of the Universe (IPMU) / University of Tokyo, the Korean Participation Group, Lawrence Berkeley National Laboratory, Leibniz Institut für Astrophysik Potsdam (AIP), Max-Planck-Institut für Astronomie (MPIA Heidelberg), Max-Planck-Institut für Astrophysik (MPA Garching), Max-Planck-Institut für Extraterrestrische Physik (MPE), National Astronomical Observatories of China, New Mexico State University, New York University, University of Notre Dame, Observatário Nacional / MCTI, The Ohio State University, Pennsylvania State University, Shanghai Astronomical Observatory, United Kingdom Participation Group, Universidad Nacional Autónoma de México, University of Arizona, University of

Colorado Boulder, University of Oxford, University of Portsmouth, University of Utah, University of Virginia, University of Washington, University of Wisconsin, Vanderbilt University, and Yale University This research has made use of the NASA/IPAC Extragalactic Database (NED), which is operated by the Jet Propulsion Laboratory, California Institute of Technology, under contract with the National Aeronautics and Space Administration. This research has made use of NASA's Astrophysics Data System (ADS).

Appendix I: Additional plots

For completeness, we plot in Figures 6.17 and 6.18 the cluster-induced rotation measure on a linear scale as a function of projected radius and column density, respectively. The electron density profiles of the clusters in our sample, as determined in Andrade-Santos et al. (2017), are shown in Figure 6.19. The structure function as defined in Equation 6.14 is shown in Figure 6.20. Finally, the q values of the full forward model for $\eta = 0.1$ are shown in 6.21, with the best-fit profiles shown in Fig 6.22. For $\eta = 0.1$, there is a clear mismatch between the depolarisation and RM scatter profiles. The depolarisation favours low values of B_0 with high values of $\Lambda_{\rm max}$, while the RM scatter favours high values of B_0 with small values of $\Lambda_{\rm max}$. A model with $\eta = 0.5$ thus more naturally predicts the behaviour of both the RM scatter and depolarisation consistently.

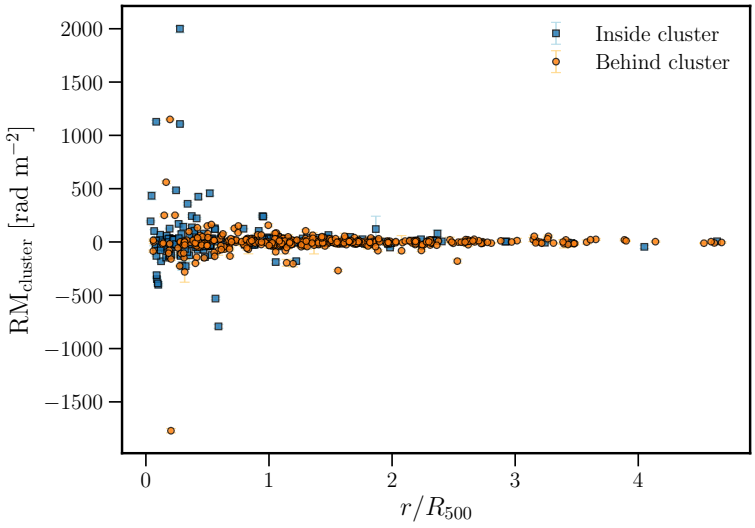

Figure 6.17: Cluster induced rotation measure as a function of normalised distance to the nearest cluster centre. The y-axis is shown on a linear scale, while a better view of sources with low RM is given by Figure 6.2.

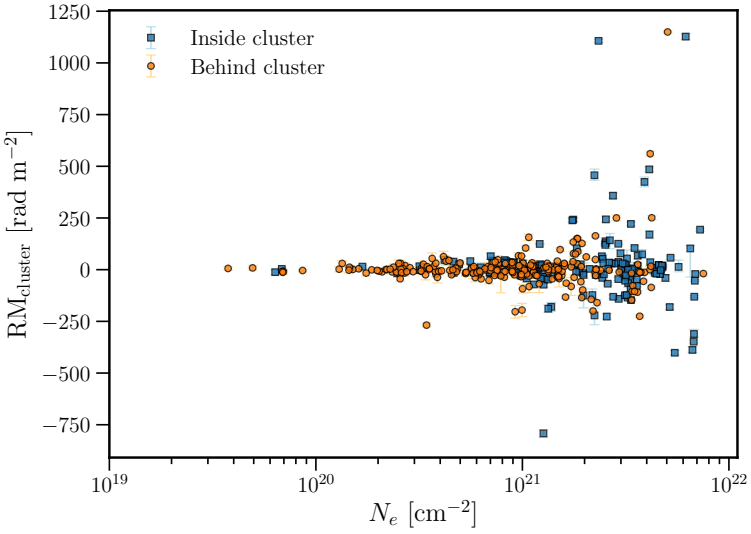

Figure 6.18: Cluster induced rotation measure as a function of electron column density. The y-axis is shown on a linear scale, while a better view of sources with low RM is given by Figure 6.4.

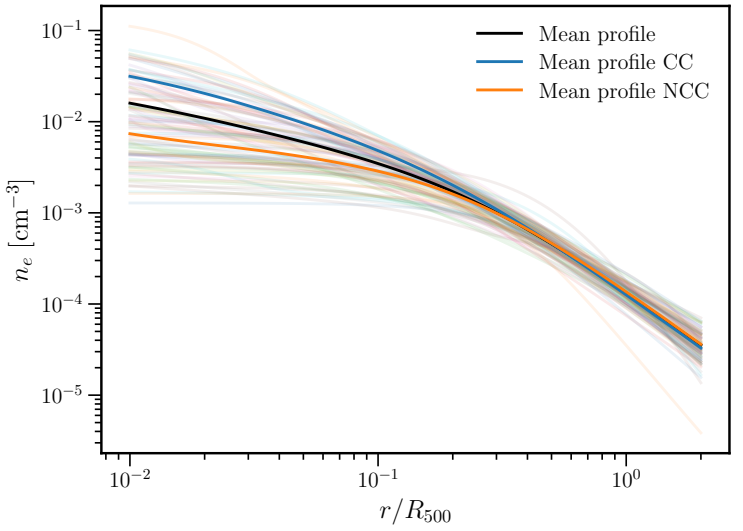

Figure 6.19: Average electron density profile as a function of normalised 3D radius for all clusters that have Chandra X-ray observations. The mean profile is shown in the black line.

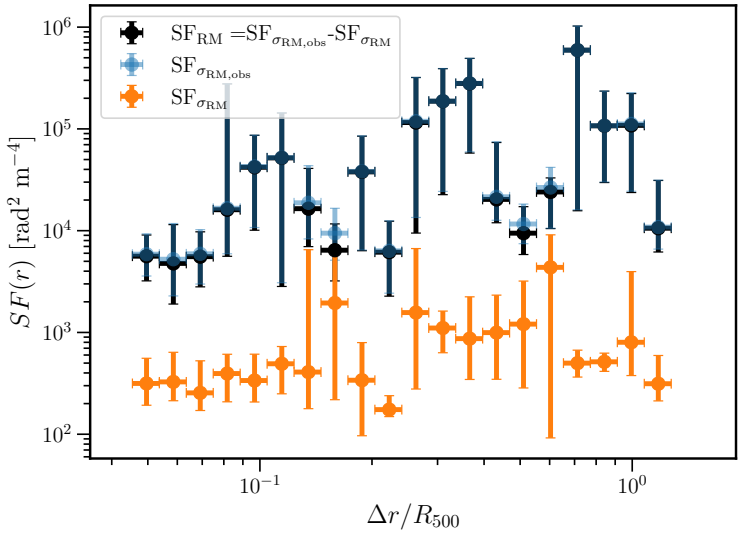

Figure 6.20: Corrected RM structure function as defined in Eq 6.14 as a function of normalised pair separation in 20 logarithmically spaced bins. The total RM structure function and the relatively small offset correction are shown in blue and orange respectively.

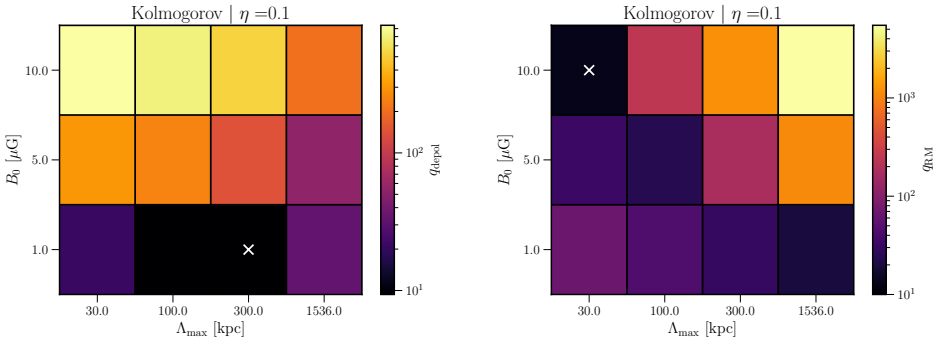

(a) (b)

Figure 6.21: Values of q_{depol} (a) and q_{RM} (b) as defined in Equation 6.15 for combinations of B_0 and Λ_{RM}. Models are simulated with a Kolmogorov power spectrum and $\eta = 0.1$. The best-fit model is marked by a cross.

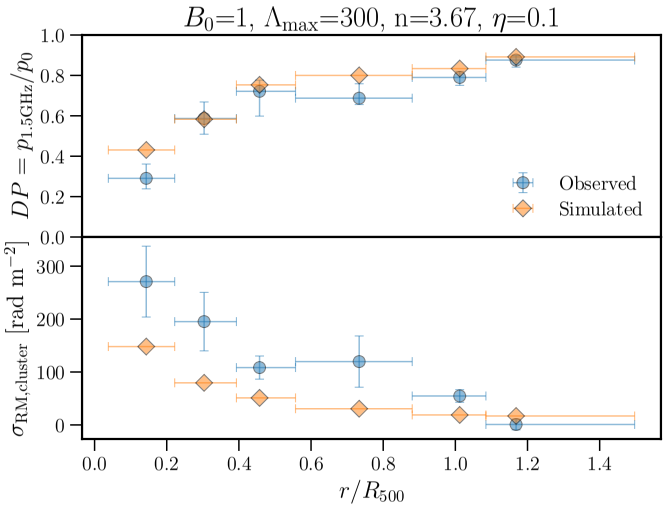

(a) Model that minimizes q_{depol}.

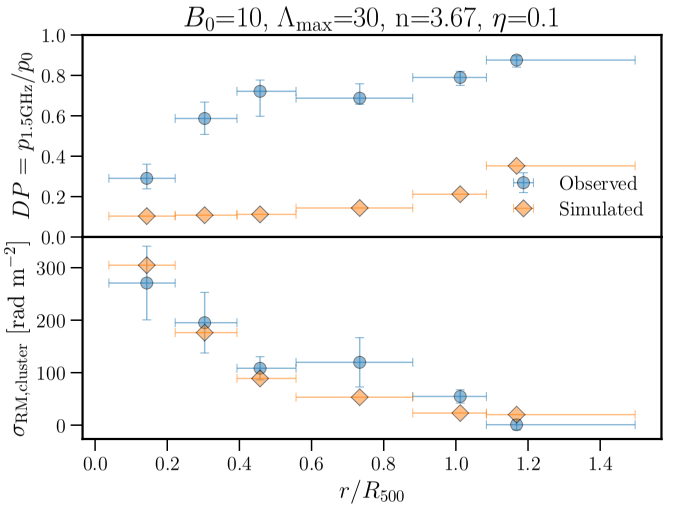

(b) Model that minimizes q_{RM}.

Figure 6.22: Comparison between observed and forward-simulated depolarisation and RM scatter for the model with $\eta = 0.1$ that minimizes the q statistics as defined in Equation 6.15.

Appendix II: Radial RM scatter

Here we investigate how to quantify the radial RM scatter in more detail than in Section 6.4.2, where the sample standard deviation was used. Figures 6.6 and Fig. 6.10 showed the scatter calculated from the standard deviation and interquartile range respectively. For a Gaussian distribution, it should hold that the standard deviation is equal to IQR/1.35, but this is clearly not the case. This is expected, however, as the distribution of RMs is only expected to be Gaussian at a single projected radius. In a radial bin of finite size, we are thus observing the sum of Gaussian distributions with different standard deviations, leading to a non-Gaussian distribution. This poses the question of how to best quantify the scatter. In Figure 6.24, we show the full RM distribution in the radial bins of Figures 6.6 and Fig. 6.10. Gaussian distributions with scatter calculated from the IQR and sample standard deviation are shown in the coloured lines. The IQR always shows a better fit to the central peak of the distribution, but underestimates the tails of the distribution. Vice versa, the standard deviation captures the tails of the distribution better but underestimates the central peaks. To compare the effect of the different estimates on the result of Section 6.4.2, we also fit the scatter calculated from the IQR to the theoretical RM scatter profile. The results are shown in Figures 6.23 and 6.25. Because the IQR is less sensitive to the excess in sources with high RM observed near the centre of clusters, the profile is flatter than the sample standard deviation radial profile, and we can thus not constrain η in this way. The resulting central magnetic field dispersion is about a factor 3 lower when calculated by means of IQR than through sample standard deviation.

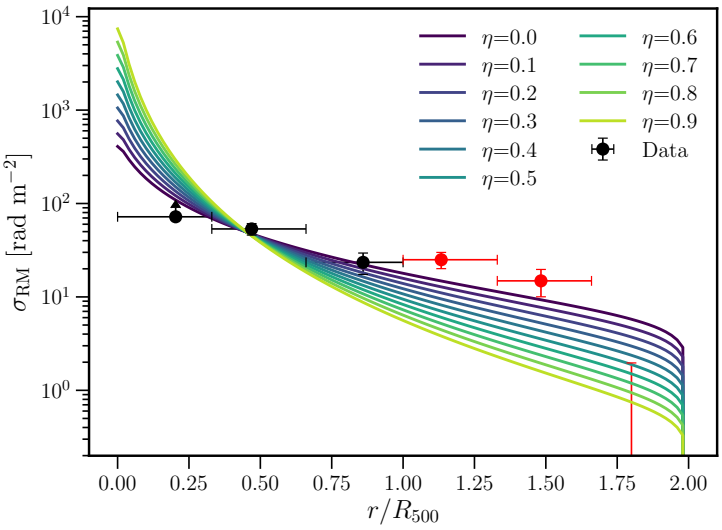

Figure 6.23: RM scatter calculated from the IQR and corrected for a baseline value of $\sigma_{\mathrm{RM}} = 15$ as a function of projected distance. The first point is plotted as a lower limit, and points outside R_{500} (shown in red) are ignored in the fit. The coloured lines show best-fit profiles computed for various values of η assuming Equation 6.10. The coloured lines show best-fit profiles computed for various values of η.

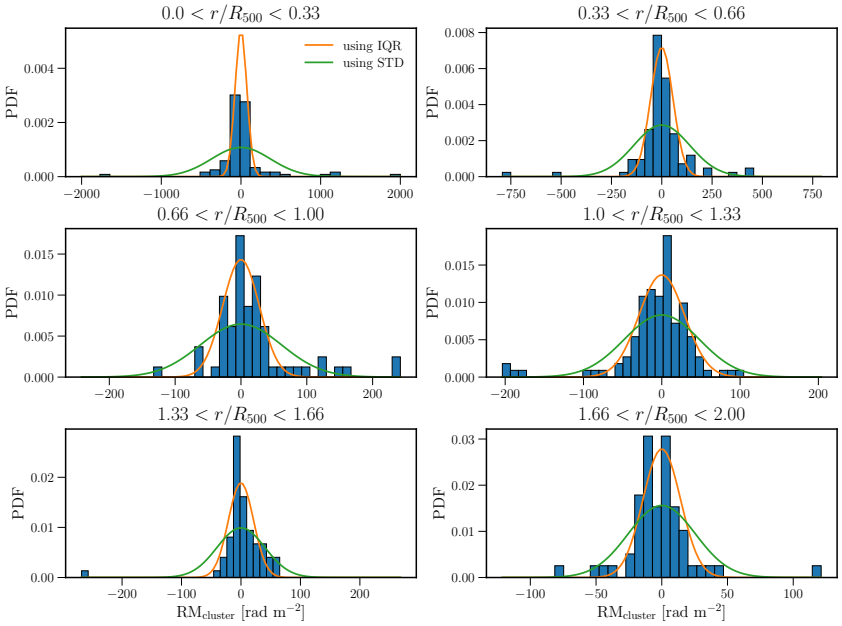

Figure 6.24: Distribution of RMs in different radial bins. The scatter is quantified in two ways, using the standard deviation and the interquartile range divided by 1.35.

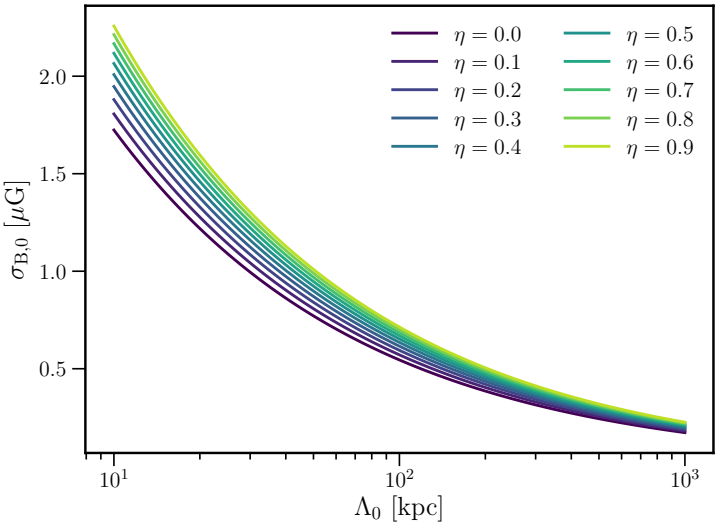

Figure 6.25: Central magnetic field dispersion as a function of the characteristic length scale Λ_0 and the magnetic field to thermal electron density scaling parameter η.

Appendix III: Updated polarised source catalogue

Table F.1: First 30 rows of the catalogue of 819 polarised radio sources that were detected in this work. The full table will become available in electronic form at the Centre de Données astronomiques de Strasbourg (CDS).

RA [deg]	DEC [deg]	Maj [″]	Min [″]	PA [deg]	p_0	χ_0 [rad]	RM [rad m^{-2}]	$\sigma_{\rm RM}$ [rad^2 m^{-4}]	I_0 [mJy]	α	$\tilde{\chi}^2_{\rm QU}$	$z_{\rm best}$	$z_{\rm best}$ source	$\theta_{\rm P}$ [arcmin]	r/R_{500}	Cluster	RA$_{\rm opt}$ [deg]	DEC$_{\rm opt}$ [deg]	MC	Flagged	Note	RM$_{\rm cluster}$ [rad m^{-2}]
19.55453 ± 0.00009	−27.16767 ± 0.00010	10.4 ± 1.1	6.11 ± 0.35	136 ± 7	$0.127^{+0.046}_{-0.030}$	$2.975^{+3.154}_{-3.154}$	20^{+6}_{-5}	8^{+5}_{-3}	$5.0^{+0.2}_{-0.2}$	$-0.45^{+0.12}_{-0.13}$	61	0.948 ± 0.077	2	11.60	2.9	G212.97-84.04	19.5606	-27.1622	False	False		10^{+11}_{11}
15.794198 ± 0.000035	−21.996243 ± 0.000030	7.03 ± 0.31	6.29 ± 0.24	117 ± 16	$0.079^{+0.029}_{-0.021}$	$0.995^{+0.498}_{-0.498}$	30^{+7}_{-7}	13^{+3}_{-3}	$12.7^{+0.2}_{-0.2}$	$-0.88^{+0.04}_{-0.04}$	52	-	-	9.49	0.6	G149.55-84.16	-	-	False	False	No counterpart.	27^{+9}_{8}
41.4094860 ± 0.0000022	−20.6108492 ± 0.0000024	9.548 ± 0.021	8.841 ± 0.018	59.7 ± 1.2	$0.104^{+0.001}_{-0.001}$	$0.465^{+0.008}_{-0.008}$	14^{+0}_{-0}	2^{+0}_{-0}	149.1^{+18}_{-18}	$-0.68^{+0.03}_{-0.03}$	434	-	-	12.41	3.5	G205.07-62.94	-	-	False	True	No counterpart.	13^{+5}_{5}
41.411690 ± 0.000009	−20.580840 ± 0.000007	9.18 ± 0.08	8.14 ± 0.06	101.3 ± 2.9	$0.119^{+0.003}_{-0.003}$	$1.643^{+3.117}_{-3.117}$	17^{+1}_{-1}	2^{+1}_{-1}	$28.6^{+0.4}_{-0.4}$	$-0.84^{+0.04}_{-0.04}$	144	-	-	11.75	3.3	G205.07-62.94	-	-	False	True	No counterpart.	18^{+6}_{6}
40.48671 ± 0.00010	−28.63936 ± 0.00021	30.8 ± 1.9	10.4 ± 0.4	113.9 ± 3.3	$0.281^{+0.024}_{-0.024}$	$0.368^{+0.071}_{-0.071}$	8^{+1}_{-1}	7^{+1}_{-1}	$16.1^{+0.5}_{-0.5}$	$-1.61^{+0.08}_{-0.08}$	89	0.238 ± 0.000	1	6.43	1.6	G222.97-65.69	40.4839	-28.6379	True	True	Radio Relic.	5^{+5}_{5}
40.47708 ± 0.00020	−28.63432 ± 0.00015	20.7 ± 2.0	10.0 ± 0.6	124 ± 6	$0.296^{+0.063}_{-0.054}$	$0.187^{+0.153}_{-0.153}$	7^{+3}_{-3}	10^{+2}_{-2}	$9.7^{+0.4}_{-0.4}$	$-2.37^{+0.13}_{-0.13}$	80	0.238 ± 0.000	1	5.95	1.5	G222.97-65.69	40.4839	-28.6379	True	True	Radio Relic.	3^{+6}_{6}
40.48939 ± 0.00025	−28.65367 ± 0.00018	20.5 ± 2.3	14.8 ± 1.4	114 ± 16	$0.140^{+0.014}_{-0.014}$	$1.909^{+3.123}_{-3.123}$	6^{+3}_{-3}	2^{+2}_{-1}	$9.6^{+0.4}_{-0.4}$	$-1.09^{+0.10}_{-0.10}$	88	0.238 ± 0.000	1	6.56	1.6	G222.97-65.69	40.4839	-28.6379	True	True	Radio Relic.	2^{+6}_{6}
40.4898 ± 0.0005	−28.64934 ± 0.00008	46 ± 4	10.2 ± 0.5	96 ± 4	$0.292^{+0.033}_{-0.031}$	$1.754^{+2.969}_{-2.969}$	9^{+2}_{-2}	6^{+1}_{-1}	$13.9^{+0.6}_{-0.6}$	$-1.89^{+0.12}_{-0.13}$	133	0.238 ± 0.000	1	6.57	1.6	G222.97-65.69	40.4839	-28.6379	True	True	Radio Relic.	7^{+5}_{5}
40.47123 ± 0.00030	−28.63765 ± 0.00029	29.7 ± 3.2	17.2 ± 1.5	134 ± 11	$0.190^{+0.042}_{-0.035}$	$2.022^{+2.799}_{-2.799}$	7^{+3}_{-3}	9^{+2}_{-2}	$20.3^{+0.7}_{-0.7}$	$-2.48^{+0.10}_{-0.10}$	88	0.238 ± 0.000	1	5.62	1.4	G222.97-65.69	40.4839	-28.6379	True	True	Radio Relic.	4^{+7}_{7}
40.33575 ± 0.00011	−28.40285 ± 0.00006	10.4 ± 1.0	7.1 ± 0.4	104 ± 9	-	-	-	-	-	-	-	1.135 ± 0.185	2	14.75	3.5	G222.97-65.69	-	-	True	True	No counterpart.	-
40.33588 ± 0.00004	−28.41099 ± 0.00004	10.4 ± 0.4	7.16 ± 0.18	138 ± 4	$0.034^{+0.005}_{-0.005}$	$1.832^{+2.927}_{-2.927}$	17^{+3}_{-3}	8^{+2}_{-1}	$52.3^{+0.7}_{-0.7}$	$-0.96^{+0.03}_{-0.03}$	90	1.135 ± 0.185	2	14.27	3.4	G222.97-65.69	40.3352	-28.4072	True	False		19^{+6}_{9}
10.94092 ± 0.00004	−20.49858 ± 0.00004	9.5 ± 0.4	7.56 ± 0.25	143 ± 8	$0.040^{+0.009}_{-0.006}$	$0.600^{+0.152}_{-0.152}$	-10^{+3}_{-3}	7^{+3}_{-2}	$17.1^{+0.3}_{-0.3}$	$-0.71^{+0.04}_{-0.04}$	72	0.414 ± 0.068	2	8.55	2.3	G106.73-83.22	10.9412	-20.4988	False	False		-21^{+9}_{9}
10.79686 ± 0.00014	−20.53360 ± 0.00005	22.8 ± 1.2	11.9 ± 0.4	84 ± 4	$0.215^{+0.025}_{-0.024}$	$2.473^{+3.143}_{-3.143}$	-6^{+2}_{-2}	7^{+1}_{-1}	$15.0^{+0.5}_{-0.5}$	$-1.85^{+0.10}_{-0.10}$	89	0.281 ± 0.013	2	5.25	1.4	G106.73-83.22	10.7947	-20.5365	False	False		-16^{+8}_{8}
10.75281 ± 0.00012	−20.58744 ± 0.00006	18.1 ± 1.2	6.67 ± 0.17	155.7 ± 2.4	$0.079^{+0.009}_{-0.008}$	$2.442^{+3.143}_{-3.143}$	-12^{+2}_{-2}	6^{+2}_{-1}	$18.3^{+0.4}_{-0.4}$	$-1.12^{+0.05}_{-0.05}$	75	0.729 ± 0.067	2	5.31	1.4	G106.73-83.22	10.7440	-20.5799	True	False		-24^{+8}_{8}
10.74349 ± 0.00005	−20.62051 ± 0.00012	14.2 ± 1.1	6.54 ± 0.22	159.5 ± 3.4	$0.001^{+0.000}_{-0.000}$	$0.238^{+0.182}_{-0.182}$	18^{+4}_{-4}	8^{+3}_{-2}	$478.9^{+5.4}_{-5.3}$	$-0.83^{+0.03}_{-0.02}$	184	0.281 ± 0.272	2	5.72	1.5	G106.73-83.22	10.7432	-20.6204	True	True		24^{+9}_{10}
10.743987 ± 0.000028	−20.57991 ± 0.00004	8.81 ± 0.35	7.17 ± 0.22	160 ± 7	$0.004^{+0.001}_{-0.001}$	$2.045^{+3.144}_{-3.144}$	-157^{+4}_{-4}	7^{+4}_{-3}	$134.3^{+1.5}_{-1.5}$	$-0.53^{+0.03}_{-0.02}$	57	0.729 ± 0.067	2	5.91	1.6	G106.73-83.22	10.7440	-20.5799	True	False		-268^{+9}_{9}
10.73185 ± 0.00011	−20.57074 ± 0.00017	14.4 ± 1.4	11.5 ± 1.0	172 ± 19	$0.090^{+0.016}_{-0.012}$	$1.111^{+0.206}_{-0.206}$	-3^{+4}_{-3}	6^{+3}_{-2}	$9.5^{+0.3}_{-0.3}$	$-0.60^{+0.08}_{-0.08}$	73	0.729 ± 0.067	2	6.73	1.8	G106.73-83.22	10.7440	-20.5799	True	False		-11^{+9}_{9}
10.8157	-20.5492	8.2	8.2	0	$0.192^{+0.047}_{-0.036}$	$2.975^{+3.151}_{-3.151}$	-19^{+4}_{-4}	6^{+3}_{-2}	$3.2^{+0.3}_{-0.3}$	$-2.24^{+0.25}_{-0.24}$	71	0.603 ± 0.041	2	3.93	1.0	G106.73-83.22	10.8167	-20.5483	False	False		-37^{+10}_{10}
46.89273 ± 0.00006	−28.725980 ± 0.000029	7.1 ± 0.5	5.03 ± 0.22	106 ± 7	$0.439^{+0.335}_{-0.271}$	$0.060^{+0.864}_{-0.864}$	85^{+76}_{-75}	41^{+5}_{-8}	$11.8^{+0.2}_{-0.2}$	$-0.57^{+0.04}_{-0.04}$	125	0.270 ± 0.020	2	7.51	1.9	G223.91-60.09	46.8925	-28.7259	False	False		121^{+120}_{119}
46.83815 ± 0.00017	−28.68291 ± 0.00004	13.7 ± 1.5	6.18 ± 0.30	95 ± 5	$0.033^{+0.018}_{-0.010}$	$2.496^{+3.154}_{-3.154}$	41^{+8}_{-7}	12^{+6}_{-3}	$20.1^{+0.3}_{-0.3}$	$-0.85^{+0.03}_{-0.03}$	78	0.383 ± 0.035	2	3.98	1.1	G223.91-60.09	46.8365	-28.6812	True	False		53^{+15}_{15}
46.83576 ± 0.00015	−28.67959 ± 0.00021	17.2 ± 2.2	6.00 ± 0.30	145 ± 5	$0.072^{+0.048}_{-0.023}$	$2.646^{+3.160}_{-3.160}$	42^{+20}_{-15}	24^{+7}_{-4}	$25.1^{+0.3}_{-0.4}$	$-0.76^{+0.03}_{-0.03}$	72	0.383 ± 0.035	2	3.83	1.1	G223.91-60.09	46.8365	-28.6812	True	False		55^{+32}_{23}
46.83814 ± 0.00005	−28.68534 ± 0.00005	7.2 ± 0.5	5.38 ± 0.26	138 ± 9	$0.046^{+0.557}_{-0.023}$	$2.559^{+3.139}_{-3.139}$	78^{+26}_{-65}	19^{+3187}_{-6}	$11.9^{+0.2}_{-0.2}$	$-0.71^{+0.04}_{-0.04}$	60	0.383 ± 0.035	2	4.00	1.1	G223.91-60.09	46.8365	-28.6812	True	False		111^{+41}_{103}
357.900782 ± 0.000032	−25.938221 ± 0.000018	7.68 ± 0.28	5.76 ± 0.15	102 ± 5	$0.038^{+0.008}_{-0.006}$	$0.442^{+0.182}_{-0.182}$	-26^{+4}_{-4}	7^{+3}_{-2}	$16.5^{+0.2}_{-0.2}$	$-0.55^{+0.04}_{-0.04}$	63	0.187 ± 0.133	3	8.47	2.0	G034.03-76.59	357.9006	-25.9388	False	False		-52^{+9}_{9}
156.14934 ± 0.00006	−27.20391 ± 0.00004	7.9 ± 0.6	6.10 ± 0.31	112 ± 10	$0.040^{+0.019}_{-0.013}$	$2.451^{+3.040}_{-3.040}$	49^{+12}_{-9}	16^{+5}_{-4}	$13.3^{+0.2}_{-0.2}$	$-0.39^{+0.04}_{-0.04}$	111	0.258 ± 0.163	3	10.01	2.4	G266.84+25.07	156.1492	-27.2033	False	False		79^{+33}_{30}
156.02742 ± 0.00005	−27.331459 ± 0.000032	8.4 ± 0.4	7.05 ± 0.27	90 ± 10	$0.058^{+0.015}_{-0.012}$	$0.385^{+0.212}_{-0.212}$	-128^{+6}_{-6}	15^{+3}_{-2}	$10.8^{+0.2}_{-0.2}$	$-0.78^{+0.04}_{-0.04}$	95	-	-	4.83	1.1	G266.84+25.07	-	-	False	False	No counterpart.	-196^{+32}_{32}
155.935295 ± 0.000027	−27.34246 ± 0.00004	8.82 ± 0.34	7.21 ± 0.22	11 ± 7	$0.069^{+0.014}_{-0.012}$	$1.115^{+1.386}_{-1.386}$	-133^{+7}_{-7}	20^{+2}_{-2}	$17.3^{+0.3}_{-0.3}$	$-0.55^{+0.04}_{-0.03}$	139	-	-	5.06	1.2	G266.84+25.07	-	-	False	False	No counterpart.	-204^{+30}_{31}
155.723060 ± 0.000033	−27.180613 ± 0.000032	9.01 ± 0.29	8.66 ± 0.26	116 ± 33	$0.025^{+0.004}_{-0.003}$	$0.873^{+0.147}_{-0.147}$	-9^{+3}_{-2}	5^{+2}_{-2}	$43.3^{+0.6}_{-0.6}$	$-1.01^{+0.03}_{-0.04}$	138	-	-	14.38	3.4	G266.84+25.07	-	-	False	False	No counterpart.	-173^{+40}_{40}
172.93573 ± 0.00008	−19.87149 ± 0.00008	8.0 ± 0.7	7.7 ± 0.6	(1.4 ± 0.8)e+02	$0.309^{+0.528}_{-0.216}$	$0.080^{+0.825}_{-0.825}$	-132^{+1279}_{-733}	$76^{+3737525578}_{-35}$	$2.6^{+0.2}_{-0.2}$	$-0.73^{+0.14}_{-0.13}$	83	0.291 ± 0.025	3	5.23	1.3	G278.60+39.17	172.9325	-19.8793	True	True		-208^{+2186}_{1252}
172.932507 ± 0.000035	−19.87992 ± 0.00007	13.5 ± 0.6	8.47 ± 0.23	20 ± 4	$0.044^{+0.005}_{-0.005}$	$2.789^{+3.142}_{-3.142}$	-0^{+2}_{-3}	4^{+2}_{-2}	$10.0^{+0.3}_{-0.3}$	$-0.95^{+0.06}_{-0.06}$	152	0.291 ± 0.025	3	5.03	1.2	G278.60+39.17	172.9325	-19.8793	True	True		18^{+19}_{19}
172.93171 ± 0.00005	−19.88390 ± 0.00005	9.1 ± 0.5	8.00 ± 0.35	139 ± 16	$0.078^{+0.018}_{-0.016}$	$2.825^{+3.149}_{-3.149}$	-115^{+6}_{-7}	14^{+3}_{-2}	$4.8^{+0.2}_{-0.2}$	$-0.69^{+0.08}_{-0.08}$	141	0.291 ± 0.025	3	4.93	1.2	G278.60+39.17	172.9325	-19.8793	True	False		-180^{+21}_{22}

Notes. The columns are identical to Osinga et al. (2022), with MC denoting whether a source has multiple components. The only newly added column is RM$_{\rm cluster}$, which is defined in Equation 6.3. If uncertainties are not available, they are not given.

Bibliography

References

Abbott, B. P., Abbott, R., Abbott, T. D., et al. 2016, Phys. Rev. Lett., 116, 061102

Abdollahi, S., Acero, F., Ackermann, M., et al. 2020, ApJS, 247, 33

Abolfathi, B., Aguado, D. S., Aguilar, G., et al. 2018, ApJS, 235, 42

Ackermann, M., Ajello, M., Albert, A., et al. 2014, ApJ, 787, 18

Ackermann, M., Ajello, M., Albert, A., et al. 2015, ApJ, 812, 159

Adam, R., Goksu, H., Brown, S., Rudnick, L., & Ferrari, C. 2021, A&A, 648, A60

Adam, R., Goksu, H., Leingärtner-Goth, A., et al. 2020, A&A, 644, A70

Adams, J., Aggarwal, M., Ahammed, Z., et al. 2005, Nuclear Physics A, 757, 102

Ahn et al. 2013, VizieR Online Data Catalog, V/139

Ahumada, R., Prieto, C. A., Almeida, A., et al. 2020, ApJS, 249, 3

Akahori, T., Nakanishi, H., Sofue, Y., et al. 2018, PASJ, 70, R2

Amaral, A. D., Vernstrom, T., & Gaensler, B. M. 2021, MNRAS, 503, 2913

Anderson, C. S., Heald, G. H., Eilek, J. A., et al. 2021, PASA, 38, e020

Andrade-Santos, F., Jones, C., Forman, W. R., et al. 2017, ApJ, 843, 76

Andrade-Santos, F., Pratt, G. W., Melin, J.-B., et al. 2021, ApJ, 914, 58

Arnaud, M., Pratt, G. W., Piffaretti, R., et al. 2010a, A&A, 517, A92

Arnaud, M., Pratt, G. W., Piffaretti, R., et al. 2010b, A&A, 517, A92

Arshakian, T. G. & Beck, R. 2011, MNRAS, 418, 2336

Bagchi, J., Enßlin, T. A., Miniati, F., et al. 2002, New A, 7, 249

Baghmanyan, V., Zargaryan, D., Aharonian, F., et al. 2022, MNRAS, 516, 562

Baldi, A., Ettori, S., Molendi, S., & Gastaldello, F. 2012, A&A, 545, A41

Ballet, J., Burnett, T. H., Digel, S. W., & Lott, B. 2020, arXiv e-prints, arXiv:2005.11208

Beck, R. & Krause, M. 2005, Astronomische Nachrichten, 326, 414

Berrington, R. C., Lugger, P. M., & Cohn, H. N. 2002, AJ, 123, 2261

Biava, N., de Gasperin, F., Bonafede, A., et al. 2021, MNRAS, 508, 3995

Bîrzan, L., Rafferty, D. A., Cassano, R., et al. 2019, MNRAS, 487, 4775

Blandford, R. & Eichler, D. 1987, Phys. Rep., 154, 1

Blandford, R. D. & Znajek, R. L. 1977, MNRAS, 179, 433

Blasi, P. & Colafrancesco, S. 1999, Astroparticle Physics, 12, 169

Blasi, P., Gabici, S., & Brunetti, G. 2007, International Journal of Modern Physics A, 22, 681

Böhringer, H., Chon, G., & Fukugita, M. 2017, A&A, 608, A65

Böhringer, H., Chon, G., & Kronberg, P. P. 2016, A&A, 596, A22

Böhringer, H., Dolag, K., & Chon, G. 2012, A&A, 539, A120

Böhringer, H., Voges, W., Huchra, J. P., et al. 2000, ApJS, 129, 435

Bonafede, A., Brunetti, G., Rudnick, L., et al. 2022, ApJ, 933, 218

Bonafede, A., Cassano, R., Brüggen, M., et al. 2017, MNRAS, 470, 3465

Bonafede, A., Feretti, L., Giovannini, G., et al. 2009, A&A, 503, 707

Bonafede, A., Feretti, L., Murgia, M., et al. 2010, A&A, 513, A30

Bonafede, A., Govoni, F., Feretti, L., et al. 2011, A&A, 530, A24

Bonafede, A., Intema, H. T., Bruggen, M., et al. 2014, MNRAS, 444, L44

Bonafede, A., Vazza, F., Brüggen, M., et al. 2013, MNRAS, 433, 3208

Bonaldi, A., Harrison, I., Camera, S., & Brown, M. L. 2016, MNRAS, 463, 3686

Botteon, A., Brunetti, G., Ryu, D., & Roh, S. 2020a, A&A, 634, A64

Botteon, A., Brunetti, G., van Weeren, R. J., et al. 2020b, ApJ, 897, 93

Botteon, A., Cassano, R., Eckert, D., et al. 2019, A&A, 630, A77

Botteon, A., Shimwell, T. W., Cassano, R., et al. 2022a, A&A, 660, A78

Botteon, A., van Weeren, R. J., Brunetti, G., et al. 2020c, MNRAS, 499, L11

Botteon, A., van Weeren, R. J., Brunetti, G., et al. 2022b, Science Advances, 8, eabq7623

Boxelaar, J. M., van Weeren, R. J., & Botteon, A. 2021, Astronomy and Computing, 35, 100464

Bradač, M., Clowe, D., Gonzalez, A. H., et al. 2006, ApJ, 652, 937

Brentjens, M. A. 2008, A&A, 489, 69

Brentjens, M. A. & de Bruyn, A. G. 2005, A&A, 441, 1217

Breuer, J. P., Werner, N., Mernier, F., et al. 2020, MNRAS, 495, 5014

Bridle, A. H. & Fomalont, E. B. 1976, A&A, 52, 107

Bridle, A. H., Fomalont, E. B., Miley, G. K., & Valentijn, E. A. 1979, A&A, 80, 201

Briel, U. G. & Henry, J. P. 1994, Nature, 372, 439

Briel, U. G., Henry, J. P., Schwarz, R. A., et al. 1991, A&A, 246, L10

Briggs, D. S. 1995, in American Astronomical Society Meeting Abstracts, Vol. 187, 112.02

Brown, S., Bergerud, B., Costa, A., et al. 2019, MNRAS, 483, 964

Brüggen, M., Bykov, A., Ryu, D., & Röttgering, H. 2012, Space Sci. Rev., 166, 187

Brunetti, G. 2003, in Astronomical Society of the Pacific Conference Series, Vol. 301, Matter and Energy in Clusters of Galaxies, 349

Brunetti, G. & Blasi, P. 2005, MNRAS, 363, 1173

Brunetti, G., Blasi, P., Reimer, O., et al. 2012, MNRAS, 426, 956

Brunetti, G., Cassano, R., Dolag, K., & Setti, G. 2009, A&A, 507, 661

Brunetti, G., Giacintucci, S., Cassano, R., et al. 2008, Nature, 455, 944

Brunetti, G. & Jones, T. W. 2014, International Journal of Modern Physics D, 23, 1430007

Brunetti, G. & Lazarian, A. 2007, MNRAS, 378, 245

Brunetti, G. & Lazarian, A. 2011, MNRAS, 410, 127

Brunetti, G. & Lazarian, A. 2016, MNRAS, 458, 2584

Brunetti, G., Setti, G., Feretti, L., & Giovannini, G. 2001, MNRAS, 320, 365

Brunetti, G. & Vazza, F. 2020, Phys. Rev. Lett., 124, 051101

Brunetti, G., Venturi, T., Dallacasa, D., et al. 2007, ApJ, 670, L5

Brunetti, G., Zimmer, S., & Zandanel, F. 2017, MNRAS, 472, 1506

Bruno, L., Brunetti, G., Botteon, A., et al. 2023, A&A, 672, A41

Bruno, L., Rajpurohit, K., Brunetti, G., et al. 2021, A&A, 650, A44

Burenin, R. A., Vikhlinin, A., Hornstrup, A., et al. 2007, ApJS, 172, 561

Burn, B. J. 1966, MNRAS, 133, 67

Burns, J. O., Hallman, E. J., Gantner, B., Motl, P. M., & Norman, M. L. 2008, ApJ, 675, 1125

Carilli, C. L. & Taylor, G. B. 2002, ARA&A, 40, 319

Cassano, R. 2010, A&A, 517, A10

Cassano, R., Bernardi, G., Brunetti, G., et al. 2015, in AASKA14, 73

Cassano, R., Botteon, A., Di Gennaro, G., et al. 2019, ApJ, 881, L18

Cassano, R. & Brunetti, G. 2005, MNRAS, 357, 1313

Cassano, R., Brunetti, G., Norris, R. P., et al. 2012, A&A, 548, A100

Cassano, R., Brunetti, G., Röttgering, H. J. A., & Brüggen, M. 2010a, A&A, 509, A68

Cassano, R., Brunetti, G., & Setti, G. 2006a, Astronomische Nachrichten, 327, 557

Cassano, R., Brunetti, G., & Setti, G. 2006b, MNRAS, 369, 1577

Cassano, R., Brunetti, G., Setti, G., Govoni, F., & Dolag, K. 2007, MNRAS, 378, 1565

Cassano, R., Cuciti, V., Brunetti, G., et al. 2023, arXiv e-prints, arXiv:2301.08052

Cassano, R., Ettori, S., Brunetti, G., et al. 2013, ApJ, 777, 141

Cassano, R., Ettori, S., Giacintucci, S., et al. 2010b, ApJ, 721, L82

Cassano, R., Ettori, S., Giacintucci, S., et al. 2010c, ApJ, 721, L82

Cavagnolo, K. W., Donahue, M., Voit, G. M., & Sun, M. 2009, ApJS, 182, 12

Chambers, K. C., Magnier, E. A., Metcalfe, N., et al. 2016, arXiv e-prints, arXiv:1612.05560

Chiaberge, M., Gilli, R., Lotz, J. M., & Norman, C. 2015, ApJ, 806, 147

Cho, J. 2014, ApJ, 797, 133

Clarke, T. E. & Ensslin, T. A. 2006, AJ, 131, 2900

Clarke, T. E., Kronberg, P. P., & Böhringer, H. 2001, ApJ, 547, L111

Clowe, D., Bradač, M., Gonzalez, A. H., et al. 2006, ApJ, 648, L109

Clowe, D., Gonzalez, A., & Markevitch, M. 2004, ApJ, 604, 596

Codis, S., Jindal, A., Chisari, N. E., et al. 2018, MNRAS, 481, 4753

Codis, S., Pichon, C., Devriendt, J., et al. 2012, MNRAS, 427, 3320

Colless, M., Dalton, G., Maddox, S., et al. 2001, MNRAS, 328, 1039

Condon, J. J., Cotton, W. D., Greisen, E. W., et al. 1998, AJ, 115, 1693

Contigiani, O., de Gasperin, F., Miley, G. K., et al. 2017, MNRAS, 472, 636

Cova, F., Gastaldello, F., Wik, D. R., et al. 2019, A&A, 628, A83

Croston, J. H., Pratt, G. W., Böhringer, H., et al. 2008, A&A, 487, 431

Croton, D. J., Springel, V., White, S. D. M., et al. 2006, MNRAS, 365, 11

Cuciti, V., Brunetti, G., van Weeren, R., et al. 2018, A&A, 609, A61

Cuciti, V., Cassano, R., Brunetti, G., et al. 2021a, A&A, 647, A51

Cuciti, V., Cassano, R., Brunetti, G., et al. 2015, A&A, 580, A97

Cuciti, V., Cassano, R., Brunetti, G., et al. 2021b, A&A, 647, A50

Cuciti, V., de Gasperin, F., Brüggen, M., et al. 2022, Nature, 609, 911

Dahlen, T., Mobasher, B., Faber, S. M., et al. 2013, ApJ, 775, 93

Dallacasa, D., Brunetti, G., Giacintucci, S., et al. 2009, ApJ, 699, 1288

Davidson-Pilon, C. 2019, Journal of Open Source Software, 4, 1317

de Gasperin, F., Brunetti, G., Brüggen, M., et al. 2020, A&A, 642, A85

de Gasperin, F., Dijkema, T. J., Drabent, A., et al. 2019, A&A, 622, A5

de Gasperin, F., Edler, H. W., Williams, W. L., et al. 2023, A&A, 673, A165

de Gasperin, F., Intema, H. T., Shimwell, T. W., et al. 2017, Science Advances, 3, e1701634

de Gasperin, F., Rudnick, L., Finoguenov, A., et al. 2022, A&A, 659, A146

de Gasperin, F., Williams, W. L., Best, P., et al. 2021, A&A, 648, A104

Dennison, B. 1980, ApJ, 239, L93

Dey, A., Schlegel, D. J., Lang, D., et al. 2019, AJ, 157, 168

Di Gennaro, G., Brüggen, M., van Weeren, R. J., et al. 2023, A&A, 675, A51

Di Gennaro, G., van Weeren, R. J., Brunetti, G., et al. 2021a, Nature Astronomy, 5, 268

Di Gennaro, G., van Weeren, R. J., Cassano, R., et al. 2021b, A&A, 654, A166

Di Gennaro, G., van Weeren, R. J., Rudnick, L., et al. 2021c, ApJ, 911, 3

Dolag, K., Bykov, A. M., & Diaferio, A. 2008, Space Sci. Rev., 134, 311

Dolag, K. & Enßlin, T. A. 2000, A&A, 362, 151

Domínguez-Fernández, P., Vazza, F., Brüggen, M., & Brunetti, G. 2019, MNRAS, 486, 623

Donahue, M., Horner, D. J., Cavagnolo, K. W., & Voit, G. M. 2006, ApJ, 643, 730

Donnert, J., Dolag, K., Brunetti, G., & Cassano, R. 2013, MNRAS, 429, 3564

Donnert, J., Vazza, F., Brüggen, M., & ZuHone, J. 2018, Space Sci. Rev., 214, 122

Duncan, K. J. 2022, MNRAS, 512, 3662

Duncan, K. J., Kondapally, R., Brown, M. J. I., et al. 2020, arXiv e-prints, arXiv:2011.08204

Duncan, K. J., Sabater, J., Röttgering, H. J. A., et al. 2019, A&A, 622, A3

Ebeling, H., Edge, A. C., Allen, S. W., et al. 2000, MNRAS, 318, 333

Eckert, D., Ettori, S., Molendi, S., Vazza, F., & Paltani, S. 2013a, A&A, 551, A23

Eckert, D., Gaspari, M., Vazza, F., et al. 2017, ApJ, 843, L29

Eckert, D., Ghirardini, V., Ettori, S., et al. 2019, A&A, 621, A40

Eckert, D., Molendi, S., & Paltani, S. 2011, A&A, 526, A79

Eckert, D., Molendi, S., Vazza, F., Ettori, S., & Paltani, S. 2013b, A&A, 551, A22

Eckert, D., Vazza, F., Ettori, S., et al. 2012, A&A, 541, A57

Edler, H. W., de Gasperin, F., Brunetti, G., et al. 2022, A&A, 666, A3

Edler, H. W., de Gasperin, F., & Rafferty, D. 2021, A&A, 652, A37

Eisenhardt, P. R. M., Brodwin, M., Gonzalez, A. H., et al. 2008, ApJ, 684, 905

Eisenstein, D. J., Zehavi, I., Hogg, D. W., et al. 2005, ApJ, 633, 560

Ensslin, T. A., Biermann, P. L., Klein, U., & Kohle, S. 1998, A&A, 332, 395

Enßlin, T. A. & Röttgering, H. 2002, A&A, 396, 83

Ensslin, T. A., Vogt, C., Clarke, T. E., & Taylor, G. B. 2003, ApJ, 597, 870

Ettori, S., Morandi, A., Tozzi, P., et al. 2009, A&A, 501, 61

Event Horizon Telescope Collaboration, Akiyama, K., Alberdi, A., et al. 2019, ApJ, 875, L1

Fabian, A. C. 1994, ARA&A, 32, 277

Fabian, A. C. 2012, ARA&A, 50, 455

Fabricant, D. G., Kent, S. M., & Kurtz, M. J. 1989, ApJ, 336, 77

Farnes, J. S., Heald, G., Junklewitz, H., et al. 2018, MNRAS, 474, 3280

Feigelson, E. D. & Nelson, P. I. 1985, ApJ, 293, 192

Feretti, L., Boehringer, H., Giovannini, G., & Neumann, D. 1997a, A&A, 317, 432

Feretti, L., Giovannini, G., & Böhringer, H. 1997b, New A, 2, 501

Feretti, L., Giovannini, G., Govoni, F., & Murgia, M. 2012, A&A Rev., 20, 54

Feretti, L., Giovannini, G., Klein, U., et al. 1998, A&A, 331, 475

Fermi, E. 1949, Physical Review, 75, 1169

Ferrari, C., Govoni, F., Schindler, S., Bykov, A. M., & Rephaeli, Y. 2008, Space Sci. Rev., 134, 93

Finner, K., James Jee, M., Webb, T., et al. 2020, ApJ, 893, 10

Fomalount, E. B. & Miley, G. K. 1975, Nature, 257, 99

Foreman-Mackey, D., Hogg, D. W., Lang, D., & Goodman, J. 2013, Publications of the ASP, 125, 306

Forman, W. & Jones, C. 1982, ARA&A, 20, 547

Frommert, M., Durrer, R., & Michaud, J. 2012, JCAP, 1, 009

Gaensler, B. M., Landecker, T. L., Taylor, A. R., & POSSUM Collaboration. 2010, in American Astronomical Society Meeting Abstracts, Vol. 215, 470.13

Garn, T., Green, D. A., Riley, J. M., & Alexand er, P. 2008a, MNRAS, 383, 75

Garn, T., Green, D. A., Riley, J. M., & Alexand er, P. 2008b, MNRAS, 387, 1037

Garon, A. F., Rudnick, L., Wong, O. I., et al. 2019, AJ, 157, 126

Gastaldello, F., Wik, D. R., Molendi, S., et al. 2015, ApJ, 800, 139

Ge, C., Liu, R.-Y., Sun, M., et al. 2020, MNRAS, 497, 4704

Geller, M. J. & Huchra, J. P. 1989, Science, 246, 897

Ghirardini, V., Eckert, D., Ettori, S., et al. 2019, A&A, 621, A41

Ghirardini, V., Ettori, S., Eckert, D., et al. 2018, A&A, 614, A7

Giacintucci, S., Markevitch, M., Cassano, R., et al. 2017, ApJ, 841, 71

Giacintucci, S., O'Sullivan, E., Vrtilek, J., et al. 2011, ApJ, 732, 95

Giacintucci, S., Venturi, T., Brunetti, G., et al. 2005, A&A, 440, 867

Giovannini, G., Bonafede, A., Feretti, L., et al. 2009, A&A, 507, 1257

Giovannini, G. & Feretti, L. 2000, New A, 5, 335

Giovannini, G., Feretti, L., Girardi, M., et al. 2011, A&A, 530, L5

Giovannini, G., Feretti, L., Venturi, T., Kim, K. T., & Kronberg, P. P. 1993, ApJ, 406, 399

Girardi, M., Boschin, W., Gastaldello, F., et al. 2016, MNRAS, 456, 2829

Gott, J. Richard, I., Jurić, M., Schlegel, D., et al. 2005, ApJ, 624, 463

Govoni, F., Dolag, K., Murgia, M., et al. 2010, A&A, 522, A105

Govoni, F. & Feretti, L. 2004, Int. J. Mod. Phys. B., 13, 1549

Govoni, F., Murgia, M., Feretti, L., et al. 2005, A&A, 430, L5

Govoni, F., Murgia, M., Feretti, L., et al. 2006, A&A, 460, 425

Govoni, F., Murgia, M., Vacca, V., et al. 2017, A&A, 603, A122

Govoni, F., Murgia, M., Xu, H., et al. 2013, A&A, 554, A102

Groeneveld, C., van Weeren, R. J., Osinga, E., et al. 2023, subm.

Gu, L., Akamatsu, H., Shimwell, T. W., et al. 2019, Nature Astronomy, 3, 838

Guidetti, D., Laing, R. A., Bridle, A. H., Parma, P., & Gregorini, L. 2011, MNRAS, 413, 2525

Guidetti, D., Laing, R. A., Croston, J. H., Bridle, A. H., & Parma, P. 2012, MNRAS, 423, 1335

Guidetti, D., Laing, R. A., Murgia, M., et al. 2010, A&A, 514, A50

Guidetti, D., Murgia, M., Govoni, F., et al. 2008, A&A, 483, 699

Guth, A. H. 1981, Phys. Rev. D, 23, 347

Ha, J.-H., Ryu, D., & Kang, H. 2018, ApJ, 857, 26

Hardcastle, M. J., Croston, J. H., Shimwell, T. W., et al. 2019, MNRAS, 488, 3416

Harrison, I., Camera, S., Zuntz, J., & Brown, M. L. 2016, MNRAS, 463, 3674

Haverkorn, M. 2015, in Astrophysics and Space Science Library, Vol. 407, Magnetic Fields in Diffuse Media, 483

Haverkorn, M., Gaensler, B. M., McClure-Griffiths, N. M., Dickey, J. M., & Green, A. J. 2004, ApJ, 609, 776

Hinshaw, G., Weiland, J. L., Hill, R. S., et al. 2009, ApJS, 180, 225

Hitomi Collaboration, Aharonian, F., Akamatsu, H., et al. 2016, Nature, 535, 117

Hitomi Collaboration, Aharonian, F., Akamatsu, H., et al. 2018, PASJ, 70, 9

Hlavacek-Larrondo, J., Gendron-Marsolais, M. L., Fecteau-Beaucage, D., et al. 2018, MNRAS, 475, 2743

Hoang, D. N., Shimwell, T. W., Stroe, A., et al. 2017, MNRAS, 471, 1107

Hoang, D. N., Shimwell, T. W., van Weeren, R. J., et al. 2018, MNRAS, 478, 2218

Hoang, D. N., Shimwell, T. W., van Weeren, R. J., et al. 2019, A&A, 622, A21

Hoeft, M. & Brüggen, M. 2007, MNRAS, 375, 77

Hopkins, P. F., Hernquist, L., Hayward, C. C., & Narayanan, D. 2012, MNRAS, 425, 1121

Hudson, D. S., Mittal, R., Reiprich, T. H., et al. 2010, A&A, 513, A37

Hutschenreuter, S., Anderson, C. S., Betti, S., et al. 2022, A&A, 657, A43

Hutsemékers, D. 1998, A&A, 332, 410

Hutsemékers, D., Braibant, L., Pelgrims, V., & Sluse, D. 2014, A&A, 572, A18

Hutsemékers, D. & Lamy, H. 2001, A&A, 367, 381

Intema, H. T., Jagannathan, P., Mooley, K. P., & Frail, D. A. 2017, A&A, 598, A78

Jaffe, W. J. 1977, ApJ, 212, 1

Jagannathan, P., Bhatnagar, S., Rau, U., & Taylor, A. R. 2017, AJ, 154, 56

Jain, P., Narain, G., & Sarala, S. 2004, MNRAS, 347, 394

Jannuzi, B. T. & Dey, A. 1999, in Astronomical Society of the Pacific Conference Series, Vol. 191, Photometric Redshifts and the Detection of High Redshift Galaxies, 111

Jeltema, T. E. & Profumo, S. 2011, ApJ, 728, 53

Johnson, A. R., Rudnick, L., Jones, T. W., Mendygral, P. J., & Dolag, K. 2020, ApJ, 888, 101

Jonas, J. & MeerKAT Team. 2016, in MeerKAT Science: On the Pathway to the SKA, 1

Kaiser, N. 1986, MNRAS, 222, 323

Kale, R. & Dwarakanath, K. S. 2010, ApJ, 718, 939

Kale, R. & Dwarakanath, K. S. 2012, ApJ, 744, 46

Kale, R., Venturi, T., Giacintucci, S., et al. 2015, A&A, 579, A92

Kang, H. 2021, Journal of Korean Astronomical Society, 54, 103

Kang, H. & Ryu, D. 2016, ApJ, 823, 13

Kang, H., Ryu, D., & Jones, T. W. 2012, ApJ, 756, 97

Kang, J., Wang, J., & Kang, W. 2020, ApJ, 901, 111

Knowles, K., Cotton, W. D., Rudnick, L., et al. 2022, A&A, 657, A56

Kogut, A., Lineweaver, C., Smoot, G. F., et al. 1993, ApJ, 419, 1

Kolmogorov, A. 1941, Akademiia Nauk SSSR Doklady, 30, 301

Komissarov, S. S. & Gubanov, A. G. 1994, A&A, 285, 27

Kondapally, R., Best, P. N., Hardcastle, M. J., et al. 2020, arXiv e-prints, arXiv:2011.08201

Kraljic, K., Davé, R., & Pichon, C. 2020, MNRAS, 493, 362

Kravtsov, A. V. & Borgani, S. 2012, ARA&A, 50, 353

Kron, R. G. 1980, ApJS, 43, 305

Kronberg, P. P. & Newton-McGee, K. J. 2011, PASA, 28, 171

Kunz, M. W., Bogdanović, T., Reynolds, C. S., & Stone, J. M. 2012, ApJ, 754, 122

La Franca, F., Fiore, F., Vignali, C., et al. 2002, ApJ, 570, 100

Lacey, C. & Cole, S. 1993, MNRAS, 262, 627

Lacy, M., Baum, S. A., Chandler, C. J., et al. 2020, PASP, 132, 035001

Laigle, C., Pichon, C., Codis, S., et al. 2015, MNRAS, 446, 2744

Laing, R. A., Bridle, A. H., Parma, P., & Murgia, M. 2008, MNRAS, 391, 521

Lamee, M., Rudnick, L., Farnes, J. S., et al. 2016, ApJ, 829, 5

Lee, W., Jee, M. J., Kang, H., et al. 2020, ApJ, 894, 60

Li, W., Xu, H., Ma, Z., et al. 2019, ApJ, 879, 104

Liang, H., Hunstead, R. W., Birkinshaw, M., & Andreani, P. 2000, ApJ, 544, 686

Linde, A. 1990, Particle Physics and Inflationary Cosmology (CRC Press)

Lockman, F. J., Jahoda, K., & McCammon, D. 1986, ApJ, 302, 432

Loi, F., Brienza, M., Riseley, C. J., et al. 2023, A&A, 672, A28

Loi, F., Murgia, M., Govoni, F., et al. 2019, MNRAS, 490, 4841

Loi, F., Murgia, M., Govoni, F., et al. 2018, Galaxies, 6, 133

Loi, F., Murgia, M., Vacca, V., et al. 2020, MNRAS, 498, 1628

Lovisari, L., Schellenberger, G., Sereno, M., et al. 2020, ApJ, 892, 102

Macario, G., Venturi, T., Intema, H. T., et al. 2013, A&A, 551, A141

Mandal, S., Intema, H. T., Shimwell, T. W., et al. 2019, A&A, 622, A22

Mandal, S., Intema, H. T., van Weeren, R. J., et al. 2020, A&A, 634, A4

Markevitch, M., Gonzalez, A. H., David, L., et al. 2002, ApJ, 567, L27

Markevitch, M., Govoni, F., Brunetti, G., & Jerius, D. 2005, ApJ, 627, 733

Markevitch, M. & Vikhlinin, A. 2007, Phys. Rep., 443, 1

McMullin, J. P., Waters, B., Schiebel, D., Young, W., & Golap, K. 2007, in Astronomical Society of the Pacific Conference Series, Vol. 376, Astronomical Data Analysis Software and Systems XVI, 127

Meisner, A. M., Lang, D., & Schlegel, D. J. 2017, AJ, 154, 161

Miley, G. 1980, ARA&A, 18, 165

Miller, C. J., Nichol, R. C., Reichart, D., et al. 2005, AJ, 130, 968

Miller, N. A., Owen, F. N., & Hill, J. M. 2003, AJ, 125, 2393

Miniati, F. & Beresnyak, A. 2015, Nature, 523, 59

Mirakhor, M. S., Walker, S. A., Runge, J., & Diwanji, P. 2022, MNRAS, 516, 1855

Mohan, N. & Rafferty, D. 2015, PyBDSF: Python Blob Detection and Source Finder, Astrophysics Source Code Library

Muldrew, S. I., Hatch, N. A., & Cooke, E. A. 2015, MNRAS, 452, 2528

Murgia, M., Govoni, F., Feretti, L., et al. 2004, A&A, 424, 429

Murgia, M., Govoni, F., Markevitch, M., et al. 2009, A&A, 499, 679

Murgia, M., Parma, P., Mack, K. H., et al. 2011, A&A, 526, A148

Myers, S. T. & Spangler, S. R. 1985, ApJ, 291, 52

Nagai, D., Kravtsov, A. V., & Vikhlinin, A. 2007, ApJ, 668, 1

Navarro, J. F., Frenk, C. S., & White, S. D. M. 1996, ApJ, 462, 563

Nikiel-Wroczyński, B., Berger, A., Herrera Ruiz, N., et al. 2019, A&A, 622, A23

Nikiel-Wroczyński, B., Urbanik, M., Soida, M., Beck, R., & Bomans, D. J. 2017, A&A, 603, A97

Nishiwaki, K. & Asano, K. 2022, ApJ, 934, 182

Offringa, A. R., McKinley, B., Hurley-Walker, N., et al. 2014, MNRAS, 444, 606

Offringa, A. R. & Smirnov, O. 2017, MNRAS, 471, 301

Offringa, A. R., van de Gronde, J. J., & Roerdink, J. B. T. M. 2012, A&A, 539, A95

Oliver, S., Rowan-Robinson, M., Alexander, D. M., et al. 2000, MNRAS, 316, 749

Osinga, E., Miley, G. K., van Weeren, R. J., et al. 2020, A&A, 642, A70

Osinga, E., van Weeren, R. J., Andrade-Santos, F., et al. 2022, A&A, 665, A71

Osinga, E., van Weeren, R. J., Boxelaar, J. M., et al. 2021, A&A, 648, A11

Osinga, E., van Weeren, R. J., Brunetti, G., et al. 2023a, A&A subm.

Osinga, E., van Weeren, R. J., Rudnick, L., et al. 2023b, A&A in prep.

O'Sullivan, S. P., Machalski, J., Van Eck, C. L., et al. 2019, A&A, 622, A16

Owen, F. N., Rudnick, L., Eilek, J., et al. 2014, ApJ, 794, 24

Pacholczyk, A. G. 1970, Radio astrophysics. Nonthermal processes in galactic and extragalactic sources (San Francisco: Freeman)

Panwar, M., Prabhakar, Sandhu, P. K., Wadadekar, Y., & Jain, P. 2020, MNRAS, 499, 1226

Paraficz, D., Kneib, J. P., Richard, J., et al. 2016, A&A, 594, A121

Pasetto, A., Carrasco-González, C., Bruni, G., et al. 2016, Galaxies, 4, 66

Paul, S., Iapichino, L., Miniati, F., Bagchi, J., & Mannheim, K. 2011, ApJ, 726, 17

Pearce, C. J. J., van Weeren, R. J., Andrade-Santos, F., et al. 2017, ApJ, 845, 81

Pearson, K. 1895, Proceedings of the Royal Society of London Series I, 58, 240

Pelgrims, V. & Hutsemékers, D. 2016, A&A, 590, A53

Penzias, A. A. & Wilson, R. W. 1965, ApJ, 142, 419

Perley, R. A. & Butler, B. J. 2017, ApJS, 230, 7

Petrosian, V. 2001, ApJ, 557, 560

Petrosian, V. & East, W. E. 2008, ApJ, 682, 175

Pfrommer, C. & Enßlin, T. A. 2004, A&A, 413, 17

Pierpaoli, E., Borgani, S., Scott, D., & White, M. 2003, MNRAS, 342, 163

Piffaretti, R., Arnaud, M., Pratt, G. W., Pointecouteau, E., & Melin, J. B. 2011, A&A, 534, A109

Pinzke, A., Oh, S. P., & Pfrommer, C. 2013, MNRAS, 435, 1061

Pinzke, A., Oh, S. P., & Pfrommer, C. 2017, MNRAS, 465, 4800

Pinzke, A. & Pfrommer, C. 2010, MNRAS, 409, 449

Pizzo, R. F., de Bruyn, A. G., Bernardi, G., & Brentjens, M. A. 2011, A&A, 525, A104

Planck Collaboration, Ade, P. A. R., Aghanim, N., et al. 2015, A&A, 581, A14

Planck Collaboration, Ade, P. A. R., Aghanim, N., et al. 2013, A&A, 550, A131

Planck Collaboration, Ade, P. A. R., Aghanim, N., et al. 2011, A&A, 536, A8

Planck Collaboration, Ade, P. A. R., Aghanim, N., et al. 2016a, A&A, 594, A27

Planck Collaboration, Ade, P. A. R., Aghanim, N., et al. 2016b, A&A, 594, A24

Planck Collaboration, Ade, P. A. R., Aghanim, N., et al. 2016c, A&A, 594, A13

Planck Collaboration, Aghanim, N., Akrami, Y., et al. 2020a, A&A, 641, A1

Planck Collaboration, Aghanim, N., Akrami, Y., et al. 2020b, A&A, 641, A6

Planck Collaboration, Aghanim, N., Akrami, Y., et al. 2020c, A&A, 641, A5

Planck Collaboration, Aghanim, N., Arnaud, M., et al. 2016d, A&A, 594, A22

Press, W. H. & Schechter, P. 1974, ApJ, 187, 425

Quici, B., Turner, R. J., Seymour, N., et al. 2022, MNRAS, 514, 3466

Rajpurohit, K., Brunetti, G., Bonafede, A., et al. 2021a, A&A, 646, A135

Rajpurohit, K., Hoeft, M., van Weeren, R. J., et al. 2018, ApJ, 852, 65

Rajpurohit, K., Hoeft, M., Wittor, D., et al. 2022a, A&A, 657, A2

Rajpurohit, K., Hoeft, M., Wittor, D., et al. 2022b, A&A, 657, A2

Rajpurohit, K., Osinga, E., Brienza, M., et al. 2023, A&A, 669, A1

Rajpurohit, K., van Weeren, R. J., Hoeft, M., et al. 2022c, ApJ, 927, 80

Rajpurohit, K., Vazza, F., Hoeft, M., et al. 2020, A&A, 642, L13

Rajpurohit, K., Vazza, F., van Weeren, R. J., et al. 2021b, A&A, 654, A41

Rees, M. J. 2006, Astronomische Nachrichten, 327, 395

Reimer, O., Pohl, M., Sreekumar, P., & Mattox, J. R. 2003, ApJ, 588, 155

Rines, K. & Diaferio, A. 2006, AJ, 132, 1275

Riseley, C. J., Bonnassieux, E., Vernstrom, T., et al. 2022, MNRAS, 515, 1871

Rojas Bolivar, R. A., Wik, D. R., Giacintucci, S., et al. 2021, ApJ, 906, 87

Röttgering, H., Snellen, I., Miley, G., et al. 1994, ApJ, 436, 654

Rudnick, L. & Blundell, K. M. 2003, ApJ, 588, 143

Rudnick, L., Cotton, W., Knowles, K., & Kolokythas, K. 2021, Galaxies, 9, 81

Rudnick, L. & Owen, F. N. 2014, ApJ, 785, 45

Russell, H. R., van Weeren, R. J., Edge, A. C., et al. 2011, MNRAS, 417, L1

Ryu, D., Kang, H., Cho, J., & Das, S. 2008, Science, 320, 909

Sabater, J., Best, P. N., Tasse, C., et al. 2020, arXiv e-prints, arXiv:2011.08211

Sarazin, C. L. 1986, Reviews of Modern Physics, 58, 1

Sarazin, C. L. 2002, in Astrophysics and Space Science Library, Vol. 272, Merging Processes in Galaxy Clusters, 1–38

Sarazin, C. L. & Kempner, J. C. 2000, ApJ, 533, 73

Savini, F., Bonafede, A., Brüggen, M., et al. 2019, A&A, 622, A24

Schinckel, A. E., Bunton, J. D., Cornwell, T. J., Feain, I., & Hay, S. G. 2012, in Society of Photo-Optical Instrumentation Engineers (SPIE) Conference Series, Vol. 8444, Ground-based and Airborne Telescopes IV, 84442A

Schlegel, D. J., Finkbeiner, D. P., & Davis, M. 1998, ApJ, 500, 525

Schnitzeler, D. H. F. M. 2010, MNRAS, 409, L99

Sebokolodi, M. L., Smirnov, O., Perley, R., Eilek, J., & Carilli, C. 2021, in American Astronomical Society Meeting Abstracts, Vol. 53, 307.05D

Sebokolodi, M. L. L., Perley, R., Eilek, J., et al. 2020, ApJ, 903, 36

Sheth, R. K. & Diaferio, A. 2011, MNRAS, 417, 2938

Shi, X.-Y., Zhang, Y., Liu, R.-Y., & Wang, X.-Y. 2022, ApJ, 927, 33

Shimwell, T. W., Brown, S., Feain, I. J., et al. 2014, MNRAS, 440, 2901

Shimwell, T. W., Hardcastle, M. J., Tasse, C., et al. 2022, A&A, 659, A1

Shimwell, T. W., Luckin, J., Brüggen, M., et al. 2016, MNRAS, 459, 277

Shimwell, T. W., Röttgering, H. J. A., Best, P. N., et al. 2017, A&A, 598, A104

Shimwell, T. W., Tasse, C., Hardcastle, M. J., et al. 2019, A&A, 622, A1

Shweta, A., Athreya, R., & Sekhar, S. 2020, ApJ, 897, 115

Sikhosana, S. P., Knowles, K., Hilton, M., Moodley, K., & Murgia, M. 2023, MNRAS, 518, 4595

Simonte, M., Andernach, H., Brüggen, M., Best, P. N., & Osinga, E. 2023, A&A, 672, A178

Smirnov & Tasse. 2015, MNRAS, 449, 2668

Smith, D. J. B., Best, P. N., Duncan, K. J., et al. 2016, in SF2A-2016: Proceedings of the Annual meeting of the French Society of Astronomy and Astrophysics, 271–280

Sokoloff, D. D., Bykov, A. A., Shukurov, A., et al. 1998, MNRAS, 299, 189

Somboonpanyakul, T., McDonald, M., Bayliss, M., et al. 2021, ApJ, 907, L12

Sommer, M. W., Basu, K., Intema, H., et al. 2017, MNRAS, 466, 996

Spearman, C. 1904, The American Journal of Psychology, 15, 72

Springel, V., Frenk, C. S., & White, S. D. M. 2006, Nature, 440, 1137

Springel, V., White, S. D. M., Jenkins, A., et al. 2005, Nature, 435, 629

Stasyszyn, F. A. & de los Rios, M. 2019, MNRAS, 487, 4768

Steinhardt, P. J. 1983, in Very Early Universe, 251–266

Steinwandel, U. P., Böss, L. M., Dolag, K., & Lesch, H. 2022, ApJ, 933, 131

Stroe, A., Harwood, J. J., Hardcastle, M. J., & Röttgering, H. J. A. 2014, MNRAS, 445, 1213

Struble, M. F. & Rood, H. J. 1991, ApJS, 77, 363

Stuardi, C., Bonafede, A., Lovisari, L., et al. 2021, MNRAS, 502, 2518

Stuardi, C., O'Sullivan, S. P., Bonafede, A., et al. 2020, A&A, 638, A48

Sun, M., Murray, S. S., Markevitch, M., & Vikhlinin, A. 2002, ApJ, 565, 867

Sunyaev, R. A. & Zeldovich, Y. B. 1970, Comments on Astrophysics and Space Physics, 2, 66

Sunyaev, R. A. & Zeldovich, Y. B. 1972, Comments on Astrophysics and Space Physics, 4, 173

Sur, S., Basu, A., & Subramanian, K. 2021, MNRAS, 501, 3332

Tarrío, P., Melin, J. B., & Arnaud, M. 2019, A&A, 626, A7

Tarrío, P. & Zarattini, S. 2020, A&A, 642, A102

Tasse. 2014, arXiv e-prints, arXiv:1410.8706

Tasse, Hugo, B., Mirmont, M., et al. 2018, A&A, 611, A87

Tasse, C., Shimwell, T., Hardcastle, M. J., et al. 2020, arXiv e-prints, arXiv:2011.08328

Tasse, C., Shimwell, T., Hardcastle, M. J., et al. 2021, A&A, 648, A1

Taylor, A. R. & Jagannathan, P. 2016, MNRAS, 459, L36

Taylor, G. B., Fabian, A. C., & Allen, S. W. 2002, MNRAS, 334, 769

Taylor, G. B., Gugliucci, N. E., Fabian, A. C., et al. 2006, MNRAS, 368, 1500

Taylor, G. B. & Perley, R. A. 1993, ApJ, 416, 554

Taylor, G. B., Perley, R. A., Inoue, M., et al. 1990, ApJ, 360, 41

Thierbach, M., Klein, U., & Wielebinski, R. 2003, A&A, 397, 53

Thompson, A. R., Clark, B. G., Wade, C. M., & Napier, P. J. 1980, ApJS, 44, 151

Tiwari, P. & Jain, P. 2013, International Journal of Modern Physics D, 22, 1350089

Trasatti, M., Akamatsu, H., Lovisari, L., et al. 2015, A&A, 575, A45

Tribble, P. C. 1991, MNRAS, 253, 147

Truemper, J. 1993, Science, 260, 1769

Tümer, A., Wik, D. R., Zhang, X., et al. 2023, ApJ, 942, 79

Turner, M. S. 2022, Annual Review of Nuclear and Particle Science, 72, 1

Turner, R. J. & Shabala, S. S. 2023, Galaxies, 11, 87

Uson, J. M. & Cotton, W. D. 2008, A&A, 486, 647

Vacca, V., Murgia, M., Govoni, F., et al. 2018, Galaxies, 6, 142

Vacca, V., Murgia, M., Govoni, F., et al. 2010, A&A, 514, A71

Vacca, V., Murgia, M., Govoni, F., et al. 2012, A&A, 540, A38

van der Tol, S., Veenboer, B., & Offringa, A. R. 2018, A&A, 616, A27

van Diepen, G., Dijkema, T. J., & Offringa, A. 2018, DPPP: Default Pre-Processing Pipeline, Astrophysics Source Code Library, record ascl:1804.003

van Haarlem, M. P., Wise, M. W., Gunst, A. W., et al. 2013, A&A, 556, A2

van Terwisga, S. E., Hacar, A., van Dishoeck, E. F., Oonk, R., & Portegies Zwart, S. 2022, A&A, 661, A53

van Weeren, R. J., Andrade-Santos, F., Dawson, W. A., et al. 2017, Nature Astronomy, 1, 0005

van Weeren, R. J., Brunetti, G., Brüggen, M., et al. 2016a, ApJ, 818, 204

van Weeren, R. J., de Gasperin, F., Akamatsu, H., et al. 2019, Space Sci. Rev., 215, 16

van Weeren, R. J., Intema, H. T., Oonk, J. B. R., Röttgering, H. J. A., & Clarke, T. E. 2009, A&A, 508, 1269

van Weeren, R. J., Röttgering, H. J. A., Intema, H. T., et al. 2012a, A&A, 546, A124

van Weeren, R. J., Röttgering, H. J. A., Rafferty, D. A., et al. 2012b, A&A, 543, A43

van Weeren, R. J., Shimwell, T. W., Botteon, A., et al. 2021, A&A, 651, A115

van Weeren, R. J., Williams, W. L., Hardcastle, M. J., et al. 2016b, ApJS, 223, 2

Vazza, F., Brüggen, M., Gheller, C., & Wang, P. 2014, MNRAS, 445, 3706

Vazza, F., Brüggen, M., van Weeren, R., et al. 2012, MNRAS, 421, 1868

Vazza, F., Brüggen, M., Wittor, D., et al. 2016, MNRAS, 459, 70

Vazza, F., Brunetti, G., Brüggen, M., & Bonafede, A. 2018, MNRAS, 474, 1672

Vazza, F., Eckert, D., Brüggen, M., & Huber, B. 2015, MNRAS, 451, 2198

Vazza, F., Wittor, D., Brunetti, G., & Brüggen, M. 2021, A&A, 653, A23

Venturi, T., Bardelli, S., Dallacasa, D., et al. 2003, A&A, 402, 913

Venturi, T., Giacintucci, S., Dallacasa, D., et al. 2008, A&A, 484, 327

Vikhlinin, A., Kravtsov, A., Forman, W., et al. 2006, ApJ, 640, 691

Vogt, C. & Enßlin, T. A. 2006, Astronomische Nachrichten, 327, 595

Wang, Q. H. S., Giacintucci, S., & Markevitch, M. 2018, ApJ, 856, 162

Webb, T., Noble, A., DeGroot, A., et al. 2015, ApJ, 809, 173

Wen, Z. L. & Han, J. L. 2013, MNRAS, 436, 275

Wen, Z. L. & Han, J. L. 2015, ApJ, 807, 178

Wen, Z. L., Han, J. L., & Liu, F. S. 2012, ApJS, 199, 34

White, S. D. M. 1984, ApJ, 286, 38

White, S. D. M. & Rees, M. J. 1978, MNRAS, 183, 341

Widrow, L. M., Ryu, D., Schleicher, D. R. G., et al. 2012, Space Sci. Rev., 166, 37

Wik, D. R., Hornstrup, A., Molendi, S., et al. 2014, ApJ, 792, 48

Wilber, A., Brüggen, M., Bonafede, A., et al. 2019, A&A, 622, A25

Wilber, A., Brüggen, M., Bonafede, A., et al. 2018, MNRAS, 473, 3536

Williams, W. L., Hardcastle, M. J., Best, P. N., et al. 2019, A&A, 622, A2

Williams, W. L., van Weeren, R. J., Röttgering, H. J. A., et al. 2016, MNRAS, 460, 2385

Wittor, D. 2021, New A, 85, 101550

Wittor, D., Ettori, S., Vazza, F., et al. 2021, MNRAS, 506, 396

Wood, M., Caputo, R., Charles, E., et al. 2017, in 35th International Cosmic Ray Conference (ICRC2017), Vol. 301, 824

Xi, S.-Q., Wang, X.-Y., Liang, Y.-F., et al. 2018, Phys. Rev. D, 98, 063006

Xie, C., van Weeren, R. J., Lovisari, L., et al. 2020, A&A, 636, A3

Yadav, J. K., Bagla, J. S., & Khandai, N. 2010, MNRAS, 405, 2009

Zandanel, F. & Ando, S. 2014, MNRAS, 440, 663

ZuHone, J., Ehlert, K., Weinberger, R., & Pfrommer, C. 2021, Galaxies, 9, 91

ZuHone, J. A., Kunz, M. W., Markevitch, M., Stone, J. M., & Biffi, V. 2015, ApJ, 798, 90

ZuHone, J. A., Markevitch, M., & Lee, D. 2011, ApJ, 743, 16

English Summary

The Big Bang is the proposed beginning of the Universe, where the cosmos suddenly emerged in an explosion from a single point that contained all the energy that ever was and ever will be. As the Universe expanded and cooled, matter began to clump together under the influence of gravity. The first stars, galaxies, and groups of galaxies formed, and the Universe started shaping itself on the grandest scale as a cosmic spiderweb. Most galaxies reside in the filaments of this web, while outside the web's strands, there are vast empty spaces known as 'voids'. At the intersections of these filaments, the largest structures in the Universe, that are still held together by gravity, formed: clusters of galaxies (also called galaxy clusters).

Galaxy clusters

Although the name suggests that they are simply large groups of hundreds of galaxies, galaxies are the least significant part of galaxy clusters. Clusters mainly consist of extremely hot and tenuous gas that is located in the space between the galaxies, in the so-called intra-cluster medium[4]. This gas is primarily composed of hydrogen and helium atoms, constituting more than 90% of the cluster's mass. The temperature of the gas is so high (10 million to 100 million degrees Celsius) that electrons are released from the atoms (ionisation). The gas is not visible in wavelengths that our eyes can see but emits X-ray radiation. Hence, clusters of galaxies are best understood as colossal clouds of gas (see Figure S.1, middle).

Figure S.1: The cluster of galaxies Abell 2256 at three different wavelengths. *Left*: Only the galaxies are visible in infrared light. *Middle*: In blue, the X-ray emission from the hot gas between galaxies is visible. *Right*: In red, radio emission is visible, originating from high-energy charged particles in the gas that bend around magnetic fields. Infrared: neoWISE (Meisner et al., 2017), X-ray: XMM-newton (Rajpurohit et al., 2023), radio: LOFAR (Osinga et al., 2023a), image overlay: Frits Sweijen

[4]We are temporarily neglecting dark matter, which constitutes the majority of the mass but is not the focus of this dissertation. When accounting for dark matter, clusters have a total mass of hundreds to thousands of trillions of solar masses ($> 10^{14} M_{\odot}$).

Clusters are still in the process of forming and growing by attracting dust and gas from their surroundings, and colliding with other clusters. Collisions between two clusters are incredibly energetic, causing the gas to become shocked and mixed. The charged particles within the gas, such as protons and electrons (separated due to the high temperature), can be accelerated to speeds close to the speed of light by shockwaves and turbulence within the gas. In the presence of a magnetic field, electrons experience the strongest deflection and emit radio radiation. This radio radiation can be observed using telescopes like the *Low-Frequency Array* (LOFAR), whose core is located in Drenthe. LOFAR is particularly well-suited for these observations because the particles predominantly emit radio radiation at low frequencies, or long wavelengths (see Figure S.1, right).

In general, we observe three distinct classes of radio emissions from clusters. First, there are *radio halos*, large roundish radio structures in the central regions of clusters. The brightness of radio halos roughly follows the distribution of the hot gas, so they are brighter in the centre and fade towards the outer parts of the clusters. We believe that radio halos primarily reveal a particle acceleration process that arises due to turbulence within the gas. Second, there are *radio shocks*, which are named as such because they exhibit long and extended structures that often trace shockwaves within the gas. In these cases, electrons are accelerated by shockwaves resulting from massive cluster collisions. Lastly, there can be radio emission directly from the galaxies themselves. When a supermassive black hole, which resides in the centre of virtually all galaxies, has enough material around it, the galaxy is said to have an 'active galactic nucleus' (AGN). Part of the material surrounding such a black hole gets consumed, while some is expelled in the form of two enormous fountains, or radio jets. These jets are often much larger than the galaxy itself, reaching sizes of several million light-years[5]. As the galaxies producing these jets move through the hot gas of the cluster, the jets are often deflected, leading to a rich diversity of shapes. Radio jets are not exclusively found in clusters, as all galaxies can harbour an active black hole. However, it is thought that these radio jets can serve as a significant source of energetic electrons that gradually spread through the cluster and are re-accelerated when clusters collide.

Magnetic Fields

The fact that we see radio emission coming from clusters means that there must be magnetic fields in the gas. This is because the radio emission exhibits characteristics of synchrotron radiation, emitted by charged particles moving within a magnetic field. However, it remains a significant mystery how these magnetic fields originated and evolved within the space between the galaxies. The prevailing theory suggests that magnetic fields in clusters gradually grew during the formation of clusters from an initially weak magnetic field that was already present during cluster formation. However, the origin of this initial magnetic field remains uncertain. Two main hypotheses exist regarding the origin of these magnetic fields. They could be a fundamental component of the Universe, generated shortly after the Big Bang or during the formation of the first structures in the cosmos (*primordial origin*), or they might have been injected into space later by supernova explosions and active

[5]To give some context to this incomprehensible scale, the distance from Earth to the Sun is about 8 light minutes, and the distance from Earth to the centre of the Milky Way is about 26,000 light years.

galaxies (*astrophysical origin*). Regardless of their origin, magnetic fields play a crucial role in energy transport through the hot gas and in particle acceleration during cluster collisions. However, little is known about the characteristics of current magnetic fields within clusters.

The most effective way to determine the properties of magnetic fields in clusters is through the Faraday effect (see Figure S.2). As light is an electromagnetic wave with both electric and magnetic field waves perpendicular to the direction of motion (and to each other), there are many possible orientations for the electric field wave. When it has only one specific orientation, we call the light (linearly) polarised. The polarization angle is rotated when light travels through a magnetic gas, such as that found in clusters. The degree of rotation depends on the strength of the magnetic field, the density of free electrons in the gas, and the wavelength of the light. By observing multiple wavelengths simultaneously with a radio telescope and using an X-ray telescope to determine the density of free electrons, the properties of the magnetic field can be inferred. However, a challenge with Faraday effect studies is that polarised radio sources are relatively rare, requiring deep observations of nearby clusters to locate enough polarised radio sources. Alternatively, observations from different clusters can be stacked on top of each other. With the (presumably strong) assumption that all clusters are approximately the same, the average properties of the magnetic field in clusters can be determined statistically.

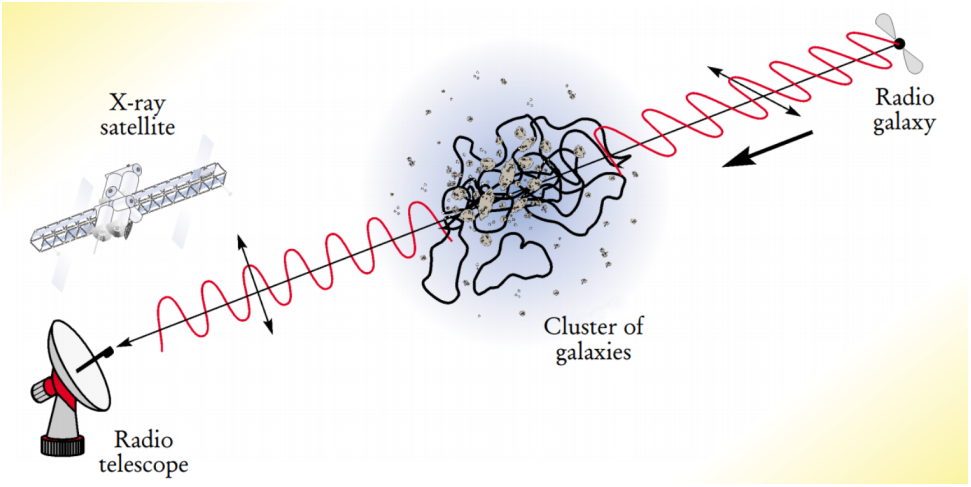

Figure S.2: An illustration of the Faraday effect. A distant active galactic nucleus emits polarised radio emission with an electric field wave at a specific angle. As the wave reaches the magnetic gas within the cluster, the angle is rotated, depending on the light's wavelength and the properties of the gas. This rotation can be observed using a radio telescope that observes at different wavelengths. Image: Philipp P. Kronberg, Physics Today, December 2002.

This Dissertation

This dissertation explores the particle acceleration process and magnetic fields that contribute to radio emission within galaxy clusters. By gaining a better understanding of these topics, we can learn more about the formation process of clusters, as cluster collisions are closely linked to both subjects. On the one hand, the particle acceleration process is best studied at low frequencies (~ 100 MHz), for which LOFAR is particularly suitable. On the other hand, magnetic fields are best investigated at higher frequencies (~ 1000 MHz), as the Faraday effect becomes too strong at lower frequencies, leading to a loss of polarization (depolarisation). Therefore, this dissertation utilises The Karl G. Jansky Very Large Array (VLA), a telescope in New Mexico, to gain a better understanding of magnetic fields within clusters.

In **Chapter 2**, the orientation of radio jets from active galaxies is investigated. Previous studies have found that the orientation of radio jets is not random across large portions of the sky, with jets of galaxies that appear closer to each other often pointing in the same direction. This could have significant implications for the formation of the Universe's structure. However, small systematic measurement errors can lead to biased results. It is therefore important to consider the distance of the radio jets to Earth (via the redshift of the host galaxy) and measure whether jets that are physically close to each other (in 3D) actually point in the same direction or merely appear to do so on the sky (in 2D). By analyzing a sample of 7,555 distinct radio jets from the *LOFAR Two Meter Sky Survey* (LoTSS), the null hypothesis that radio jets have no preferred direction in both 3D and 2D is tested. Evidence is found that the null hypothesis can be rejected in 2D, confirming that radio jets from galaxies that appear close to each other in the sky indeed have a preferred direction. However, no evidence is found to reject the null hypothesis in 3D, indicating that there are probably unknown systematic measurement errors in the data, and that the orientation of jets in the Universe is random at large distances.

In **Chapter 3**, we investigate whether smaller galaxy clusters with lower mass and thus less energetic collisions compared to those previously studied, can still exhibit radio emission in the form of radio halos. The deepest radio maps ever created at a frequency of 150 MHz, as part of the *LOFAR Two Metre Sky Survey Deep Fields*, were analyzed. The observations revealed that a cluster with relatively low mass (only 300 trillion solar masses), even at a relatively high redshift (z=0.77), exhibited a radio halo. A possible detection was also made in another cluster with a slightly lower mass. Combined with upper limits set on clusters from which no radio emissions were detected, the results were consistent with the known relationship between cluster mass and radio halo luminosity, although the sample size was small.

In **Chapter 4**, LOFAR is pushed to its limits with observations of the nearby galaxy cluster Abell 2256 down to the extremely low frequency of 16 MHz. This is difficult because the upper layer of the atmosphere, the ionosphere, strongly deflects and changes the direction of radio waves at low frequencies. Still, we present good quality LOFAR images of Abell 2256 between 16 and 168 MHz where we detect and resolve the radio shock, radio halo and various other radio sources. By comparing with literature data at higher frequencies, we measure the integrated spectrum of the radio halo between 24 and 1500 MHz and the radio shock between 24 and 3000 MHz. Both exhibit simple power laws, where the radio emission S becomes brighter at lower frequency ν as $S \propto \nu^{\alpha}$, with $\alpha = -1.56 \pm 0.02$

for the radio halo and $\alpha = -1.00 \pm 0.02$ for the radio shock. Additionally, a new source of aged radio plasma is detected with an extremely steep spectrum ($\alpha = -1.90 \pm 0.1$) that was missed at higher frequencies. Finally, a model for generating the radio halo is tested using a combination of radio and gamma-ray observations.

In **Chapters 5 and 6**, observations of 124 clusters with the VLA radio telescope are presented. The goal of these observations is to statistically infer the properties of the magnetic field in clusters by stacking them together. A total of 819 polarised radio sources were found, of which the magnitude of the Faraday effect has been measured. **Chapter 5** presents the analysis of the depolarization of the radio emission. For the first time, a clear trend is observed in which polarised sources behind clusters (as shown in Figure S.2) increasingly depolarise as their projected distance to the centre of the cluster decreases. Using X-ray data from the *Chandra* telescope, theoretical models are compared with the data to determine the properties of the magnetic fields. **Chapter 6** improves this analysis by incorporating information from the Faraday rotation of the polarization angle. A clear increase in the variance of rotation measures towards the centre of clusters is observed, consistent with an average magnetic field strength of about $3\,\mu$G. By combining depolarization and rotation measures and comparing them with a model, the best agreement is found for a magnetic field with a central strength of $B = 5\,\mu$G that decreases with the density n of the hot gas as $B \propto n^{0.5}$. In the best-fitting model, the magnetic field fluctuates on scales exceeding a million light years, indicating turbulence injected on large scales, for example by cluster mergers.

Nederlandse Samenvatting

De Oerknal is het voorgestelde begin van het Universum, waarbij het heelal opeens ontstond in een explosie vanuit één punt dat alle energie bevatte die er ooit was en ooit zal zijn. Terwijl het Universum uitdijde en afkoelde begon materie samen te klonteren onder invloed van zwaartekracht. De eerste sterren, sterrenstelsels en groepen van sterrenstelsels vormden, en het Universum begon zich op de allergrootste schaal vorm te geven als een kosmisch spinnenweb. De meeste sterrenstelsels leven in de draden van dit web, terwijl buiten de draden van het web grote lege ruimtes ('holtes') zijn. Op de knooppunten van deze draden ontstonden de grootste structuren in het heelal die nog door zwaartekracht bij elkaar gehouden worden: clusters van sterrenstelsels (ook wel clusters van melkwegstelsels).

Clusters van sterrenstelsels

Hoewel de naam doet vermoeden dat het simpelweg grote groepen van honderden sterrenstelsels zijn, zijn de sterrenstelsels het minst belangrijke deel van de clusters. Clusters bestaan vooral uit een erg heet en ijl gas, dat zich in de ruimte tussen de sterrenstelsels bevindt, in het zogenoemde *intra-cluster medium*[6]. Dit gas bestaat vooral uit waterstof- en heliumatomen, en omvat meer dan 90% van de massa van een cluster. De temperatuur van het gas is zo hoog (10 miljoen tot 100 miljoen graden Celsius) dat de elektronen loskomen van de atomen (ionisatie). Het gas is dan ook niet meer zichtbaar op golflengtes die ons oog kan zien, maar zendt röntgenstraling uit. Clusters van sterrenstelsels kunnen dus het beste worden gezien als enorme gaswolken (zie Figuur S.3, midden).

Figuur S.3: De cluster van sterrenstelsels Abell 2256 op drie verschillende golflengtes. *Links:* alleen de sterrenstelsels zijn zichtbaar in infraroodlicht; *Midden*: in blauw is de röntgenstraling van het hete gas tussen de sterrenstelsels te zien. *Rechts:* in rood is de radiostraling te zien, afkomstig van hoog-energetische geladen deeltjes in het gas die om magnetische velden gebogen worden. Infrarood: neoWISE (Meisner et al., 2017), röntgen: XMM-newton (Rajpurohit et al., 2023), radio: LOFAR (Osinga et al., 2023a), beeldoverlap: Frits Sweijen

[6]Hier negeren we donkere materie even, wat het grootste deel van de massa beslaat, maar niet de focus is van dit proefschrift. Met donkere materie erbij hebben clusters een totale massa van honderden tot duizenden biljoenen zonsmassa's ($> 10^{14} M_{\odot}$).

Clusters zijn nog steeds aan het vormen en groeien, door stof en gas aan te trekken vanuit hun omgeving en door botsingen met andere clusters. Botsingen van twee clusters zijn geweldig energetisch, en zorgen ervoor dat het gas gehusseld en geschokt wordt. De geladen deeltjes in het gas, protonen en elektronen (die van elkaar gescheiden zijn omdat het gas zo heet is), kunnen door de schokgolven en turbulentie in het gas versneld worden tot snelheden die dicht bij de lichtsnelheid liggen. In de aanwezigheid van een magnetisch veld worden de elektronen het sterkst afgebogen en zullen ze radiostraling uitzenden. Deze radiostraling is zichtbaar met telescopen zoals de *Low-Frequency Array* (LOFAR), waarvan de kern in Drenthe staat. LOFAR is bijzonder geschikt voor dit soort waarnemingen, omdat de deeltjes voornamelijk radiostraling uitzenden op lage frequenties, ofwel lange golflengtes (zie Figuur S.3, rechts).

We zien over het algemeen drie verschillende klassen van radiostraling in clusters. Als eerste zijn er *radiohalo's*, grote ronde radiostructuren in het midden van clusters. De lichtkracht van radiohalos volgt grofweg de verdeling van het hete gas, dus ze zijn feller in het centrum en worden zwakker naar de buitenkant van de clusters. We denken dat radiohalos vooral een deeltjesversnellingsproces laten zien dat onstaat door de turbulentie in het gas. Als tweede zijn er *radioschokken*, die zo genoemd zijn omdat ze lange en uitgestrekte structuren hebben die vaak schokgolven in het gas volgen. Hier worden elektronen versneld door schokgolven die ontstaan in grote botsingen van clusters. Als laatste komt er soms ook nog radiostraling van de sterrenstelsels zelf. Als een supermassief zwart gat, wat zich in het centrum van praktisch alle sterrenstelsels bevindt, genoeg materiaal om zich heen heeft wordt een sterrenstelsel actief genoemd. Een deel van het materiaal om zo'n zwart gat heen wordt opgeslokt, maar een deel wordt ook uitgeworpen in de vorm van twee immense fonteinen, of radiojets. Deze jets zijn vaak vele malen groter dan het sterrenstelsel, met afmetingen tot enkele miljoenen lichtjaren[7]. Omdat de sterrenstelsels die de jets produceren door het hete gas van de cluster bewegen, worden de jets vaak afgebogen en zien we een rijke diversiteit aan vormen. Radiojets komen niet uitsluitend voor in clusters, aangezien alle sterrenstelsels, ook die buiten clusters, een actief zwart gat kunnen hebben. Wel denken we dat de radiojets een belangrijke bron kunnen zijn van energetische elektronen die geleidelijk door de cluster kunnen verspreiden en opnieuw versneld kunnen worden wanneer clusters botsen.

Magnetische velden

Het feit dat we radiostraling zien komen van clusters betekent dat er magnetische velden moeten zijn in het gas. Dit is omdat de radiostraling de kenmerken heeft van synchrotronstraling, die uitgezonden wordt door geladen deeltjes in een magnetisch veld. Het is echter een groot mysterie hoe deze magnetische velden zijn ontstaan en geëvolueerd in de ruimte tussen de sterrenstelsels. De beste theorie is dat de magnetische velden in clusters geleidelijk aan zijn gegroeid tijdens het vormingsproces van clusters vanuit een initieel zwak magnetisch veld, dat al aanwezig is bij het ontstaan van de clusters. Maar de oorsprong van het initiële magnetische veld is nog onbepaald. Er zijn twee denkrichtingen voor het ontstaan van de magnetische velden. Ze kunnen een fundamenteel deel van het

[7] Om deze onbevattelijke schaal toch enige context te geven: de afstand van de Aarde tot de Zon is ongeveer 8 lichtminuten, en de afstand van de Aarde tot het centrum van de Melkweg is ongeveer 26.000 lichtjaar.

Universum zijn, gecreëerd net na de Oerknal of tijdens de formatie van de eerste structuren in het heelal (*de fundamentele oorsprong*), of ze kunnen later de ruimte in geslingerd zijn door supernova explosies en actieve sterrenstelsels (*de astrofysische oorsprong*). Wat de oorsprong ook is, magnetische velden hebben een belangrijk effect op hoe energie wordt getransporteerd door het hete gas, en hoe deeltjes versneld worden tijdens botsingen van clusters. Echter is van de eigenschappen van de huidige magnetische velden in clusters, ook niet veel bekend. De meest effectieve manier om de eigenschappen van magnetische velden in clusters te bepalen is door het Faraday effect (zie Figuur S.4). Aangezien licht een elektromagnetische golf is, met een elektrische en magnetische veldgolf die loodrecht op de bewegingsrichting staan (en loodrecht op elkaar), zijn er veel mogelijke oriëntaties van de elektrische veldgolf. Wanneer deze slechts één bepaalde oriëntatie heeft noemen we het licht (lineair) gepolariseerd. De polarisatiehoek wordt gedraaid wanneer licht door een gemagnetiseerd gas gaat zoals die in clusters. Hoeveel graden de hoek gedraaid wordt, is afhankelijk van de kracht van het magneetveld, de dichtheid van de vrije elektronen in het gas, en de golflengte van het licht. Door op meerdere golflengtes tegelijkertijd te observeren met een radiotelescoop, en een röntgentelescoop te gebruiken om de dichtheid van de vrije elektronen te bepalen, kunnen eigenschappen van het magnetisch veld worden afgeleid. Een probleem met studies van het Faraday effect is echter dat gepolariseerde radiobronnen vrij zeldzaam zijn, en hele diepe waarnemingen nodig zijn van nabije clusters om genoeg gepolariseerde radiobronnen te vinden. Als alternatief kunnen waarnemingen van verschillende clusters op elkaar gestapeld worden. Met de (allicht sterke) aanname dat alle clusters ongeveer hetzelfde zijn, kunnen dan gemiddelde eigenschappen van het magnetisch veld in clusters op statistische wijze bepaald worden.

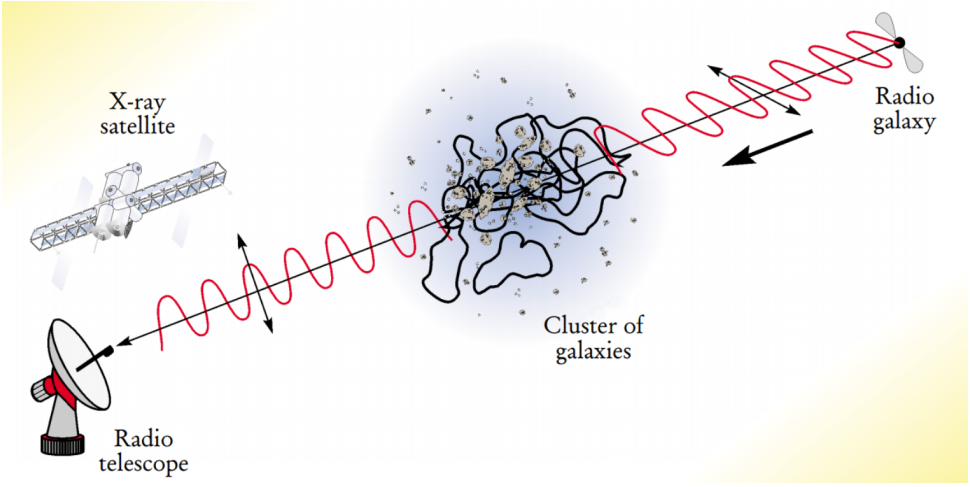

Figuur S.4: Een illustratie van het Faraday-effect. Een ver actief sterrenstelsel zendt gepolariseerde radiostraling uit met een elektrische veldgolf onder een bepaalde hoek. Wanneer de golf het magnetische gas van de cluster bereikt, wordt de hoek gedraaid, afhankelijk van de golflengte van het licht en de eigenschappen van het gas. Deze draaing kan worden waargenomen met een radiotelescoop die op verschillende golflengtes waarneemt. Afbeelding: Philipp P. Kronberg, Physics Today, December 2002.

DIT PROEFSCHIFT

Dit proefschift onderzoekt het deeltjesversnellingsproces en de magnetische velden die tot de radiostraling in clusters van sterrenstelsels leiden. Door deze onderwerpen beter te begrijpen leren we meer over het vormingsproces van clusters, aangezien botsingen van clusters sterk verbonden zijn met beide zaken. Het deeltjesversnellingsproces kan het beste worden bestudeerd op lage frequenties (~ 100 MHz), waar LOFAR uitermate geschikt voor is. Magnetische velden daarentegen kunnen het beste worden onderzocht op hogere frequenties (~ 1000 MHz), aangezien het Faraday effect op lagere frequenties zo sterk wordt dat de polarisatie-eigenschappen verloren gaan. Daarom wordt in dit proefschrift de Karl G. Jansky Very Large Array (VLA), een telescoop in New Mexico, gebruikt om de magnetische velden in clusters beter te begrijpen.

In **Hoofstuk 2** wordt de oriëntatie van radiojets van actieve sterrenstelsels onderzocht. Eerdere studies hebben gevonden dat de oriëntatie van radiojets niet willekeurig is over grote stukken van de hemel, maar dat jets van sterrenstelsels die dichter bij elkaar lijken te staan aan de hemel vaak dezelfde richting op wijzen. Dit zou sterke implicaties hebben voor de formatie van de structuur van het Universum. Echter kunnen kleine systematische meetfouten leiden tot een vertekening van de resultaten. Het is daarom belangrijk om ook de afstand van de radiojets tot de aarde mee te nemen (via de roodverschuiving van het actieve sterrenstelsel) en te meten of de jets die fysiek dicht bij elkaar staan (in 3D) ook echt dezelfde richting op wijzen of dat alleen lijken te doen aan de hemel (in 2D). Door een steekproef te nemen met 7,555 duidelijke radiojets uit de *LOFAR Two Meter Sky Survey* (LoTSS) wordt de nulhypothese getest dat de radiojets geen voorkeursrichting hebben in 3D en in 2D. We vinden bewijs dat de nulhypothese incorrect is in 2D, dus dat radiojets van sterrenstelsels die aan de hemel dicht bij elkaar lijken te staan inderdaad een voorkeursrichting hebben. Echter vinden we geen bewijs dat de nulhypothese incorrect is in 3D, wat er op duidt dat er waarschijnlijk onbekende systematische meetfouten in de data zitten en de oriëntatie van de jets in het Universum wel echt willekeurig is op grote afstanden.

In **Hoofdstuk 3** wordt onderzocht of kleinere clusters van sterrenstelsels, met lagere massa en dus minder energetische botsingen dan tot nu toe bestudeerd zijn, toch nog steeds radiostraling in de vorm van radiohalo's kunnen vertonen. We analyseerden de diepste radiokaarten ooit gemaakt op de frequentie van 150 MHz, als onderdeel van de *LOFAR Two Metre Sky Survey Deep Fields*. Uit de observaties bleek dat er inderdaad een cluster met een relatief lage massa (slechts 300 biljoen zonsmassa's), ook nog op een vrij hoge roodverschuiving (z=0.77), een radiohalo liet zien. Een mogelijke detectie werd ook gedaan in een andere cluster met nog iets lagere massa. Gecombineerd met bovengrenzen die gesteld konden worden op clusters waar geen radiostraling vandaan kwam, waren de resultaten consistent met de bekende relatie tussen cluster massa en radiohalo lichtkracht, al was de steekproefgrootte klein.

In **Hoofdstuk 4** wordt LOFAR tot het uiterste gedreven, met observaties van de nabijgelegen cluster van sterrenstelsels Abell 2256 tot de uiterst lage frequentie van 16 MHz. Dit is lastig omdat de bovenste laag van de atmosfeer, de ionosfeer, radiogolven op lage frequenties sterk afbuigt en van richting verandert. Desalniettemin lukt het om goede kwaliteit LOFAR beelden van Abell 2256 tussen 16 en 168 MHz te maken, waarin we de radioshock, radiohalo en verschillende andere radiobronnen detecteren en

onderscheiden. Door vergelijking met literatuurgegevens op hogere frequenties, meten we het geïntegreerde spectrum van de radiohalo tussen 24 en 1500 MHz en de radioschok tussen 24 en 3000 MHz. Beiden vertonen ze eenvoudige machtswetten, waarbij de radiostraling S feller wordt op lagere frequentie ν als $S \propto \nu^{\alpha}$, met $\alpha = -1,56 \pm 0,02$ voor de radiohalo en $\alpha = -1,00 \pm 0,02$ voor de radioschok. Ook wordt een nieuwe bron van oud radioplasma gedetecteerd met een extreem steil spectrum ($\alpha = -1,90 \pm 0,1$) die gemist was op hogere frequenties. Ten slotte wordt een model voor het genereren van de radiohalo getoetst met de combinatie van radio en gammastraling waarnemingen.

In **Hoofdstukken 5 en 6** worden waarnemingen van 124 clusters met de VLA radiotelescoop gepresenteerd. Het doel van deze waarnemingen is om statistisch de eigenschappen van het magnetisch veld van clusters af te leiden door de clusters op elkaar te stapelen. Er zijn in totaal 819 gepolariseerde radiobronnen gevonden, waarvan het Faraday effect bepaald is. **Hoofdstuk 5** presenteert de analyse van de depolarisatie van de radiosignalen. Voor de eerste keer wordt een duidelijke trend waargenomen waarbij gepolariseerde bronnen achter clusters (zoals in Figuur S.4) steeds meer depolariseren naarmate de geprojecteerde afstand tot het centrum van de cluster afneemt. Met behulp van röntgengegevens van de *Chandra* telescoop worden theoretische modellen vergeleken met de data, en worden zo de eigenschappen van de magnetische velden bepaald. **Hoofdstuk 6** verbetert deze analyse door informatie van de Faraday rotatie van de polarisatiehoek toe te voegen. We zien een duidelijke toename in de variantie van de rotatiematen naar het centrum van clusters, in overeenstemming met een gemiddelde magnetische veldsterkte van ongeveer $3\,\mu$Gauss. Door de depolarisatie en rotatiemaat te combineren en te vergelijken met een model, wordt de beste overeenstemming gevonden voor een magnetisch veld met een centrale sterkte van $B = 5\,\mu$Gauss die afneemt met de dichtheid n van het hete gas als $B \propto n^{0.5}$. In het best passende model fluctueert het magnetisch veld op schalen van meer dan een miljoen lichtjaar, wat duidt op turbulentie die op grote schalen wordt opgewekt, bijvoorbeeld door botsingen van clusters.

Fryske gearfetting

De Oerknal is it foarstelde begjin fan it Universum, wêrby't it hielal ynienen ûntstie yn in eksploazje fanút ien punt dat alle enerzjy hie dat der ea wie en ea wêze sil. Wylst it Universum útdyde en ôfkuolle, begûn matearje te klústerjen ûnder ynfloed fan swiertekrêft. De earste stjerren, stjerrestelsels en groepen fan stjerrestelsels foarmen en it Universum begûn har op de aldergrutste skaal te foarmjen as in kosmysk spinreach. De measte stjerrestelsels libben yn de trieden fan dit reach, wylst bûten de trieden fan it web grutte lege romten ('holtes') binne. Op de knooppunten fan dizze trieden ûntstiene de grutste struktueren yn it hielal dy't noch troch swiertekrêft by inoar hâlden wurde: klusters fan stjerrestelsels (ek wol klusters fan molkeweistelsels).

Klusters fan stjerrestelsels

Hoewol de namme docht tinke dat it gewoanwei grutte groepen fan hûnderten stjerrestelsels binne, binne de stjerrestelsels it minst wichtige diel fan 'e klusters. Klusters bestean foaral út in tige hjit en tin gas, dat tusken de stjerrestelsels leit, yn it saneamde *yntra-kluster medium*[8]. Dit gas is foaral wetterstof en helium atomen, en omfettet mear as 90% fan de massa fan in cluster. De temperatuer fan it gas is sa heech (10 miljoen oant 100 miljoen graden Celsius) dat de elektroanen loskomen fan de atomen (ionisaasje). It gas is dan ek net mear sichtber op weachlingtes dy ús each kin sjen, mar stjoert röntgenstrieling út. Klusters fan stjerrestelsels kinne dus it bêste wurden sjoen as enoarme gaswolken (sjoch Figuer S.5, midden).

Figuer S.5: It kluster fan stjerrestelsels Abell 2256 op trije ferskillende weachlingtes. *Links*: allinnich de stjerrestelsels binne sichtber yn ynfraread ljocht. *Midden:* yn it blau is de röntgenstrieling fan it hjitte gas tusken de stjerrestelsels sichtber. *Rjochts* it read toant de radiostrieling fan heech-enerzjyke laden dieltsjes yn it gas dy't om magnetyske fjilden bûge. Ynfraread: neoWISE (Meisner et al., 2017), röntgen: XMM-newton (Rajpurohit et al., 2023), radio: LOFAR (Osinga et al., 2023a), byldoerlap: Frits Sweijen

[8] Hjir negeare wy tsjustere matearje, wat it grutste part fan de massa yn beslach nimt, mar net de fokus is fan dit ûndersyk. Mei tsjustere matearje derby hawwe klusters in totale massa fan hûnderten oant tûzenen biljoenen sinnesmassa's ($> 10^{14} M_{\odot}$).

Klusters foarmje en groeie noch hieltyd, troch stof en gas oan te lûken út har omjouwing en troch botsingen mei oare klusters. Botsingen fan twa klusters binne enoarm enerzjyk en soargje derfoar dat it gas skodde en skokke wurdt. De laden dieltsjes yn it gas, protoanen en elektroanen (dy't fan inoar skieden binne om't it gas sa hjit is), kinne fersneld wurde ta faasjes dy't ticht by de ljochtfaasje lizze troch de skokweagen en turbulinsje yn it gas. Yn de oanwêzigens fan in magnetysk fjild wurde de elektroanen it meast ôfbûgd en sille se radiostrieling útstjitte. Dy radiostrieling is sichtber mei teleskopen lykas de *Low-Frequency Array* (LOFAR), wêrfan de kern yn Drenthe stiet. LOFAR is benammen geskikt foar dit soarte fan waarnimmingen, omdat de dieltsjes foaral radiostrieling útstjoere by lege frekwinsjes, oftewol lange weachlingtes (sjoch Figuer S.5, rjochts).

Wy sjogge oer it algemien trije ferskillende klassen fan radiostrieling yn klusters. Earst binne der *radiohalo's*, grutte rûne radiostruktueren yn it midden fan klusters. De ljochtsterkte fan radiohalo's folget rûchwei de ferdieling fan it hjitte gas, dus se binne helderder yn it sintrum en wurde swakker nei de bûtenkant fan de klusters. Wy tinke dat radiohalo's benammen in dieltsjesfersnellingproses sjen litte dat feroarsake wurdt troch de turbulinsje yn it gas. Twads binne der *radioskokken*, dy't sa neamd binne om't se lange en útstrekke struktueren hawwe dy't faak skokweagen yn it gas folgje. Hjir wurde elektroanen fersneld troch skokweagen dy't ûntstean by grutte botsingen fan klusters. As lêste komt der soms ek noch radiostrieling fan de stjerrestelsels sels. As in supermassyf swart gat, dat yn it sintrum fan hast alle stjerrestelsels leit, genôch matearje om him hinne hat, wurdt in stjerrestelsel aktyf neamd. In part fan 'e matearje om sa'n swart gat hinne wurdt opslokke, mar in part wurdt ek útstjitten yn de foarm fan twa ymminske fonteinen, of radiojets. Dy jets binne faak folle grutter as it stjerrestelsel sels, mei ôfmjittingen oant in pear miljoen ljochtjier[9]. As dizze stjerrestelsels mei jets troch it hjitte gas fan it kluster bewege, wurde jets faak ôfbûge en sjogge wy in ryk ferskaat oan foarmen. Radiojets komme net allinnich yn klusters foar, om't alle stjerrestelsels, ek dy bûten klusters, in aktyf swart gat hawwe kinne. Wol tinke wy dat de radiojets in wichtige boarne wêze kinne fan enerzjyke elektroanen dy't stadichoan troch it kluster ferspriede kinne en opnij fersneld wurde as klusters botse.

Magnetyske fjilden

It feit dat wy radiostrieling sjen komme fan klusters betsjut dat der magnetyske fjilden moatte wêzen yn it gas. Dat komt om't de radiostrieling de skaaimerken hat fan synchrotronstrieling, dy't útstjoerd wurdt troch laden dieltsjes yn in magnetysk fjild. It is lykwols in grut mystearje hoe't dizze magnetyske fjilden ûntstien en ûntwikkele binne yn de romte tusken de stjerrestelsels. De bêste teory is dat de magnetyske fjilden yn klusters stadichoan groeid binne by it foarmingsproses fan klusters fanút in swak magnetysk fjild, dat al oanwêzich is by it ûntstean fan de klusters. Mar de oarsprong fan it earste magnetyske fjild is noch net fêststeld. Der binne twa tinkwizen foar de oarsprong fan de magnetyske fjilden. Se kinne in fûneminteel diel fan it Universum wêze, makke krekt nei de Oerknal of by de foarming fan de earste struktueren yn it hielal (*de fûnemintele oarsprong*), of se kinne letter yn de romte slingere wurde troch supernova-eksploazjes en aktive stjerrestelsels (*de*

[9] Om dizze ûnbefetlike skaal dochs wat kontekst te jaan: de ôfstân fan de Ierde oant de Sinne is likernôch 8 ljochtminuten, en de ôfstân fan de Ierde ta it sintrum fan de Molkewei is likernôch 26.000 ljochtjier.

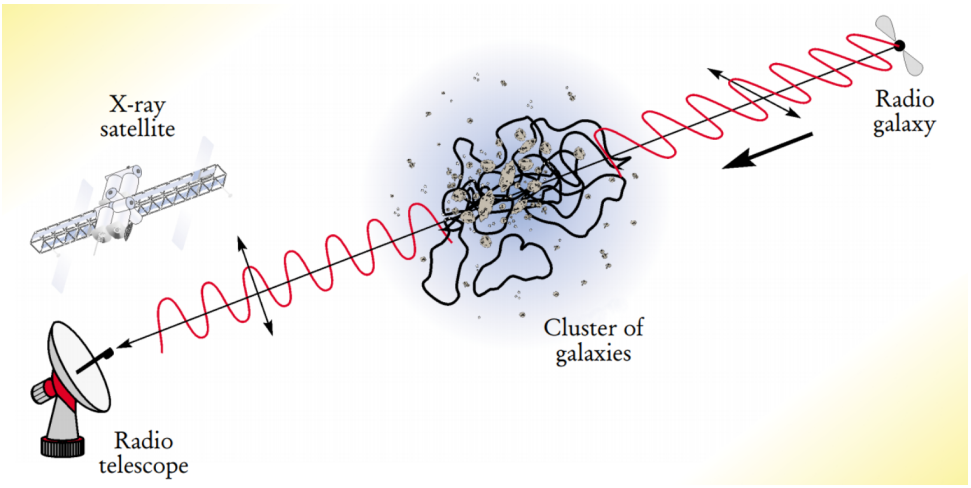

Figuer S.6: In yllustraasje fan it Faraday-effekt. In fier aktyf stjerrestelsel stjoert polarisearre radiostrieling út mei in elektryske fjildweach yn in bepaalde hoeke. As de weach it magnetyske gas fan it kluster berikt, wurdt de hoeke draaid, ôfhinklik fan de weachlingte fan it ljocht en de eigenskippen fan it gas. Dizze rotaasje is te sjen mei in radioteleskoop dy't op ferskillende weachlingtes waarnimt. Ôfbylding: Philipp P. Kronberg, Physics Today, Desimber 2002.

astrofysyske oarsprong). Wat de oarsprong ek is, magnetyske fjilden hawwe in wichtich effekt op hoe't enerzjy troch it hjitte gas ferfierd wurdt, en hoe't dieltsjes fersneld wurde by botsingen fan klusters. Oer de eigenskippen fan de hjoeddeiske magnetyske fjilden is lykwols net folle bekend. De meast effektive metoade om de eigenskippen fan magnetyske fjilden yn klusters fêst te stellen, is troch it Faraday-effekt (sjoch Figuer S.6). Om't ljocht in elektromagnetyske weach is, mei in elektryske en in magnetyske fjildweach dy't leadrjocht steane op de bewegingsrjochting (en leadrjocht op inoar), binne der in protte mooglike oriïntaasjes fan de elektryske fjildweach. As dit mar ien spesifike oriïntaasje hat, neame wy it ljocht (lineêr) polarisearre. De polarisaasjehoeke wurdt draaid als ljocht troch in magnetysk gas giet, lykas dy yn klusters. Hoefolle graad de hoeke draait hinget ôf fan de krêft fan it magnetyske fjild, de tichtens fan de frije elektroanen yn it gas, en de weachlingte fan it ljocht. Troch op ferskate weachlingtes tagelyk te observearjen mei in radioteleskoop, en in röntgenteleskoop te brûken om de tichtens fan de frije elektroanen te bepalen, kinne eigenskippen fan it magnetysk fjild ôflaat wurde. In probleem mei stúdzjes fan it Faraday-effekt is lykwols dat polarisearre radioboarnen frij seldsum binne, en dêrom binne tige djippe observaasjes fan neiste klusters nedich om genôch polarisearre radioboarnen te finen. As alternatyf kinne waarnimmingen fan ferskate clusters boppe inoar steapele wurde. Mei de (grif sterke) oanname dat alle clusters likernôch itselde syn, kinne dan trochsneed eigenskippen fan it magnetysk fjild yn clusters bepaald wurde.

Dit proefskrift

Dit proefskrift ûndersiket it dieltsjesfersnellingsproses en de magnetyske fjilden dy't liede ta de radiostrieling yn klusters fan stjerrestelsels. Begrip fan dizze ûnderwerpen sil

ús helpe mear te learen oer it proses fan klusterfoarming, om't klusterbotsingen sterk ferbûn binne oan it fersterkjen fan it magnetysk fjild en it fersnellen fan dieltsjes. It dieltsjesfersnellingsproses kin it bêste bestudearre wurde by lege frekwinsjes (~ 100 MHz), wêrfoar LOFAR by útstek geskikt is. Magnetyske fjilden, oan 'e oare kant, wurde it bêste ûndersocht by hegere frekwinsjes (~ 1000 MHz), om't it Faraday-effekt sa sterk wurdt by legere frekwinsjes dat de polarisaasje eigenskippen ferlern gean. Dêrom wurdt yn dit proefskrift The Karl G. Jansky Very Large Array (VLA), in teleskoop yn New Mexico, brûkt om de magnetyske fjilden yn klusters better te begripen.

Yn **Haadstik 2** wurdt de oriïntaasje fan radiojets fan aktive stjerrestelsels ûndersocht. Eardere ûndersiken hawwe útwiisd dat de oriïntaasje fan radiojets net willekeurich is oer grutte stikken fan de himel, mar dat jets fan stjerrestelsels dy't tichter byinoar ferskine yn 'e himel faak yn deselde rjochting wize. Dit soe sterke gefolgen hawwe foar de foarming fan de struktuer fan it Universum. Mar, lytse systematyske mjitflaters kinne liede ta ferkearde resultaten. It is dêrom wichtich om ek de ôfstân fan de radiojets oan 'e Ierde mei te nimmen (troch de readferskowing fan it aktive stjerrestelsel) en te mjitten oft de jets dy't fysyk ticht byinoar steane (yn 3D) echt yn deselde rjochting wize of dat allinne sa lykje te dwaan oan 'e himel (yn 2D). Troch in stekproef te nimmen fan 7.555 dúdlike radiojets út 'e *LOFAR Two Meter Sky Survey* (LoTSS) wurdt de nulhypoteze hifke dat de radiojets gjin foarkarsrjochting hawwe yn 3D en 2D. Wy fine bewiis dat de nulhypoteze net kloppet yn 2D, wat betsjut dat radiojets fan stjerrestelsels dy't ticht byinoar likje oan de himel in foarkarsrjochting hawwe. Wy fine lykwols gjin bewiis dat de nulhypoteze yn 3D ferkeard is, wat derop wiist dat der wierskynlik ûnbekende systematyske mjitflaters yn de data sitte en de oriïntaasje fan de jets yn it Universum wier willekeurich is op grutte ôfstannen.

Yn **Haadstik 3** wurdt ûndersocht oft lytsere klusters fan stjerrestelsels, mei legere massa en dêrtroch minder enerzjike botsingen as oant no ta ûndersocht binne, dochs noch altyd radiostrieling yn de foarm fan radiohalo's útstjitte kinne. Wy analysearren de djipste radiokaarten dy't ea makke binne op 'e frekwinsje fan 150 MHz, as ûnderdiel fan 'e *LOFAR Two Metre Sky Survey Deep Fields*. De waarnimmingen lieten sjen dat der in kluster wie mei in relatyf lege massa (mar 300 biljoenen sinnemassa's), ek noch op in frij hege readferskowing (z=0.77), dy 't in radiohalo sjen liet. Ek yn in oare kluster mei in wat legere massa is in mooglike deteksje dien. Yn kombinaasje mei boppegrinzen dy't steld wurde kinne foar klusters dêr't gjin radiostrieling wei kaam, wiene de resultaten yn oerienstimming mei de bekende relaasje tusken kluster massa en radiohalo ljochtsterkte, al wie de stekproef lyts.

Yn **Haadstik 4** wurdt LOFAR ta it uterste dreaun, mei observaasjes fan it kluster fan stjerrestelsels Abell 2256 oant de uterst lege frekwinsje fan 16 MHz. Dit is lestich om't de boppeste leech fan de atmosfear, de ionosfear, radiostrieling op lege frekwinsjes sterk ôfbûgd en fan rjochting feroaret. Lykwols slagget it om goede kwaliteit LOFAR bylden fan Abell 2256 tusken 16 en 168 MHz te meitsjen, wêryn wy de radioskok, radiohalo en ferskate oare radioboarnen detektearje en ûnderskiede. Troch fergeliking mei literatuergegevens op hegere frekwinsjes, mjitte wy it yntegrearre spektrum fan de radiohalo op tusken 24 en 1500 MHz en de radioskok tusken 24 en 3000 MHz. Beide fertoane se ienfâldige machtswetten, wêrby 't de radiostrieling S fûler wurdt by leagere frekwinsje ν as $S \propto \nu^{\alpha}$, mei $\alpha = -1,56 \pm 0,02$ foar de radiohalo en $\alpha = -1,00 \pm 0,02$ foar de radioskok. Ek wurdt in nije boarne fan âld radioplasma detearre mei in ekstreem steil spektrum ($\alpha = -1,90 \pm 0,1$)

dy't mist wie op hegere frekwinsjes. As lêste wurdt in model foar it generearen fan de radiohalo hifke mei de kombinaasje fan radio- en gammastrieling waarnimmingen.

Yn **Haadstikken 5 en 6** wurde waarnimmingen fan 124 klusters mei de VLA radioteleskoop presintearre. It doel fan dizze waarnimmingen is om statistysk de eigenskippen fan it magnetysk fjild fan klusters ôf te lieden troch de klusters opinoar te steapeljen. Der binne yn totaal 819 polarisearre radioboarnen fûn, wêrfan 't it Faraday-effekt bepaald is. **Haadstik 5** presintearret de analyze fan de depolarisaasje fan de radiosinjalen. Foar it earst wurdt in dúdlike trend waarnommen dêr't polarisearre boarnen efter klusters (lykas yn Figuer S.6) stadichoan mear depolarisearje neigeraden dat de projektearre ôfstân ta it sintrum fan it kluster ôfnimt. Mei help fan röntgengegevens fan de saneamde *Chandra* teleskoop wurde teoretyske modellen ferlike mei de data, en wurde sa de eigenskippen fan de magnetyske fjilden fêststeld. **Haadstik 6** ferbetteret dizze analyse troch ynformaasje fan de Faraday-rotaasje fan de polarisaasjehoeke ta te foegjen. Wy sjogge in dúdlike tanimming yn de fariânsje fan de rotaasjemjitten nei it sintrum fan klusters, yn oerienstimming mei in trochsneed magnetyske fjildsterkte fan sa likernôch $3\,\mu$G. Troch de depolarisaasje en rotaasjemaat te kombinearjen en te ferlykjen mei in model, wurdt de bêste oerienstimming fûn foar in magnetysk fjild mei in sintrale sterkte fan $B = 5\,\mu$G dat ôfnimt mei de tichtens n fan it hjitte gas as $B \propto n^{0.5}$. Yn it bêst oerienkommende model fluktuearret it magnetysk fjild op skalen fan mear as in miljoen ljochtjier, wat tsjut op turbulinsje dy 't op grutte skalen opwekt wurdt, bygelyks troch botsingen fan klusters.

List of Publications

Part of this thesis.

First Author

1. **E. Osinga**, R. J. van Weeren, L. Rudnick, F. Andrade-Santos, A. Bonafede, T. Clarke, K. Duncan, S. Giacintucci, Tony Mroczkowski, H. J. A. Röttgering, *Probing cluster magnetism with embedded and background radio sources in Planck clusters*, A&A to be submitted.

2. **E. Osinga**, R. J. van Weeren, G. Brunetti, R. Adam, K. Rajpurohit, A. Botteon, J. R. Callingham, V. Cuciti, F. de Gasperin, G. K. Miley, H. J. A. Röttgering, T. W. Shimwell, *Probing particle acceleration in Abell 2256: from to 16 MHz to gamma rays*, A&A submitted.

3. **E. Osinga**, R. J. van Weeren, F. Andrade-Santos, L. Rudnick, A. Bonafede, T. Clarke, K. Duncan, S. Giacintucci, Tony Mroczkowski, H. J. A. Röttgering, *The detection of cluster magnetic fields via radio source depolarisation*, A&A, 665, A71 (2022)

4. **E. Osinga**, R. J. van Weeren, J. M. Boxelaar, G. Brunetti, A. Botteon, M. Brüggen, T. W. Shimwell, A. Bonafede, P.N. Best, M. Bonato, R. Cassano, F. Gastaldello, G. di Gennaro, M. J. Hardcastle, S. Mandal, M. Rossetti, H. J. A. Röttgering, J. Sabater, C. Tasse, *Diffuse radio emission from galaxy clusters in the LOFAR Two-metre Sky Survey Deep Fields*, A&A, 648, A11 (2021)

5. **E. Osinga**, G. K. Miley, R. J. van Weeren, T. W. Shimwell, K. J. Duncan, M. J. Hardcastle, A. P. Mechev, H. J. A. Röttgering, C. Tasse, W. L. Williams, *Alignment in the orientation of LOFAR radio sources.*, A&A, 642, A70 (2020)

Contributing author

1. C. J. Riseley, N. Biava, G. Lusetti, A. Bonafede, E. Bonnassieux, A. Botteon, F. Loi, G. Brunetti, R. Cassano, **E. Osinga**, K. Rajpurohit, H. J. A. Rottgering, T. Shimwell, R. Timmerman, R. J. van Weeren, *A MeerKAT-meets-LOFAR study of Abell 1413: a moderately disturbed non-cool-core cluster hosting a* $\sim$ *500 kpc mini-halo*, MNRAS, 524, 4 (2023).

1. M. Simonte, H. Andernach, M. Brüggen, P. N. Best, **E. Osinga**, *Revisiting the alignment of radio galaxies in the ELAIS-N1 field*, A&A, 672, A178 (2023)

2. K. Rajpurohit, **E. Osinga**, M. Brienza, A. Botteon, G. Brunetti, W. R. Forman, C. J. Risely, F. Vazza, A. Bonafede, R. J. van Weeren, M. Brüggen, S. Rajpurohit, A. Drabent, D. Dallacasa, M. Rossetti, A. S. Rajpurohit, M. Hoeft, E. Bonnassieux, R. Cassano, G. K. Miley, *Deep low-frequency radio observations of Abell 2256. II. The ultra-steep spectrum radio halo*, A&A, 669, A1 (2023)

3. K. Rajpurohit, R. J. van Weeren, M. Hoeft, F. Vazza, M. Brienza, W. R. Forman, D. Wittor, P. Dominguez-Fernandez, S. Rajpurohit, C.J. Risely, A. Botteon, **E. Osinga**, G. Brunetti, E. Bonnassieux, A. Bonafede, A.S. Rajpurohit, C. Stuardi, A. Drabent, M. Brüggen, D. Dallacasa, T.W. Shimwell, H. J. A. Röttgering, F. de Gasperin, G. K. Miley, M. Rossetti, *Deep Low-frequency Radio Observations of A2256. I. The Filamentary Radio Relic*, ApJ, 927, 1 (2022)

4. G. di Gennaro, R. J. van Weeren, R. Cassano, G. Brunetti, M. Brüggen, M. Hoeft, **E. Osinga**, A. Botteon, V. Cuciti, F. de Gasperin, H. J. A. Röttgering, C. Tasse, *A LOFAR-uGMRT spectral index study of distant radio halos*, A&A, 654, A166 (2021)

5. D. N. Hoang, T. W. Shimwell, **E. Osinga**, A. Bonafede, M. Brüggen, A. Botteon, G. Brunetti, R. Cassano, V. Cuciti, A. Drabent, C. Jones, H. J. A. Röttgering, R. J. van Weeren, *LOFAR detection of a low-power radio halo in the galaxy cluster Abell 990*, MNRAS, 501, 1 (2020)

6. A. Botteon, R. J. van Weeren, G. Brunetti, F. de Gasperin, H.T. Intema, **E. Osinga**, G. di Gennaro, T.W. Shimwell, A. Bonafede, M. Brüggen, R. Cassano, V. Cuciti, D. Dallacasa, F. Gastaldello, S. Mandal, M. Rossetti, H. J. A. Röttgering, *A giant radio bridge connecting two galaxy clusters in Abell 1758*, MNRAS Letters, 499, 1 (2020)

Curriculum Vitæ

Erik Osinga

I was born on 28 December 1995 in Amsterdam, the Netherlands, and grew up in the nearby city of IJmuiden. Perhaps I was subconsciously influenced to pursue astronomy because I lived in a neighbourhood full of streets named after constellations or asterisms. I grew up in the *Lierstraat* (Lyra street), just adjoining streets such as the *Perseusstraat* and the *Herculesstraat*, and attended a primary school called *de Pleiaden* (The Pleiades). When I was 12, we moved to Drachten, Friesland, where I went to high school and started to be consciously interested in astronomy. I remember the elective course *Natuur, Leven en Technologie* (Nature, Life and Technology), which really sparked my interest in (astro)physics as we could study any subject we wanted. I wrote a report on time dilation, the fact that time flows differently for observers who are experiencing different gravitational forces or are moving with respect to each other. The fact that the Universe legitimately adheres to these bizarre rules that seem like science fiction made a big impression on me, which has never really gone away.

After high school, I started the Bachelor's program in astronomy at Leiden University in 2014. In the first year, I came into contact with programming and realised its importance in modern astronomy. Luckily, I loved that as well and thus pursued a minor in Data Science. I graduated with a Bachelor of Science in 2017. Opportunely, that year was the first year that the Master's programme *Astronomy & Data Science* was offered, which I immediately signed up for. During my Master's programme, I was introduced to scientific research through various projects. I did a research project in the Low-Frequency Array (LOFAR) group on the alignment of radio galaxy jets, which was the seed that sparked my interest in a PhD and would develop into the first publication of my PhD two years later. I graduated (cum laude) in 2019, with a graduation project on using machine learning to extract the optimal amount of information from future weak lensing surveys.

My PhD started in October 2019, a study of magnetic fields and particle acceleration in galaxy clusters with state-of-the-art radio telescopes, supervised by Prof. Huub Röttgering and Dr. Reinout van Weeren. I worked mainly with LOFAR and The Karl G. Jansky Very Large Array but have also had the opportunity to observe on-site with the Isaac Newton Telescope on La Palma and the IRAM 30m telescope on the Sierra Nevada mountain range in Spain. During my PhD, I supervised various students: two Master's students, one Bachelor's student and a summer student as part of LEAPS. In the spring of 2022, I spent just over two months in Bologna visiting the INAF-IRA Istituto di Radioastronomia, where I worked with Dr. Gianfranco Brunetti on theoretical models of particle acceleration in galaxy clusters. In the first half of my PhD, many conferences were online due to the COVID-19 pandemic, but I was fortunate enough to be able to present my work at various

in-person conferences as well, such as the LOFAR KSP meeting in Turin (Italy), the GLOW meeting in Garching (Germany), the LOFAR Family meeting in Cologne (Germany), the IAU General Assembly in Busan (South-Korea), and SPARCS XI near Johannesburg (South Africa). I had a lot of fun in various other activities as well, such as managing the setup of the Radio Galaxy Zoo: LOFAR citizen science project, for which I have given a few interviews, writing a Zenit article on my PhD research, organising the PhD talks at the Sterrewacht, and organising scavenger hunts and various other social activities for new PhD students.

Starting in December 2023, I will move to Toronto, Canada, to work as a postdoctoral researcher as part of the POSSUM (Polarisation Sky Survey of the Universe's Magnetism) collaboration. There, I will continue studying magnetic fields in galaxy clusters and the Universe.

Acknowledgments

As with many acknowledgements, the list of people to thank is too long, and written too hastily in the stressful final stages of finishing a draft, to not inadvertently miss a few people. I hope I have referenced everyone, but if not, please know that I value all the interactions I had during my PhD.

First, I have to thank my supervisors, Huub and Reinout. During the applications for a PhD, I was in doubt about which of your projects I would put highest on the preference list, but in the end, decided to go with the project more focused on radio astronomy. I am happy that I did, not just because of the science, but also because I feel like this way I got the best of having you both as supervisors. Huub, thanks for always being critical, stimulating discussions and showing me how to think bigger. Reinout, I cannot thank you enough for your input, enthusiasm, and incredible engagement. In my opinion, you are the best supervisor walking around the Sterrewacht. I do not know how you do it but, as Gabriella once hypothesised, I would not be surprised if you reveal at some point that you were actually twins the whole time, like in *The Prestige*.

To the great people of the 2019 PhD year: Anniek, Evgenii, Maite, Margot, Marta, Pooneh, Roland, Sun-Sheng, Yapeng, and Zhenlin, I am glad to have made this journey with you all. I really enjoyed our weekend getaways where we tried to figure out who was lying when they said they were liberal. Marta, we had some great workouts together, and I'm very glad that after some doubts you decided to come on the PhSki trip to be part of the best ski house. Anniek, Roland, my LOFAR siblings, I am very happy to have started and finished the journey of the PhD with you both so closely. Anniek, I loved all the (friendly) competitions we had, from board games to bowling, and *I know it is not a competition but...* congratulations on winning the PhD by finishing first. Roland, you are one great guy, I was absolutely sure of that when, after having only just met, you showed up to my birthday in Drachten during the Christmas break to party with random people. It is unfortunate that you have such poor taste in what constitutes a great MOBA, but your movie night hosting skills make up for it. Many thanks also to Christian and Jurjen (completing *Reinout's Radio Rascals*), with whom we four make a pretty good travel gang that knows how to make the best use of a conference trip. I particularly appreciated the ease with which we all just clicked when travelling together, and I hope we will still get to do that in the next few years.

The LOFAR group has many layers, and the Leiden group is quite a close family within the whole collaboration, with many people to thank. Frits, I am glad we shared the intimate moment of your first kapsalon. Maria, thanks for your yoga sessions in lunch breaks while on safari. Rafael and Martijn, the philosophical discussions we had during the LOFAR Family meeting have really stuck with me, but unfortunately COVID kind of got in the way of spending more time together. Andrea, Gabriella, Joe, Kim, Sarah, Tim, Wendy and George, thanks for being great examples to look up to on how to be a good researcher and person. The broader European LOFAR collaboration was also a great family to be in. I cannot name everyone here as the list would be too long, but if we shared a drink at

one of the LOFAR Family Meetings, you know who you are. One highlight was getting to know the Italian side of the collaboration and in particular, visiting Bologna. Gianfranco, many thanks for hosting me (and Reinout & Huub for pushing me to go) and Luca thanks for being a great host. I should also thank the whole gang of PhDs there for the instant inclusion of me (and Tjissa) in their group, and Xavi for teaching us how to lead climb!

The Sterrewacht in Leiden is a great place to work. The astronomy department, although of course not perfect, is a social bundle of joy with many activities and borrels. I am grateful to the IT department for keeping everything running so smoothly, and for their very rapid response time to all my questions. I also want to express my gratitude to the secretariat for so seamlessly managing all the administrative work that I rarely had to worry about it. Some highlights of my time at the Sterrewacht were the barbecues (including swimming at the beach), playing secret Sinterklaas, and random or themed house parties, I thank everyone with whom I have shared those moments. A big highlight was the ski trip, where I first learned how to ski together with Silvia, Alessia, Josh, Marta and Timo, and had a great time in house Gryffindor thanks to Amy, Anniek, Chris, Billy, Jelle, Mantas and Marta. Mantas, also thanks to you in particular for being my thesis design sempai, but that does not mean I will go easy on you next time.

Although nearly forgotten, I also had a life at the Sterrewacht before the PhD. To the *Bierspons* gang, who have been with me since I first stepped foot into the observatory nine long years ago, and without whom I would probably not have made it into the PhD: thanks Auke, Chris, Couzy, Jelle, Joey, Len and last but not least: Jonah (it's you and me, baby, let's destroy the Universe together). Thanks for all the good times and rants we shared about professors, coursework, cosmology and Karels. I love the hiking trips we take together (except the Toubkal before lunch), and honestly can anyone name a more iconic duo than astronomers and mountains?

It is also greatly important to be surrounded by non-astronomers. To the set of friends I made for exploring my new hobby of bouldering and dungeons: Tom, Noah, Stefan, Guilia, Marije, Daan and Wessel: thanks for the good times, (on the subject of bouldering, it is still impossible to avoid astronomers, so I should say I am also grateful for the fun sessions with Billy, Elia, Jinyi, Thijs and Timo). Thanks to the boys from *de Klik* for a great place to blow off steam with all the great 'workouts': Jivan, Jorik, Boudewijn, Dick, Guido, Pieter, Stan, Siem, Lennart and Emile. And of course, Steef for keeping the old guard together, and focused on our touring life. To friends that have stuck with me from *the before times* even throughout the PhD, especially Axel, Floris and Robin, you guys are real life-long friends. Although I am not the best at keeping in touch, I will try my best to keep those friendships alive and thriving.

Aan mijn ouders en broertje. Bedankt voor de onvoorwaardelijke liefde en steun in alles wat ik doe. Al is er soms misschien zelfs te veel zorg, zoals opa altijd zegt: het barst van de goede bedoelingen. Ik snapte dat als tiener misschien nog niet zo, maar dat realiseer ik me nu heel goed. *Heitie* en *Memmie*, bedankt voor mij zo snel op te nemen als één van de de Witjes, en bedankt voor de Friese samenvatting proeflezen. Lastly, and therefore most importantly, Tjissa. You are my biggest supporter, I cannot thank you enough for everything, you make my life an immeasurable amount of times better. You were present to some extent in literally everything mentioned above, and I would not have wished it any other way. You are my Universe.